Parity-Violating Elastic Electron Nucleon Scattering:
Measurement of the Strange Quark Content of the Nucleon and Towards a Measurement of the Weak Charge of the Proton

Juliette M. Mammei

Dissertation submitted to the Faculty of the
Virginia Polytechnic Institute and State University
in partial fulfillment of the requirements for the degree of

Doctor of Philosophy
in
Physics

Mark L. Pitt, Chair
Marvin Blecher
Tetsuro Mizutani
Beate Schmittmann
Bruce Vogelaar

April 30, 2010
Blacksburg, Virginia

Keywords: Strange quark, transverse, beam normal single spin asymmetry, G0, Qweak

Parity-Violating Elastic Electron Nucleon Scattering:
Measurement of the Strange Quark Content of the Nucleon
and Towards a Measurement of the Weak Charge of the Proton

Juliette M. Mammei

ABSTRACT

The experiments discussed in this thesis exploit parity violation in elastic electron proton scattering in order to measure properties of the nucleon. Both experiments make use of the high quality, highly polarized electron beam available at Thomas Jefferson National Accelerator Facility. Q_{weak} will measure the weak mixing angle, $\sin^2\theta_W$, via a measurement of the weak charge of the proton, at a four-momentum transfer, $Q^2 \sim 0.026\ GeV^2/c^2$. The precision of this measurement gives Q_{weak} access to new physics at the scale of 2.3 TeV, making it a test of the standard model. The G^0 experimental program provides the fully separated contributions of the strange quark to the charge and magnetization distributions of the nucleon at two different values of four-momentum transfer, $Q^2 \sim 0.22$ and $0.63\ GeV^2/c^2$. The measurement of the strange quark content of the proton in the G^0 experimental program and other parity-violating electron scattering experiments provides a measurement of the hadronic contribution to the asymmetry in Q_{weak}.

In addition, G^0 was able to measure the parity-conserving beam normal single spin asymmetries that provide a measurement of the imaginary part of two photon exchange. The measurement of this asymmetry is necessary to understand the systematic contribution to measurements of parity-violating asymmetries, but it is also an important physics result. Recent theoretical work has shown that higher order radiative effects, such as two photon exchange, may be able to explain discrepancies between experiments which measure the ratio of the electric and magnetic form factors of the proton. The measurement of the transverse or beam normal single spin asymmetries provides a benchmark for theories that estimate the size of radiative corrections that are important for precision electroweak scattering experiments such as those described in this thesis. The results of the measurement of the transverse asymmetries at backward angles in G^0 are presented at the two values of $Q^2 \sim 0.22$ and 0.63 GeV^2/c^2 for hydrogen. Results for deuterium, which can provide the first measurements of the beam normal single spin asymmetries on the neutron, are also presented.

This work was funded by the NSF, Virginia Tech, DOE

Dedication

This thesis is dedicated to my son Ethan, who missed me while I was writing...

It really is for you, baby boy - someday I hope you'll understand!

Acknowledgments

First I would like to thank my advisor, Mark Pitt. It has been a privilege to have the opportunity to learn from him during my tenure as a graduate student at Virginia Tech, and I am happy that we will continue to be colleagues and collaborators on future experiments. Not only is he an intelligent and well-respected scientist, I appreciate that he is able to bring humor to most situations (although I admit I still sometimes can't tell when he's joking). He helped me when I needed help and pushed me when he knew I didn't. It is my hope that people see a reflection of his integrity and scientific ability in me as I venture into the world as a professional physicist.

Without the loving, patient support of my family I would never have finished my thesis. Thanks to my husband who took up the slack in the parenting department so that I could work in the evenings and on weekends without feeling too guilty about not spending time with our son, Ethan. And special thanks to my mom who gave up her life and living near her sisters and her son in order to help us take care of her grandson. Thank you for helping me to fulfill all of my dreams. Thanks to my father, for teaching me that 'science fact' can be as much fun as 'science fiction'. I am grateful to have such a wonderful baby boy - for whom this work is dedicated - Ethan, thanks for cheering me up when my spirits were down and giving me a reason to go on.

I would of course like to thank the Q_{weak} and G^0 Collaborations (there is quite a bit of overlap). There are too many of them to name each individual, but I would especially like to thank my Hall C colleagues who have known me since I was in metaphorical physics diapers - during my first internship at the lab - Dave Mack and Greg Smith. Thanks for teaching me that 'excellence is the enemy of good enough'. Thanks to Dave Armstrong for vouching for me to the G^0 Collaboration when it became apparent that Q_{weak} wasn't going to run in my lifetime as a graduate student, and for also recommending me for my post doc position. Thanks to Doug Beck and Betsy Beise for accepting me into the G^0 backward group, unfortunately referred to as the 'B Team', despite our colorful protests. Thanks to the 'A Team' members who helped with the backward angle analysis, including Paul King, Jianglia Lui, Damon Spayde and others. Their experience with the forward angle was invaluable. And thanks to Katherine Myers for rescuing me from being the only person

simulating Q_{weak}!

I have to especially thank the other students from the G^0 backward angle running, ahem, I mean, give a shout out to my homies - 'G^0 Unit'. Besides being great analysis team members, I have to thank them for making my graduate career, well, enjoyable! I am only sorry that our home institutions were spread around the world, except for the part where we got to travel around for the 'analysis meeting tour'. Thanks to Alex Coppens for being around to chat from a distance, and to Colleen Ellis for making shifts and collaboration dinners truly interesting. I am grateful to Maud Versteegen for her endless enthusiasm, and to Carissa Capuano for her willingness to talk about life when work became too tedious. John Schaub - thank you for ensuring that we had sufficiently long lunch breaks, and Fatiha Benmokhtar for all the advice. Thanks to Mat Muether for appreciating and contributing to my sarcastic streak.

Thanks to everyone at Virginia Tech who contributed in invaluable ways, especially the VT Q_{weak} Group - Norm Morgan, Elizabeth Bonnell and John Leacock. Special thanks to the many undergrads who worked on Q_{weak}, to Tina Lawrence and Betty Wilkins for putting up with the many quirky financial issues that I brought to their desks, and to Sue Conner for lending her ear (and sharing the refrigerator). Christa Thomas - what can I say? I am honored to call you a friend and eternally grateful for all the help and support you offered over the years - I will miss you.

Contents

List of Figures

List of Tables

Chapter 1

Introduction and Theory

This thesis will describe three measurements; the first measurement of the weak charge of the proton in Q_{weak}, the fully separated contribution of the strange quarks to the spatial charge and magnetization distributions in the nucleon sea at two values of momentum transfer in G^0, and the interference of two photon exchange with single photon exchange at backward angles in G^0. All three measurements form an asymmetry to isolate the interference of a small effect with a dominant exchange mechanism in the elastic scattering of electrons from a proton (or quasi-elastic scattering from a proton or neutron in deuterium). Q_{weak} and the main G^0 measurement exploit the fact that the weak interaction violates parity while the electromagnetic interaction does not, which results in an interference term that changes sign as the helicity (the projection of the spin onto the momentum) of the incoming electron changes. The transverse (perpendicularly polarized) electron asymmetries arise because of the interference of single and two photon exchange, which also can be measured by forming an asymmetry, although in this case it is a parity-conserving asymmetry that is proportional to the projection of the polarization of the electron on the normal to the scattering plane.

Both experiments have been or will be performed in Hall C of Jefferson Lab. The Q_{weak}

experiment is an A rated experiment which will measure the weak charge of the proton. Due to its high precision it is sensitive to new physics at the TeV scale, a physics reach that is complementary to the Large Hadron Collider at CERN (see Section 1.1.4 and Chapter 2). The G^0 Experiment has measured the strange quark contribution to the charge and magnetization distributions of the nucleon, separating the strange electric and magnetic form factors and the isovector part of the effective axial form factor with a series of measurements at forward angles on the proton and at backward angles on the proton and deuteron (see Section 1.2.3 and Chapter 3). My work includes hardware and simulation for Q_{weak} and data taking and analysis for G^0.

The G^0 experiment is a rich program which consists of several auxiliary physics measurements. Measurement of parity-violating asymmetries in the N-Δ transition and single pion production, which provide information about the axial transition form factor, will be the topics of other theses. Parity-conserving transverse asymmetries in elastic electron-proton scattering arise due to the interference of single and two photon exchange (see Section 1.2.4). This asymmetry can enter the longitudinal measurement as an additive correction, so it has to be measured to place a bound on the size of the correction (see Section 4.4). There is, however, interest in two-photon exchange (TPE) as a possible explanation for discrepancies between two independent methods of measuring the ratio of the electric and magnetic form factors of the proton (see Section 1.1.3). The primary physics result presented in this thesis is the analysis of the beam normal single spin asymmetries obtained from measurements of the transverse asymmetries in the backward angle phase of G^0.

The two experiments are related theoretically and are similar experimentally. Each experiment measures the parity-violating asymmetry in elastic electron-nucleon scattering, using the high-quality polarized electron beam at Jefferson Lab (typically 85% during G^0 running). Both have 8-fold symmetry around the beam axis. A toroidal magnet is used to

bend and focus the scattered particles in each experiment to provide kinematic separation; G^0 used a superconducting magnet, while Q_{weak} will use a water-cooled copper magnet. The experiments will use a lot of the same standard Hall C equipment, such as beam current and position monitors, the Møller polarimeter and much of the same beamline (including the accelerator itself). In addition to the Møller and Mott polarimeters currently in use in Hall C, Q_{weak} will have a Compton polarimeter for continuous polarization measurements and a tracking system to measure the four momentum transfer, Q^2, because the beam polarization and $< Q^2 >$ need to be known to a higher precision than in G^0.

Both experiments will make use of the parity-violating asymmetry due to the interference of the scattering via a Z boson with the scattering via a photon. Because the experiments are run at different Q^2, G^0 ($\sim 0.12 - 1\,(GeV/c)^2$) can assume the standard model weak charges and use the known proton and neutron electric and magnetic form factors to measure the strange quark contribution. The G^0 result will be used in constraining the hadronic contribution to the asymmetry measured in Q_{weak}, allowing for a precise measurement of the weak charge of the proton at small Q^2 ($\sim 0.026\,(GeV/c)^2$). The transverse asymmetries as measured in G^0 will test the theoretical framework that calculates the electroweak radiative corrections that are important in precision electroweak experiments by providing information about the imaginary part of two photon exchange.

1.1 The Standard Model and Beyond

The standard model describes our current understanding of the fundamental particles and interactions. It is tempting to compare it to Mendeleev's periodic table of the elements, because atoms were so called because they were believed to be the fundamental, indivisible constituents of matter. We now know that atoms are made of a central nucleus surrounded

by a cloud of orbital electrons, and that the nucleus itself is made up of smaller particles. Protons and neutrons, collectively called nucleons, are in turn made of what we believe to be fundamental particles, quarks. A more appropriate comparison to Mendeleev's summary may then be the categorization of mesons and baryons seen in high energy physics according to their properties. The periodicity of the properties of the atoms was an indication of their substructure: a central nucleus and orbiting electrons, the interactions of which are responsible for the chemical properties of the atoms. The categorization of mesons and baryons into multiplets is the analog of the periodic table of the elements, indicating a substructure to the various mesons and baryons (including the nucleons).

1.1.1 Standard Model Particles and Interactions

The standard model consists of 6 quarks and 6 leptons (and their antiparticles) (see Table 1.1). There are three "generations" of matter, categorized by increasing mass. The lowest generation of matter consists of the electron and its corresponding neutrino[1], and up and down quarks (u and d). The elements which are categorized in Mendeleev's table are made of these lowest mass particles, except for the neutrino. Particles are differentiated from each other by their properties, such as mass, the familiar electric charge, and spin, as well as some additional quantum numbers. The heavier generations consist of the μ and τ leptons and the strange and charm (s and c) and top and bottom (t and b) quarks.

There are believed to be four fundamental forces, and an exchange particle to mediate each - a photon for the electromagnetic force, $W^{\pm}$ and Z^0 bosons for the weak force, gluons for the strong force and gravitons for the gravitational force. These particles are also differentiated by their properties such as mass and whether they carry "charge". The elec-

[1]If the neutrino mass hierarchy is "normal" then the lowest mass neutrino will be mostly an electron neutrino, otherwise the lowest mass neutrino may not have much to do with the electron.

Table 1.1: Summary of the standard model particles and selected properties. There are corresponding antiparticles for each of the fermions with opposite quantum numbers (neutrinos may be their own antiparticles). The charges are labeled Q with a subscript EM for the electromagnetic charge, s for the strong (or color) charge, and W for the weak charge, where the superscript V and A refer to the vector and axial-vector weak charges, respectively. The particles listed in the table are the mass eigenstates.

Fermions, Spin 1/2							
	Family			Q_{EM}	Q_W^V	Q_W^A	Q_S
	1	2	3				
Leptons	ν_1	ν_2	ν_3	0	1	-1	
	e	μ	τ	-1	$-1+4\sin^2\theta_W$	+1	
Quarks	u	c	t	+2/3	$1-8/3\sin^2\theta_W$	-1	r, g, b
	d	s	b	-1/3	$-1+4/3\sin^2\theta_W$	+1	

tromagnetic and weak and strong nuclear forces have a corresponding charge that can be assigned to the various particles as a measure of how the particle couples via a particular force. The "charge" for the electromagnetic interaction is what we normally think of as charge. In addition there is a weak charge and a color charge for the strong force. Weak charges are written in terms of the weak mixing angle, and the strong color charge is red, green or blue. As a model for the strong charge, particles can only exist in "colorless" clusters, that is red, green and blue add to "white" (baryons - qqq), and a color and its anti-color add to "clear" (mesons - $q\bar{q}$).

The properties of composite particles, in the simplest models, take on the additive properties of their constituents[2]. For example the neutral weak vector charge of the neutron, the valence structure of which is two down quarks and an up quark, is -1. It is interesting to note that the sizes of the vector couplings of particles to the weak currents is the opposite of

[2]Note that the masses of the constituent quarks are not the same as the masses of the "bare" quarks (what would be measured in the limit of $Q^2 \to \infty$. Constituent quarks have a cloud of gluons and quark-antiquark pairs around them that effectively increase their size and mass.

Table 1.2: Summary of the standard model forces and mediating particles. None of the force carriers has a weak charge. Only the gluons carry color charge, and only the $W^{\pm}$ carry electric charge. They along with the Z^0 also have mass.

Bosons, Spin 1 (*or 2)				
Particle	Mediates Interaction	Mass (GeV)	Q_{EM}	Q_S
γ	Electromagnetic	0	0	0
$W^{\pm}$, Z^0	Weak	80.4, 91.2	± 1, 0	0
gluons (8)	Strong	0	0	yes
graviton*	Gravitational	0	0	0

the coupling to the electromagnetic currents. The electromagnetic charge of a proton is 1, and 0 for a neutron, but the neutral weak vector charge of the proton is very nearly 0, while the neutral weak vector charge of the neutron is -1, because $\sin^2\theta_W \sim 1/4$. Similarly for the weak and electric forces of the electron, muon and tau compared to the neutrinos. This relationship between the particles is partially reflected in the assignment of "weak isospin", the weak analog to the strong isospin that relates the neutron and proton as different isospin states of the nucleon.

This thesis is essentially concerned with the interference of the weak and electromagnetic forces, so the strong force will not be discussed in detail, and the gravitational force not at all beyond listing the particle masses and graviton properties in Tables 1.1 and 1.2. The concept of isospin in both the strong and weak forces, however, is relevant to G^0 and Q_{weak}. Strong isospin, denoted by I, was introduced to explain the fact that the strong nuclear force does not seem to distinguish protons and neutrons as separate particles; isospin invariance originates with the valence u and d quarks, which have approximately equal constituent masses ($\sim 300\,MeV/c^2$). The u(d) quarks in the proton(neutron) act like the d(u) quarks in the neutron(proton).

The neutral weak current does not couple to all particles with the same strength. The vector coupling depends on the electric charge and the third component of weak isospin, as

well as the weak mixing angle, and the axial-vector coupling depends on the weak isospin. This is explained in the unification of the electromagnetic and weak forces into the electroweak force, known as the Weinberg-Salam model. In the theory, the electroweak force is an $SU(2) \times U(1)$ gauge symmetry group. The bosons of the charged weak current form an "isospin triplet" with a third, neutral W^0 boson. The neutral bosons we see experimentally, the γ and the Z^0, are a mixture of the W^0 and the B^0 (which is the isospin singlet in the theory) in a manner similar to the mixing of the quarks via the CKM matrix

$$\begin{pmatrix} |\gamma\rangle \\ \\ |Z^0\rangle \end{pmatrix} = \begin{pmatrix} \cos\theta_W & \sin\theta_W \\ \\ -\sin\theta_W & \cos\theta_W \end{pmatrix} \begin{pmatrix} |B^0\rangle \\ \\ |W^0\rangle \end{pmatrix} \tag{1.1}$$

The parameter that describes the mixing is the electroweak mixing angle, θ_W. It is this angle that appears in the neutral weak vector charges listed in Table 1.1.

The mixing described by the Weinberg-Salam model has important implications for particle theory. Normally an isospin singlet and triplet group described by the $W^{\pm}$, W^0 and B^0 should only occur for particles of similar masses. But while the weak bosons have large masses, the photon is massless. A theoretical model that explains this was simultaneously proposed by Higgs [72] and Englert and Brout [51], who postulated that the masses of the heavy bosons are produced by scalar "Higgs" fields which are absorbed by the heavy bosons via spontaneous symmetry breaking as the universe cooled. That the photon remains massless requires, in this model, that there be a non-absorbed Higgs boson which can be detected experimentally. The Large Hadron Collider (LHC) at CERN has the search for such a particle as its primary goal.

1.1.2 Strangeness in the Nucleon

The introduction of the strange quantum number, S, was used to describe particles that were "strange", such as kaons which decay via the weak interaction (despite being produced in a strong interaction). Strange quarks, s, are the next lightest quarks after the u and d quarks. The valence quarks do not fully account for the properties of the nucleons. For example, gluons in the nucleon contribute $\sim 50\%$ to the momentum of the nucleon, though they don't affect its other quantum numbers. In addition to the valence u and d quarks present in the nucleon, there are also quark-antiquark pairs that, together with the gluons, make up a "quark sea" within the nucleon (see Figure 1.1), which makes up a relatively small fraction of the nucleon's momentum.

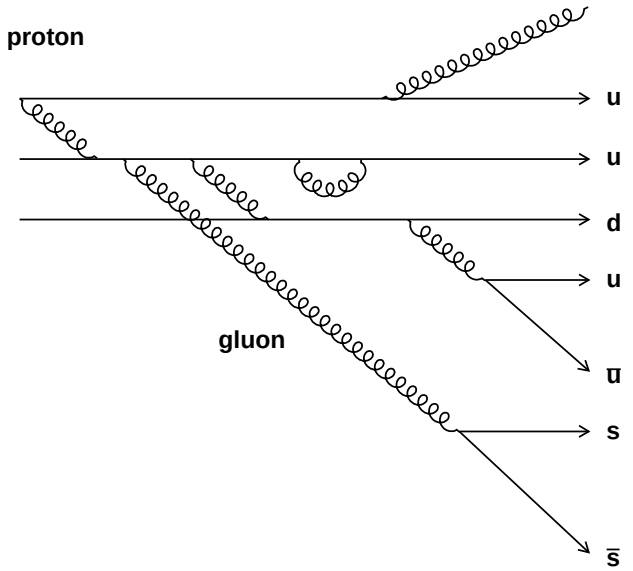

Figure 1.1: Pictorial representation of the proton as composed of strongly interacting valence u and d quarks. There is a sea of gluons as well as quark-antiquark pairs, which can be the same species as the valence quarks or $s\bar{s}$ pairs. The contribution of sea quarks with higher mass is assumed to be small.

Table 1.3: Summary of the knowledge of the strange quark contributions to the nucleon.

Property	Experimental Value	Source
Momentum	$\int_0^1 x(s+\bar{s})\,dx \approx 2\%$	ν DIS
Spin	$\langle N\vert\,\bar{s}\gamma^\mu\gamma^5 s\,\vert N\rangle \approx 0\,to\,-10\%$	Polarized DIS
Mass	$\langle N\vert\,\bar{s}s\,\vert N\rangle \approx 0\,to\,30\%$	π N - σ term

Naively one would expect that the effective contribution of the sea to the quantum numbers of the nucleon would average to zero, since the sea quarks exist only as $q\bar{q}$ pairs. We know that there is a strange quark contribution to the momentum of the proton from deep inelastic scattering (DIS) experiments, and to the nucleon mass from low energy pion-nucleon scattering data (Table 1.3). There is also evidence from polarized DIS experiments that the $s\bar{s}$ pairs may contribute as much as -10% to the nucleon spin. A difference in the spatial distribution of the s and $\bar{s}$ within the nucleon would be evident in the charge and magnetization distributions.

Charm production in deep inelastic scattering of muon neutrinos from the proton by the NuTeV collaboration provides information about the fraction of the nucleon momentum carried by the strange sea[2]. The fraction of the momentum of the strange to the non-strange sea is

$$\frac{2\int_0^1 x(s+\bar{s})\,dx}{\int_0^1 x(u+\bar{u}+d+\bar{d}\,)\,dx} \sim .42 \pm .07 \pm .06 \tag{1.2}$$

where x is the fractional momentum of the struck quark and the $s(x)$ and $\bar{s}(x)$ etc., represent the parton momentum distributions for each type of quark. This result unambiguously reveals the presence of strange quarks in the nucleon. The contribution of the light sea quarks to the nucleon momentum is about 5%[18], so the strange quark contribution to the total momentum of the nucleon is $\sim 2\%$. More recent experimental efforts have studied the difference in the distribution of the s and $\bar{s}$ distributions within the nucleon. The NuTeV experiment has measured $S^- \equiv \int_0^1 dx x[s(x) - \bar{s}(x)] = 0.00196 \pm 0.00135$[4]. Incidentally,

the $S^- \neq 0$ result affects the published NuTeV measurement of $\sin^2\theta_W$ (which assumed a symmetric strange quark sea), though not enough to explain the entire difference from the theoretical prediction (see Figure 1.4).

The contribution of the strange quarks to the nucleon spin can be measured in polarized deep inelastic scattering experiments. It is related to the axial matrix element, $\Delta q_i \sigma_\mu = \langle p, \sigma_i \left| \bar{q}_i \gamma_\mu \gamma_5 q_i \right| p, \sigma_i \rangle$, where $\Delta q_i \sigma_\mu$ defines the helicity content of the individual quarks. The cross section in these experiments, where both the incoming lepton and target are polarized, can be parameterized by two spin-dependent structure functions $g_1(x, Q^2)$ and $g_2(x, Q^2)$. The difference in the cross section for a target aligned and anti-aligned with the incident lepton is insensitive to $g_2(x, Q^2)$, and with

$$\Delta q_i = q_i \uparrow - q_i \downarrow + \bar{q}_i \uparrow - \bar{q}_i \downarrow \tag{1.3}$$

we can write $g_1(x, Q^2)$ for the proton (or neutron) as the charge weighted sum of these differences in the individual quark number densities

$$g_1(x, Q^2) = \frac{1}{2} \sum_i e_i^2 \Delta q_i \tag{1.4}$$

where contributions from c and heavier quarks are generally neglected. If one assumes $SU(3)_f$ symmetry and doesn't require the strange quark content to be zero, analysis of the experimental results for the Ellis-Jaffe[3] ($\int_0^1 g_{1p,n}(x)dx$) sum rule yields a strange quark contribution to the nucleon spin on the order of -10%[53].

The strange quark also makes a contribution to the mass of the nucleon. Quantum mechanically the mass is an eigenstate of the QCD Hamiltonian for identical initial and final states of the nucleon $M_N = \langle N \left| \mathcal{H}_{QCD} \right| N \rangle$. The πN sigma term is a measure of the

[3]It is the experimental violation of this sum rule which is referred to as the "proton spin crisis".

contribution of the quark masses to the mass of the nucleon

$$\sigma_N = \frac{\langle N \left| \bar{m}(\bar{u}u + \bar{d}d - 2\bar{s}s) \right| N \rangle}{1 - y} \tag{1.5}$$

where the scalar strange quark content of the nucleon is given by

$$y = \frac{2 \langle N \left| \bar{s}s \right| N \rangle}{\langle N \left| \bar{m}(\bar{u}u + \bar{d}d \right| N \rangle} \tag{1.6}$$

This quantity cannot be determined directly, but can be constrained by either considering leading order baryon mass differences (hyperon mass splitting [34])

$$\frac{1}{3}\left(1 - \frac{m_s}{\bar{m}}\right)(1 - y)\sigma_N = M_\Lambda - M_\Xi \tag{1.7}$$

or through dispersion relations to reach the Cheng-Daschen point in πN scattering (and relate it to $\sigma_N(0)$) [63][62]. The values are not consistent ($\sim$32 MeV and 45 $\pm$ 8 MeV) and have large error bars, but together they imply a strange quark content of $y \approx 0.2 \pm 0.2$. In fact, a more recent analysis yields an even higher value of 64 $\pm$ 7 MeV[115], or $y \approx 0.44 \pm 0.13$. The strange quark mass contribution is highly sensitive to the value of σ_N, so it is of great theoretical interest (the error of $\sim$7 MeV alone corresponds to a 90 MeV difference in the strange quark mass contribution [150]). Recent lattice QCD calculations have yielded the most accurate results, suggesting that the strangeness content is much smaller than previously thought, on the order of $y \approx 0.09$ or smaller[150].

The contributions of the strange quarks to the properties of the nucleon as summarized in Table 1.3 don't provide any information about the spatial structure of the sea, and some of them have large theoretical and experimental errors. As will be discussed in more detail in Sections 1.2.2 and 1.2.3, the charge and magnetization distributions of the nucleon can be

separated into contributions from the individual quarks. That is, if the charge or magnetization distributions of the s and $\bar{s}$ in the sea are different, it should be possible to measure the difference by exploiting a property of the weak interaction, that of parity violation. Several experiments have made measurements of the contribution of strange quarks in the sea to the nucleon's spatial charge or magnetization distributions (see Section 1.3), and G^0 has been able to successfully separate the contributions at two different values of four-momentum transfer, or Q^2 (see Appendix A).

1.1.3 Radiative Corrections and 2 Photon Exchange

As will be discussed in more detail in Section 1.2, in quantum electrodynamics (QED), whenever an exchange boson is absorbed or emitted by a particle a factor proportional to the charge of the particle enters the expression for the scattering or decay. Each particle has a different charge depending on which type of interaction is taking place. For example, the coupling constant of the electromagnetic interaction is the so-called fine structure constant, $\alpha = e^2/4\pi$, where e is the familiar electric charge. Thus a factor of $\sqrt{\alpha}$ enters at each vertex of a particle and a photon. The same is true for the strong force, where a factor of $\sqrt{\alpha_S}$ enters at each emission of a gluon.

In reality, the coupling constants are not constant, but are functions of Q^2 due to the effects of higher order radiative effects, such as e^+e^- loops which can surround an electron, for example. This is a real effect in QED that is measurable; in the interaction of an electron with a nucleus the observed "Lamb shift" can be explained by including graphs up to $\mathcal{O}(e^4)$. The inclusion of these effects results in the "running" of the coupling constant, that is $\alpha \rightarrow \alpha(Q^2)$. In a similar way, quark and anti-quark pairs surround a single quark, but because the gluons carry color charge, they can form additional loops containing just gluons.

The QED coupling constant asymptotically approaches the value of 1/137 at large distances (small Q^2), but because of the gluon loops the QCD coupling constant gets larger at large distances (confinement) and actually becomes small for large Q^2. This is the property of asymptotic freedom that allows perturbative methods (pQCD) to be used at large Q^2.

Calculations for predictions of scattering cross sections begin with the lowest order (tree-level) diagrams, and higher order terms are generally neglected, because the coupling constant is small (only at high Q^2 in QCD) and the corrections are, in general, small. But in some cases the higher order diagrams are more important than first realized. As an example, consider recent electron scattering experiments to determine the ratio of the electric and magnetic form factors of the proton, G_E^p and G_M^p, which provide the description for the charge and magnetization distributions of the proton as a function of Q^2 (see Section 1.2.2). Comparison of the results revealed a disagreement between two independent methods of obtaining the ratio (see Figure 1.2, top).

The Rosenbluth method (open pink circles in the figure) uses the kinematic dependence of the unpolarized electron-proton cross section to extract G_E^p and G_M^p separately, and then forms the ratio. At backward angles the cross section is dominated by the G_M^p, but is a combination of the two at smaller angles; at large Q^2 the dependence on G_E^p is small. The polarization transfer method (filled blue diamonds), however, is sensitive only to the ratio of $\mu_p G_E^p/G_M^p$, and so is not subject to the reduced sensitivity to G_E^p at large Q^2. In light of the discrepancy, both experiments re-examined their methods and analysis and it was determined that it was necessary to include the effect of two photon exchange (TPE), a higher order radiative correction, in the analysis of the Rosenbluth data. In order to bring the two experiments into agreement, it is necessary to apply the TPE corrections directly to the cross sections [12]. TPE corrections are not as significant in the polarization transfer method because the corrections are on the ratio $\mu_p G_E^p/G_M^p$ and are not subject to

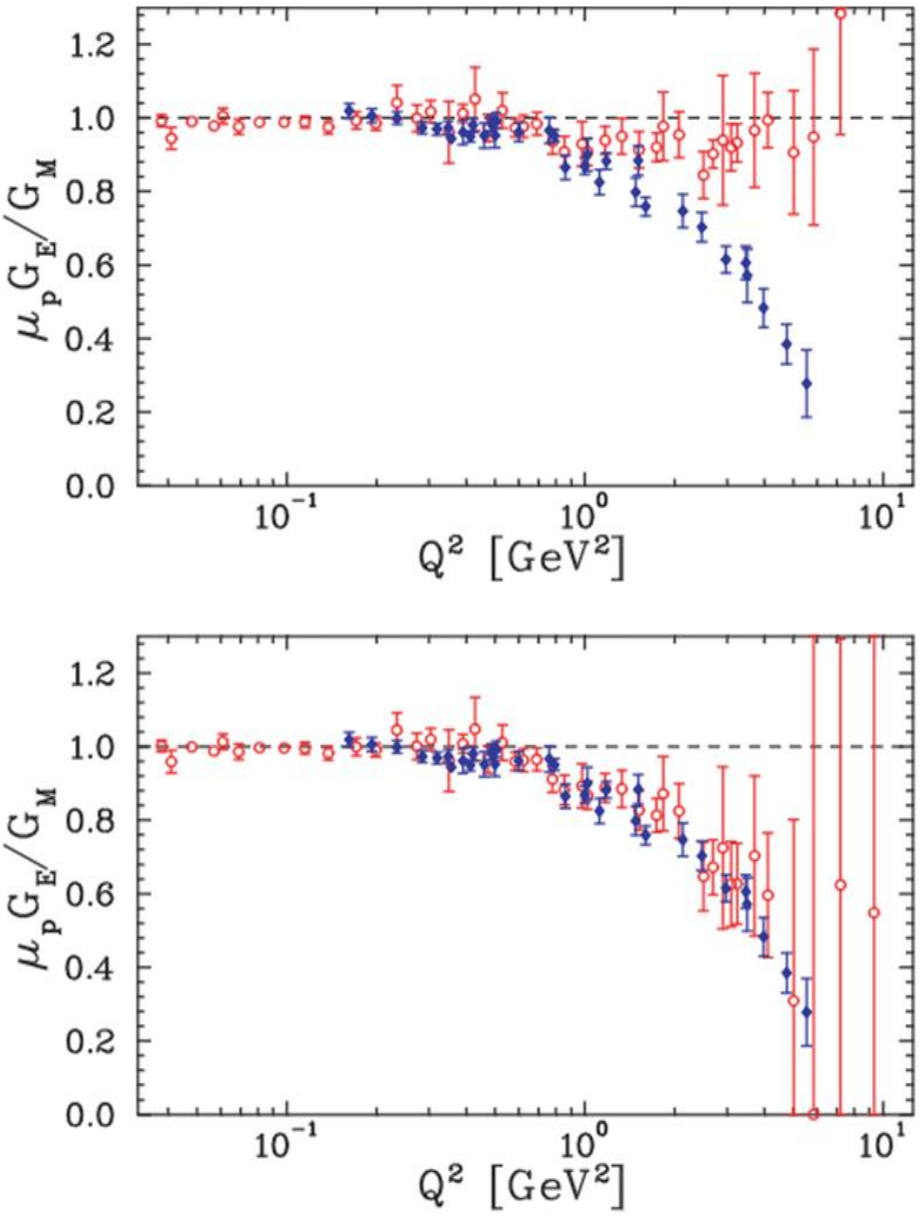

Figure 1.2: Comparison of the ratio G_E^p/G_M^p as a function of four-momentum transfer as determined from Rosenbluth separation (open pink circles) and polarization transfer measurements (filled blue diamonds)[136]. The top plot shows the discrepancy between the two datasets without the additional two photon exchange (TPE) corrections in the Rosenbluth data. The bottom plot shows the comparison with the corrected Rosenbluth data. The error bars on the Rosenbluth data in the bottom plot reflect the additional uncertainty due to the TPE correction.

the "magnification" at high Q^2.

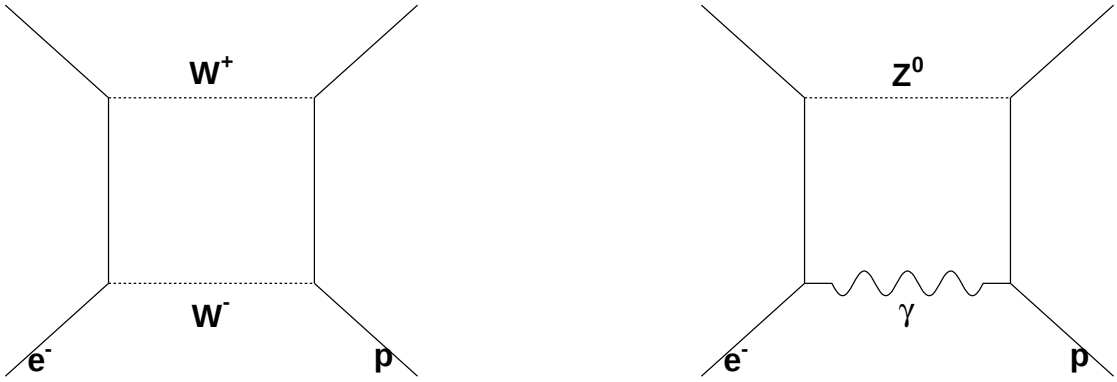

a b

Figure 1.3: Feynman diagrams showing the higher order W^+W^- (a) and γZ (b) "box" diagrams that contribute to radiative corrections, which become more important as experimental sensitivities improve.

The measurement of the transverse asymmetries in G^0 (see Section 1.2.4) provides information about the imaginary part of two photon exchange. It also helps test the theoretical framework that calculates the W^+W^- and γZ box diagrams (see Figure 1.3) which, in addition to TPE, are important radiative corrections for precision electroweak experiments such as those described in this thesis. While some estimates for corrections to the asymmetries have been made, recent dispersion calculations of such two boson exchange corrections show that they may be much larger than originally anticipated in Q_{weak}, which will run at a low Q^2 [66]. This disagrees with alternate analysis which was performed by including the intermediate hadronic states using form factors[136] (see Section 4.1.4). As the experimental precision of these electroweak experiments continues to improve, it will become more important to have a good understanding of the radiative corrections.

In addition to the higher order corrections discussed above, there is also γZ mixing, in

which the Z (γ) fluctuate into a $q\bar{q}$ pair and then into a γ (Z). These corrections involve interactions effectively with a single quark. There are additional parity-violating interactions which can occur which involve multiple quarks. For example, during the interaction with single photon exchange between the electron and proton, quarks within the proton can interact via Z exchange and while the effect is small, it is also uncertain. In other words, even with an interaction involving a single photon there can be parity violation. These effects make up the anapole moment, an effective parity-violating coupling of the photon to the nucleon[152].

1.1.4 Beyond the Standard Model

The weak coupling constant which appears in the vertex factors for charged current and neutral weak interactions, g, is related to the masses of the weak exchange bosons W$\pm$ and Z by

$$g^2 = \frac{8G_F M_W^2}{\sqrt{2}} = \frac{8G_F M_Z^2 cos^2\theta_W}{\sqrt{2}} \tag{1.8}$$

where G_F is the Fermi constant. The relevant standard model parameter is $sin^2\theta_W$, which appears in the neutral weak vector charges of the standard model particles, and in the electroweak theory g is related to the electromagnetic charge by $gsin\theta_W = e$. Just as the electromagnetic and strong couplings exhibit running, so does the weak coupling (see Figure 1.4), due to radiative corrections[52]. The solid blue line in the figure is the predicted running, and a deviation in the measured values could be an indication of new physics. Figure 1.5 shows the current world data on the measurement of $sin^2\theta_W$, and the approximate Q^2 of several future measurements, with their anticipated error bars. The most accurate measurements that set the scale of the running are at the Z-pole, where real Z bosons can be produced in colliders[113]. The APV value at low Q^2 comes from measurements of atomic

parity violation in atomic cesium[24][147]. The highest Q^2 value, which is not very significant, comes from measurements of the lepton forward-backward asymmetry in CDF[35]. The NuTeV value from deep inelastic neutrino scattering that exhibits a large deviation from the running value has theoretical uncertainties that are still being worked out[151]. The measurement of $Q_w(e)$ in Møller scattering from the Stanford Linear Accelerator is the most precise measurement, with fewer theoretical concerns[7].

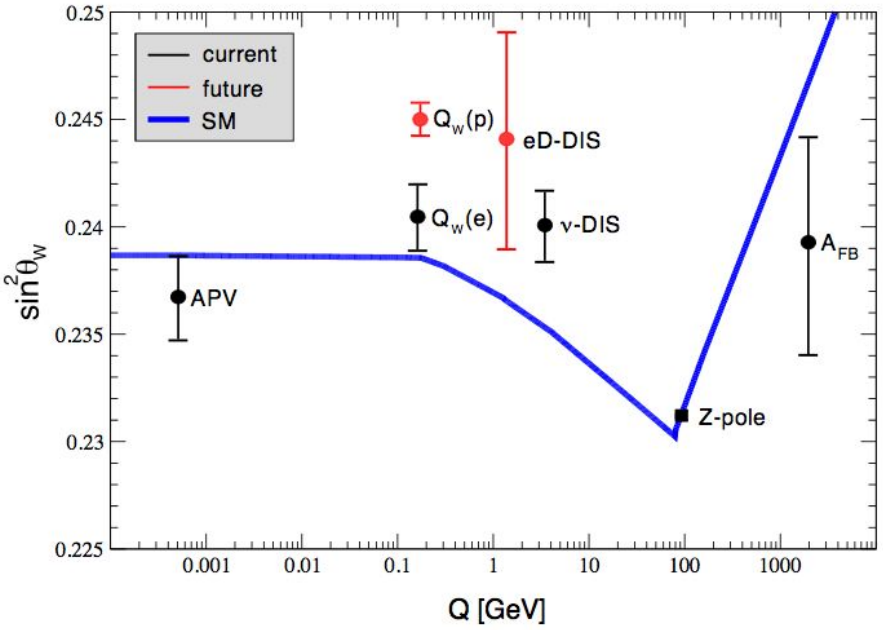

Figure 1.4: Running of the weak mixing angle as a function of four momentum transfer in the modified minimal subtraction scheme $\overline{MS}$[42]. The solid blue line shows the predicted running. The Q_{weak} data point is at an arbitrary y location at the approximate Q of the experiment, with the expected error bars.

An experiment can serve as a standard model test if the expected uncertainty is so small that it can "see" possible new couplings, that is, it can search for physics beyond the standard model. Measurements of the properties of the "strange sea", such as the contribution to the spatial charge and magnetization distributions within the nucleon (which are measured by

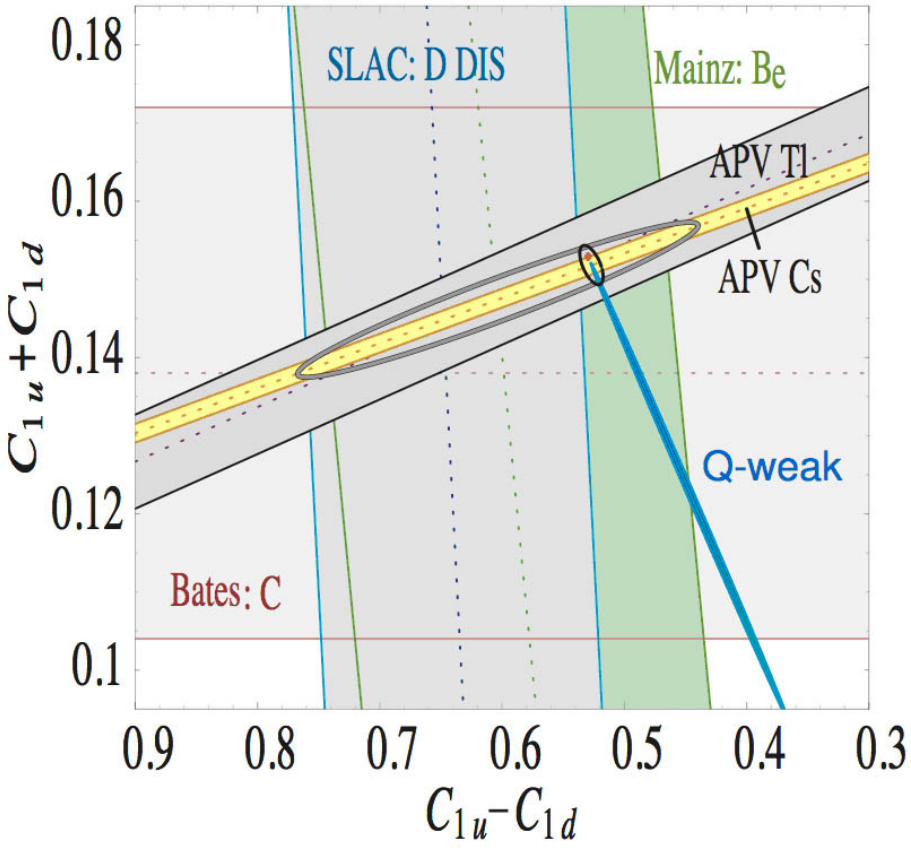

Figure 1.5: World data on the value of the effective neutral weak coupling coefficients of the quarks[42]. Q_{weak} will greatly reduce the uncertainty on the weak charges of the quarks from the large grey ellipse to the small black ellipse. Note that it has a nearly orthogonal sensitivity compared to the atomic parity violation measurements. The Standard Model value is marked with a small red dot.

G^0) are not strictly tests of the standard model, though it will help to characterize the ground state properties of the nucleon. The Q_{weak} experiment, which expects to measure $sin^2\theta_W$ to 0.3% uncertainty, will have access to mass scales of new physics in the TeV range. The Q_{weak} experiment involves the interaction of electrons and the u and d quarks within the proton; the effective low-energy Lagrangian is expressed as:

$$\mathcal{L}_{NC}^{eq} = \frac{-G_F}{\sqrt{2}} A_e^{NC} \sum_q C_{1q} \bar{q} \gamma_\mu q \tag{1.9}$$

where the current world knowledge of the quark couplings is summarized in Figure 1.5[4] [149]. Q_{weak} will greatly reduce the uncertainty in the weak charges of the quarks, but to see how the sensitivity to new physics arises, assume that the standard model errors are small. The parity-violating part of the Lagrangian can be written as a sum of the standard model lagrangian and a lagrangian for new physics

$$\mathcal{L}^{PV} = \frac{-G_F}{\sqrt{2}} A_e^{SM} V_q^{SM} + \frac{g'^2}{4\Lambda^2} A_e^{New} V_q^{New} \tag{1.10}$$

where the A and V refer to the electron axial vector and quark vector currents of the interaction, respectively. The coefficient on the new physics part is analogous to $G_F = \sqrt{2}g^2/8M_W^2$ where in the electromagnetic interaction $gsin\theta_W = e$; g' is a measure of the coupling strength and Λ is the mass scale of the new physics. If the Q_{weak} measurement agrees with the standard model, it will place considerable new constraints on new physics.

The more precise the measurement of Q_W^p, the more significant the observation of new physics, given by

$$S = \left(\frac{g'^2}{4\Lambda^2} Q_{SW}^p\right) / \left(\frac{-G_F}{\sqrt{2}} \Delta Q_W^{exp}\right) \tag{1.11}$$

where ΔQ_W^{exp} is the experimental uncertainty on the measurement of $Q_W^p = 2C_{1u} + C_{1d}$, and $Q_{SW}^p = 2(2h_1^u + h_1^d)$ is the "charge" for the new interaction. Taking $g'^2 Q_{SW}^p \to 1$ and assuming 95% confidence level (S=2σ) and rearranging, the sensitivity to the mass scale of new physics assuming a 4% measurement of Q_{weak} is

$$\frac{\Lambda}{g'} = \frac{1}{\sqrt{4\sqrt{2} G_F \Delta Q_W^{exp}}} \sim 2.3\ TeV \tag{1.12}$$

that is complementary to measurements at the LHC. Figure 1.6 shows the sensitivity that

[4]Knowledge of the C_{2q}'s, which arises from the $V_e^{NC} A_q^{NC}$ part of the Lagrangian, cannot be obtained without additional information from nonperturbative QCD[149].

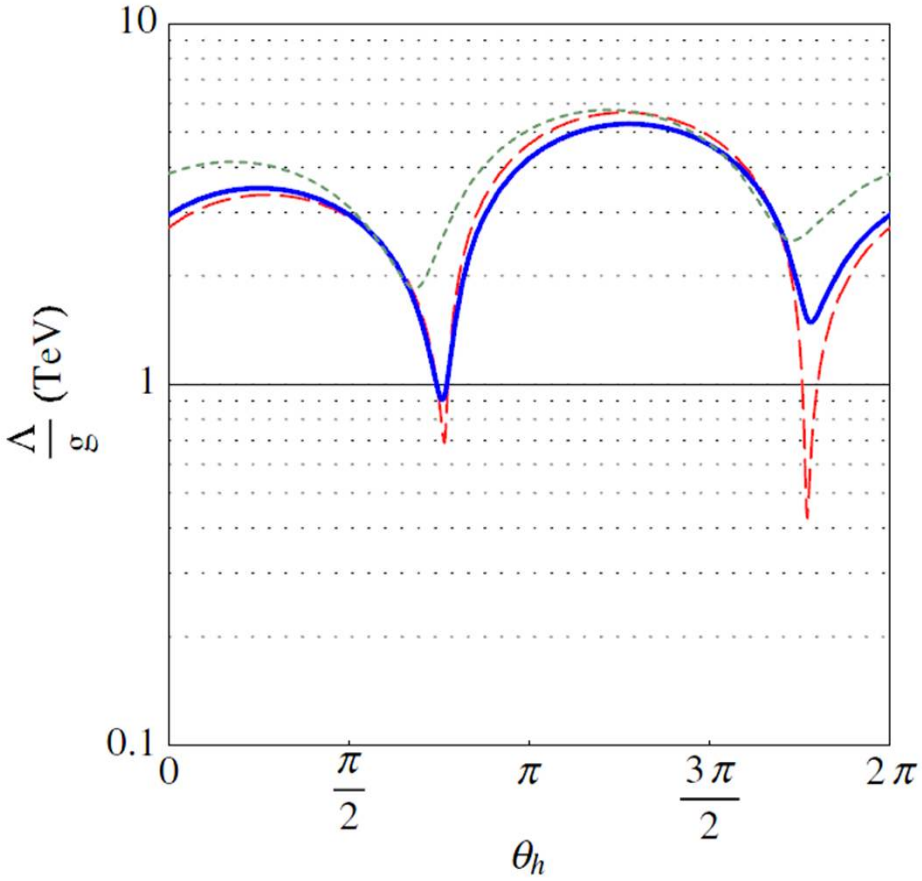

Figure 1.6: Experimental sensitivity to the mass scale Λ(normalized by the coupling constant of new physics, g) at the 95% confidence level[149]. The sensitivity would vary with a mixing angle between the quarks. The red, long-dashed curve corresponds to the grey ellipse in Figure 1.5. The solid blue curve is the present limit (including PVES data), and the green, short-dashed curve is the anticipated Q_{weak} limit, assuming that no deviation from the standard model is measured.

will be obtained in Q_{weak} as a function of the possible quark mixing angle of the new physics (with the isospin dependence given by $h_V^u = \cos\theta_h$ and $h_V^d = \sin\theta_h$).

A deviation of $\sin^2\theta_W$ (and thus Q_W^p) from the standard model prediction is an indication of new physics, as discussed above. Q_{weak} will be sensitive to various proposed extensions to the standard model, including extra neutral gauge bosons (Z'), leptoquarks (able to change a quark into a lepton and vice-versa) and various supersymmetric models [52]. SLAC E158

is a measurement of electron-electron (Møller) scattering and is thus purely leptonic. Figure 1.7 summarizes the sensitivity of Q_{weak} to various models compared to the SLAC $Q_w(e)$ measurement. Together the two measurements could serve as evidence for SUSY loops or Z'. The SLAC measurement could act as a control for the leptoquark sensitivity. The modified minimal subtraction $\overline{MS}$ scheme is the renormalization scheme used in most of the theory calculations presented here.

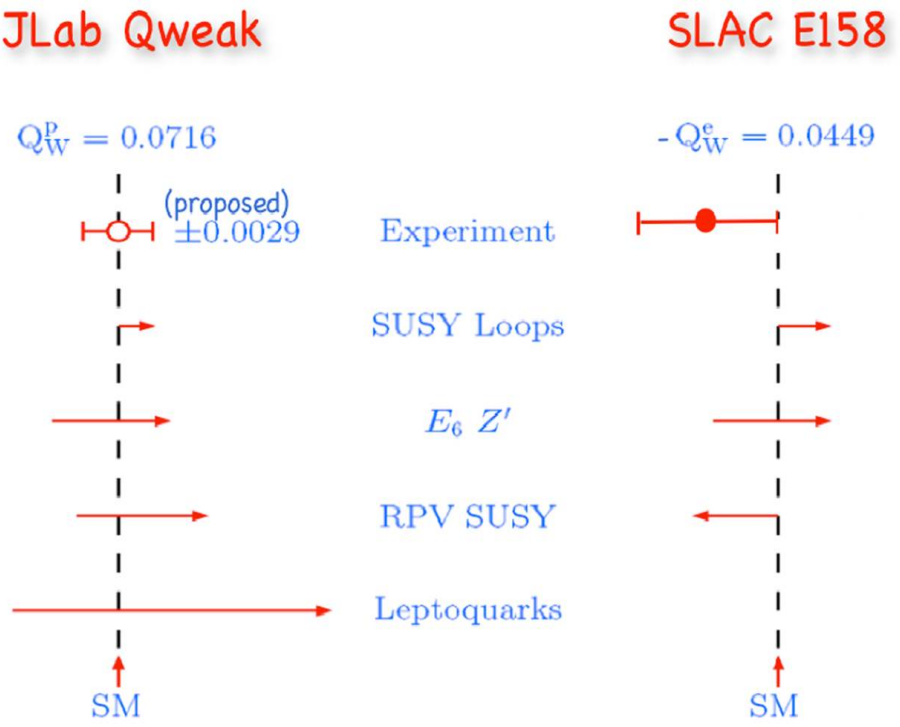

Figure 1.7: The anticipated errors bars for each experiment are shown at the top, while the expected deviations from the SM value are shown for various extensions that are allowed at the 95% confidence level based on fits to world data[39]. Note that for SUSY loops and Z', the two experiments have similar sensitivity, but are anti-correlated for RPV SUSY. Q_{weak} is sensitive to leptoquarks, while the SLAC measurement is not.

The supersymmetric extensions to the standard model to which Q_{weak} is sensitive include SUSY loops and R-parity violating (RPV) SUSY. R-parity in supersymmetry differentiates between interactions where both lepton (L) and baryon (B) number are conserved, and

interactions where one or the other is not conserved. Normal particles have a positive R-parity and supersymmetric particles have negative R-parity; the value is given by $R = (-1)^{3(B-L)+2s}$. If R-parity is exactly conserved, then supersymmetric particles appear only at loop level, however, proton stability can be preserved even if the B conservation is relaxed. Thus tree-level interactions can appear in low energy processes if R-parity is not conserved. Whether SUSY is RPV or only appears at loop level has a direct consequence for dark matter searches; if R-parity is conserved then the lightest supersymmetric particle is stable and is a viable dark matter candidate [123].

1.2 Electroweak Theory

So far a great deal of motivation has been generated for the 3 measurements that will be presented in this thesis - the measurement of the weak charge of the proton and a search for new physics, the separation of the strange quark contributions to the charge and magnetization distributions of the nucleon, and the imaginary part of two photon exchange which is relevant to important radiative corrections in various experiments. The formalism of how these measurements would be attained has been left to this section. All of the experiments measure an asymmetry; Q_{weak} and G^0 measure a parity-violating (PV) asymmetry, while the transverse asymmetries are parity-conserving. The asymmetry is a ratio of the difference over the sum of elastic cross sections

$$A = \frac{\sigma_+ - \sigma_-}{\sigma_+ + \sigma_-} \tag{1.13}$$

for positively and negatively polarized incoming electrons incident on an unpolarized proton (or deuteron) target. The formalism used to describe elastic electron-proton scattering will be presented, though a detailed discussion of the relevant kinematics is left to Appendix A.

The scattering cross sections are calculated within the standard model unified electroweak theory, which will be discussed in the following sections.

1.2.1 Elastic Electron Nucleon Scattering

In the standard model, the unified electroweak theory arises from the spontaneous symmetry breaking of an $SU(2) \times U(1)$ group, which generates the massless neutral exchange boson, the photon, and the massive neutral and charged bosons, the Z^0 and $W^{\pm}$. In the theory the particles are treated as interacting currents (see Figure 1.8). The differential cross section is proportional to the square of the sum of the invariant amplitudes, which are the products of the currents of the interacting particles and the propagator for each type of interaction. In the current for each of the particles there is a piece for the incoming and outgoing spinors and the vertex factor, which depends on the type of the interaction which is taking place (see Section 1.1.3).

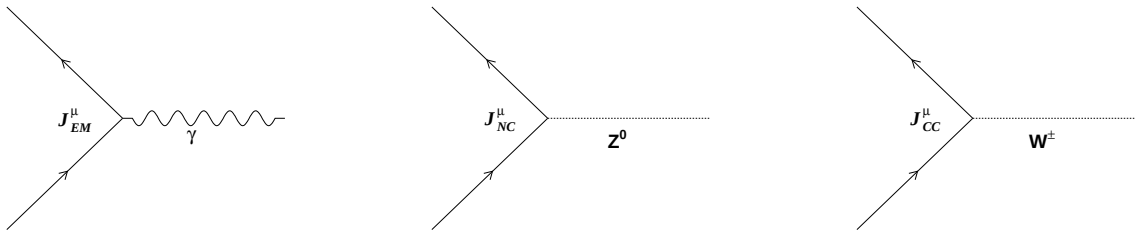

a *b* *c*

Figure 1.8: Feynman diagrams showing the electromagnetic (a), neutral weak (b), and charged currents (c).

The electromagnetic (EM) currents, denoted with superscripts of e for the electron and

N for the proton (nucleon), can be written as

$$J^{\mu}_{e,EM} = -ie\bar{\psi}\gamma^{\mu}\psi \tag{1.14}$$

and

$$\langle N|\, J^{\mu}_{N,EM}\, |N\rangle = i\bar{\psi}_N \left[F_1(q^2)\gamma^{\mu} + \frac{i\sigma^{\mu\nu}q_{\nu}}{2M_N}F_2(q^2)\right]\psi_N \tag{1.15}$$

where ψ and $\bar{\psi}$ are the incoming and outgoing spinors, respectively, and $-e$ is the charge in the vertex factor for the electron, and the proton charge and anamolous magnetic moment are contained in the structure functions. The electron, because it is pointlike, simply has a vector (γ^{μ}) term in its vertex factor, while the complicated structure of the proton is parameterized by the Dirac and Pauli form factors, F_1 and F_2, which are functions of the four momentum transfer, q^2. They multiply a vector (γ^{μ}) and a tensor ($\sigma^{\mu\nu}q_{\nu}$) term, respectively, giving the most general four-vector form for the nucleon current that conserves parity.

The neutral weak currents (NC) can be written in an analogous way

$$J^{\mu}_{e,NC} = \bar{\psi}i\left[g^e_V\gamma^{\mu} + g^e_A\gamma^{\mu}\gamma^5\right]\psi \tag{1.16}$$

and

$$\langle N|\, J^{\mu}_{N,NC}\, |N\rangle = \bar{\psi}_N \left[F_1^{NC}(q^2)\gamma^{\mu} + \frac{i\sigma^{\mu\nu}q_{\nu}}{2M_N}F_2^{NC}(q^2) + G_A^{N,NC}\gamma^{\mu}\gamma^5\right]\psi_N \tag{1.17}$$

where the vertex factor in each current now has an additional axial vector ($\gamma^{\mu}\gamma^5$) piece. In Section 1.2.3 we will see how this gives rise to the parity-violating asymmetries. Because the weak neutral current is not maximally parity-violating, the vector and axial vector pieces have different charges, $g^e_V = -1 + 4sin^2\theta_W$ and $g^e_A = +1$ for the electron (see Table 1.1). For the proton, the weak couplings are "absorbed" into the propagator and the neutral current

form factors and so are not shown explicitly here.

In general, the cross section, σ, is proportional to the square of the sum of the invariant amplitudes (transition matrix elements) of the relevant processes, including radiative corrections and/or transitions to intermediate nucleon states. In the case of elastic electron-proton scattering, we have

$$\sigma \propto (M_{EM} + M_{NC})^2 \tag{1.18}$$

where the relevant amplitudes are the tree-level electromagnetic and neutral weak current interaction amplitudes

$$M_{EM} = J^{\mu}_{e,EM} \frac{g_{\mu\nu}}{Q^2} J^{\nu}_{N,EM} \tag{1.19}$$

and

$$M_{NC} = \frac{g^2}{16 cos^2\theta_W} J^{\mu}_{e,NC} \frac{g_{\mu\nu} - p_\mu p_\nu / M^2}{Q^2 - M_Z^2} J^{\nu}_{N,NC} \tag{1.20}$$

where the nucleon is in the ground state before and after the scattering, and the factor $g/4cos^2\theta_W$ from each vertex is shown explicitly (so that the neutral weak couplings can be written as shown in Table 1.1). Note that because $Q^2 \ll M_Z^2$, the Q^2 dependence of the Z^0 propagator can be neglected, and using $G_F/\sqrt{2} = g^2/8M_Z^2 cos^2\theta_W$, we have simply

$$M_{NC} = J^{\mu}_{e,NC} \frac{G_F g_{\mu\nu}}{2\sqrt{2}} J^{\nu}_{N,EM} \tag{1.21}$$

for the neutral weak amplitude, where the Fermi constant, $G_F \sim 1.17 \times 10^{-5} GeV^{-2}$.

1.2.2 Electric and Magnetic Form Factors of the Nucleon

The form factors are usually written as linearly independent combinations of F_1 and F_2, with the electric form factor of the nucleon's electromagnetic current given by

$$G_E(q^2) = F_1(q^2) - \tau F_2(q^2) \tag{1.22}$$

and the magnetic form factor given by

$$G_M(q^2) = F_1(q^2) + F_2(q^2) \tag{1.23}$$

where $\tau = Q^2/4M_N$ is a kinematic variable. Identical expressions can be written for both the proton and the neutron. The reason for the nomenclature becomes clear when one considers the Fourier transform of G_E and G_M in the Breit frame (or brick wall frame) where no energy is transferred to the nucleon in the scattering. In this frame the nucleon momentum before and after the scattering is equal in magnitude but opposite in sign $\vec{p'} = -\vec{p}$, and the Fourier transform yields the spatial distributions of the charge and magnetization of the proton or neutron. Note also that at $Q^2 \to 0$ the electric (magnetic) form factor goes to the charge (magnetic moment) of the proton or neutron. The unpolarized elastic electron-proton scattering cross section in the lab frame is given by

$$\frac{d\sigma}{d\Omega} = \frac{\alpha^2}{4E^2 sin^2\frac{\theta}{2}} \frac{E'}{E} \left(\frac{G_E^2 + \tau G_M^2}{1+\tau} cos^2\frac{\theta}{2} + 2\tau G_M^2 sin^2\frac{\theta}{2} \right) \tag{1.24}$$

where α is the fine structure constant, E is the incident beam energy, θ is the scattered electron angle, and E$\prime$ is the scattered electron energy. The kinematic factor τ is given by $\tau = Q^2/(4M_N)$, and Ω is the solid angle.

The world data for the electric and magnetic form factors of the proton and neutron is

shown in Figure 1.9 for a large range of Q^2 [79]. All but the neutron electric form factor are normalized to the dipole form

$$G_D(Q^2) = \left(1 + \frac{Q^2}{0.71}\right)^{-2} \tag{1.25}$$

because the deviation from the dipole form is less than 10% up to $Q^2 \leq 1$ for each of these quantities. At higher Q^2 the deviation becomes larger for the magnetic form factor of the proton compared to the electric form factor, and this result is reflected in the ratio $\mu G_E^p/G_M^p$ that was the subject of section 1.1.3.

It is interesting to note that while the dipole form implies an exponential shape for the proton's spatial charge and magnetization distributions, and also for the neutron's magnetization distribution, the charge distribution of the neutron is non-trivial (see Figure 1.10). It could have been zero everywhere; instead there is a positive core with a negative outer region (with the integral being zero). A plausible model for this is that the neutron fluctuates into a proton and a pion, with the heavier proton at the center and the negative pion orbiting further away.

The neutral weak form factors (associated with the exchange of a Z boson) can be written in a similar way to the electromagnetic form factors, with neutral weak "electric" and "magnetic" form factors given by

$$G_E^Z(q^2) = F_1^{NC}(q^2) - \tau F_2^{NC}(q^2) \tag{1.26}$$

and

$$G_M^Z(q^2) = F_1^{NC}(q^2) + F_2^{NC}(q^2) \tag{1.27}$$

where similarly as $Q^2 \to 0$, the neutral weak electric form factor is the weak vector charge

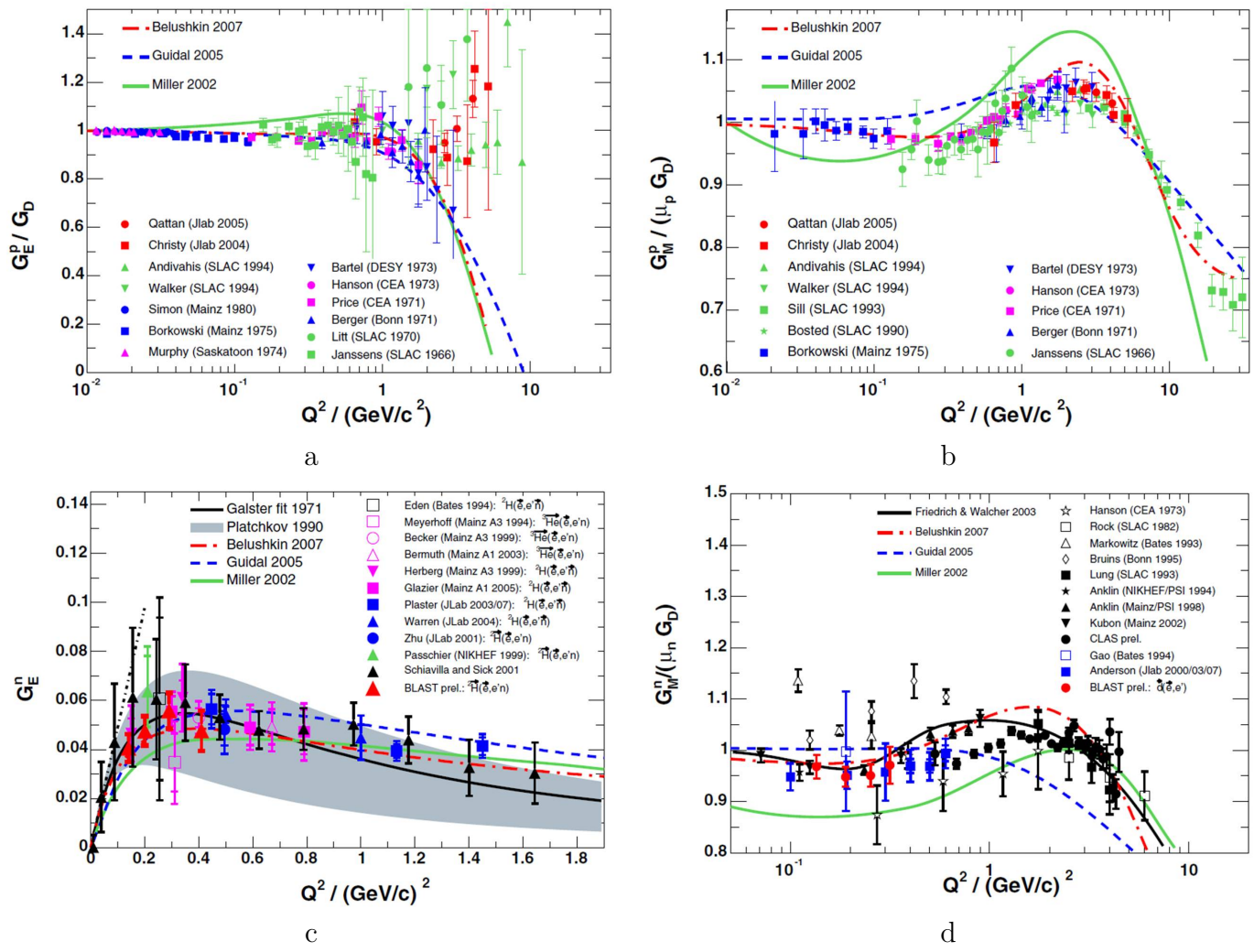

Figure 1.9: World data for the electric (left) and magnetic (right) form factors of the proton (top) and neutron (bottom)[79]. All but the neutron electric form factor (c) follow the dipole form for $Q^2 < 1GeV$, and are shown as normalized to the dipole form factor. Also shown are several theoretical predictions in each case.

of the proton, $G_E^Z(0) = Q_W^p = 1 - 4sin^2\theta_W$. While the electric and magnetic form factors for the proton and neutron $G_{E,M}^{p,\gamma}$ and $G_{E,M}^{n,\gamma}$ (the γ superscript refers to the electromagnetic interaction), are relatively well known as a function of Q^2 (see Figure 1.9), very little is known about the neutral weak current analog, $G_{E,M}^{p,Z}$. By exploiting the parity-violating aspect of the weak interaction, as will be described in the next section, it is possible to

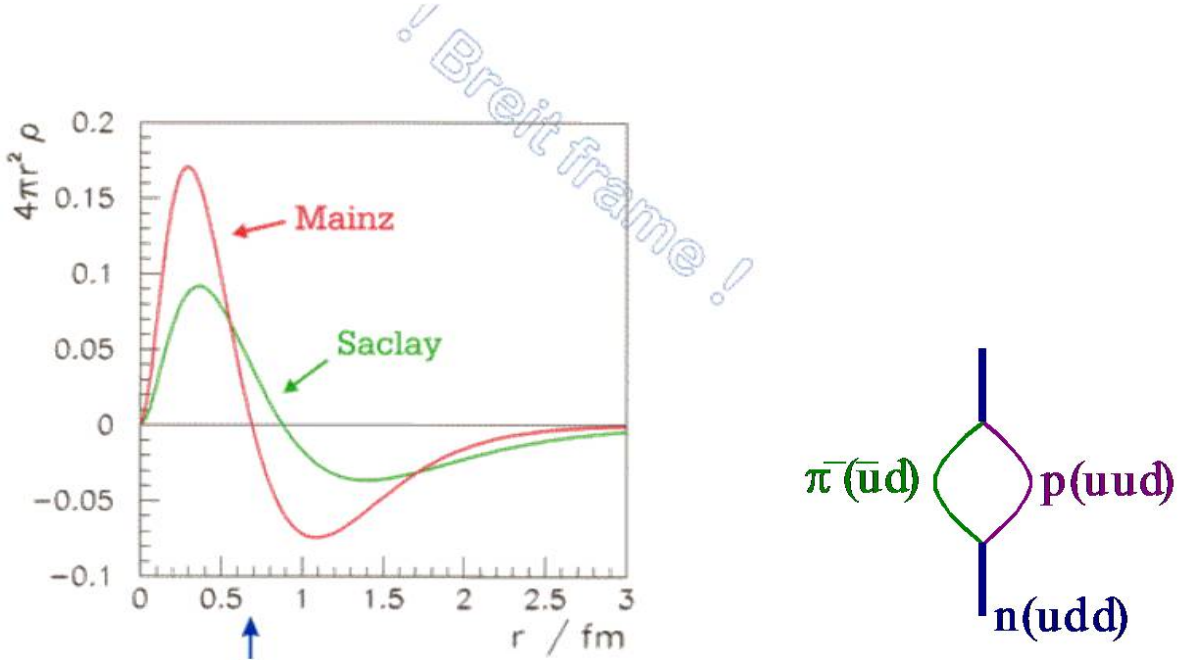

a b

Figure 1.10: Plot of the neutron charge distribution in the breit (brick wall) frame for two different fits (a). Description of a plausible model to explain the positive core and the negative shell, the neutron fluctuates into a proton and a negative pion (b)[120].

make a measurement of this form factor, at least at particular Q^2 values. In G^0, this gives access to the strange quark contribution to the charge and magnetization distributions of the proton and neutron (see below), and in Q_{weak} it provides the measurement of the weak mixing angle.

Each of the electric and magnetic form factors can be written as charge-weighted sums over the form factors for the individual quark currents in the nucleon, where, for example

$$G_E^{q,Z}(q^2) = F_1^{q,NC}(q^2) - \tau F_2^{q,NC}(q^2) \tag{1.28}$$

for an individual quark current. In a similar way the vector neutral weak charge of the proton is the sum of the vector neutral weak charges of the individual quarks. Only the

three lightest quarks, the u, d and s are considered, because contributions from heavier quarks are expected to be small [75]. Once the charges have been factored out, the vector part of the nucleon matrix elements for the electromagnetic and neutral weak currents is the same. The same is not true of the axial-vector part of the neutral weak proton current - it is not a simple sum of axial vector pieces of quarks[5]. The axial form factor measured in charged-current neutrino-proton scattering follows a dipole form

$$G_A(Q^2) = G_A(0)\left(1 + \frac{Q^2}{M_A^2}\right)^{-2} \tag{1.29}$$

similar to the electromagnetic vector form factors, where M_A is the axial mass and the value of G_A at $Q^2 = 0$ is fixed by neutron beta decay[4]

$$G_A(0) = -g_A = 1.2695 \pm 0.0029 \tag{1.30}$$

The axial-form factor measured in electron scattering has significant radiative corrections, and so will be denoted as G_A^e to reflect that these corrections must be taken into account to compare to the value of G_A obtained in neutrino scattering. The isovector piece of this effective form factor is $G_A^{e,T=1}$ where

$$G_A^e(Q^2) = G_A^{e,T=1} + G_A^{e,T=0} = G_A + R + G_A^{e,T=0} \tag{1.31}$$

and there are significant radiative corrections, R, that cause it to deviate from what is measured in charged current neutrino scattering G_A (see Section 4.1.4). It is the isovector piece that has been measured by G^0, in addition to the strange electric and magnetic form factors, at two values of $Q^2 > 0$ (see Section 1.2.3).

[5]This is because the axial-vector part of the current is modified by QCD interaction corrections, whereas the conserved vector current (CVC) hypothesis protects the vector part of the current from such complications[70].

In order to access the strange quark contribution to the charge and magnetization distributions of the nucleon, it is necessary to invoke isospin (or charge) symmetry in the nucleon. This means that in the form factors the u(d) quarks in the proton(neutron) act like the d(u) quarks in the neutron(proton), which is a good assumption to the $\sim 1\%$ level [103] (see Section 1.1). So it is possible to write the electric and magnetic form factors of the neutron and proton and the neutral current as a sum over the form factors for the individual quark flavors

$$\begin{pmatrix} G_{E,M}^{p,\gamma} \\ G_{E,M}^{n,\gamma} \\ G_{E,M}^{p,Z} \end{pmatrix} = \begin{pmatrix} \frac{2}{3} & -\frac{1}{3} & -\frac{1}{3} \\ -\frac{1}{3} & \frac{2}{3} & -\frac{1}{3} \\ Q_W^u & Q_W^d & Q_W^s \end{pmatrix} \begin{pmatrix} G_{E,M}^{u,p} \\ G_{E,M}^{d,p} \\ G_{E,M}^{s,p} \end{pmatrix} \tag{1.32}$$

As described above, the electromagnetic form factors of the proton and neutron are relatively well known, especially at low Q^2, but in order to separate out the contribution of the strange quarks it is necessary to measure the neutral weak form factor. The determination of G_E^s and G_M^s will be a measurement of the charge and magnetization distributions of the sea, since there are no valence strange quarks.

Predictions for the strange quark contribution to the proton and neutron charge and magnetization distributions can be made using a number of approaches, including heavy baryon chiral perturbation theory (HBχPT), vector meson dominance and dispersion relations. One model for how strange quarks can appear in the nucleon is similar to the explanation given in Figure 1.10,b to explain the charge distribution of the neutron. Instead of the neutron (udd) fluctuating into a proton (uud) and a π^- ($\bar{u}d$), it could fluctuate into a Λ^0 (uds) and a K^+ ($\bar{s}u$), for example. The different spatial distributions for the Λ^0 and K^+ (because of the difference in their masses) leads to a different spatial distribution for the s

and $\bar{s}$, which is necessary to measure a non-zero G_E^s. Alternatively it could be described as fluctuations of gluons into $s\bar{s}$ in the sea. Ultimately the answer should come from a lattice QCD calculation, but for now it is necessary to rely on models such as this.

1.2.3 Parity-Violating Asymmetries

In the elastic scattering of electrons from protons the electromagnetic and neutral weak currents can interfere with each other (see Figure 1.11). The neutral weak form factor can be measured by exploiting the fact that while the electromagnetic interaction conserves parity, the neutral weak interaction does not. Thus by comparing the cross sections for positive and negative helicity electrons scattered from an unpolarized proton (or deuteron) target, it is possible to access the neutral weak part of the transition matrix element. The helicity of the electron is given by

$$\hat{h} = \frac{\vec{s} \cdot \vec{p}}{|\vec{s}|\,|\vec{p}|} \tag{1.33}$$

with the eigenfunctions of $\hat{h}$ being either ± 1. The total matrix element squared, given in the cross section

$$\sigma \propto (M_{EM} + M_{NC})^2$$

can be expanded as

$$M_{tot}^2 = (M_{EM} + M_{NC})^2 = |M_{EM}|^2 + 2Re\,(M_{EM}^* M_{NC}) + |M_{NC}|^2 \tag{1.34}$$

where the sign of the axial-vector parts of the M_{NC} changes with the electron's helicity. By forming the asymmetry it is possible to eliminate the multiplicative factors (by dividing by the sum) as well as the parts of the cross section that don't change sign under parity in the

numerator

$$A = \frac{\sigma_+ - \sigma_-}{\sigma_+ + \sigma_-} = \frac{2Re\left(M^*_{EM} M^{PV}_{NC}\right)}{|M_{EM}|^2 + \cdots} \tag{1.35}$$

where $|M_{NC}|^2 << |M_{EM}|^2$ and the parity-violating parts of the weak neutral current matrix element involve cross terms with either the vector part from the electron and the axial-vector part from the nucleon, or the vector part from the nucleon and the axial-vector part from the electron. An evaluation of the invariant amplitudes given in equations 1.19 and 1.21 yields a factor of $\frac{G_F|Q^2|}{4\pi\alpha\sqrt{2}}$ which at typical Q^2 values in Q_{weak} and G^0 is on the order of $10^{-6} - 10^{-4}$, which sets the scale for the size of the asymmetries as parts per million (ppm).

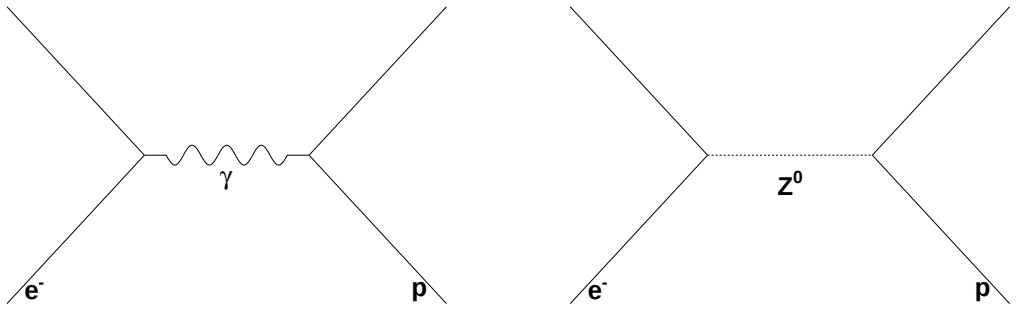

a b

Figure 1.11: Feynman diagrams depicting electron-proton scattering via the electromagnetic (a) and neutral weak (b) currents. The parity-violating asymmetries arise due to the interference of the scattering amplitudes of these two processes.

The most general form of the asymmetry in elastic electron proton scattering is[107]

$$\begin{aligned} A_{LR} = & -\frac{1}{2} A^0_{LR} \\ & \times \left\{ \xi^p_V + \left[\epsilon G^p_E \left\{ \xi^n_V G^n_E + \xi^{(0)}_V G^{(s)}_E \right\} + \tau G^p_M \left\{ \xi^n_V G^n_M + \xi^{(0)}_V G^{(s)}_M \right\} \right. \right. \\ & \left. \left. - \left(1 - 4sin^2\theta_W\right) \epsilon' G^p_M \tilde{G^p_A} \right] / \left[\epsilon (G^p_E)^2 + \tau (G^p_M)^2 \right] \right\} \end{aligned} \tag{1.36}$$

where $A^0_{LR} = \frac{G_F|Q^2|}{2\pi\alpha\sqrt{2}}$ and the various kinematic factors are given by

$$\tau = \frac{Q^2}{4M_N^2}, \quad \epsilon = \left(1 + 2(1+\tau)tan^2\frac{\theta}{2}\right)^{-1}, \quad and \quad \epsilon' = \sqrt{\tau(1+\tau)(1-\epsilon^2)} \tag{1.37}$$

and the ξ factors are related to the electroweak radiative corrections

$$\begin{aligned} \xi_V^p &= \left(1 - 4sin^2\theta_W\right)\left[1 + R_V^p\right] \\ \xi_V^n &= -\left[1 + R_V^n\right] \\ \xi_V^{(0)} &= g_V^u + g_V^d + g_V^s \end{aligned} \tag{1.38}$$

where g_V^i are the weak vector charges Q_W^V of individual quarks from Table 1.1. R_V^p and R_V^n are electroweak radiative corrections. As $Q^2 \to 0$ the quantity $\tau \to 0$. At far forward scattering angles, or $\theta \to 0$, the quantity $\epsilon \to 1$, and at large scattering angles, or $\theta \to 180°$ the quantity $\epsilon \to 0$.

At low Q^2 the asymmetry can be used to measure the value of the weak charge of the proton. Alternatively, at higher Q^2 you can assume the standard model weak charges are correct and use the asymmetry to measure the strange quark content of the proton. Thus for low Q^2, forward angle scattering as in Q_{weak}, the asymmetry can be written as

$$A \sim \frac{-G_F}{4\pi\alpha\sqrt{2}}\left[Q^2 Q_W^p + Q^4 B(Q^2)\right] \tag{1.39}$$

where the hadronic factor $B(Q^2)$ depends on the nucleon electric and magnetic form factors and the strange quark contribution[107]. For the G^0 kinematics the asymmetry can be written as an electric, magnetic and axial piece, where the superscript p has been dropped. The electromagnetic form factors have a γ superscript and the corresponding electroweak

form factors have a Z superscript

$$A = -\frac{G_F Q^2}{4\pi\alpha\sqrt{2}} \frac{A_E + A_M + A_A}{[\epsilon G_E^\gamma(Q^2) + \tau G_M^\gamma(Q^2)]} \tag{1.40}$$

The designations become clear when each is written out as products of the electric and magnetic form factors of the electromagnetic and weak neutral currents

$$\begin{aligned} A_E &= \epsilon G_E^Z(Q^2) G_E^\gamma(Q^2) \\ A_M &= \tau G_M^Z(Q^2) G_M^\gamma(Q^2) \\ A_A &= -(1 - 4sin^2\theta_W)\epsilon' G_A^e(Q^2) G_M^\gamma(Q^2) \end{aligned} \tag{1.41}$$

where $\tilde{G_A^p}$ is replaced by $G_A^e(Q^2)$. The A_E and A_M terms originate with the axial-vector part of the electron current and the vector part of the proton current, and the A_A term from the axial-vector part of the proton current and the vector part of the electron current. Note that there are three unknowns, G_E^Z, G_M^Z and G_A^e.

In order to isolate the neutral weak form factors and the axial form factor, three measurements will be required. This can be accomplished by either varying the kinematics or the target for a given value of Q^2. At forward angles, the A_E term dominates, and at backward angles the axial A_A term dominates, with some A_M contribution at both forward and backward angles. Enhanced sensitivity to the axial term can be achieved in quasi-elastic scattering from the deuteron, where the asymmetry is a cross section weighted average of the proton and neutron asymmetries

$$A = \frac{\sigma_p A_p + \sigma_n A_n}{\sigma_d} \tag{1.42}$$

where the neutron asymmetry is written using the neutron form factors instead of those of the proton[21]. Thus, the three measurements made at each Q^2 in G^0 are a forward and backward angle measurement of the asymmetry in elastic $\vec{e}-p$ scattering and a backward angle measurement of the asymmetry in quasielastic $\vec{e}-d$ scattering.

1.2.4 Beam Normal Single Spin Asymmetries

The transverse asymmetries are a parity-conserving asymmetry that arises due to the interference of single photon exchange and the imaginary[6] part of the two photon exchange amplitude (see Figure 1.12). The asymmetry

$$B_n = \frac{2M_\gamma Im(M_{\gamma\gamma})}{|M_\gamma|^2} \tag{1.43}$$

arises because of an electron helicity flip. The cross section can be parameterized using 6 complex invariant amplitudes $\tilde{G}_M(\nu, Q^2)$, $\tilde{G}_E(\nu, Q^2)$ and $\tilde{F}_i(\nu, Q^2)$ where $i = 3, 4, 5, 6$ which are functions of the four-momentum transfer Q^2 and ν is given by $\nu = K \cdot P$, where K and P are the average of the incoming and outgoing four-momenta of the electron and proton, respectively[65]. In the Born approximation the complex EM form factors reduce to the familiar form factors $\tilde{G}_M(\nu, Q^2) \rightarrow G_M(Q^2)$, $\tilde{G}_E(\nu, Q^2) \rightarrow G_E(Q^2)$ and the form factors that parameterize the intermediate hadronic states vanish $\tilde{F}_i(\nu, Q^2) \rightarrow 0$. Using this parameterization, with ϵ, the virtual photon polarization parameter, given by

$$\epsilon = \frac{\nu^2 - M^4\tau(1+\tau)}{\nu^2 + M^4\tau(1+\tau)} \tag{1.44}$$

[6]The real part of two photon exchange can be measured by comparing elastic electron-proton and positron-proton scattering[114].

the beam normal single spin asymmetry can then be written

$$B_n = \frac{2m_e}{Q}\sqrt{2\epsilon(1-\epsilon)}\sqrt{1+\frac{1}{\tau}}(G_M^2+\frac{\epsilon}{\tau}G_E^2)^{-1}$$

$$\times\{-\tau G_M \Im(\tilde{F}_3+\frac{1}{1+\tau}\frac{\nu}{M^2}\tilde{F}_5) - G_E\Im(\tilde{F}_4+\frac{1}{1+\tau}\frac{\nu}{M^2}\tilde{F}_5)\}$$

$$+\vartheta(e^4) \tag{1.45}$$

where terms of order α^2 and higher are neglected. There is an order m_e/E suppression in addition to the factor of α leading to asymmetries on the order of $10^{-6}-10^{-5}$. Thus the techniques developed for measuring the small parity-violating asymmetries are also useful for measuring these asymmetries.

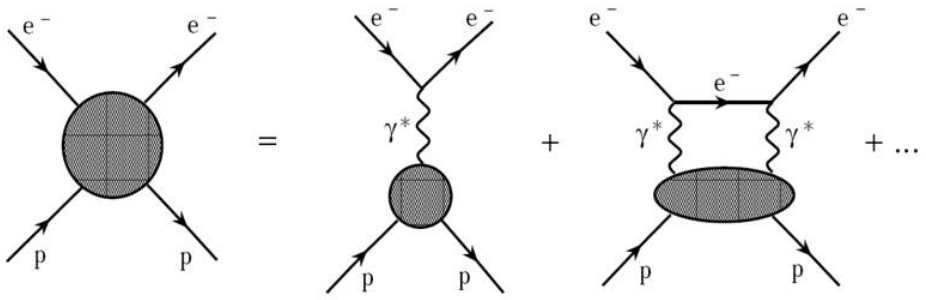

Figure 1.12: Diagram depicting the single and two photon exchange amplitudes that go into the calculation of the electron-proton scattering cross section.

These asymmetries can be studied either by polarizing the target perpendicular (transverse) to the incoming unpolarized electron beam (yielding a different expression for the asymmetry, A_n), or by using an unpolarized target and a transversely polarized beam. In the latter case, the asymmetries are called beam normal single spin asymmetries (B_n) where the measured asymmetry has a sinusoidal dependence about the beam axis

$$A_\perp = \frac{\sigma_\uparrow - \sigma_\downarrow}{\sigma_\uparrow + \sigma_\downarrow} = B_n \vec{p}_e \cdot \hat{n} \tag{1.46}$$

where $\vec{p}_e$ is the direction of the beam polarization and $\hat{n}$ is the normal to the scattering plane (see Figure 1.13). The $\sigma_\uparrow$ ($\sigma_\downarrow$) refer to the cross section when the electron's spin is parallel (anti-parallel) to $\hat{n}$, which is defined as

$$\hat{n} = \frac{\vec{k}_e \times \vec{k}'_e}{\left|\vec{k}_e \times \vec{k}'_e\right|} \tag{1.47}$$

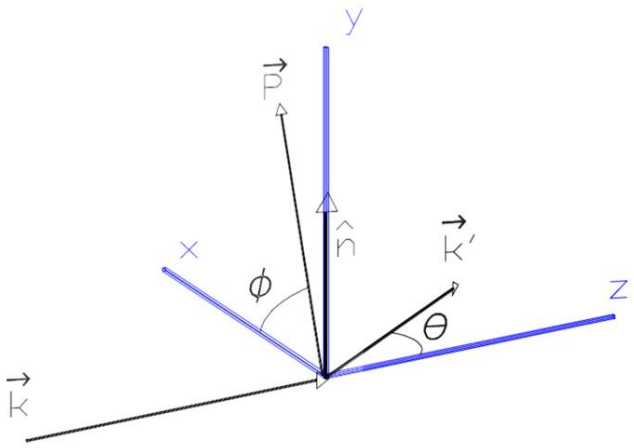

Figure 1.13: Diagram showing the angles between an arbitrary polarization vector $\vec{P}$ and the normal to the scattering plane $\hat{n}$ defined by the incoming and outgoing electron momentum vectors, $\vec{k}$ and $\vec{k}'$.

There are different models for the asymmetries in different kinematic regions, low energy threshold, resonance, high energy forward scattering and the hard scattering region. The forward angle G^0 measurements, for example, lie between the predictions for the resonance and high energy scattering regions[11]. The asymmetry in the threshold region can be calculated using HBχPT [47]. The high energy forward scattering region employs an optical thereom approach [3], [64]. In the hard scattering region the partonic handbag model can be employed[65]. Ultimately, the real answer has to come from lattice QCD, but for now it is necessary to rely on these model calculations.

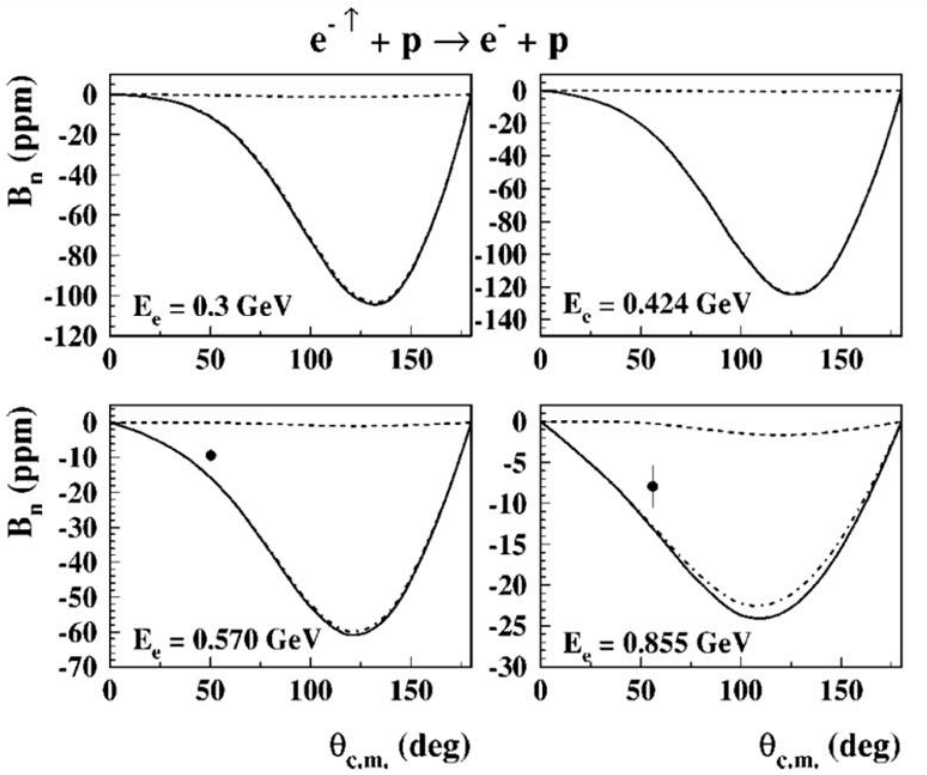

Figure 1.14: Calculations of the beam normal single spin asymmetries (ppm) in electron-proton scattering as a function of center of mass angle for different energies[114]. The results for the different intermediate hadronic states (elastic - dotted, πN - dash-dotted) as well as the total (solid line) are shown. The data points at forward angle are from PVA4[15]. If the intermediate hadronic states are not included in the calculation, the prediction is nearly flat (~ 0) as a function of the center-of-mass angle, $\theta_{c.m.}$.

The model that is relevant for the backward angle transverse asymmetries from electron-proton scattering, which are presented in Section 5.2.1, is the resonance region calculation. This calculation relates the imaginary part of the two photon exchange to the absorptive part of the doubly virtual Compton scattering tensor on the nucleon[114]. The asymmetry at backward angles is dominated by the quasi-real Compton scattering (quasi-RCS) where the intermediate electron is soft (its momentum is zero). In this case the first (second) photon takes on the full momentum of the incoming (outgoing) electrons and both photons are quasi-real. Figure 1.14 shows predictions for the asymmetry vs. center of mass angles for

different energies, where the calculations for the different intermediate hadronic states (π^0p and π^+n, see Figure 1.15) as well as the total are shown. The magnitude of the transverse asymmetry without including the intermediate hadronic states is practically flat as a function of center-of-mass angle. The PVA4 data at forward angle show that the intermediate states are important, and this is consistent with the forward angle G^0 results.

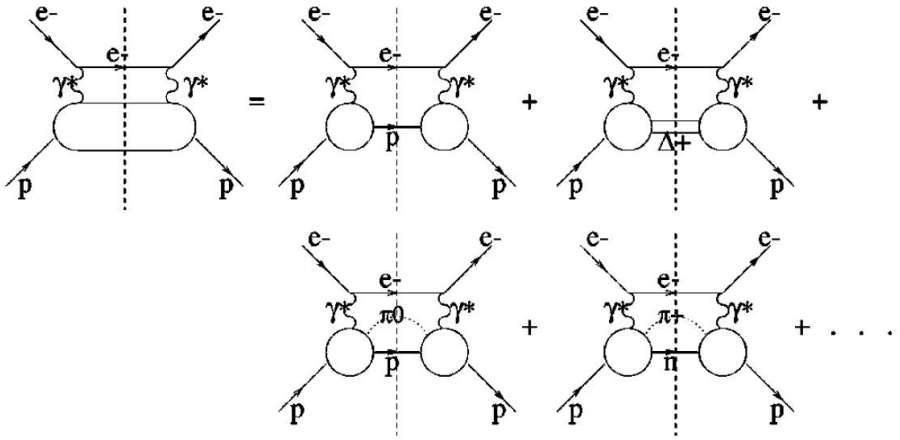

Figure 1.15: Feynman diagrams included in the expansion of the two-photon exchange amplitude for the intermediate states of the nucleon[145].

To calculate the value of B_n for a given energy and center-of-mass angle, an integral over W (the invariant mass of the intermediate hadronic state) is performed[114]. The phenomenological MAID model[73] is used to calculate the inelastic contribution for both the resonant and non-resonant pion production mechanisms. The quasi-RCS contribution comes from the endpoint of the integration, $W_{max} = \sqrt{s} - m_e$ where s is the Mandelstam variable (square of the sum of the four momenta of the incoming electron and nucleon). The peak, or maximum (absolute) value of B_n in Figures 1.14 and 1.16 is determined by the quasi-RCS contribution, which is of the opposite sign of the rest of the integrand. Because this contribution increases in magnitude faster than the rest of the integrand when going to backward angles, it causes the absolute value of B_n to have a peak (around $\sim$120° for the

energies shown).

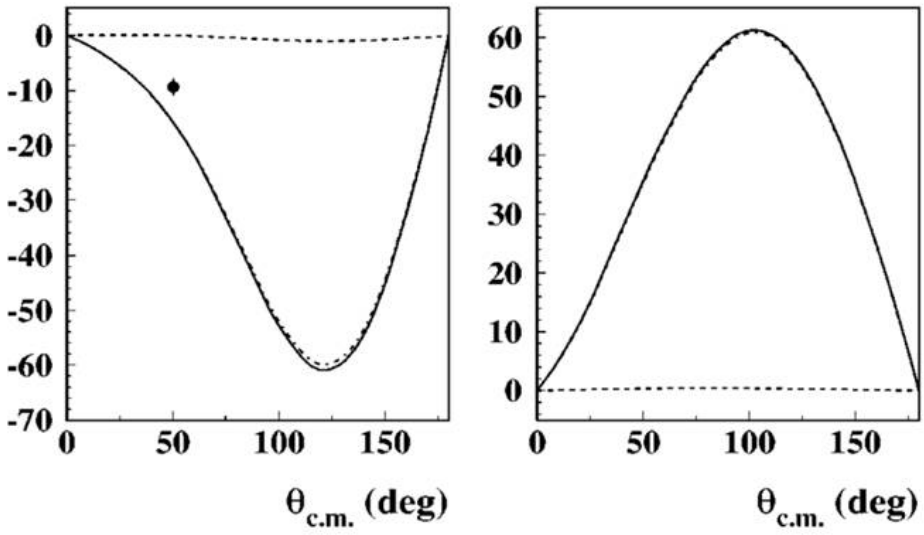

Figure 1.16: Predictions for the proton and the neutron asymmetries (ppm) vs. center of mass angle at a beam energy of 570MeV[114]. Again, the results for the different intermediate hadronic states (elastic - dotted, πN - dash-dotted) as well as the total (solid line) are shown. The proton (left panel) is the same as the lower left panel in Figure 1.14. The prediction as a function of $\theta_{c.m.}$ is nearly flat without the intermediate states.

In addition to predictions for the proton asymmetries, there are some predictions for the beam normal single spin asymmetries from the neutron. Figure 1.16 shows the predictions for the proton and the neutron vs. center of mass angle at a beam energy of 570 MeV. At this energy it appears that the predicted asymmetry for the neutron is roughly equal and opposite to that of the proton. First results for the neutron transverse asymmetries at two beam energies at backward angles have been obtained in G^0 (see Section 5.2.2).

1.3 Previous Experiments

In this section I will briefly describe the previous experiments relevant to the three measurements discussed in the preceding sections. Although I already mentioned E158, the Møller

experiment at SLAC that measured $Q_w(e)$, in Section 1.1.4, I will discuss it in a little more detail here since it is the most precise low Q^2 measurement of $sin^2\theta_W$ and is complementary to Q_{weak} in its physics reach. Then I will discuss the recent program of experiments that has studied the strange electric and magnetic form factors, including the G^0 forward angle measurement. Many of these experiments also measured the transverse asymmetries not only as a systematic control, but for the physics content as well. The results for the strange form factors and transverse asymmetries from the experiments will be summarized at the end of this section.

1.3.1 General Considerations

The general requirements for all of the experiments are the same[120]. To achieve the desired precision it is necessary to have a high intensity, highly polarized beam, with precision polarimetry (continuous if possible). Beam monitoring and feedback mechanisms can help to reduce differences in the position and angle of the beam on target, as well as its energy and intensity. Clearly changes in these quantities on the time scale of the helicity reversal is undesirable. The asymmetries are formed on "pulse pairs" (or quartets, as in the case of G^0) where the helicity of the incoming beam is reversed in various patterns. Rapid helicity reversal is desired to reduce systematics, while an independent, slow helicity reversal is employed as a cross check (usually an easily insertable half-wave plate). Because of the high beam intensity it is necessary to have a cryogenic target capable of withstanding a high power load. Finally, some sort of kinematic separation is needed in order to isolate the elastic events, since most of the experiments are run in "integrating mode" where the rate in the detectors is too high to distinguish individual pulses, and tracking events to determine their kinematics is generally not possible.

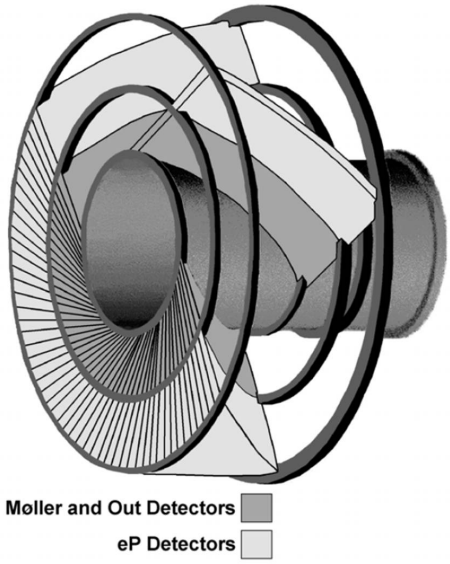

a (E158, SLAC)

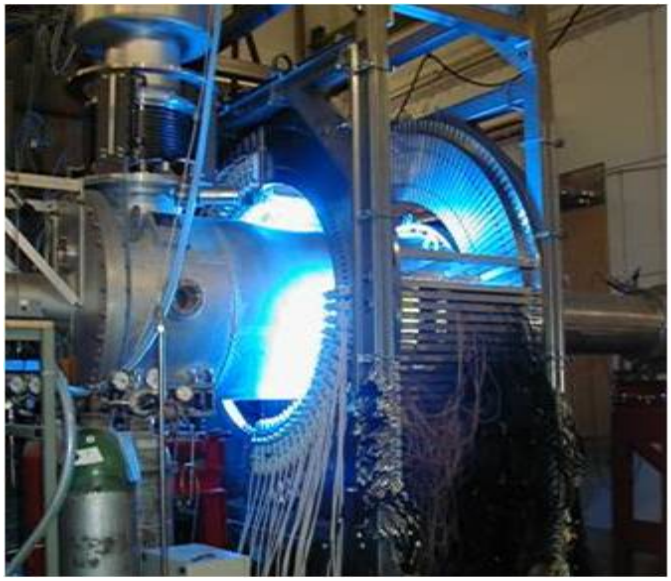

b (PVA4, Mainz)

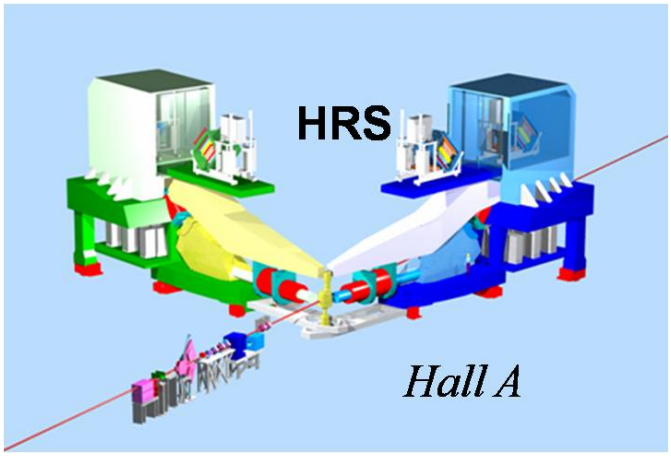

c (HAPPEx, JLab)

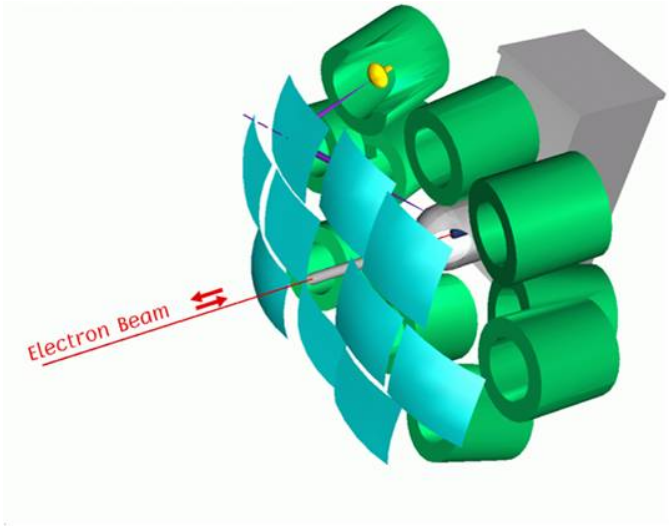

d (SAMPLE, MIT-Bates)

Figure 1.17: Pictures or diagrams from each of the previous experiments that will be discussed in this section. Part of the calorimeter in the Møller experiment is shown in (a)[74]. The PbF_2 calorimeter from PVA4 is shown in (b), diagrams of the HAPPEx spectrometers and the SAMPLE mirrors/PMTs are shown in (c) and (d) respectively [120].

1.3.2 Experimental Descriptions

There has been a rich experimental program to study the contribution of the strange quark

to the nucleon's charge and magnetization distributions. Until G^0 backward angle data were taken, these experiments had access only to linear combinations of G_E^s and G_M^s (see Figure 1.18). With the full G^0 program, as discussed above, it is possible to fully separate the strange form factors, and the axial form factor, G_A^e. These experiments are also relevant to the other measurements discussed in this thesis. Each of the experiments will be discussed briefly, and their contributions will be summarized below. Table 1.4 has a summary of the kinematics and sensitivities of each of the experiments which measured the strange and axial form factors.

E158

The E158 experiment is a parity-violating Møller scattering experiment. It was performed at the Stanford Linear Accelerator Facility (SLAC) using a longitudinally polarized electron beam at energies of 45 and 48 GeV incident on a 1.57 m liquid hydrogen target[7]. The electrons, which scattered from atomic electrons in the hydrogen (Møller electrons), were detected in a copper/fused silica fiber sandwich calorimeter (see Figure 1.17a). The angular range of the scattered electrons was $4.4 < \theta_{lab} < 7.5$ mrad - the detectors were located 60 m downstream of the target. The polarization was $\sim$60% for most of the run period. The data were collected at 120 Hz (8 ms), using helicity pairs to form the asymmetries. An insertable half-wave plate was used to achieve slow helicity reversal. An additional slow helicity reversal was accomplished by running at two different energies; the spin precession of the electrons in a bending magnet caused opposite helicity orientations in the experimental hall.

SAMPLE

SAMPLE was performed at the MIT-Bates Laboratory and measured electrons backward

Table 1.4: Summary of the kinematics and asymmetries for Sample, HAPPEx, PVA4, and G^0. Also shown are the experimental sensitivities and the (*expected) date of completion.

Expt/Lab	Target/Angle	Q^2 (GeV^2)	A_{phys} (ppm)	Sensitivity	Status
Sample/Bates					
SAMPLE I	$LH_2/145^\circ$	0.1	-6	$G_M^s + 0.4G_A^e$	2000
SAMPLE II	$LD_2/145^\circ$	0.1	-8	$G_M^s + 2G_A^e$	2004
SAMPLE III	$LD_2/145^\circ$	0.04	-4	$G_M^s + 3G_A^e$	2004
HAPPEx/JLab					
HAPPEx	$LH_2/12.5^\circ$	0.47	-15	$G_E^s + 0.39G_M^s$	2001
HAPPEx II	$LH_2/6^\circ$	0.11	-1.6	$G_E^s + 0.1G_M^s$	2006, 2007
HAPPEx He	$^4He/6^\circ$	0.11	+6	G_E^s	2006, 2007
HAPPEx III	$LH_2/14^\circ$	0.63	-24	$G_E^s + 0.5G_M^s$	2009*
PVA4/Mainz					
	$LH_2/35^\circ$	0.23	-5	$G_E^s + 0.2G_M^s$	2004
	$LH_2/35^\circ$	0.11	-1.4	$G_E^s + 0.1G_M^s$	2005
	$LH_2/145^\circ$	0.23	-17	$G_E^s + \eta G_M^s + \eta' G_A^e$	2009
	$LH_2/35^\circ$	0.63	-28	$G_E^s + 0.5G_M$	2009*
G^0/JLab					
Forward	$LH_2/35^\circ$	0.1 to 1	-1 to -40	$G_E^s + \eta G_M^s$	2005
Backward	$LH_2/LD_2/110^\circ$	0.23, 0.63	-12 to -45	$G_E^s + \eta G_M^s + \eta' G_A^e$	2009

scattered from hydrogen and deuterium targets [135]. The incident beam was longitudinally polarized at an energy of 200 MeV, incident on a 40 cm cryogenic target. The Cerenkov light (produced in air) from the scattered electrons was detected in 10 8" phototubes after being reflected by ellipsoidal mirrors, integrated over 25 μs pulses. The polarization of the beam was about 36%, and the background dilution was about 30% of the yield. A third measurement on deuterium was performed with different systematics (beam energy 125 MeV) in order to verify the results [134]. The transverse asymmetry was also measured at this energy at a backward angle of $\sim 150^{\circ}$[145].

HAPPEx

HAPPEx is an ongoing program of measurements taking place in Hall A at Jefferson Lab using a longitudinally polarized electron beam with an energy of 3 GeV incident on a 15 cm long cryogenic target. The elastically scattered electrons were detected in two high resolution spectrometers by measuring the Cerenkov light from the lead-lucite sandwich calorimeters in the focal plane, using a helicity window of $\sim$33.3 ms. The first measurements on hydrogen[5] had beam polarizations of 38% and 70% while during the first helium measurement polarizations as high as 85% were achieved[6]. The improvement in the polarization came from using a strained GaAs photocathode to produce the polarized beam (see Section 3.2.1). Improved measurements of the hydrogen and helium asymmetries have been made using 20 cm long targets[1].

PVA4

The PVA4 experiment has been performed using the A4 experimental setup at the MAMI accelerator facility in Mainz [89]. Longitudinally polarized electrons with a beam energy of

854 MeV (average polarization $\sim 80\%$) were incident on a 10 cm cryogenic target. Hydrogen and deuterium data have been taken, but so far only the hydrogen results have been reported. The scattered electrons were detected using a calorimeter which consists of 1022 PbF_2 crystals, using a 20 ms time window for recording data. Data were also taken at a lower beam energy of 570 MeV (same angle, lower Q^2)[90] and at backward angles (same Q^2, lower energy - 315.1 MeV) [16]. Higher Q^2 measurements are in progress. The experimental setup has also been used to acquire measurements for the transverse asymmetries at the two higher energies and forward angles[91]. Measurements of the transverse asymmetries at a backward angle of $\sim 145^\circ$ and a beam energy of 315 MeV have also been reported[124].

G0 Forward

The G^0 forward angle running took place in Hall C of Jefferson Lab using a 3GeV longitudinally polarized electron beam incident on a 20 cm liquid hydrogen target[11]. The scattered protons were detected in a toroidal spectrometer which was 8-fold symmetric about the beamline. A set of 16 scintillator detectors in the focal plane of each octant (FPDs) detected the protons which ranged in Q^2 from 0.12 to 1 GeV^2. The average beam polarization was $\sim 74\%$, with a helicity window of $\sim 33.3\,ms$. A 32 ns beam structure allowed for time-of-flight (TOF) kinematic separation of the elastically scattered protons and pion backgrounds, as well as further division of the Q^2 bins in the two detectors at largest radius. Transverse data were also taken, but with fewer Q^2 bins to improve the statistical uncertainties[11].

1.3.3 Summary of Contributions

The world data on linear combinations of G_E^s and G_M^s at $Q^2 \sim 0.1$ are summarized in the plot from the 2007 Long Range Plan (see Figure 1.18), but so far a full separation of G_E^s and

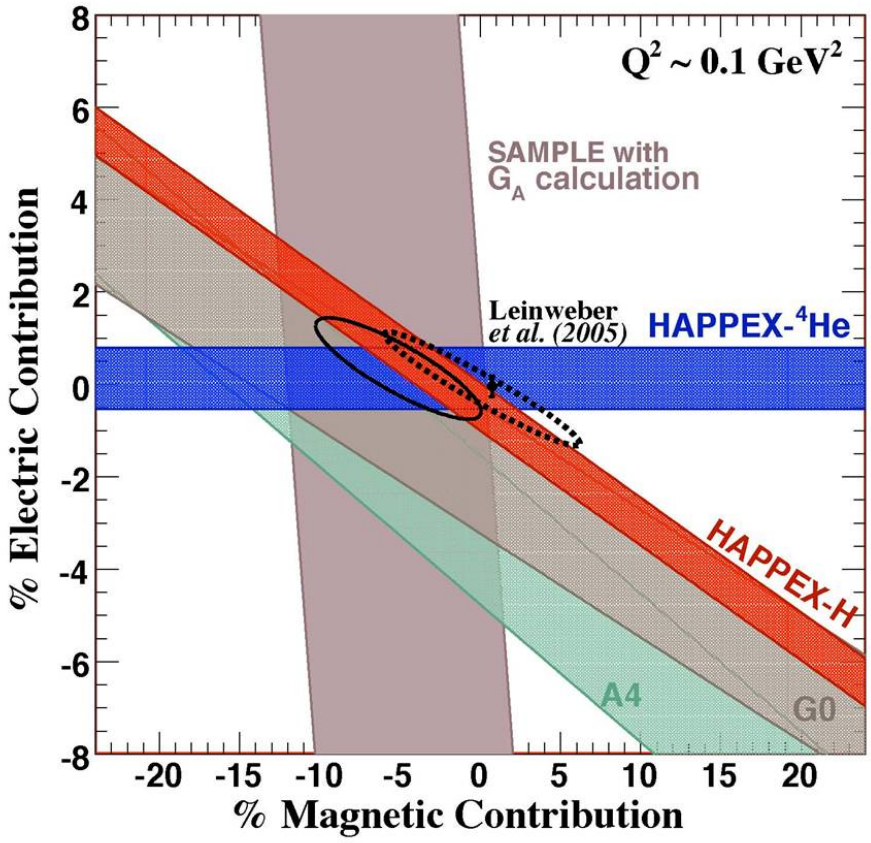

Figure 1.18: Summary of data on G_E^s and G_E^s at $Q^2 = 0.1$ for various experiments[137]. Data are shown as the percent contributions to the electric and magnetic form factors of the proton. Note that each experiment is sensitive to a linear combination of the two form factors.

G_M^s at multiple Q^2 has not been possible using the data from a single experiment. Note that the future HAPPEx and PVA4 measurements will complement the two values ($Q^2 = 0.23$ and $Q^2 = 0.63$) at which G^0 can fully separate the form factors. The limits on the strange quark contributions to the electric and magnetic form factors of the proton obtained in fits

to the world data at this Q^2 are[88]

$$\begin{aligned} G_E^s &= -0.008 \pm 0.016 \\ G_M^s &= 0.29 \pm 0.21 \end{aligned} \tag{1.48}$$

where a theoretical calculation of the axial form factor which is consistent with SAMPLE measurements is used. The G^0 program, including the backward angle measurements, provides full separation of G_E^s and G_M^s at two additional Q^2 points, Q^2=0.21 and 0.63 GeV^2/c^2, with a measurement of the effective axial form factor. The combination of the world data on the longitudinal asymmetries at various kinematics, including the G^0 backward angle data, will be used to constrain the hadronic uncertainties in the measurement of Q_{weak} by extrapolating to $Q^2 = 0$ (see Section 5.1.3).

In addition to measuring linear combinations of the strange form factors (summarized in Table 1.4), many of these experiments also measured the transverse asymmetries as a possible systematic error to the longitudinal asymmetry measurements. The data were also analyzed for physics relevant to improving the understanding of two photon exchange effects. The backward angle transverse data from these experiments will be presented in comparison to the G^0 backward transverse asymmetries in Section 5.2, along with a summary of forward angle measurements. The values of the beam normal single spin asymmetries obtained from the transverse data will serve as benchmarks for the models which are attempting to calculate the effect of two boson exchange corrections.

1.4 Summary

A whole program of experiments which have exploited parity violation in electron-proton

scattering have been carried out at Jefferson Lab and in laboratories around the world. These experiments have measured the strange quark contribution to the hadronic form factors, which are a measure of the spatial charge and magnetization distributions within the nucleon. In addition, transverse asymmetry measurements have been made. Not only are these parity-conserving asymmetries an important systematic for the PV asymmetry measurements, they also provide valuable information about two-photon exchange effects which will help to benchmark the theoretical framework that calculates the radiative corrections for precision electroweak measurements such as those described here. I have contributed to the backward angle portion of the G^0 program through the completion of several analysis tasks, and to Q_{weak} through the design and testing of several major components, including the collimators (which determine the acceptance of the experiment). In addition I analyzed the transverse asymmetries as measured in the G^0 backward angle for both their contribution to the systematics of the main measurement and for the physics merit. The measurements of hadronic structure in G^0 and the other parity-violating electron scattering experiments, as well as the effects of higher order radiative effects (such as two boson exchange) in the transverse asymmetries, will be used to constrain these effects in the measurement of Q_{weak}. With the SLAC E158 measurement acting as a "control", the precision of the measurement of $\sin^2\theta_W$ in Q_{weak} will allow it to be sensitive to new physics on a mass scale that is competitive with and complementary to the LHC.

Chapter 2

The Qweak Experiment

2.1 General Description

Q_{weak} proposes to measure $sin^2\theta_W$ to a precision of 0.3% via a 4% measurement of the weak charge of the proton. The measurement will take place in Hall C of Jefferson Lab, utilizing much of the standard hall equipment including beam current and position monitors and the Møller polarimeter (see Section 3.2.1). The Jefferson Lab polarized source group has consistently achieved beam polarizitions of 85%. Longitudinally polarized electrons with a beam energy of 1.165 GeV at 180 μA will bombard a 35 cm liquid hydrogen target for 2200 total hours. The planned precision gives access to new physics at the TeV scale. Elastically scattered electrons will be bent away from the beamline in an eight-fold symmetric copper-cooled toroidal magnet and focused onto a set of eight fused-silica quartz bars. The rate on each of the detectors will be 0.8 GHz. Although simple conceptually, the experiment presents many experimental challenges in control of backgrounds and precision of polarimetry, reduction of helicity correlated effects and knowledge of the Q^2.

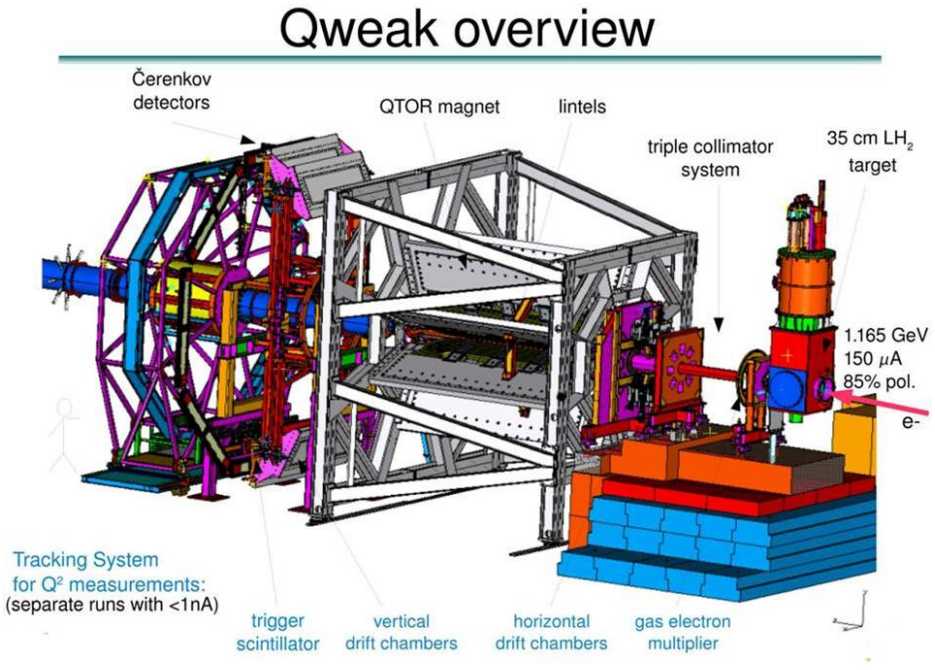

Figure 2.1: Schematic of the Q_{weak} experiment without the shield wall in place[42]. There are three regions, going from left to right along the beamline: Region I, which is defined as upstream of the first (cleanup) collimator, Region II which is between the second (acceptance defining collimator) and the third (cleanup) collimator, and Region III which is defined as after the magnet.

2.1.1 Target and Luminosity Monitors

The target will be the highest power cryogenic target in the world at 2500 W[131]. The fluid dynamics has been modeled using ANSYS (a fluid dynamics simulation code) in an attempt to minimize boiling in the target, specifically at the end windows. The resulting design is for a target with transverse flow, rather than flow along the beam axis (see Figure 2.3). GEANT3 simulations have been used to design the body of the target to ensure that the design does not interfere with the scattered electrons that are in the acceptance of the main detectors (see Section 2.2.1). The cell windows are a significant source of background due to the 10x larger asymmetry of aluminum and uncertainty in the calculations of the

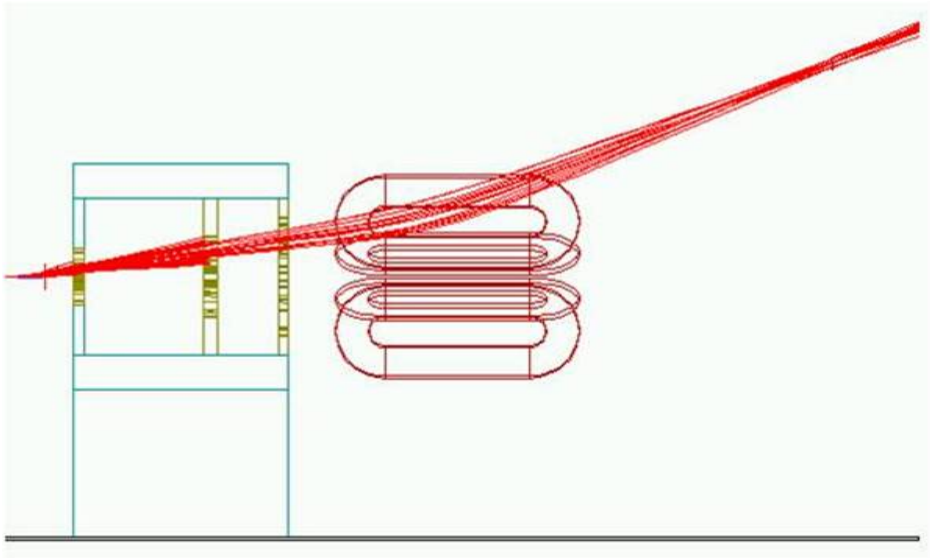

Figure 2.2: This simplified view of the experiment shows the elastic electron tracks (red) as they go from the target (far left), through the 3 collimators, and then are bent in the QTOR to be focused onto the quartz bar (far upper right). Not shown are the Møller electrons or the neutral particles from showers in the target. Note that the second, middle collimator is the primary (acceptance defining) collimator, so ideally none of the ep elastic electrons that make it through this collimator hit the third cleanup collimator. The first collimator (closest to the target) is needed to shield the Region I GEM detectors.

asymmetry[112]. Adequate time will be needed to measure the aluminum asymmetry with the required precision. The cell windows will be made as thin as possible (0.003" if aluminum) although a beryllium endwindow is being considered to mitigate the backgrounds.

Although film boiling can occur at the endwindows, even without actual boiling in the target there can be density fluctuations that will affect the measured yield. The luminosity is proportional to the density of the target

$$\mathcal{L} = \Phi N \tag{2.1}$$

where Φ is the incoming particle flux and $N = nA_{beam}t$ is the number of scattering centers in the target with n being the number of particles per unit volume and t is the length of the

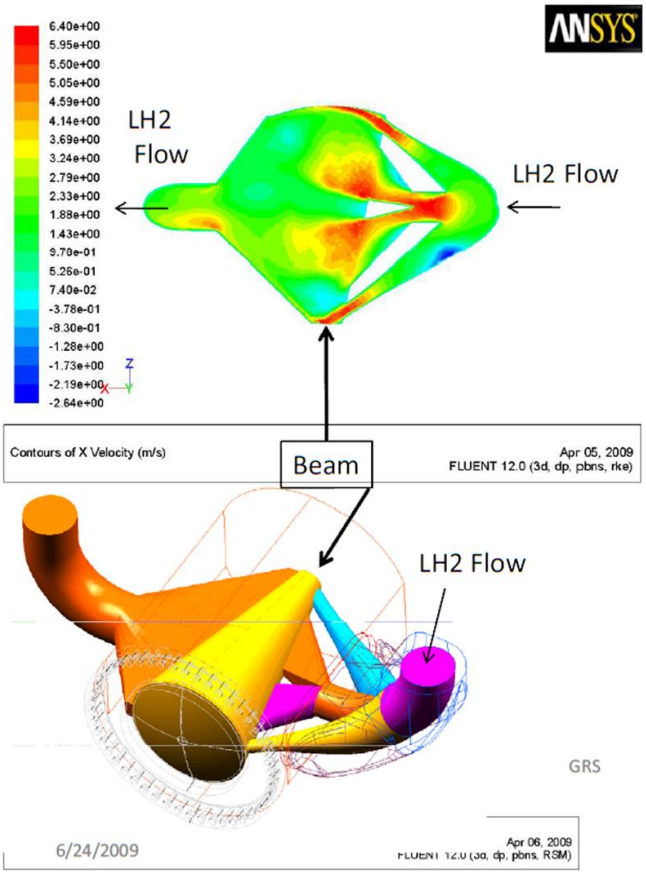

Figure 2.3: Schematic of the transverse flow target which is being designed for use in Q_{weak}. Top shows contours in the LH2 flow velocity and bottom is schematic of the actual design[131].

target. The flux can be calculated from the incoming beam current per beam area, A_{beam}, which cancels out. The asymmetry is calculated from the number of counts in each helicity state

$$A = \frac{N_+ - N_-}{N_+ + N_-} \tag{2.2}$$

and the width of the asymmetry distribution depends on the number of events in each helicity state (counting statistics), the electronic noise in the detectors, fluctuations in the

beam parameters, and fluctuations in the density of the target

$$\Gamma^2_{total} = \Gamma^2_{count} + \Gamma^2_{electronics} + \Gamma^2_{beam} + \Gamma^2_{density} \tag{2.3}$$

where a solid target can be used to understand the widths without the density term. The density fluctuations can be controlled by changing the target parameters (see Section D.1). Experience has shown that the density fluctuation term can be reduced by increasing the helicity flip rate[83].

Luminosity monitors can be used to monitor the target density fluctuations. The monitors can be placed closer to the beamline where the rates are very high, and so have small statistical widths compared to the main detector, making them more sensitive to target density fluctuations as well as increases in the asymmetry width due to beam parameter fluctuations. In Q_{weak} there will be two sets of luminosity monitors (LUMIs). The first set of four monitors will be located upstream of the acceptance defining collimator at angles slightly smaller than that of the experiment ($\sim 5^\circ$) and will detect mostly Møller electrons. These upstream LUMIs will primarily be used as target density fluctuation monitors, because they will be relatively insensitive to beam angle and energy changes, and will be sensitive to most of the target, with decreased sensitivity to the downstream end of the target. The second set of eight LUMIs will be located far downstream, past the main detector. This set of LUMIs will be at very small angles ($\sim 0.6^\circ$), and will be used primarily to monitor the helicity-correlated beam properties. The downstream LUMIs have sensitivity only to the downstream end of the target. Although the designs of the upstream and downstream LUMIs differ, both sets have detectors that consist of quartz to detect the cerenkov light created by the incident electrons in a specific angular range, with an air light guide to transport the light to a photomultiplier tube (PMT).

2.1.2 Spectrometer and Main Detectors

The spectrometer system and main detectors consist of 3 collimators, a toroidal magnet with 8-fold symmetry about the beam axis (QTOR) and 8 fused-silica quartz bars. The elastically scattered electrons from ep scattering as well as Møller scattering travel through the openings in the first cleanup collimator, the second, acceptance defining collimator, and the third and final cleanup collimator. As they travel through the magnetic field of QTOR the Møller electrons are swept away and the ep scattered electrons are bent and focused onto the quartz bars in each octant (see Figure 2.2). Neutral backgrounds from shower events in the target go straight through the magnet, and hit a shield wall. The system has been studied extensively in simulation to design away sources of background (where possible) and to try to understand them when it is not possible for them to be eliminated (see Section 2.2.3).

a b

Figure 2.4: The assembled QTOR with the field mapping device at MIT-Bates (a) and the assembled primary collimator (b)[32].

The spectrometer is a resistive, water-cooled copper toroidal magnet with a field integral

of $\int Bdl \sim 1.6\,Tm$. It has eight open sectors, spaced symmetrically about the beam axis, and 8 double pancakes of copper "wire" (actually ~2.3"x1.5" with a 0.8" diameter hole in the center for the water cooling. Each coil has a 2.2 m long straight section and two semi-circular sections with an inner radius of 0.235 m and an outer radius of 0.75 m[39]. It has been constructed and field-mapped at MIT-Bates and has since been shipped to JLab (see Figure 2.4a). The collimators were designed to accept as much of the primary ep elastic scattering rate that would pass through the QTOR without hitting any part of the coils or the support structure, and then sculpted to further reduce backgrounds (see Figure 2.4b and Section 2.2.3).

Figure 2.5: Photograph of two of the bars in the housing that will provide strain relief on the joint as well as structural support for the PMTs and the lead that will shield them[93].

The main detectors are a set of 8 fused-silica quartz bars. Each bar is made of two 1 m long, 18 cm tall, 1.25 cm thick pieces that will be glued together end-to-end (see Figure 2.5). The cerenkov light from the incident electrons will be collected in PMTs attached to either

end of the bars. During the main measurement the rate on each of the main detector bars is about 800 MHz. The beam current will be reduced drastically for the Q^2 measurement so that individual events can be tracked. The PMTs can be used in low gain (2000) current mode readout for the main measurement, or in high gain (2×10^6) pulsed mode readout for the tracking measurement. It is necessary that the PMTs in pulsed mode be capable of resolving single photoelectron backgrounds, while in current mode it is the DC anode current that will be measured. Different voltage dividers will be used to obtain the different gain, with 7 stages being used in current mode and 10 stages with additional amplification in pulsed mode[41]. Custom low noise electronics has been developed by TRIUMF for the readout of the PMTs. Bench testing indicates that the electronic noise is about 3 orders of magnitude smaller than the counting statistics of the experiment[93].

2.1.3 The Tracking System

The tracking system is necessary to measure the Q^2 and backgrounds in the experiment. The asymmetry in Q_{weak} is proportional to the Q^2

$$A \sim \frac{-G_F}{4\pi\alpha\sqrt{2}}\left[Q^2 Q_W^p + Q^4 B(Q^2)\right] \tag{2.4}$$

with the higher moments important in the hadronic term, $B(Q^2)$. The acceptance defining collimator would determine Q^2 to $\sim 1\%$, but due to the precision of the Q_{weak} measurement it is necessary to measure the mean Q^2 with a fractional error smaller than $\partial Q^2/Q^2 = 0.5\%$. It will also be necessary to weight the Q^2 by the analog response of the cerenkov bars in order to determine the effective Q^2. A dedicated tracking system will be used in "pulsed mode" at low current (1 nA) to track individual events to determine the $< Q^2 >$ on the main detectors as well as measure the background rates [41]. Only two opposing octants will be

instrumented at any given time, but the detectors in each region will be mounted to rotators so that the calibration can be performed in each octant, and the detectors will be pulled out to a "parked" position during the main measurement. The tracking system will be used to measure the light weighted response of the cerenkov bars as well as a sanity check on our understanding of the toroidal field and the collimators, and provide limited diagnostics on backgrounds[9].

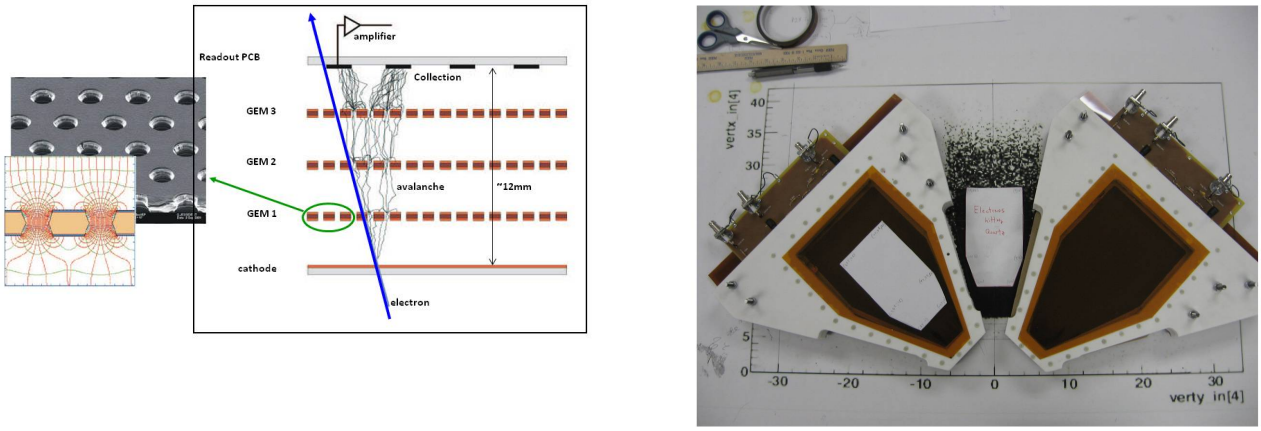

a b

Figure 2.6: Diagram depicting an electron track and the resulting avalanche through an example GEM, with a picture of a GEM foil, and a diagram of the electric field lines and equipotential contours (a)[68]. Picture of the two completed GEM chambers straddling a plot of the electron beam envelope at that location, the white paper shows the envelope that eventually hits the main detectors (b)[56].

The detectors in Region I, which is located closest to the target, just after the first cleanup collimator, will be gas electron multipliers (GEMs). The rotator in this region will be fully motorized, due to the highly radioactive environment so close to the target, the first collimator and the beam plug (see Section 2.2.1). The GEMs are extremely rad hard to be able to survive in this environment. The detector consists of ionization chambers with preamplifier foils with 50 μm holes, separated by 100 μm, that magnify the signal through

a series of avalanches. The charge is collected on copper strips in a "charge collector" plane before being read out to an amplifier (see Figure 2.6a). The size of the electric field in the region of the holes is on the order of 40 kV/cm. The expected rate on the GEMs during a tracking run is 1000 Hz/mm^2, with a position resolution of 100 μm [39].

Drift chambers will be used in Regions II and III to provide position and angle measurements of each track before and after the magnet. A drift chamber consists of planes of parallel sense wires strung between cathode planes (consisting of aluminized mylar) on either side of the wire plane, within a volume of ionizing gas. Field wires are placed between the sense wires (in the same plane) in order to help shape the electric field in the cell. A cell consists of a sense wire between two field wires and a cathode plane on either side (see Figure 2.7, a). As a charged particle traverses the chamber it ionizes the gas in particular cells in each plane, and the electrons "drift" to the sense wires because of the electric field in the cell. By changing the angle at which the wires are strung in different planes, the position can be determined. Both horizontal (HDC) and vertical (VDC) drift chambers use the measured drift time between an electron trigger signal and the signal on the wires with a parameterization of the drift velocity to obtain better resolution than the actual spacing of the wires. The difference between a VDC and an HDC is the direction of the drift. When the cells are viewed so that the wires are coming out of the page and the electron track is in the plane of the page (see Figure 2.7, a), if the electrons drift primarily in the horizontal direction, then it is a horizontal drift chamber. A vertical drift chamber (Figure 2.8, b) exhibits primarily vertical drift, and has tracks that are more shallow relative to the wire plane, which generates a signal in multiple wires (with different drift times in each wire) for each track.

A set of horizontal drift chambers will be located in Region II, which is after the primary collimator and before the third (cleanup) collimator. In each instrumented octant there are

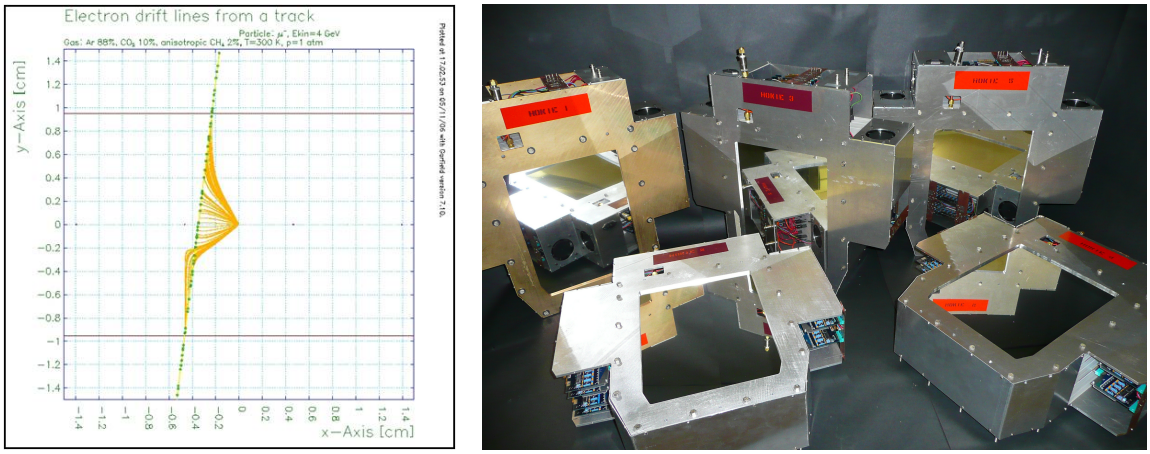

a b

Figure 2.7: Diagram showing how an incident electron creates tracks with horizontal drift in a horizontal drift chamber (a). Picture of the constructed Region II HDCs (b).

two chambers, separated along the beamline by ∼0.4 m. This allows not only for position determination but also for an angle at the entrance to the magnet. Each chamber consists of 6 planes (x, x′, u, u′, v and v′) where the primed u and v planes are rotated by ±53.231° relative to the unprimed planes. The frame material is ertalyte, which is easily machinable. The angle of the incoming electrons obviates the need for an offset between the x,u,v and x′,u′,v′ planes in order to resolve the left-right ambiguity (on which side of the wire that was hit did the electron pass). Each plane has alternating sense and field shaping wires, for a total of 768 electronics channels in the four chambers. Cathode planes constructed of aluminized mylar are placed between each of the wire planes. The active area of these chambers is trapezoidal, covering approximately 50x70 cm^2.

It was originally thought that the Møller electron rates (∼2600 kHz/nA, compared to the ep elastic rate of ∼5 kHz/nA) in Region II would necessitate the use of an additional toroidal magnet, a minitorus, that would sweep the Møller electrons away before the horizontal drift chambers (see Section 2.2.5). The horizontal drift chambers require a total rate < 1 MHz

for high tracking and reconstruction efficiency [39]. This option has been ruled out due to a plan to perform the tracking at ∼100 pA beam currents with the HDCs in place and at ∼10 nA currents with them pulled to the "parked" position. Beam tests performed in March 2007 showed that the beam was stable enough at such low currents and that monitoring of the beam current and position could be achieved (see Section 2.3.1).

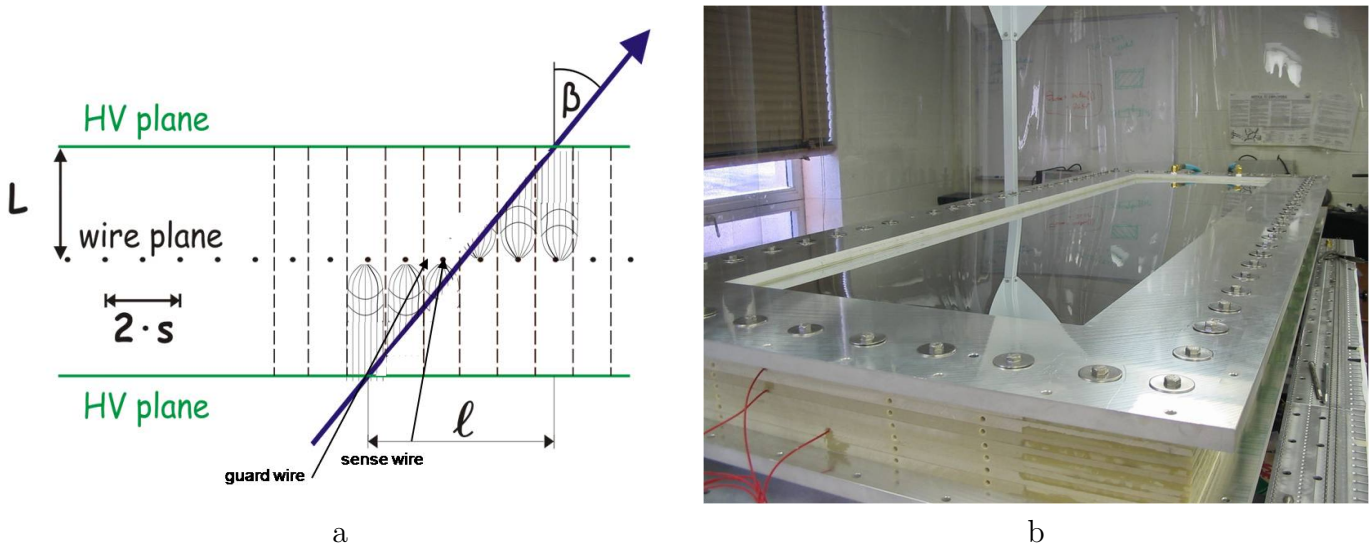

a b

Figure 2.8: Diagram showing how an incident electron creates tracks with vertical drift in a vertical drift chamber (a). Picture of a constructed Region III VDC (b)[84].

Region III, which consists of vertical drift chambers, is located after the magnet, just before the main detectors. There will also be two chambers in each instrumented octant in this region, in order to provide a position and direction after the magnet. These chambers are rectangular in shape, with an active area of about 21"x80.5", with 2248 sense wires. Due to the large size of the chambers it was necessary to use a more rigid material, G10, to avoid sagging. The readout of these chambers is also a little different, due to the large number of channels which need to be instrumented. The wire signals are "multiplexed" with a delay line to reduce the number of electronics channels by a factor of 9[41]. The signals from 18

wires from separated locations are ganged together and sent to two signal paths (2 electronic channels). The drift time is decoded from the sum of the two times, and the wire that was hit is identified from the difference.

In order to determine the Q^2 it is necessary to have an algorithm capable of creating tracks from the multiple hits in the detectors in the three regions. A trigger scintillator that will provide the trigger and time reference for the calibration system will be placed near the main detectors. Hits will be recorded in each of the detectors whenever a trigger is signaled. From these hits it will be necessary to reconstruct tracks that have gone through the toroidal magnetic field. The GEMs will provide a "point" near the target and the Region II HDCs will provide a line (two points separated along the beam axis). It will be necessary to use the knowledge from the field mapping to "swim" the particle through the magnetic field, and the Region 3 chambers will provide a line after the magnet. Coincidence with the main detector will also be required for Q^2 determination. The study of backgrounds may not involve coincidences with all of the detectors, and so may prove more difficult.

2.1.4 Expected Uncertainties

A summary of the expected uncertainties in the Q_{weak} experiment is listed in Table 2.1. The error due to counting statistics is limited by the running time of the experiment, which is approximately 2200 hours at a beam current of 180 μA. The beam polarization will need to be measured to 1% on the asymmetry. The helicity correlated beam properties (energy, position, angle and charge at the target) will be measured in order to control them with active feedback to the accelerator, and in order to regress out the remaining effects if necessary. The experiment is designed to minimize the uncertainty due to backgrounds by making the relative contribution from backgrounds as small as practical, and the hadronic

Table 2.1: Summary of the estimated uncertainties in Q_{weak} for both the physics asymmetry and the extracted value of Q_W^p. The error magnification due to the 33% hadronic diluation is 1.49, except in the case of the Q^2 where it is slightly larger.

Source of Uncertainty	Contribution to $\Delta A_{phys}/A_{phys}$	Contribution to $\Delta Q_W^p/Q_W^p$
Counting Statistics	2.1%	3.2%
Hadronic Structure	—	1.5%
Beam Polarimetry	1.0%	1.5%
Absolute Q^2	0.5%	1.0%
Backgrounds	0.5%	0.7%
Helicity Correlated Beam Properties	0.5%	0.7%
Total	2.5%	4.1%

structure term was taken into consideration as well. The tracking system will be used to help measure the backgrounds and to determine the Q^2 to the necessary precision.

2.2 Simulation and Design

Because I joined the Q_{weak} collaboration at such an early stage my involvement consisted of a great deal of simulation and design work. I performed GARFIELD simulations [139] to help optimize the gas for the horizontal drift chambers as well as the cathode and field shaping wire high voltage settings. GEANT3, another monte carlo simulation program[8], was used to study many aspects of the experiment from optimizing the collimation system in conjunction with placement of the main detectors, designing (a now obsolete) additional minitorus, optimizing the beamline to eliminate sources of background and to help choose and optimize a target cell design. As is the case in the work I did on early construction and

testing, many of these studies were the basis for later improvements. I will summarize my work and provide references for the final studies.

2.2.1 Target

Several designs were considered for the target before deciding on the transverse flow version discussed in Section 2.1 (see Figure 2.9). The fluid flow and heat transport were studied using ANSYS, but GEANT3 simulations could be used to answer questions about how the geometry of the cell affected the acceptance in the experiment, or conversely, the cell could be designed to minimize the effect on the acceptance. There were several other aspects of target design that were studied, including the effect of using a beryllium vs. an aluminum end window and the effect of the target radius on the ep elastic rate on the main detectors.

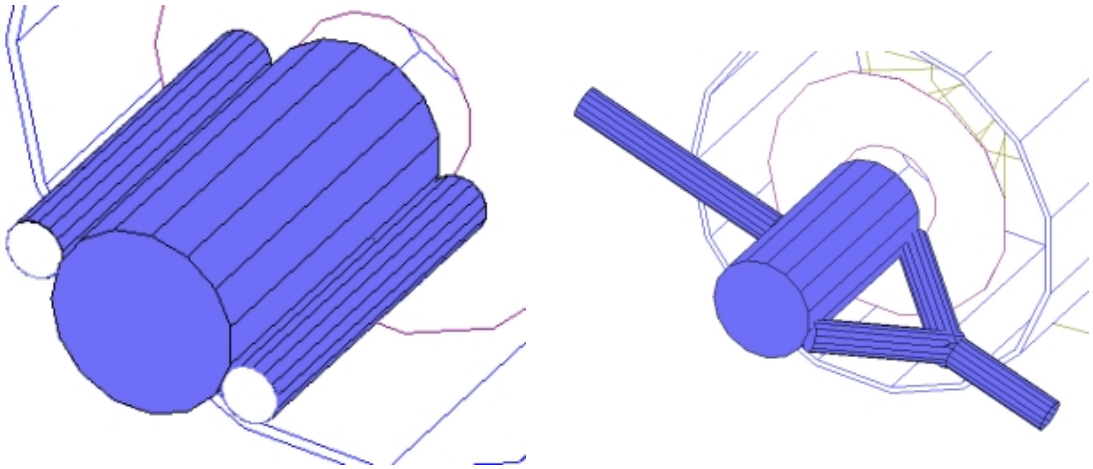

a b

Figure 2.9: Note that these drawings are not at the same scale; the target tube has the same radius and is the same length in each design. One version involved transverse flow through holes in the pipes on either side of the target (a). The final design is a transverse flow target similar to this version, with two pipes for input flow and one for output (b).

The effect of the target cell radius was studied by looking at the ep elastic rate on the

main detector with the target cell inner diameter ranging from 0 to 6". The cell wall is 10 mils thick aluminum, and for this study the endwindows are 3.5 mils thick aluminum. For a radius of 0, the target cell consists only of the aluminum cell walls. The elastic rate increases as the target radius increases because more of the scattered electrons are exiting through the endwindow instead of the cell wall at an oblique angle. The additional energy loss and multiple scattering change the way the particles are focused by the QTOR magnet, causing the rate on the detector to decrease. The mean scattered angle is approximately 8°, making the effective thickness of the cell wall about 70 mils. The rate levels off when the lower half of the angular range (most of the rate) of the scattered electrons that hit the main detector exit through the endwindow (see Figure 2.10a). The final design has a conical shape with a diameter of 12" at the downstream end of the target (6.83" for the 0.02" thick exit window region), ensuring that all the scattered electrons of interest exit through the 20mil endwindow[133].

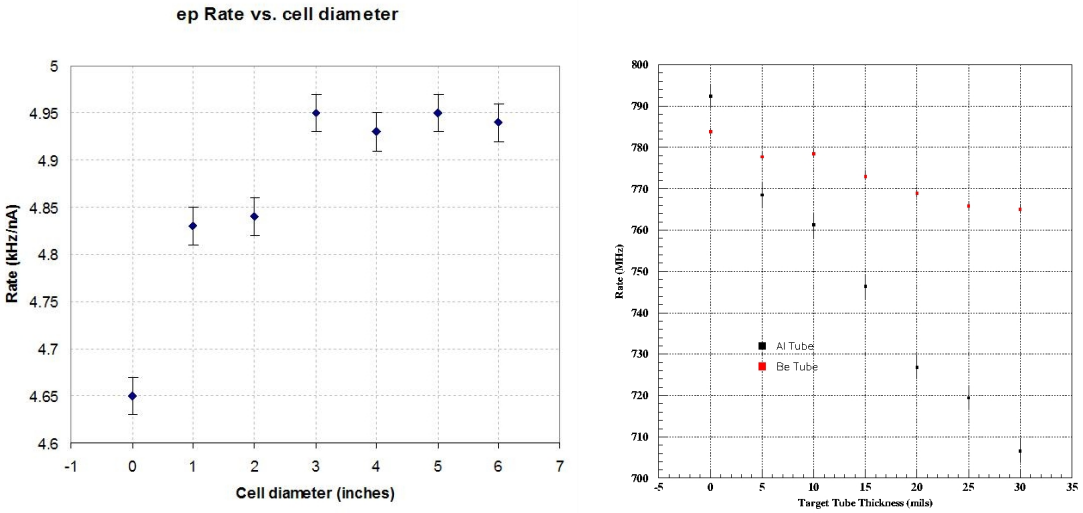

a b

Figure 2.10: As the cell diameter is increased, the ep elastic rate increases because less aluminum in the target cell is traversed (a). For both materials, the rate decreases as the window thickness increases, but the effect is smaller in beryllium than in aluminum (b).

The ep elastic rate decreases as the thickness of the end window increases, and the rate is higher for beryllium than for aluminum (see Figure 2.10b). Beryllium was considered as a possible alternative for the aluminum end window because the rate of scattering from aluminum (eAl elastic) is large, and the uncertainties in the asymmetry (which is 10x higher than the ep elastic asymmetry) are also large due to high Z impurities in the actual material. It will be difficult to measure the aluminum asymmetry with sufficient precision. Although the asymmetry of the beryllium is slightly higher than aluminum, the asymmetry weighted background from beryllium windows is 2.4x smaller than for aluminum windows because the cross section is 10x smaller. The uncertainties in the asymmetry in scattering from beryllium are also smaller, making it a more desirable end window material[110]. Unfortunately it is prohibitively expensive to machine either window of beryllium, so in the current design the primary beam exits the target through a 5 mil aluminum "nipple" with a radius of 0.622"[133].

In addition to optimizing the cell radius and endwindow material, the geometry of the transverse parts of the target could be optimized to minimize the effect of the target on the acceptance. Tests of the background rates in each of the regions were done with the various target cell designs, to see that scattering from the transverse target attachments did not create additional sources of background (especially for the main detectors). Octant to octant "cross talk" was also investigated, with no obvious difference due to transverse target attachments (within errors). In order to aid in the final design, the azimuthal (ϕ) acceptance of electrons that hit the main detectors were provided for various z locations along the target length[97](Figure 2.11a). The octant at 12 o'clock is shown with two adjacent octants, at a particular z location along the length of the target. The "ϕ profile" was also provided for different radial bins at each z location (see Figure 2.11). This plot shows the distribution of the azimuthal angle for a radial bin of 4.5 to 5 cm at the same z location as the profile

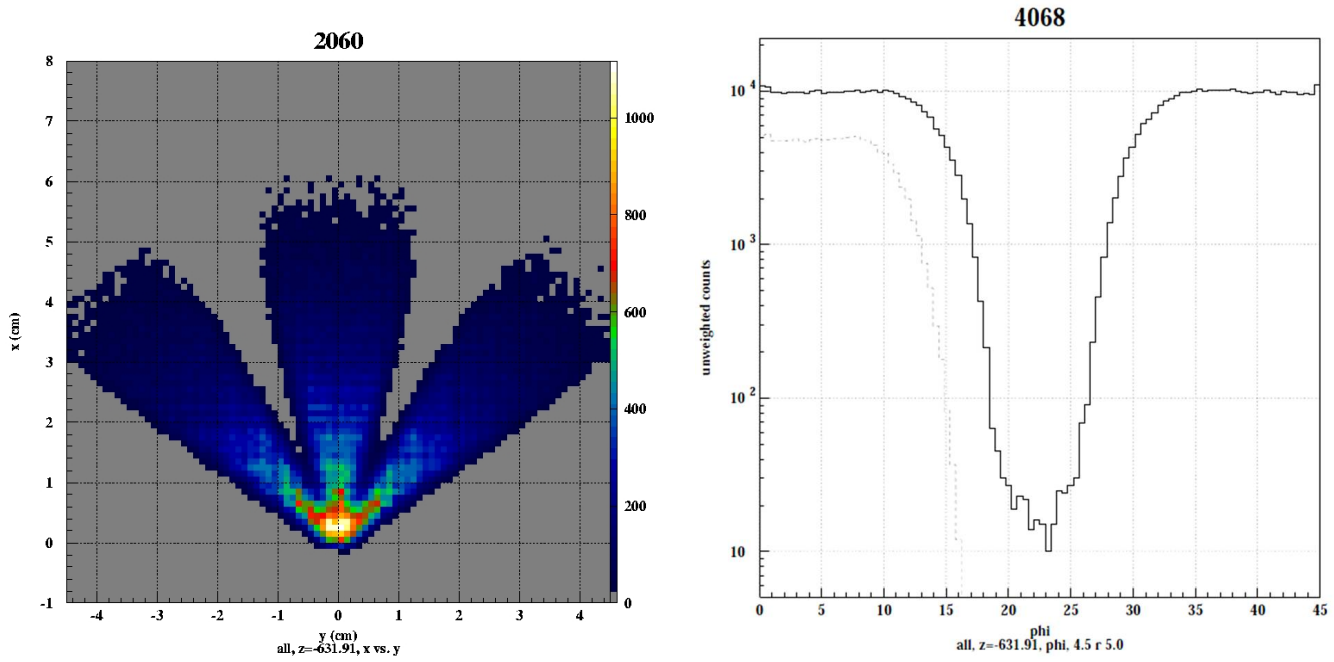

a b

Figure 2.11: The distribution of events that will make it through the first collimator, in the plane perpendicular to the beam axis, at a z location near the end of the target for the top three octants(a). A profile of the ϕ distribution at the same z location for events that make it through the first collimator (solid line) and events that eventually hit the main detector in the octant at 12 o'clock (dashed line) where $\phi = 22.5°$ is between the octants (b). This plot is for $4.5 < radius < 5.0$.

that is shown on the left. The dotted line shows the distribution of events that hit the main detectors in the octant at 12 o'clock, while the solid line shows the distribution of what would make it through the first collimator. The "dip" occurs in the region between the octants. The target manifolds were designed to be in the regions of ϕ that would be in this dip, that is, the shadows of the collimators. If possible they would not interfere with anything that would make it through the first collimator, but it was essential that the target manifolds not interfere with what hits the main detectors.

2.2.2 Beamline

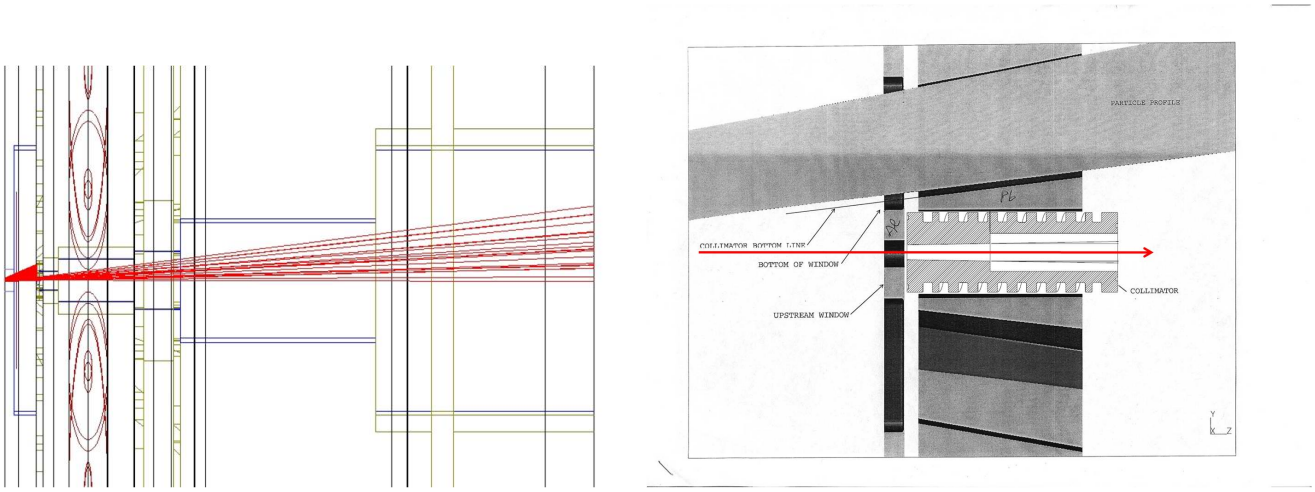

a b

Figure 2.12: Scattered primary beam events (red tracks) that are not stopped in the beam defining collimator (far right) do not interfere with any of the downstream beam line elements (note the z axis is scaled down by a factor of 10)(a). The nearly final design of the beam defining collimator embedded in the first collimator, with the scattered ep elastic electron profile shown (b)[32]. The final design is tapered along the entire length (this picture is not scaled).

The beamline was designed with the idea that scattered particles that were not in our angular acceptance not interact anywhere in the beamline downstream of the target until it reaches the beam dump in order to minimize the "single-bounce" backgrounds caused by interactions in the beamline. This design requires a "beam defining collimator" in addition to the primary collimation system, located somewhere near the target (within the beamline) to limit the angular range of particles scattered at low angles. The scattered particles that do not interact with this collimator will travel through the beamline to the main beam dump without interacting in any of the downstream beamline elements. The limiting aperture in the beamline came from the size of the beampipe through the QTOR (see Figure 2.12a). The beam defining collimator is designed such that no electron that passes through it will hit the

end of the beampipe that passes through the center of the QTOR (with a single bounce). The showers from this beam defining collimator are shielded by the primary collimation system as well as some lead shielding placed around the beamline.

It is necessary to take into account the heat load and radiation dose on the plug, and the generation of secondaries from showers in the plug, including the generation of neutral backgrounds. The presence of the plug in the first cleanup collimator increases the radioactivity in Region I. Studies by Pavel Degtiarenko, an environmental health and safety officer at Jefferson Lab, which estimated the size of the neutron flux at the main detector indicated that even without the collimators or shield house in Region II or the shield wall in Region III the neutral background contributed less than 1% of the anode current of the main detectors. The beam defining collimator will be made of a machineable tungsten-copper alloy that is water cooled to manage the heat load, which is on the order of 1000W. The final design is optimized to minimize the rate at the end of the QTOR exit pipe, and is tapered all the way to the end of the plug instead of only about half way (see Figure 2.12b)[132].

The rest of the beamline was designed in conjunction with early designs of the beam defining collimator. The beamline was designed by using the radius at the end of the QTOR pipe to create a reference design. It has a telescoping structure, with as few changes in radius as possible. When possible the radius increases in or near one of the collimators. The simulation was used to check that no single bounce primary electrons hit the beam pipe anywhere, with as small a clearance as possible to maximize the room for shielding around the beamline (should it prove to be necessary). The upper limit of the radius of the beampipe and any shielding is given by the low angle of the scattered ep elastic envelope of the signal. The clearances were then adjusted by simulating secondary tracks and studying the sources of backgrounds for the main detector which would occur at the end of a beampipe if the radius was too small. Although the shielding was not optimized, the simulation indicated

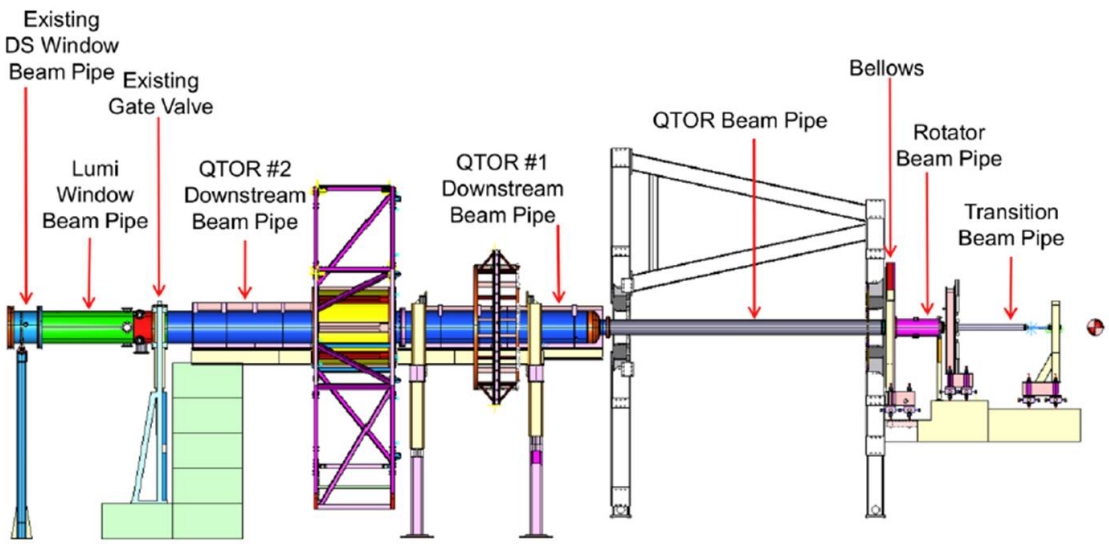

Figure 2.13: A drawing of the beam line throughout the experiment [32]. The limiting aperture for the beamline is given by the downstream end of the QTOR beampipe. The beam defining collimator is located in the first cleanup collimator (far right). Note that in this figure the beam enters from the right instead of from the left.

that the sources of background due to the beampipe itself were small. A CAD drawing with the final design is shown in Figure 2.13.

2.2.3 Collimators

The original Q_{weak} proposal quoted a rate per octant of 763 MHz, with a mean scattering angle of 9°, with a mean $Q^2 = 0.030$ and a 4% error on the measurement of the weak charge of the proton[38]. Several factors conspired to make it necessary to redesign the collimation system from the one assumed in this original proposal. The process went through several iterations because not all of these factors were discovered at the same time; abbreviated descriptions of the various issues and the complete process for the final design will be described below.

In the original simulations the target cell material was, in fact, beryllium. Due to cost considerations it was decided that the target should instead be made from aluminum (see Section 2.2.1). This change caused a reduction in the overall rate at the main detectors. In addition, the simulation was not properly accounting for internal bremsstrahlung and when this effect was taken into consideration it was found that the rate dropped by an additional 17%. These rate losses prompted the idea of increasing the acceptance of the experiment by increasing the size of the collimator openings.

In the initial studies for increasing the collimator acceptance, there were some issues with how the collimators were optimized. The collimator design in the original proposal optimized the rate, while these studies used an approximate figure of merit (FOM) which attempted to maximize the asymmetry and the rate. This was eventually replaced by what was considered the true FOM, the error on Q_W^p, which included estimates of the "hadronic dilutions". The weak charge of the proton is determined by measuring the parity-violating asymmetry in the elastic scattering of longitudinally polarized electrons from a hydrogen target (Eq. 1.39). The asymmetry can be written as a sum of a part that is sensitive to Q_W^p and a vector and axial-vector hadronic piece[119]

$$A = A_{Q_W^p} + A_{hadV} + A_{hadA} = k < Q^2 > Q_W^p + \overline{A_{hadV}(Q^2)} + \overline{A_{hadA}(Q^2)} \tag{2.5}$$

where the acceptance averaged hadronic asymmetries and Q^2 are used, and k$\equiv G_F/(4\pi\alpha\sqrt{2})$. The error on Q_W^p was estimated using a point acceptance approach, and included the anticipated errors on the measurement of the beam polarization, P, as well as the background and false asymmetries due to helicity correlated beam properties, and the error in the mea-

surement of the mean Q^2 (see Table 2.1):

$$\frac{\Delta Q_W^p}{Q_W^p} = \frac{1}{1 - f_{hadV} - f_{hadA}} \times \left\{ \left(\frac{\Delta A_{stat}}{A}\right)^2 + \left(\frac{\Delta P}{P}\right)^2 + \left(\frac{\Delta A_{back}}{A}\right)^2 + \left(\frac{\Delta A_{false}}{A}\right)^2 + (1 + f_{hadV} + f_{hadA})^2 \left(\frac{\Delta Q^2}{Q^2}\right)^2 + \left(f_{hadV}^2\right) \left(\frac{\Delta A_{hadV}}{A_{hadV}}\right)^2 + \left(f_{hadA}^2\right) \left(\frac{\Delta A_{hadA}}{A_{hadA}}\right)^2 \right\}^{1/2} \tag{2.6}$$

where the hadronic dilutions f_{hadV} and f_{hadA} as well as the statistical uncertainty varied with different collimator designs/detector positions. One of the reasons for the multiple iterations was because of a mistake in the calculation of the error on Q_W^p; a total hadronic dilution factor of 1.4 was being used instead of 1.64. Correcting this caused an increase in the error. Also, an additional factor of 1.03 on the statistical error due to electronic noise in the main detector was included in the final results.

The method for determining the optimum collimator design was as follows. In order to improve the finite target effects, which limit the angular acceptance from the ends of the target, the collimator was moved as far downstream as possible, leaving room for the Region II chambers and a cleanup collimator before the entrance to the QTOR. Then the acceptance was made as large as it could possibly be without interfering with the one component of the experiment which was nearly complete at the time - the QTOR and its support structure (see Figure 2.14). Once this largest possible acceptance was known, it was a matter of working iteratively with the main detector design (size, shape and position) to minimize the error on Q_W^p and the inelastic percentage which behave differently as a function of the radial position of the bars (see Figure 2.15 and Appendix D.2). Finally, it was necessary to trim the collimator so that it would have a shape that is reasonable to machine.

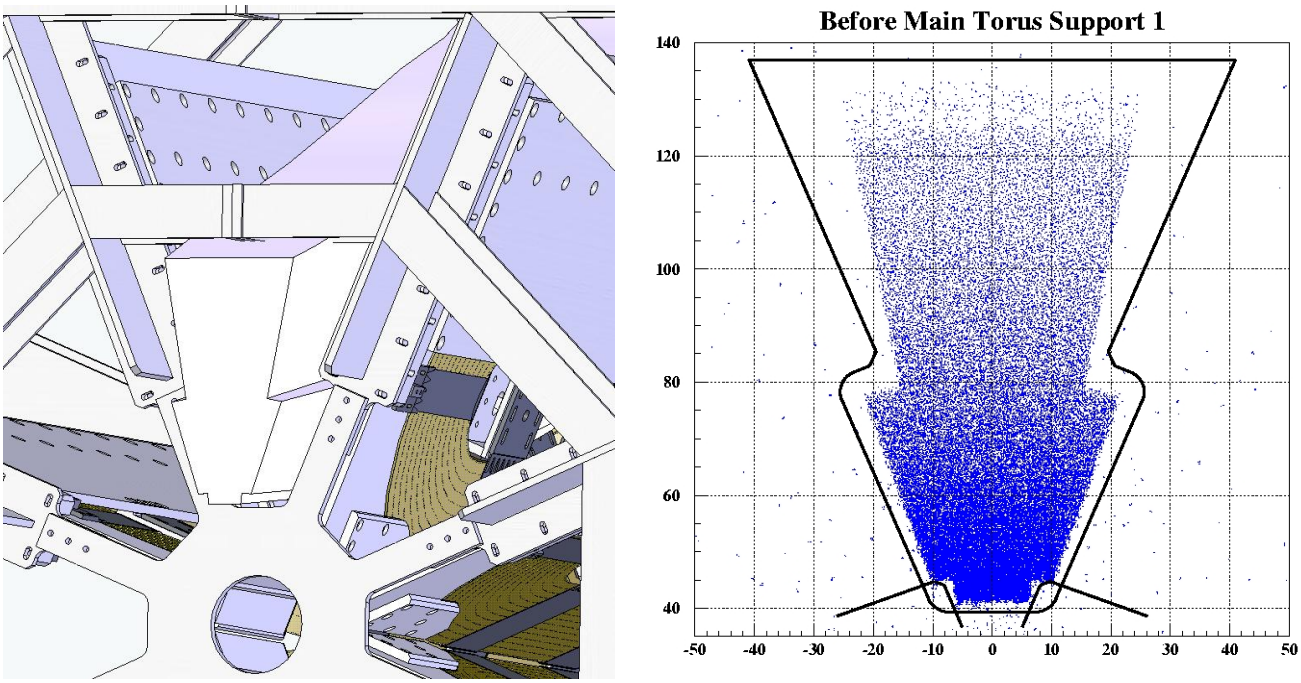

a b

Figure 2.14: Picture of the upstream end of the QTOR support structure with the accepted profile of scattered electrons (shown in white) causing an interference (a). Plot of the scattered electron profile with the outline of the upstream QTOR support structure with the interference removed (b).

The collimator at this point optimized the error on Q_{weak} assuming the backgrounds could be understood at the 0.5% level. It was decided that although this design optimized the acceptance through the main torus and support structure while minimizing the inelastic contribution, it should be modified to reduce other backgrounds, including electrons and photons that are created by Møller electrons. The collimator design was finalized by Katherine Myers, a graduate student at The George Washington University[109]. The inner radial edge of the opening in the acceptance defining collimator was visible by "line-of-sight" at the main detector location, which meant that shower photons from electrons which grazed this edge could be seen at the main detector.

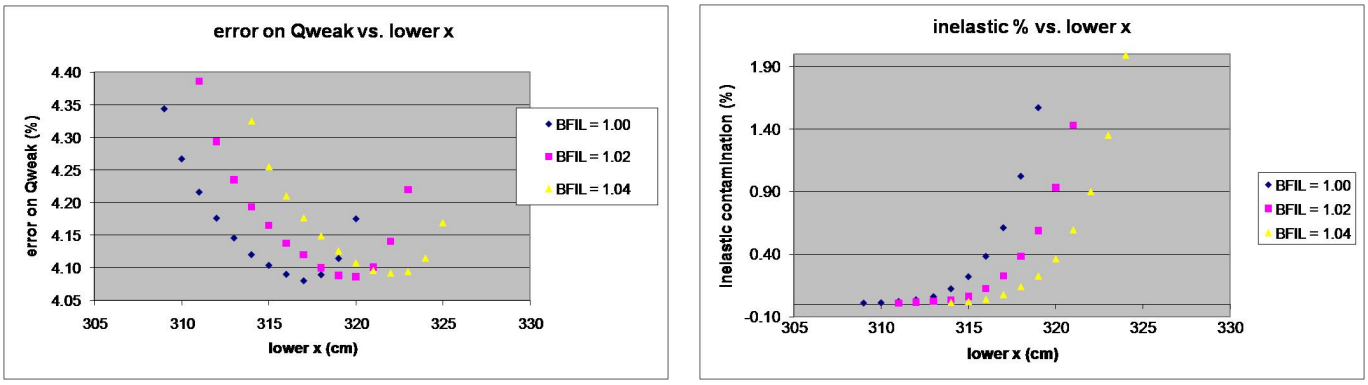

a b

Figure 2.15: The error on Q_W^p as a function of the x position of the lower edge of the main detector quartz bar (a). The inelastic percentage as a function of the x position of the lower edge of the main detector quartz bar (b).

In order to reduce backgrounds related to the primary collimator, a set of lintel collimators were proposed. These collimators would be placed in the QTOR magnet in each octant. They could be placed after the Møllers have been swept away, where the separation of the ep electrons and line-of-sight photons is large enough so that the lintels do not interfere with the signal ep electrons. In order to make the lintel concept work, it was necessary to move the primary collimator back upstream and to lower the maximum angle of acceptance to increase the separation of the photons and ep electrons. The primary collimator material was also studied, and the final primary collimator is 15 cm thick (25 radiation lengths) and is made of 95.5% lead + 4.5% antimony[111]. The error on Q_W^p is 4.25% with the proposed version of the collimator, compared to the 4.1% proposed error, but the backgrounds were reduced by a factor of 2.

Sensitivity studies were performed for the various designs of the collimator to ensure that the false asymmetries weren't going to become a problem. Jim Birchall, a professor at the University of Manitoba, studied effects of beam position, size, angle and energy modulation

for several of the collimator designs, including a nearly final version[27]. Sensitivity to the positioning of the collimators, including roll, pitch and yaw were also considered for a nearly final version of the collimators. Detailed background studies (performed by Katherine Myers) are ongoing, including (but not limited to) window backgrounds[110] and optimizing the position of the main detectors[112].

2.2.4 Region II Drift Chambers

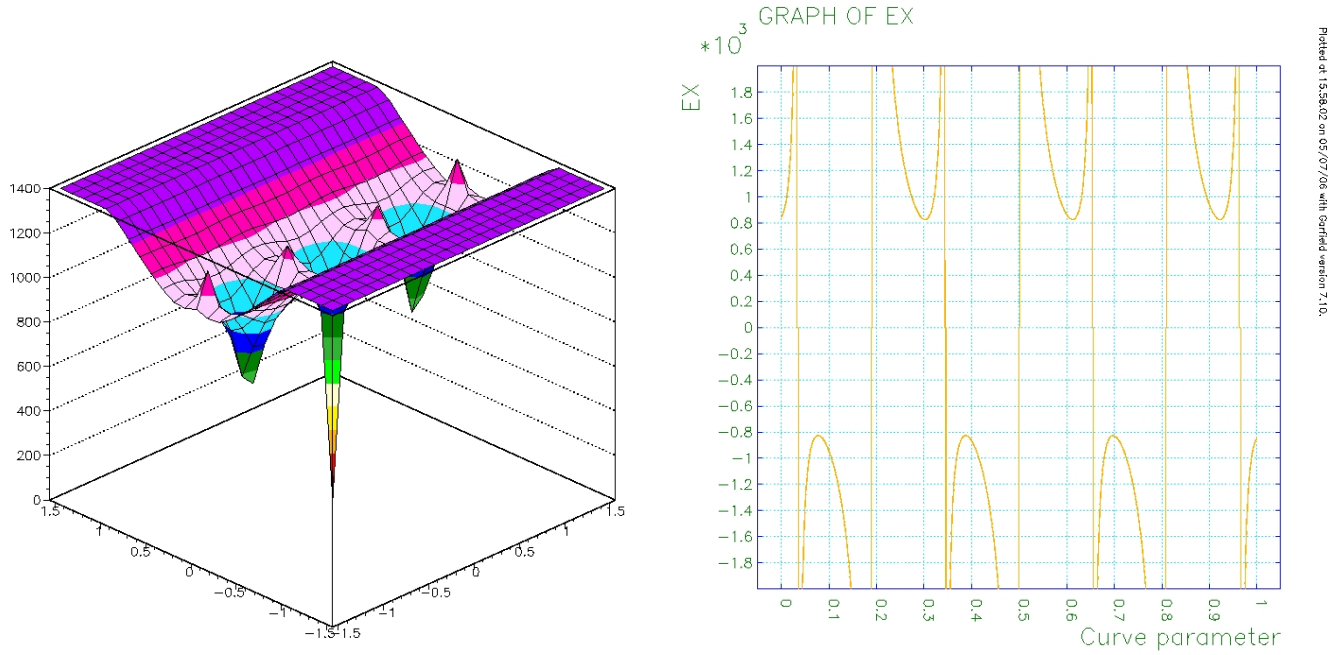

a b

Figure 2.16: Potential surface (-V) for the case of 1400 V on both the cathode and the field wires (a). The sense wires form wells for the drift electrons and the field shaping wires should be hills. Plot of E_x in the line containing the wires; minimum value occurs between the field and sense wires, and could even be zero if the field wires are wells instead of hills (b).

Virginia Tech is responsible for the design and construction of the horizontal drift chambers that will be used in Region II. The drift chamber simulation program GARFIELD

was used to simulate the drift chamber to optimize the design and estimate the chamber resolutions[139]. It can model drift times for different HV settings, gases and cell sizes. Part of the functionality of the program is to calculate the drift velocity as a function of electric field for a particular composition of gas (see Figure 2.17a). The electric field in the cell is then determined from the geometry (see Figure 2.16a, b). The drift times can be used to determine drift distances, and ultimately the drift velocity parameterization is used to determine the resolution of the chamber[54].

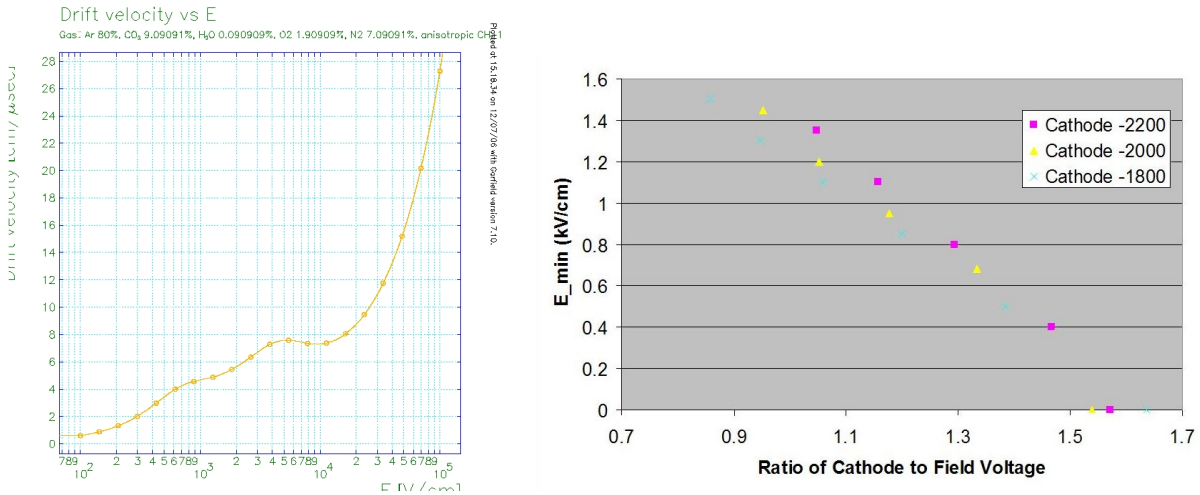

a b

Figure 2.17: Plot of the drift velocity vs. the electric field (a). Plot of the minimum electric field as a function of the ratio of the cathode and field wire high voltages (b).

Although recently we have switched to the mixture we will use in the hall, which is 35% ethane 65% argon, most of the testing was done with a gas mixture of 2% methane, 10% $C0_2$ and 88% argon. The modelling of the gas helps to determine the minimum desired electric field in a given cell by revealing the region in which the drift velocity is approximately constant, in this case approximately 600 V/cm (see Figure 2.17, a). The minimum electric field occurs between the field and sense wires and is a function of the relative potential between the two. There needs to be a "hill" for the electrons at the location of the field

wires (see Figure 2.16, a and b). A study on the minimum electric field as a function of the ratio of cathode to field wire voltages shows that the minimum electric field decreases as the ratio increases (see Figure 2.17, b). The conclusion is that the ratio of the cathode to field voltage has to be less than 1.4 in order for the minimum electric field to be greater than 600 V/cm.

Besides the various GARFIELD simulations related to the response of the chamber to individual tracks, the design of the chamber active area and frame were aided by GEANT3 simulations. The design of the collimators affected the size and shape of both the Region I and II chambers. Figure 2.18 shows the outline of the frame which would hold the electronics cards superimposed on a plot of the scattered electron profile that makes it through the primary collimator. The original design would have had a large dose on the electronics cards and frame (2 rads/nA/hour) as well as been an unacceptable source of background (a). The final chamber design has no interference in adjacent octants (b).

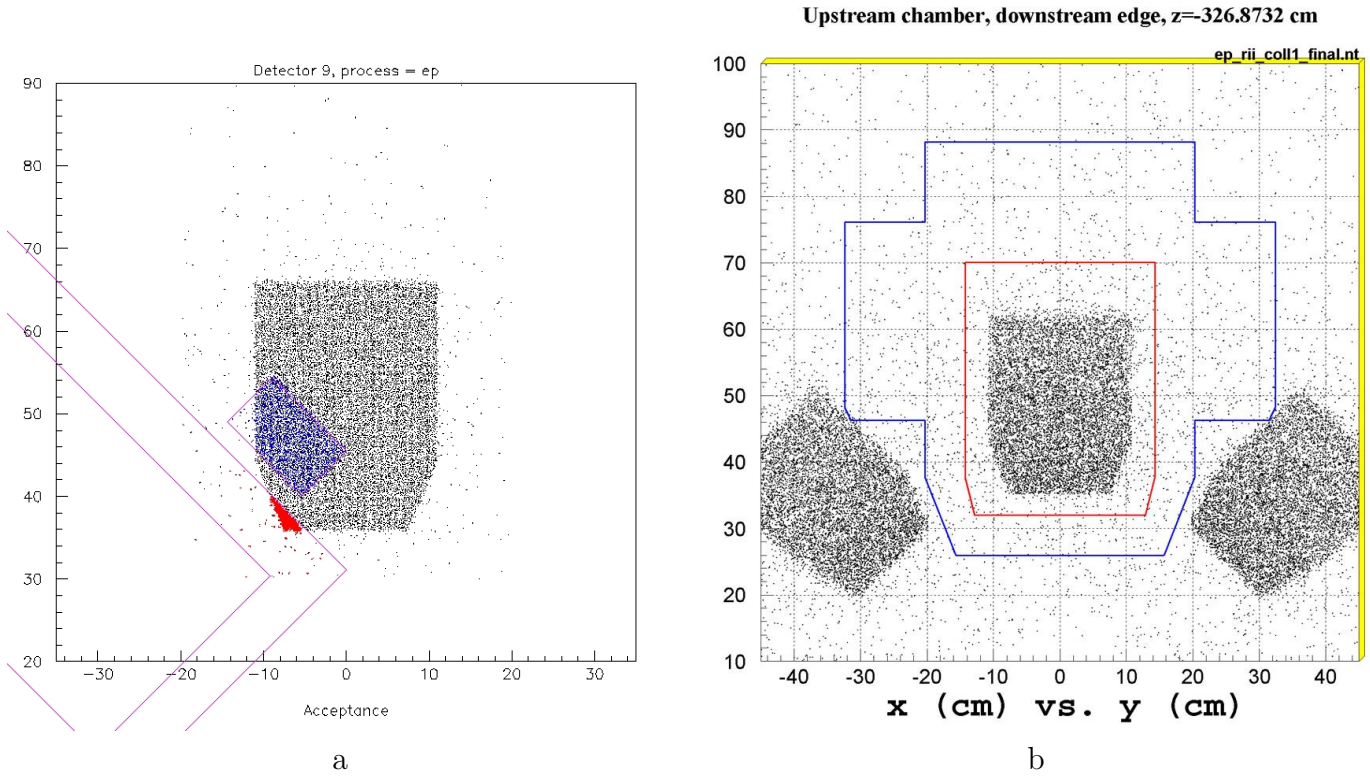

a b

Figure 2.18: The design of the Region II chamber caused an interference with the scattered electron profile after the optimization of the collimators (a). The outline of the drift chamber frame on a plot of the scattered electron profile in the top three octants (b).

2.2.5 Minitorus

The minitorus was designed to reduce the Møller rate on the Region II chambers without affecting the focus of the ep elastic electrons at the main detectors. Even without the minitorus the Møller rate is not an issue for the main detectors, because the lower energy Møllers are already swept away by the main magnet, QTOR (see Figure 2.19). The Møller rate on the Region II horizontal drift chambers during a 10 nA tracking run would be ~ 26 MHz, more than 26x the maximum rate for good track reconstruction in the chambers. The ep elastic electron rate is only about 4 kHz/nA. Because the beam is sufficiently stable at lower currents, and beam position and current monitoring can be accomplished (see Section 2.3.1) the total rate at Region II, including Møller electrons, will be reduced by running at $\sim$100 pA, or 100x smaller current than originally planned. Although the minitorus is no longer needed[130], it will be described here since it was a fully designed and viable solution to the Region II Møller rate issue.

The minitorus would have consisted of 8 coils in a toroidal configuration. Each coil consisted of 2 double pancakes of 0.7 cm^2 water cooled copper conductor, 25 turns per pancake. The inner radius of a coil is 8.75 cm and the outer radius is 26.25 cm, giving a cross sectional area of 49 cm^2. The current density is about 470 A/cm^2, which reduces the Møller rate sufficiently while bending the ep elastic electrons with as small an angle as possible. Taking into account the 0.39 cm diameter hole for the water cooling, that gives us a total minitorus current of about 175 A. Even the magnetic forces on the coils, water cooling circuits and weight of the coils had been taken into consideration in the design[95].

In order to perform the minitorus studies, I utilized a program originally developed to create a field map for the QTOR. Each minitorus design required its own field map, which was read into the GEANT3 simulation to study the effects on the ep elastic and Møller

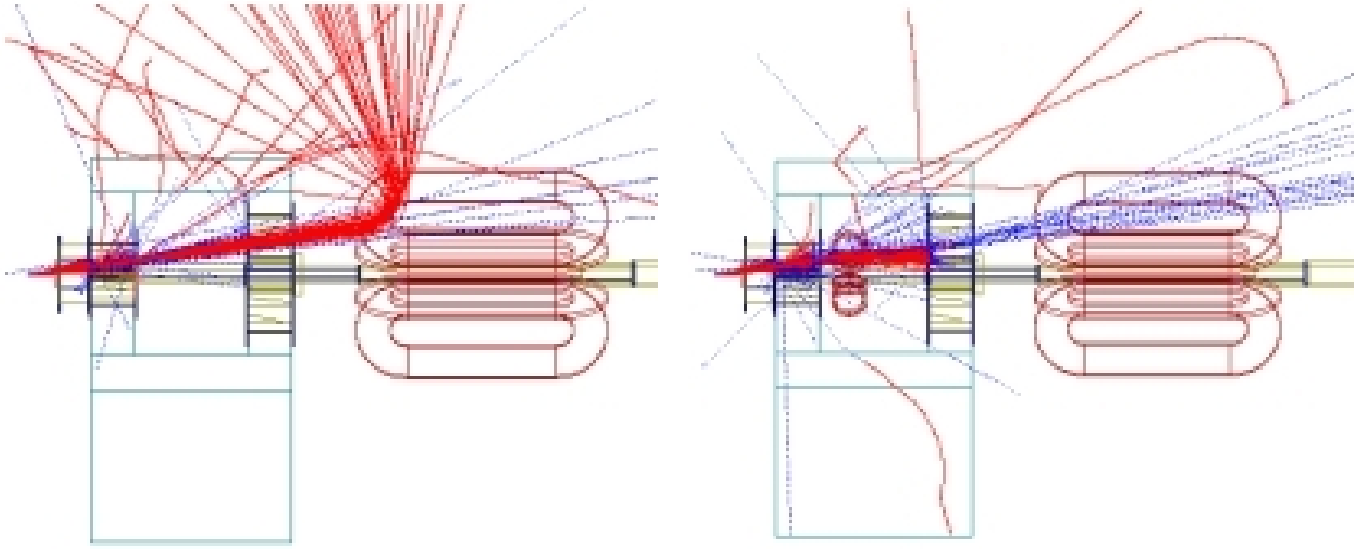

a b

Figure 2.19: The Møller tracks are shown in red (with neutral secondaries in blue) with the minitorus turned off (a) and with the minitorus turned on (b). The minitorus is not necessary for the main detectors, because the Møllers will be swept away in the main magnet.

electrons. Not only the size and shape of the minitorus, but the radial placement of the coils and the location along the beamline all contributed to the effectiveness in reducing the Møller rate. It was found that bending down, into the part of the primary collimator closest to the beamline, was more effective than trying to bend them radially away as the case with the QTOR. The minitorus would have been placed just after the primary collimator, with the outer radius about 10cm away from the outer radius of the beamline. In this configuration, the maximum B field halfway between the coils at the center of the coils is at a radius of about 25 cm. The value of the B field here is about 0.9 kG.

The minitorus was originally proposed to be placed downstream of the primary (acceptance defining) collimator. In that position it wouldn't have affected the $< Q^2 >$ of the experiment, it would only have changed the focus of the electrons that made it through the

collimator [118]. In that scenario it would have been part of the experiment and would have been run continuously. Because of the collimator redesign (see Section2.2.3) it became necessary to place the minitorus before the primary collimator due to space constraints. This complicated things because the minitorus then becomes part of the acceptance of the experiment because it changes the electron envelope that goes through the primary collimator. This is part of the reason it became more desirable to simply run at a lower beam current to perform the calibration runs, if possible.

2.3 Construction and Testing

Most of the work included in this section provided proof-of-principle for later design improvements. My contributions included participating in early construction and testing of the first prototype horizontal drift chamber and a prototype luminosity monitor. During the Q_{weak} beam tests at the end of the G^0 backward running I was able to apply my experience as a trained target operator and my familiarity with the G^0 data acquisition software to assist in testing the beam monitors at low current as well as the target boiling tests. I also designed, built and tested the wire position and tension measuring device used in the quality control and characterization of the horizontal drift chambers. Summaries of these contributions will be provided below.

2.3.1 Target Boiling and Beam Monitoring Tests

During March 2007, at the end of the G^0 backward running, Q_{weak} obtained some time for testing using the G^0 target, electronics and data acquisition (DAQ) [40]. It was necessary to test the functionality of the beam monitors at low currents (150 pA - 100 nA) as well as

the performance of the beam (see Section 2.1). The tracking runs will be performed at beam currents of ∼1 nA or smaller in order to keep the rate at the Region II chambers manageable without the use of the minitorus. The conditions during the tracking runs need to be as similar to that of the main measurement as possible, so the beam has to be stable (energy, position, angle) during the low current running so that the Q^2 of the experiment can be measured. The general conclusion was that it would be possible to use the cavity monitors to monitor the beam current down to 1 nA, but probably not lower than that[92]. It should be possible to use the luminosity monitors to monitor the beam current and position at lower beam currents[121].

The beam also seemed to behave reasonably well, according to measurements of the beam motion using the superharp, a wire scanner with absolute position readout that is normally used to perform beam energy measurements [148]. Three wires, two along the y and one along the x direction are scanned diagonally across the beam. In these tests the scattering from the wires was detected with downstream charged particle monitors, so when a wire crossed the beam it increased the rate in the detectors. By knowing the position of the wire assembly via the linear encoder on the motor used to move it, it was possible to measure the x and y position of the beam. Scans were performed every half hour during the low current runs, and the position differences from the average seemed to be smaller than the resolution ($\pm 250\ \mu m$) of the superharp (see Figure 2.20) [96]. According to Q^2 sensitivity studies performed by Jim Birchall, a 0.3 mm position shift corresponds to a <0.18% shift in Q^2[26], so this should be adequate for the Q_{weak} running.

Tests of the sensitivity to target boiling for various combinations of circulating fan speed, fast raster size, helicity reversal rate and beam current were also performed. The G^0 luminosity monitors (LUMIs - see Section 2.1.1) were used to measure the asymmetry widths for the different settings. To see the plots from all the various combinations, see Appendix

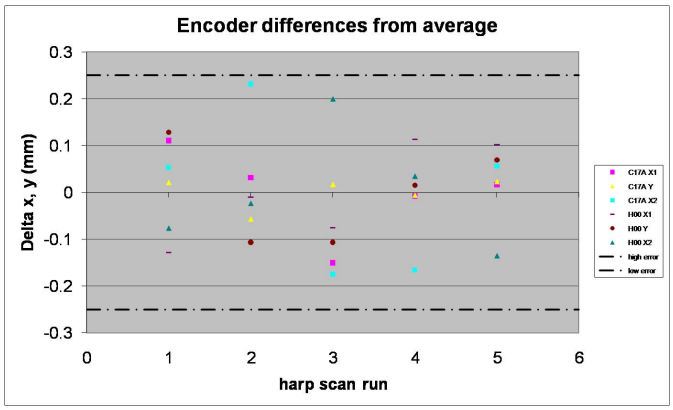

Figure 2.20: Plot of the difference from the average of the position measurements during the five superharp scans at low beam current.

D.1. I assisted in the data taking and also performed the calibration of the luminosity monitors which improved the measurement of the LUMI widths (see Figure 2.21). Generally you would expect less boiling (smaller asymmetry widths) with lower currents, higher fan speeds and larger raster size, which in general was the case. Note however that although the width from boiling should decrease with increased data taking (helicity reversal) rate, the statistical error due to the smaller time window dominates, and the width decreases with increased current. A more recent study on carbon models this effect phenomenologically and finds that the density fluctuation term decreases with a power law exponent of 0.4[83].

2.3.2 Luminosity Monitors

Two prototype Q_{weak} luminosity monitors were tested in the Hall C beamline [94]. A housing held a piece of quartz attached to a vacuum photodiode (similar to a one-stage photomultiplier tube) and two LEDs for testing purposes. The housing was made of delrin, but it is probably an understatement to say that the material was not sufficiently radiation hard for our purposes (see Figure 2.22 a). The vacuum photodiode was also too close to the beamline

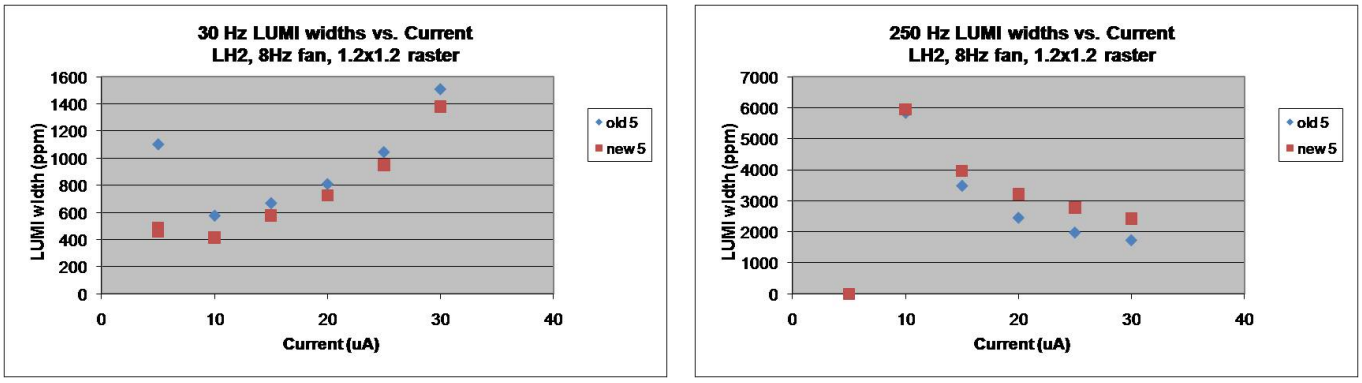

a b

Figure 2.21: Widths for LUMI5 vs. beam current for 8 Hz fan speed and a 1.2x1.2 mm^2 raster for data taking rates of 30 and 250 Hz. Shown are the comparison of the rates for the nominal luminosity monitor calibration and the new calibration performed for the purpose of this test.

(see Figure 2.22 b). The current designs use an aluminum air light guide to mount the quartz close to the beamline and transport the cerenkov light further away from the beamline to a PMT modified to use only one stage in current mode operation, with the bases being switched to high gain during event mode operation [82].

2.3.3 Region II Drift Chambers

Five horizontal drift chambers have been constructed and characterized at Virginia Tech for use in the Q_{weak} experiment, four chambers and a spare. The construction and testing of the chambers was completed primarily through the efforts of Norman Morgan, Elizabeth Bonnell and Mark Pitt. I participated in the construction and testing of a prototype chamber that is slightly different than the five chambers, due to design changes that occurred as a result of testing the prototype. I designed, constructed and tested the apparatus that was used to measure the wire tension and position of the four chambers. One of the chambers was

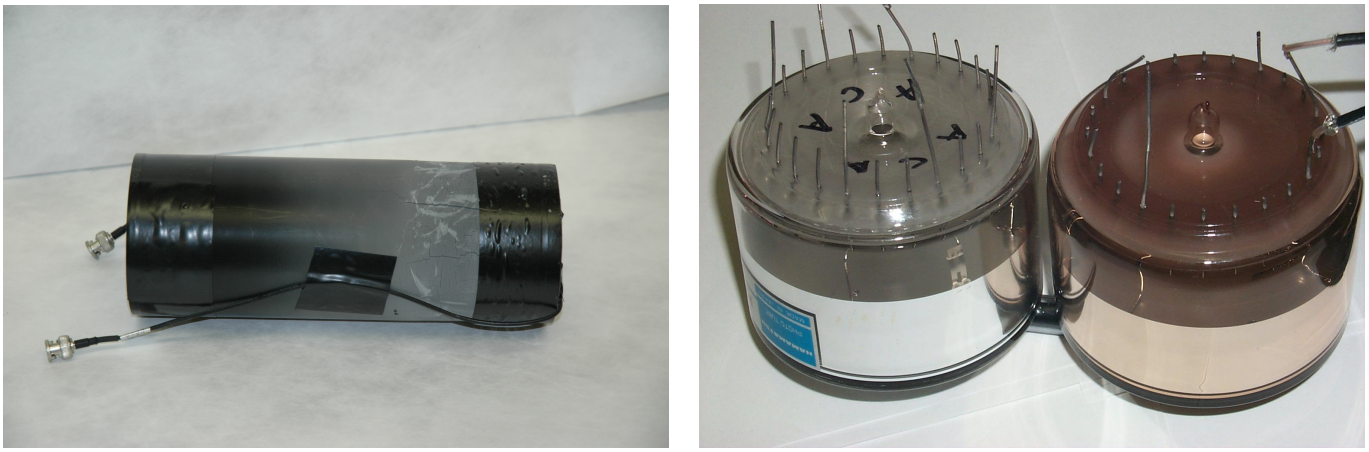

a b

Figure 2.22: Picture of the prototype luminosity monitor housing after the beam test, with radiation damage evident in the discoloration of the normally black delrin to a brittle white on the right (a). Also shown is a comparison of an unused VPD (left) and one damaged by radiation (right).

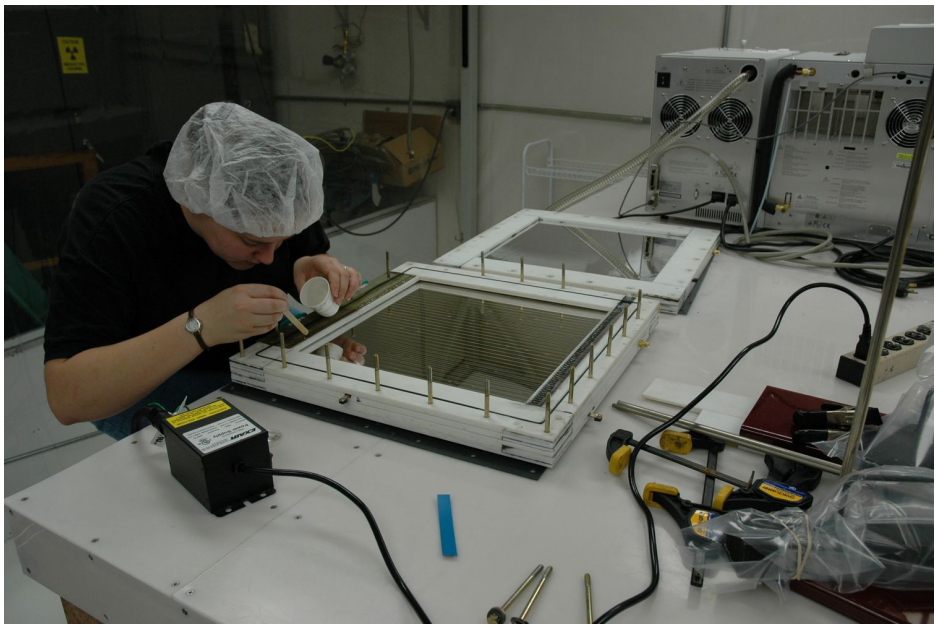

Figure 2.23: Picture of me applying some epoxy to the ends of the wires in one of the planes in the prototype drift chamber.

constructed before this apparatus was built, and the tension was estimated by measuring the wire positions with the planes mounted vertically and comparing the positions at the left, middle and right along the length of the wire. I also made preliminary measurements of the wire tension in the prototype chamber and helped to measure the wire positions in several planes.

The wire positions in each plane of the four chambers were measured relative to a precision bolt hole in the outer part of the frame in each plane. A video camera was translated using a linear stage along the length of the frame and the wire was lined up with a horizontal line that was marked on the monitor (see Figure 2.24 a). The position was read from the linear stage. Measuring the position and tension for each of the wires is tedious at best and at worst puts a severe strain on the eyes of whoever is performing the measurement. The original design used a stage that was adjusted by hand, and the frame was mounted separately from the stage/camera. This was sufficient for measurements of the wire location, but for the tension measurements it was exceedingly difficult to mount the magnet behind the wire properly aligned with the camera. In the original design it required adjusting the position of the magnet in an ad-hoc way for each wire.

The wire tension can be measured by applying an oscillating current through the wire in the presence of a magnetic field. The wire will oscillate due to the magnetic force on the current in the wire. By determining the frequency (f) at which the maximum amplitude occurs (the resonant frequency of the first harmonic) and knowing the mass per unit length of the wire (μ) it is possible to calculate the tension in the wire

$$T = \mu(2Lf)^2 \tag{2.7}$$

if the length (L) is known. Preliminary measurements indicated that it would be possible to

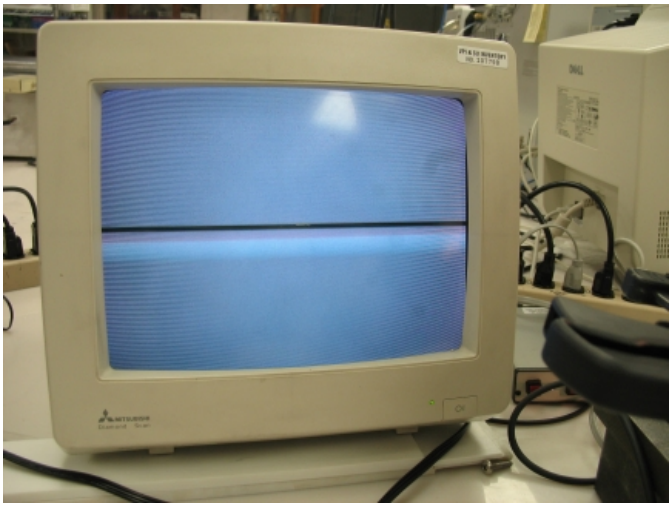

a

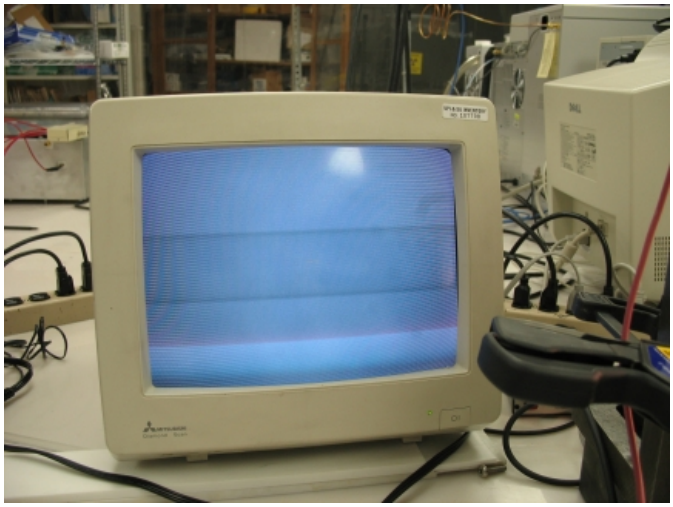

b

Figure 2.24: On the left is a picture of the image of a wire from the camera (a). The left image is with the same wire, but with the magnet in place and an oscillating current close to the resonance frequency of the wire. The wire is seen as a blur (b).

measure the tension using this method (see Figure 2.24 b).

By designing an apparatus to permanently mount the magnet on the opposite side of the wire from the camera it eliminated the messy step of positioning and aligning it for every wire (see Figure 2.25). In addition it incorporated the mounting of the frames (x, u, v and u′, v′) in a consistent way. The hand operated linear stage was replaced by a motorized stage with a linear encoder to read out the position. This allowed for automatic stepping to subsequent wires, although the fine tuning of the position still had to be done by eye. The adjustment of the frequency for the tension measurement had to be done by hand as well. The controls for the position adjustment were incorporated into a labview program and the readout of the position and frequency were automated by an undergraduate student at Virginia Tech, James Dowd. The position and tension measurements for each of the planes in each chamber are summarized in the Virginia Tech Qweak elog[29].

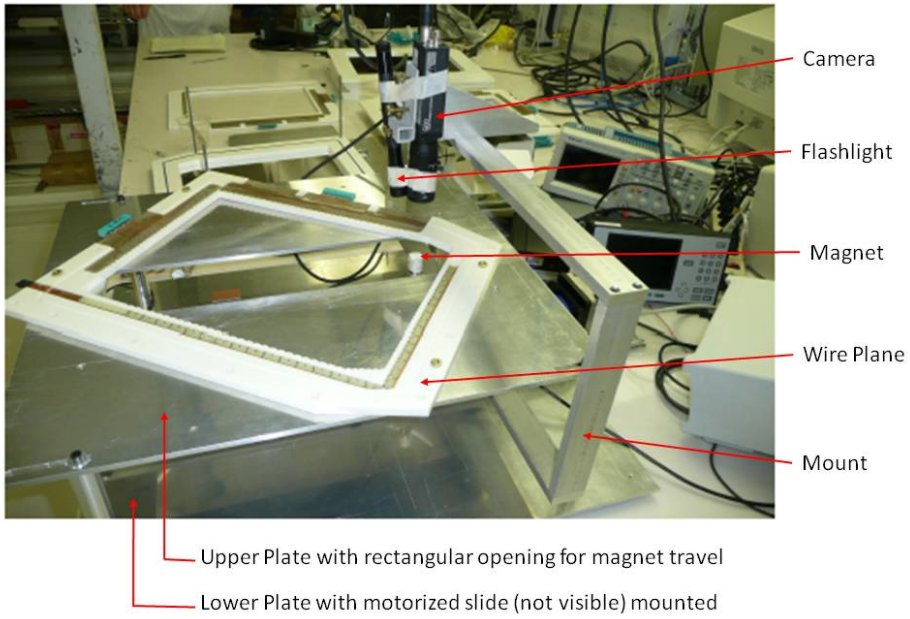

Figure 2.25: Picture of the wire scanner showing the camera mounted opposite the magnet, with a wire 'u' plane between them. The motorized slide which would translate the camera/magnet system from right to left is mounted to the lower plate, but is not visible in this picture.

Typical results for the position and tension measurements in one plane are shown in Figure 2.26. The applied tension is 20 g for a sense wire and 30 g for a field wire. For this plane the averages are 18.6 g and 25.1 g for the sense and field wires, respectively. The main motivation for a tension measurement in these chambers is to find wires that were very loose, and there is no evidence of that. The wires were also all within <0.1 mm of where they were supposed to be, which is better than our desired position resolution of 0.2 mm. The final calibration of wire positions will be performed with cosmic ray tests.

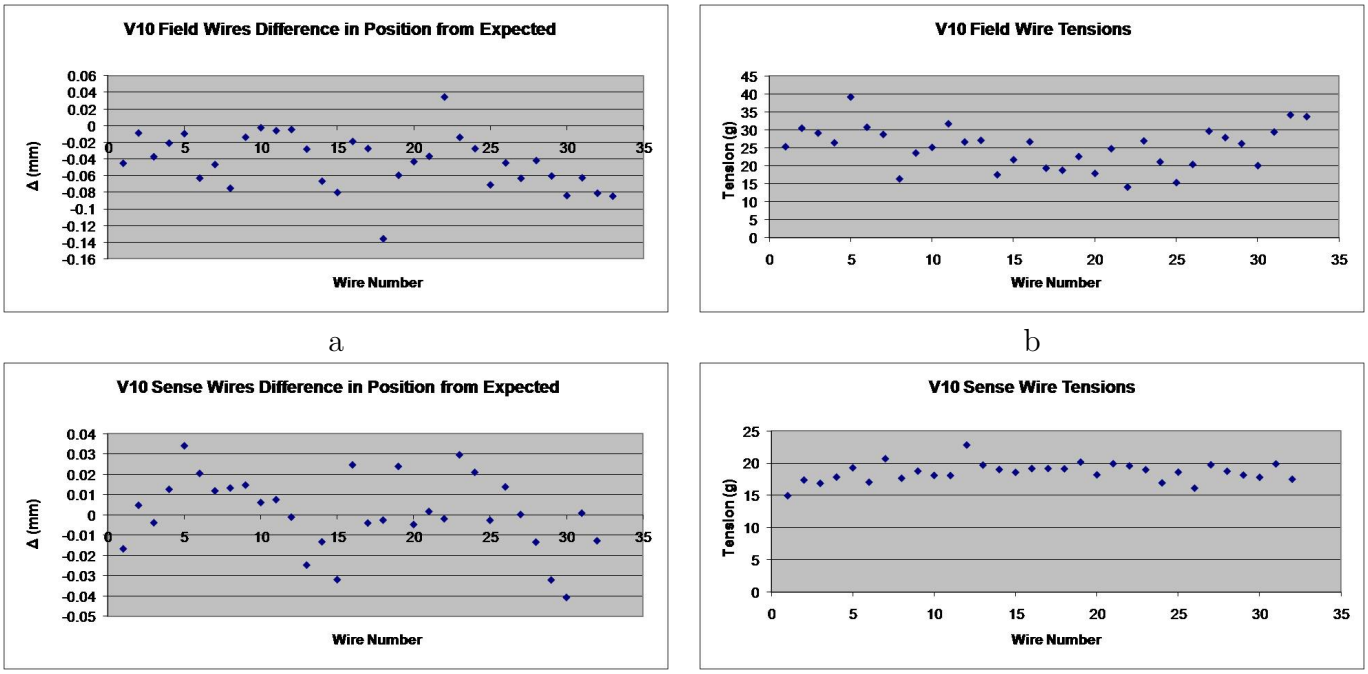

Figure 2.26: Plots of the difference in the measured positions from the expected position for the field (a) and sense (c) wires, as well as the measured tensions in the field (b) and sense (d) wires for one of the 'v' planes[29].

Chapter 3

The G0 Experiment

3.1 General Description

The G^0 backward experiment uses the forward angle detector package rotated around to the upstream side of the magnet (SMS) (see Figure 3.1). In the forward angle measurement the elastically scattered protons were detected, and time-of-flight (TOF) was used for particle identification and kinematic separation of the inelastic events[10]. Only one set of detectors was needed, a set of 16 focal plane detectors (FPDs) in each octant, which provided 16 Q^2 values between 0.12 and 1.0 GeV^2. In the backward angle the elastically scattered electrons are detected, and it was necessary to add two detectors to perform the functions of inelastic separation and particle identification[43]. The Cerenkov detector is used to separate negative pions from the electrons, and the addition of the cryostat exit detectors (CEDs) gives sufficient kinematic separation to distinguish elastic and inelastic electrons.

The backward angle kinematics and the spectrometer acceptance do not allow for multiple Q^2 values to be determined at a given energy. Two values of Q^2 for each target, hydrogen

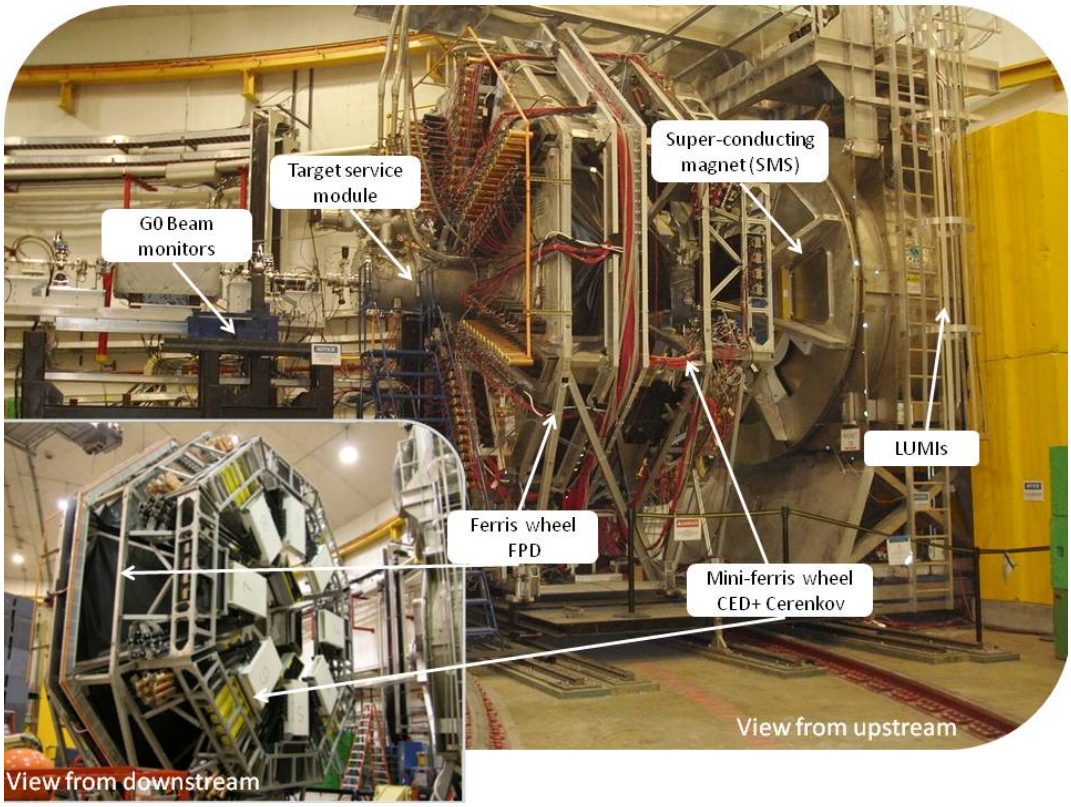

Figure 3.1: Views from upstream and downstream (inset) showing the "ferris wheels" which support the focal plane detectors (FPDs), cryostat exit detectors (CEDs) and the Cerenkov detectors. Also shown is the superconducting magnet (SMS) and the locations of the luminosity monitors, G^0 beam monitors and target service module.

and deuterium, were obtained by running at different values of the beam energy, approximately 362 and 687 MeV (see Section 4.3). The beam polarization during the experiment was ∼86%, and the current ranged from 20-60 μA depending on the target/energy combination. The ep elastic electrons scattered at backward ($\sim 108^\circ$ angles and were bent toward the beam onto the detectors. A total of ∼325 C of data were taken during the longitudinal running[20], and ∼8.4 C during the transverse running. Combined with the previously completed forward angle measurements, the strange electromagnetic form factors G_E^s and G_M^s and the effective axial form factor G_A^e were fully separated at two values of Q^2, 0.221 and 0.628 $(GeV/c)^2$.

Because I joined the G^0 collaboration at such a late stage, there were very few hardware tasks left to be done. The backward angle phase used the same FPDs as the forward angle measurements, which were already complete, and the Cerenkov and CEDs had already been installed, so most of my work for G^0 is analysis and simulation related. During the backward angle data taking I was largely responsible for the calibration of the beam monitors, which will be discussed in Section 3.3.1, and the analysis and simulation work will be discussed in Chapters 4 and 5.

3.2 Polarized Beam at Jefferson Lab

Jefferson Lab has a continuous electron beam accelerator facility (CEBAF) that can produce electron beams up to 6 GeV which can be delivered (with some restrictions) simultaneously to three experimental halls with different beam currents and energies in each hall[129]. When polarized beam is required in one (or all) of the halls, those restrictions increase, but the accelerator group consistently provided high quality, highly polarized ($\sim$ 85%) for the G^0 experiment. There are actually two linear accelerators (north and south linacs) made from superconducting niobium radio-frequency (RF) cavities. After the electrons are accelerated in the injector to about 45 MeV they enter the north linac, are bent around an arc (using magnets) to the south linac, where they can be accelerated again (see Figure 3.2, a). This can be done up to 5 times to achieve $\sim$6 GeV beam energies. To obtain the G^0 energies of 687 MeV and 362 MeV the electrons were diverted into the hall before going through the second arc; the lower energy was obtained with the south linac turned off.

3.2.1 Polarized Electron Source

The repetition frequency in each of the halls is 499 MHz, and in the accelerator the fundamental frequency is thus 1497 MHz. The polarized electron beam is produced by bombarding a strained gallium-arsenide crystal with circularly polarized light (see Figure 3.2b). The circularly polarized laser light is produced using a Pockels cell to flip helicity every 1/30 s in a random way over a helicity "quartet". Some of the experiments discussed in Section 1.3 used a bulk gallium-arsenide photocathode, but HAPPEx was the first experiment to make use of a strained GaAs crystal[5]. In a bulk (unstrained) crystal there is a degeneracy in the $\pm 1/2$ and $\pm 3/2$ levels in the valence band, allowing electrons of the wrong helicity to be excited to the conduction band (see Figure 3.2b). By straining the crystal the degeneracy between the energy levels is broken, allowing for a theoretical maximum polarization of 100% instead of $\sim 50\%$ with an unstrained crystal. The relevant figure of merit for minimizing the error on the asymmetry is IP^2, because the measured asymmetry is corrected by dividing by the beam polarization.

During the G^0 experiment the helicity was changed every 1/30 s, called a macropulse (MPS), in a random way over a set of four helicity states, called a quartet. The asymmetry is formed by taking the difference of the charge normalized detector yields between the two states with positive helicity and the two states with negative helicity over the total yield in the quartet. In addition to the rapid helicity reversal, an insertable half wave plate in the laser line was used to change the helicity every day or so in an independent, mechanical way in order to check for false asymmetries in the electronics and accelerator. The direction of the electron's polarization vector precesses relative to it's velocity due to the fact that $g - 2 > 0$ (see Appendix D.6). A Wien filter is used to compensate for the precession of the electron's spin in the arcs between the north and south linacs and the arc going into Hall C. The Wien filter is also used to produce the transversely polarized electron beam.

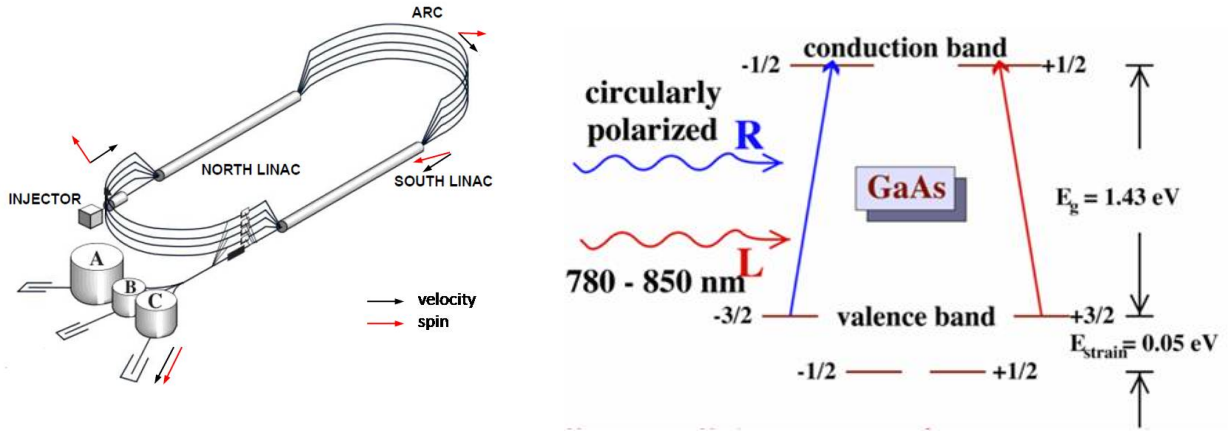

a b

Figure 3.2: During the 687 MeV running, the beam that was produced at the injector is actually transversely polarized (a). The precession of the electron's spin through the arc between the north and south linac and the Hall C arc results in longitudinally polarized beam at the location of the target (adapted from [81]). Diagram of the broken degeneracy in the energy levels in the strained GaAs photocathode[120] (b).

3.2.2 Polarimetry

The beam polarization must be measured with high precision in order to correct the measured asymmetries and limit the impact on the systematic uncertainties[67]. The polarimetry in G^0 backward was performed using the Hall C Møller polarimeter and the injector Mott polarimeter, both of which are destructive measurements. The Mott polarimeter diverts the beam from the nominal axis into the polarimeter and measures the asymmetry caused by the coupling between an electron spin and its orbital angular momentum in the coulomb field of the target nucleus, and measures both of the transverse components of the beam polarization. The Møller polarimeter measures the asymmetry in doubly longitudinally polarized Møller scattering, where both the incident and target electron are polarized in the direction of the beam, and thus is sensitive to the longitudinal polarization of the beam[116]. A thin foil of pure iron is magnetized by a superconducting solenoid with a field of 4 T in the direction of

the beam[14]. The scattered and recoil electrons are focused by a quadrupole magnet and passed through collimators to choose the desired scattering angles, and then defocused by a second quadrupole magnet and detected in coincidence by detectors placed symmetrically on either side of the beam axis.

There were no Møller measurements at the 362 MeV, so the Mott measurement was used to determine the value of the polarization at this energy[61]. The Mott measurements of the polarization are consistent between the two energies, so the value from the Møller measurement at 687 MeV is used, while the Mott measurements demonstrate that the value at the lower energy is consistent with that during the higher energy running. The measured polarizations are 85.78 $\pm$ 0.07(stat) $\pm$ 1.38(sys)% at 687 MeV and 85.78 $\pm$ 0.07(stat) $\pm$ 1.95(sys)% at 362 MeV, with the larger statistical uncertainty at the low energy reflecting the point-to-point uncertainties in the Mott measurement. The magnitude of the polarization is the same for the transverse running because it is only the direction of the spin that changes (using the Wien filter).

3.3 Beam Monitors and Calibrations

3.3.1 General

Helicity correlated effects caused by the way the polarized beam is produced must be minimized because they can lead to false asymmetries (see Section 4.1.3). This can be achieved with careful setup at the laser table and active feedback to the accelerator, and linear regression can be performed to correct for remaining effects. The beam position, angle, energy and current must all be measured in order to provide the information for the feedback to the accelerator and to perform the linear regression. As part of the infrastructure of the ac-

Table 3.1: Summary of expected and achieved beam properties for G^0 during the backward angle running.

Beam Property	Required[33] Asymmetry (or Difference)	Achieved[22] Asymmetry (or Difference)
Charge	<2 ppm	<1 ppm
Position	<40 nm	<20 nm
Angle	<4 nrad	<1 nrad
Energy	$<5\text{x}10^{-8}$	$<1\text{x}10^{-8}$
Halo	10^{-6}	$0.3\text{x}10^{-6}$

celerator and the hall there are separate beam current and beam position monitors, though G^0 had some additional monitors as part of its installation. The measurements from sets of position monitors can provide angle information at the target, and the difference in the energy from nominal can be measured in a position monitor in the Hall C arc, where the dispersion in the bending magnet is proportional to the energy of the beam. The run averaged values of the required beam parameter asymmetries (or differences) are shown in Table 3.1 along with what was actually achieved during the backward angle running. The requirements are necessary to minimize the false asymmetry corrections due to fluctuations in the beam parameters.

In addition to the luminosity monitors (see Section 3.4) and beam current and position monitors, there were halo monitors that could be used to determine whether the beam is interacting somewhere in the accelerator. The halo monitors are charged particle detectors that monitor the beam "halo" - the part that is outside of the core of the beam. This halo can be caused by scraping against the beam pipe, interactions with residual gas in the beamline, and can even be caused as laser interacts with the photocathode at the source[14].

The beam passes through a small aperture in a 2 mm thick piece of carbon. If the halo is small enough then there will be minimal interaction with the carbon. The two halo targets can be moved in and out of the beam as necessary. The smaller 3 mm radius opening is used to test the limit of the halo. The larger 5.5 mm radius target can be used more continuously as a monitor. The scattering from the halo target is detected in various sets of monitors. Two are located at $\sim$15° immediately downstream of these targets (G0HALO3 and 4). Two monitors are located at the entrance to the hall (upstream of the halo targets). The last four are located between the halo targets and the G^0 detectors. The monitors at the hall entrance and two of the downstream monitors are bare phototubes (PMTs). G0HALO3 and 4 are pieces of lucite attached to PMTs, and the remaining two downstream monitors are scintillators attached to PMTs.

Special data were taken that deliberately moved the beam position and angles at the target by pulsing corrector coils ("coil-pulsing") in the beamline, and the energy can then be modulated by adjusting one of the superconducting cavities in the south linac. The intensity of the beam could also be deliberately changed at the laser table to induce large charge asymmetries, but this is done separately and not during the coil-pulsing runs so that the effects of charge modulation can be decoupled from the other quantities. The coil-pulsing data could be used to check the systematics due to helicity-correlated beam properties, but the linear regressions slopes are ultimately determined from natural beam motion during each run, using the measured beam parameters and the yield measured in each detector coincidence cell. These slopes are consistent with those measured during the coil-pulsing data.

3.3.2 Descriptions of the Monitors

The beam charge monitors (BCMs) are "pillbox" cavities with a resonant frequency in the TM_{010} mode at the beam acceleration frequency[37] (see Figure 3.3a). The beam electrons excite the resonance in the cavity and the energy is read out with an antenna, providing a measurement of the current. The beam position monitors (BPMs) consist of four quarter-wavelength wires oriented 90° from each other that run parallel to the beam axis (see Figure 3.3b). The signal on each wire depends on the distance from the beam, and the four signals can be combined to determine the position of the beam. Relative energy measurements can be performed by making use of the known dispersion of the beam in the Hall C arc (40 mm/%) and measuring the position in a BPM in the arc[33]. Absolute energy measurements are made in dedicated runs using the superharp (see Section 2.3.1) where the beam is set up in a dispersive tune. Cavity-type monitors can also be used to measure beam position; they were tested for Q_{weak} during G^0 running with limited reliability.

3.3.3 Beam Monitor Calibrations

The gains of the beam current monitors and the pedestals (output of the electronics in the absence of real beam signal) of the beam position monitors can change over time, so it is necessary to perform periodic calibrations of the monitors. Dedicated calibration runs were taken with the beam current being increased and then decreased incrementally, with "beam off" periods between each current setting (see Figure 3.4b). An absolute monitor of the beam current is the UNSER monitor, which is a parametric current transformer that measures the beam current through electromagnetic induction. It has stable gain but an unstable pedestal, and so can be used to calibrate the two G^0 beam current monitors, after determining its pedestal during the beam off periods. Then the average UNSER current is

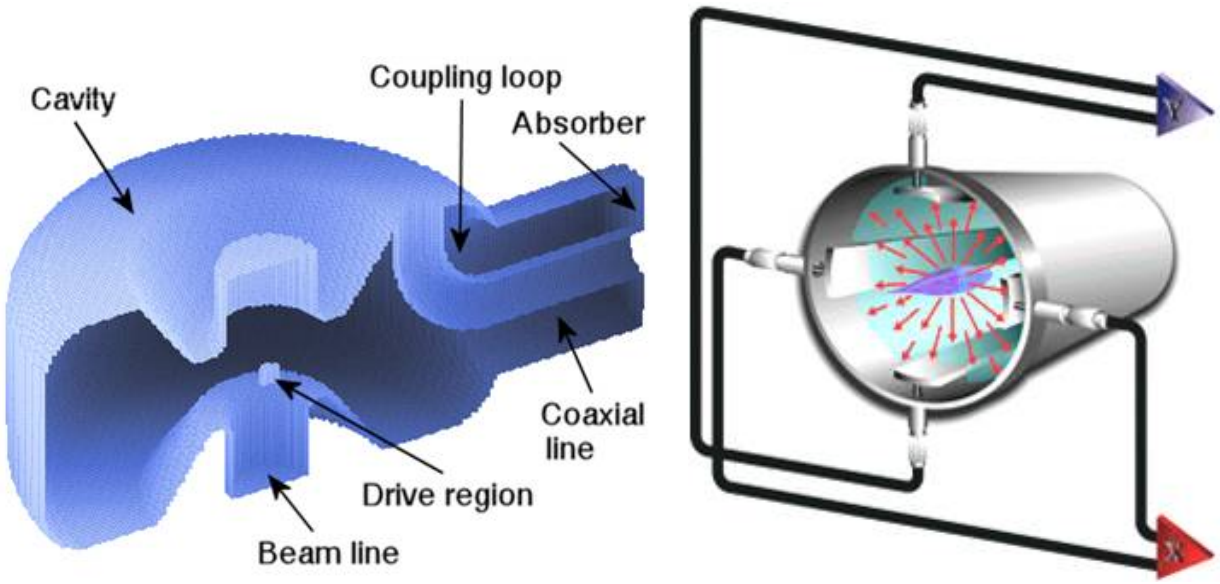

a c

Figure 3.3: Pillbox cavity beam current monitor (BCM) (a). Four-wire stripline beam position monitor (BPM) (b)[108].

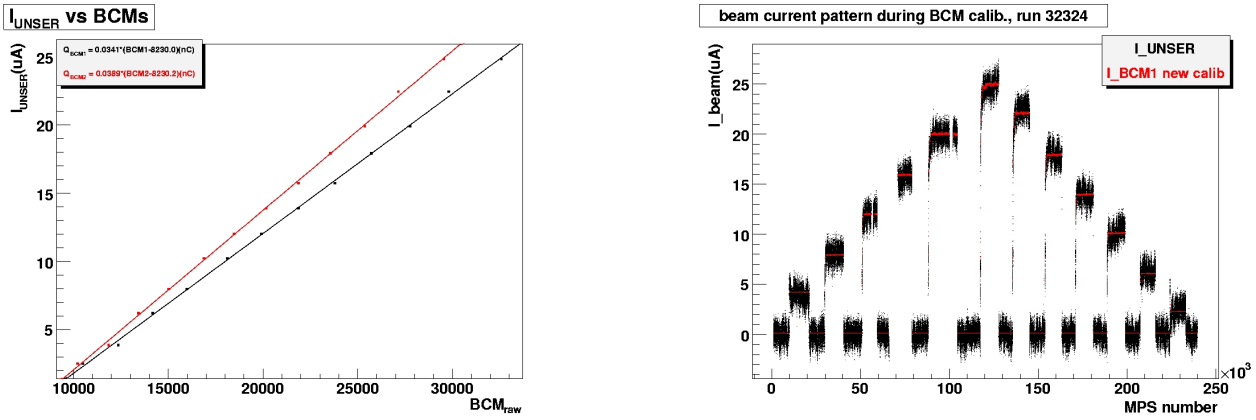

a c

Figure 3.4: Average UNSER current (after pedestal determination) vs. average BCM channels during "beam on" periods (a). The BCM current (after calibration) overlaid on the UNSER current vs. MPS (b).

plotted vs. the average BCM channel during the "beam on" periods and is fit with a line to determine the gain of each BCM. There are two BCMs for redundancy, BCM1 was used for most of the running but it did malfunction for a brief time, so it was necessary to use the second monitor as a measure of the current. Otherwise there was no significant difference between the current measured by each monitor.

Once the BCMs are calibrated, the BPMs are calibrated using the current measured by the BCMs. This is accomplished using the same calibration run as for the current calibration. The signal from individual wires in each of the BPMs, which is proportional to the current, is then plotted vs. the calibrated BCM signal to determine the pedestal for each wire. The luminosity monitor gains and pedestals are calculated in a similar way. The calibration constants for all of the monitors are then input into the database for use in the calculation of the beam charge, position and energy.

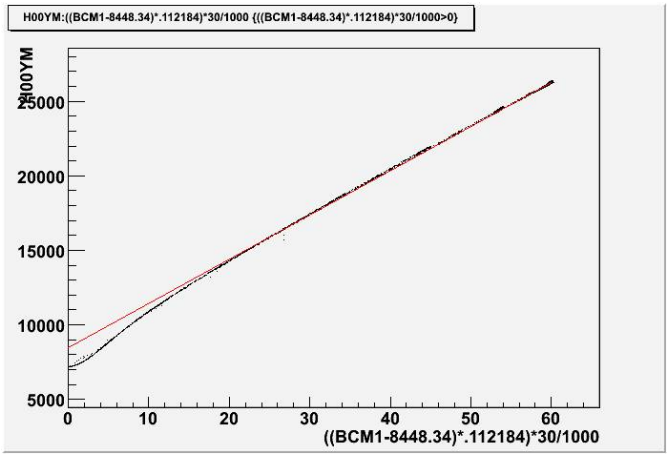

Figure 3.5: Plot of the Y^- wire channels vs. the current (black dots), using a calibrated BCM, and a line (red) fitted to the data at higher currents, showing the non-linearity at low beam currents.

The determination of the pedestal of the beam position monitors is critical because of the effect that an incorrect pedestal can have on the helicity correlated beam position differences. The position is proportional to the difference of the signals from two wires over the sum[80]

which can be written

$$x = \frac{X_1 - X_2}{X_1 + X_2} \tag{3.1}$$

where Q is the beam charge in the measurement period and the wire signals $X_i = Q\alpha_i(L \pm X) + P_i$ take into account the relative gains α_i between the two wires and the pedestals P_i are determined in the procedure described here. L is half the distance between the two wires, and X is the actual distance the beam is from this mid-way point, which is also the center of the beamline. An asymmetric pedestal difference (difference in incorrectly determined pedestal values, P_i, for different wires) of 6% can create a systematic error proportional to the charge asymmetry of 1 nm/ppm (an effect first discovered by Kent Paschke, now a professor at the University of Virginia). The "beam off" or electronic pedestal can vary by as much as 1000 channels from the "beam-based" pedestal determined by the calibration. A typical pedestal value is around 7000 channels, corresponding to a pedestal difference of as much as 15% (if the incorrect "beam off" pedestal value were used), so it was necessary to perform the beam monitor calibrations carefully (see Figure 3.5). The non-linearity at low beam currents made it necessary to use low current cuts in order to properly do the fits.

3.4 Target and Luminosity Monitors

The G^0 target design is based on the SAMPLE target[46]. The target is designed with a high flow rate so that target boiling effects contribute less than 5% to the systematic uncertainties. It is a 20 cm long cryogenic target capable of holding liquid hydrogen (19 K) or liquid deuterium (22 K). It is a cylindrical cell made of aluminum with longitudinal fluid flow, and is located inside the vacuum enclosure of the superconducting magnet system (SMS). Inside the cell is a "windsock" with perforations that allow the fluid to flow through it in order to generate some transverse flow (see Figure 3.6b). The heat load in the forward

angle, for a nominal beam current and energy of 40 μA and 3 GeV, was 320 W. The high-power heat exchanger, which is made of copper tubing with cold helium gas running through it, was designed to be able to remove up to 1000 W, and so the ∼650 W at 80 μA in the backward angle running wouldn't have been an issue. The helium cell was designed so that the entrance and exit window have the same radius of curvature. A high-power heater is used to replace the heat that is normally deposited by the beam when the beam is off. This occurs automatically during a beam trip, but the settings can be adjusted by hand if necessary.

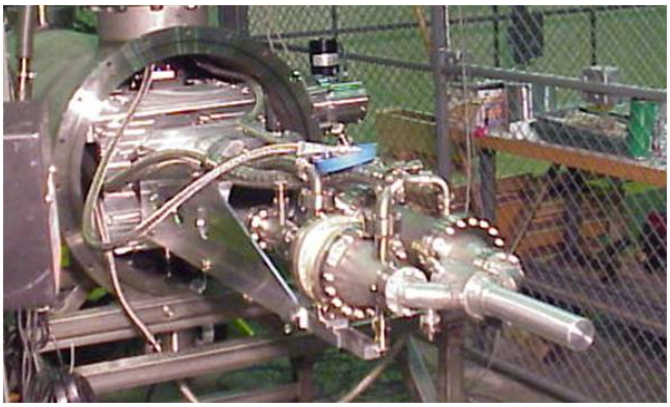

a

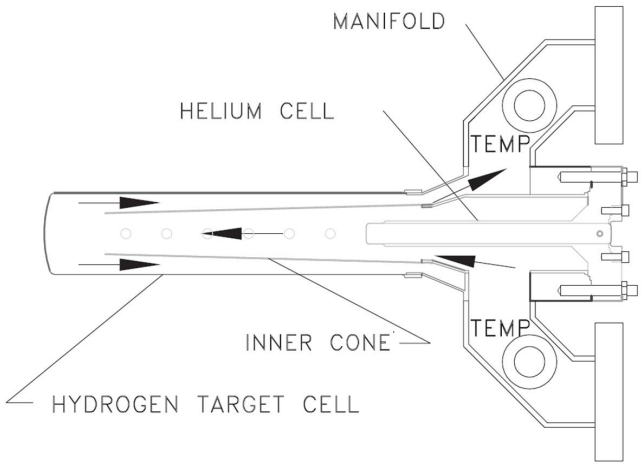

b

Figure 3.6: A picture of the target module; the beam would come out of the page through the target[46] (a). A diagram of the target cell showing the input and output fluid flow, the wind sock and the helium cell; the beam would go from right to left (b).

Although the detectors and SMS are turned around for the backward angle running, the orientation of the target remains the same. The manifolds - the heat exchanger and the high-power heater - are located upstream of the target cell. There are three thin aluminum windows that the primary beam passes through. The entrance to the helium cell (furthest upstream), the helium cell exit window which is the beginning of the target fluid volume (called the entrance window), and the hydrogen target cell exit window. The distance from

Table 3.2: Summary of target element thicknesses and densities.

Source	Thickness (cm)	Density (g/cm^3)
Helium window	0.047	2.699
Entrance window	0.062	2.699
Exit window	0.021	2.699
Helium cell	16	0.000166
Liquid Hydrogen	20	0.0723
Liquid Deuterium	20	0.1674

the end of the helium cell and the exit window of the hydrogen cell is 20 cm. These windows are the source of backgrounds which will be discussed in section 4.5. The thicknesses and densities are given in table 3.2.

The luminosity monitors are used as a monitor for false asymmetries caused by beam or target density fluctuations[50]. The beam is rastered in a square area 1.8x1.8 mm^2 in order to mitigate target boiling (and damage to the target cell). Beam fluctuations include changes in position, angle, energy or current and small effects can be corrected for using linear regression (see section 4.1.3). Target density fluctuations are also an issue, because they increase the statistical width (see Section 2.1.1). The G^0 luminosity monitors are synthetic quartz cerenkov detectors located at far forward angles (4 at $\sim 3.74^\circ$ and 4 at $\sim 3.98^\circ$) and see very high scattered electron rates from both electron-proton, electron-aluminum, and electron-electron (Møller) scattering (see Figure 3.7a). The high rates make it possible to achieve good statistical uncertainties on a shorter time scale than the main detector signal. The luminosity monitors have such small statistical errors that it is possible to see an octant variation due to small transverse components of the beam (see section 4.4).

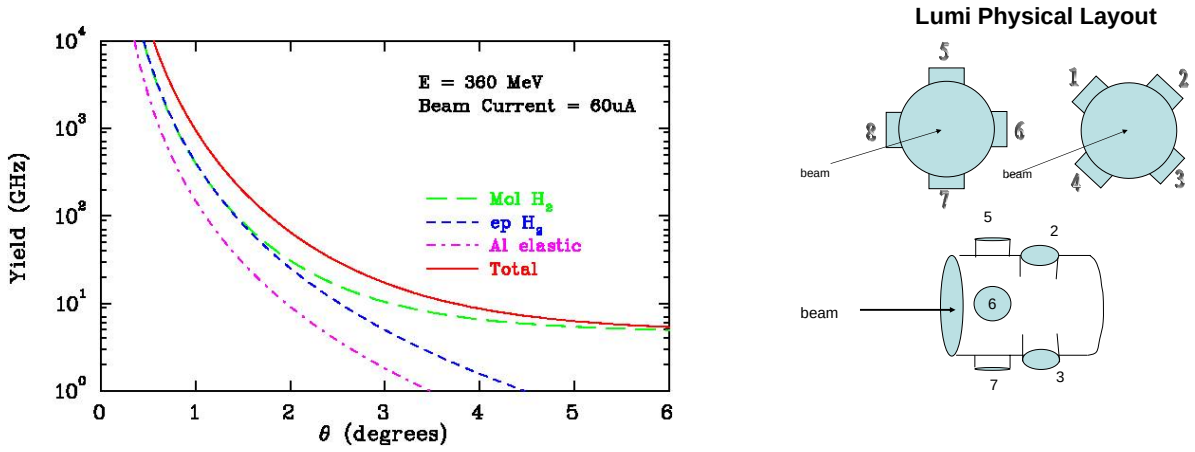

a b

Figure 3.7: Yields vs. lab scattering angle for electron-proton, electron-aluminum, and electron-electron (Møller) scattering from hydrogen at 360 MeV (a)[50]. The layout of the luminosity monitors; note that the ordering is not the same as for the main detectors, and there is nothing preventing an offset in ϕ (b).

3.5 The Spectrometer: Magnet and Detectors

The G^0 experiment is eight-fold symmetric around the beam axis. Half of the octants (the even numbers) were built and instrumented in France, the other half (odd numbers) in North America, with the octant numbering starting with 1 at the noon position, and in the backward angle, running counterclockwise (if you are looking downstream)[43]. Each octant has the sixteen focal plane detectors (FPDs) that were also used in the forward angle, nine cryostat exit detectors (CEDs) and a aerogel cerenkov counter that covers the whole active area.

The CEDs and FPDs are supported by a "ferris wheel" which also supports the cerenkov detector. The CEDs and FPDs are sets of curved scintillators which are each read out from both ends by PMTs through lucite light guides. The FPDs consist of pairs of scintillator

(front and back) that are 60-120 cm in length and the first four are 5 cm thick while the rest are 1 cm thick (see Figure 3.8, a). They vary in width from 5-10 cm. The CEDs are 1 cm thick, approximately 53 - 66 cm in length[85] and vary in width from 3.5 to 16.9 cm wide[128].

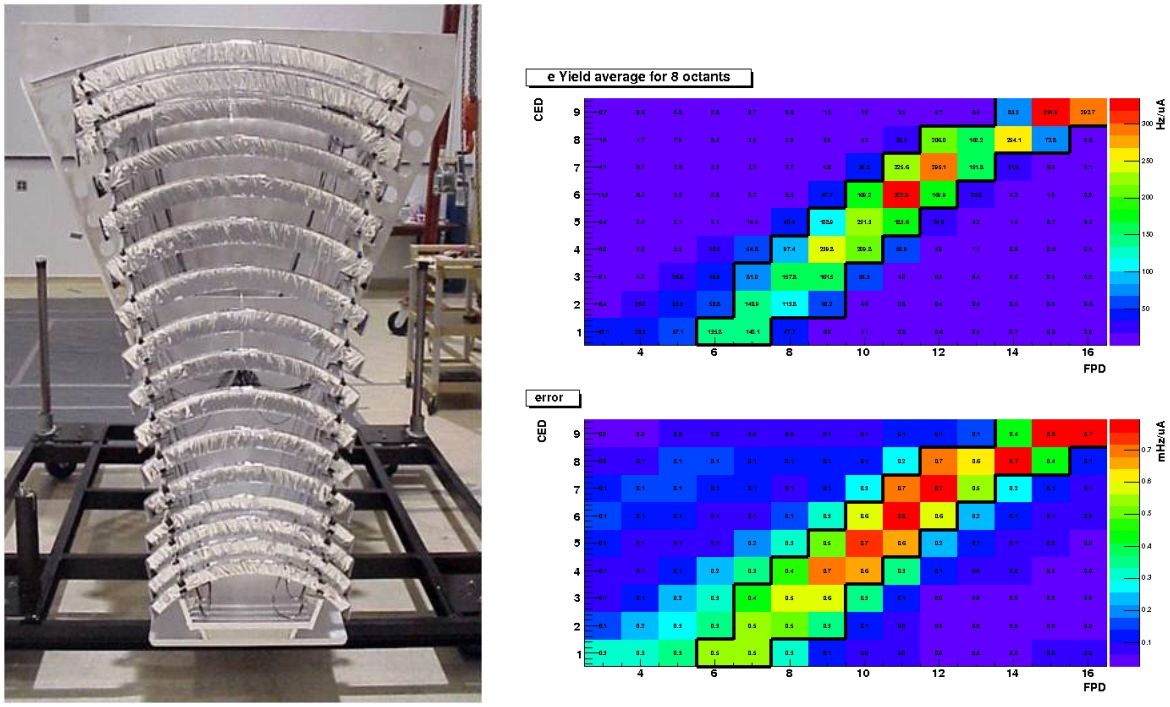

a b

Figure 3.8: Picture of the FPD assembly for one octant (a). The CED/FPD coincidence matrix of the octant average yields (top, Hz/μA) and errors (bottom, mHz/μA) for hydrogen at 362 MeV with the elastic electron locus outlined (b).

The superconducting magnetic system (SMS) is a toroidal spectrometer with 8 coils, and 8 open sections where the detectors are located (the octants). Each coil is a double pancake of integrated superconductor, and each of these 4 layers has 36 turns of superconductor[146]. The coils and the superconducting electrical bus are cooled with liquid helium, and the cold mass (the coils, cold bus and collimators) is shielded with liquid nitrogen. The acceptance of the experiment is defined in part by the collimator and magnet. The presence of the

magnetic field allows for the kinematic separation of the elastic and inelastically scattered electrons. The momentum and angle dependence of the transport of the particles through the magnetic field creates loci in the CED/FPD coincidence space - referred to as a matrix (see Figure 3.8, b). The collimators are located within the field region of the magnet, and act to define the angular acceptance and to shield the detectors from neutral particles created in the target by blocking the "line-of-sight".

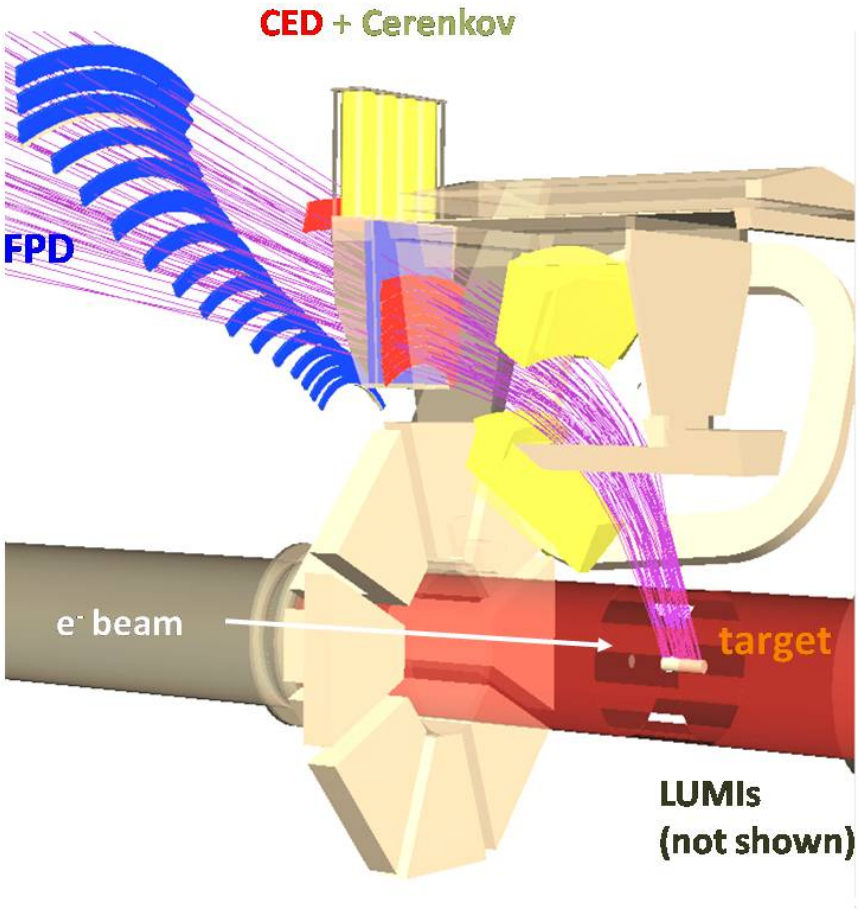

Figure 3.9: Diagram of the experiment, with electrons backward scattered onto the detectors. Coincidences between a CED and FPD allow for kinematic separation of the elastic and inelastic events. A third coincidence with the cerenkov detector determines that the scattered particle is an electron.

The cerenkov counter is an aerogel box that is read out at the outer radius of the box

by four PMTs[43]. Multiple hits in the PMTs are required to generate a signal. A triple coincidence between a CED/FPD pair and the cerenkov indicates an electron event, because the momentum of the negative pions is too low to generate a signal. The index of refraction of the aerogel is $n = 1.03$, and only particles with $\beta > 1/1.03$ will generate a signal. Thus pions with a momentum of up to 570 MeV/c will not produce any light. At 362 MeV the pion momentum range is approximately $100MeV < p_\pi < 220MeV$ and at 687 MeV it is $100\,MeV < p_\pi < 340\,MeV$, so the cerenkov is used in coincidence to indicate an electron. A CED/FPD coincidence that doesn't trigger the cerenkov is sent to the pion matrix. Although manufactured with the same specifications, the North American and French detectors (CEDs, FPDs and cerenkov) were manufactured independently of each other, and therefore could have slight differences.

3.6 Electronics and DAQ

The G^0 electronics were separately designed by the North American (NA) and French (FR) groups, with the odd-numbered octants designed by the NA group, and the even-numbered octants by the FR group. The differences in the design allow for the study of false asymmetries that may have been introduced due to detector electronics artifacts. The asymmetries between the NA and FR octants are consistent in the forward angle measurements, indicating that there are no false asymmetries due to the forward angle detector electronics[100]. The benefit of using nearly independent electronics designs became apparent when an artifact of the NA electronics caused a problem for a small percentage of the backward angle data. The problem manifested itself as an increase in the asymmetry width beyond that calculated from counting statistics, which was monitored during the experiment as the ratio (of the measured width) to counting statistics (RCS) in each run (see Appendix B). Because

the FR electronics did not suffer from the "RCS problem" they could be used to gauge the effect on data from the NA octants (see Section 4.1.2).

The electronics were designed with both the forward and backward angle requirements in mind[37]. The forward angle had especially high rates, $\sim$2 MHz per scintillator pair (front and back of an FPD), while the backward angle electronics had to sort the signals in real-time from the 16x9x2 possible FED/CED/Cerenkov coincidences in each octant. In the forward angle specialized electronics stored histograms of time of flight (ToF) information for each FPD in each macropulse (MPS - 1/30 s) and a special (31 MHz or 32 ns) beam structure was needed in order to perform the TOF. In the backward angle the normal beam structure (499 MHz or every 2 ns) was used, and the number of coincidences in each detector pair in each MPS is recorded by custom scalers, with particle identification provided by the Cerenkov. These coincidence yields (see Figure 3.8, b) are then used to form the asymmetries in software for both electrons and pions. Some dedicated 31 MHz data were taken in the backward angle for ToF analysis of Cerenkov efficiencies, though this data was not able to be used for Q^2 determination (see Sections 4.2.1 and 4.3). In both the forward and backward angle data taking, a small fraction of the events were taken with information about the individual detector pulse (time of the event into a TDC and the integrated pulse charge into an ADC) recorded for monitoring purposes (FastBus).

In the forward angle the NA electronics was modular, with separate units for discrimination of the PMT signals, mean timing of the signals from each end of the scintillators, coincidence units and time encoding electronics. For the backward angle measurement, the time encoding boards that recorded the ToF information in the forward angle were replaced by custom logic boards which determined the CED and FPD coincidences, with or without a Cerenkov coincidence. The FR electronics was highly integrated, with the discrimination, mean timing, coincidence and time encoding done on a single mother board. These same

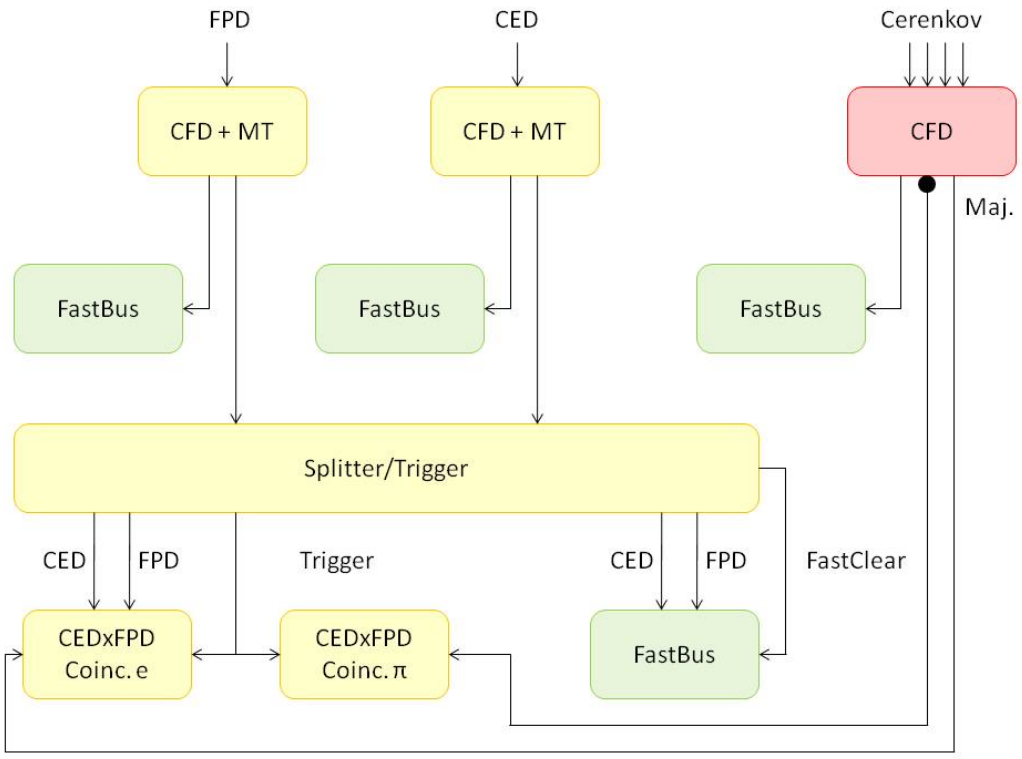

Figure 3.10: Diagram summarizing the coincidence electronics in the backward angle (adapted from [143]).

boards were used in the backward angle to determine the CED/FPD coincidences, with an additional unit to check for Cerenkov coincidences. Instead of recording ToF spectra, the scalers recorded the number of coincidences for each CED/FPD pair per MPS. These counts/MPS are later normalized to form yields in Hz/μA as shown in Figure 3.8, b.

The signals from the PMTs on either end of an individual scintillator (either the front or back of an FPD or a CED) are sent to constant fraction discriminators (CFDs) and a mean timer (MT) is used to determine the mean time between the PMTs, resulting in a time that is relatively independent on where the scintillator was struck. The trigger pulse is formed in the Splitter/Trigger from an OR of all the CEDs ANDed with an OR of all the FPDs in a given octant. The trigger pulse is then ANDed with each individual CED and each

FPD signal which helps to eliminate multiple hits. The trigger splitter involves a multi-hit function which determines if more than one CED or FPD has been hit, and an 8-bit encoder generates a word with 4 bits each corresponding to the CED and FPD information. If there was only a hit in one CED and one FPD then the word is stored. In general, if at least two of the four Cerenkov PMTs have also been hit (multiplicity 2, or M2), then the word is decoded into the individual CED and FPD signals as an electron, otherwise, the event was a pion. The Cerenkov can also be used with different multiplicities, or requiring more or fewer PMTs to be hit. A delayed trigger pulse clears the stored data in preparation to accept the next event.

The data acquisition (DAQ) was built on the CODA (CEBAF Online Data Acquisition) system at Jefferson Lab[69]. At the end of each MPS there is a "helicity stabilization" period (500 μs) when the helicity is reversed, and it is during this time that the data are stored to be read out during the next MPS. Each "event" is built from the number of counts from each of the coincidence pairs, along with the beam parameters that are being recorded[14]. A designated DAQ computer ran the CODA system and communicated with 11 readout controllers (ROCs), one in each electronics crate containing the modules for the different subsystems. The ADC spectra of each PMT as well as the TDC for each mean timer (MT) and constant fraction discriminator (CFD) output are recorded as FastBus data for a small fraction of the data. When it is enabled, the "fast clear gate" is used to determine if a CED and an FPD have a coincidence in a particular time window, and is cleared and reset if not. When the fast clear is disabled, there is no reset and clear and most of the time the FastBus events are empty.

Chapter 4

Analysis

4.1 General Description

In order to obtain physics asymmetries from the raw asymmetries, it is necessary to perform various corrections to the raw data, which are summarized in Figure 4.1. The raw asymmetries are blinded with an unknown multiplicative factor (different for each dataset) before the various corrections are applied. A blinding factor is applied in order to lend credibility to the final result, because many of the aspects of the analysis rely on subjective judgments and there is an 'expected' answer (or previous experimental results) which can influence the experimenter. The raw yield data in each run are processed in four separate "passes". In the first pass, various cuts are applied automatically to eliminate data taken during a beam trip or excursion, and rates are normalized to the charge and stored as charge-normalized yields. In each pass the asymmetry is formed from the yields in a "quartet"

$$A_{meas} = \frac{Y_1 - Y_2 - Y_3 + Y_4}{\sum_i Y_i} \tag{4.1}$$

where the yields in the negative helicity states are subtracted from those in the positive states in the numerator, and the blinding factors are applied. Run-averaged values are stored in a MYSQL database (for each pass) and other cuts to the data are made "by hand" on a run-by-run basis during data quality checks.

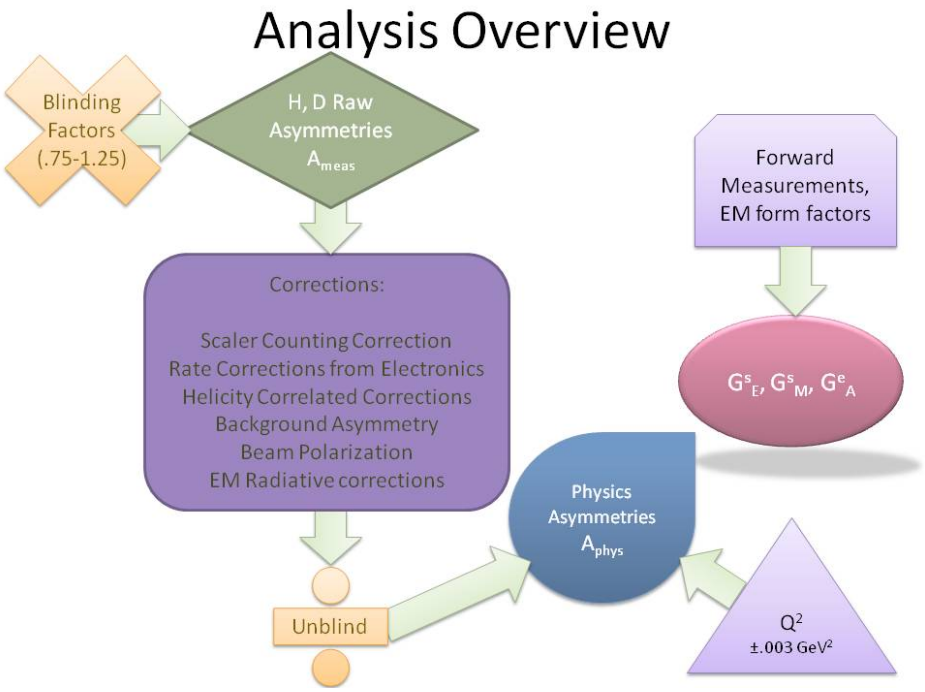

Figure 4.1: Overview of the analysis process from raw asymmetries to strange magnetic form factors. The data are looped through at the yield level for each of four passes (standard cuts and blinding factors are applied, then the scalar counting correction, rate corrections from electronics and helicity correlated corrections). The run averaged cell-by-cell yields and asymmetries are then used to correct for background asymmetries and radiative corrections are applied. Finally the asymmetries are corrected for beam polarization and unblinded. The forward angle measurement and Q^2 are then used to obtain the strange form factors.

In the second and third passes, the normalized yields are corrected for various electronics corrections, in this case for a scaler counting error in addition to the corrections for dead-time and randoms. The cut for the scalar counting error was done separately in order to gauge the effects without the deadtime corrections. Helicity correlated false asymmetries are removed in the final pass, using linear regression. The run averaged yields and asymmetries

are stored in the database on a cell-by-cell basis; these asymmetries are corrected for the beam polarization. Background dilutions are studied and the asymmetries of the background are estimated in order to correct the measured asymmetries. The various yield and asymmetry corrections are performed on a cell-by-cell basis for both the electron and pion data. Electromagnetic and electroweak radiative corrections are also applied in order to obtain the physics asymmetries. Once the various corrections are finalized the data are unblinded. The asymmetries are then averaged over the locus of interest (elastic and inelastic electron and pion loci for each energy setting). A summary of the effect of the corrections on the asymmetries is shown in Table 4.1.

In order to obtain the strange electromagnetic form factors it is necessary to determine the $< Q^2 >$. This is achieved through simulation and knowledge of the acceptance of the experiment. The forward angle asymmetries are then parameterized as a function of Q^2 in order to estimate the value at the backward angle Q^2, and the physics asymmetries are combined to obtain the strange electromagnetic form factors and the effective axial form factor. The method of obtaining the various corrections and data quality checks will be summarized here. The application of the forward angle asymmetries to obtain the final strange form factor results will be discussed in Chapter 5.1. My contributions for determining the cell-by-cell Cerenkov efficiencies, Q^2 determination, the transverse asymmetry correction to the longitudinal data as well as an alternate method for determining the background asymmetries will be discussed in this chapter in more detail.

4.1.1 Data Quality

Plots of the normalized yields and asymmetries as a function of octant number and run number give a general idea of the quality of the data. Figure 4.2 shows examples of the raw

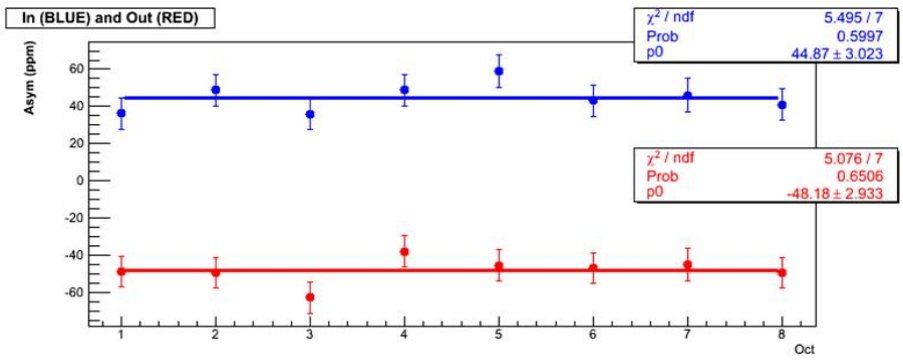

a

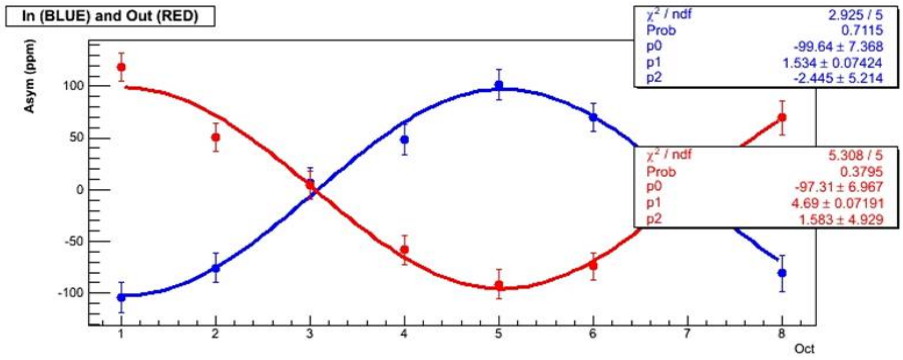

b

Figure 4.2: Raw asymmetries vs. octant number for the insertable half wave plate (IHWP) IN (blue) and OUT (red) states for run periods where the beam was longitudinally polarized in the hydrogen 687 MeV dataset (a) and one where the beam is transversely polarized in the deuterium 362 dataset (b). In both cases the asymmetries change sign on an octant-by-octant basis for the two IHWP states.

asymmetry reversing with the insertable half wave plate (IHWP) IN (blue) vs. OUT (red) for a longitudinal (top) and a transverse (bottom) run. Run averaged values were studied with plots like Figure 4.3 which shows the raw asymmetry vs. run number for the hydrogen 687 MeV dataset. The IHWP was changed every day or so from IN (blue) to OUT (red). This slow helicity reversal changes the sign of the physics asymmetry without changing the signal that reports the helicity to G^0 and so could be used to look for false asymmetries due to the electronics. The data in both the longitudinal and transverse running properly change sign with the IHWP insertion, and the octant to octant data are in good agreement.

The data quality checks consisted of looking at the run averaged values of beam parameters and singles rates in each of the detectors, including individual cerenkov PMTs. The beam parameters included halo rates, lumi widths, position, energy, angle differences and charge asymmetries. Data quality was checked by looking at plots of the run averaged values of the singles rates in each detector in each octant, as well as the beam parameter differences vs. run number. If these quantities were significantly different (varied outside of the error) for a particular run, then the whole run would be eliminated. Essentially if one of the beam parameters drifts enough, then we are not doing the same experiment anymore. For example, a run with large halo rates compared to nearby runs might indicate that there are significant background rates for that run which aren't present in other runs. Although plots of the detector coincidence yields and asymmetries (Figures 4.2 and 4.3) were also considered during data quality checks, if a large difference in the yields or asymmetries for a particular run could not be correlated with large deviations in one of the beam parameters or a problem with the singles rates, the run was kept in the dataset.

In principle some of the runs that were eliminated could probably be added back into the dataset by using judicious cuts on an event by event basis within the run, but this was not considered to be necessary considering that such a small number of runs were eliminated. The exceptions are an issue with particular PMTs causing the data in octant 1, CED 5 and octant 5, CED 8 to be thrown out, but the data for the rest of the detectors is okay. In the H362 transverse dataset there is also a problem with missing singles rates which necessitate eliminating octant 2 from the data. As you can see in Figure 4.2b the effect of this problem may not be noticeable (at least in the raw asymmetries), but it isn't possible to calculate electronics corrections without the singles rates that are missing. In addition to the transverse datasets for each target/energy combination, in the dataset that I was primarily responsible for, the H687 MeV longitudinal dataset, only 14 out of 562 total runs

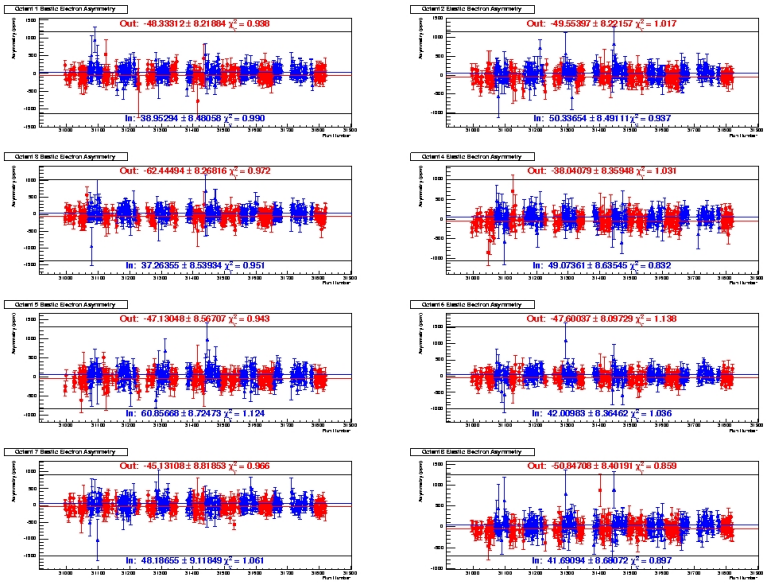

Figure 4.3: Plots of the longitudinal asymmetries vs. run number in each octant for the hydrogen 687 dataset. The insertable half wave plate state was changed from IN (blue) to OUT (red) every couple of days.

were eliminated. About half of the 14 runs were eliminated because they didn't make it through all of the analysis passes, probably because the data had been corrupted in some way. Others were 'mislabeled' and were actually part of one of the other datasets or test runs. One run appeared to have had the electron rates going to the pion matrix. The standard corrections in each analysis pass were performed on the 'good runs' that remained in the dataset.

4.1.2 Electronics Corrections

The asymmetries are formed from charge normalized yields, so that $\partial Y/\partial Q = 0$, unless there is a rate dependent effect (such as deadtime or random coincidences) on the yields. In that case a charge asymmetry can lead to a false asymmetry (see Figure 4.4). For example, the

effect of the deadtime on the measured asymmetry due to a charge asymmetry is given by[14]

$$A_{meas} \simeq A_{phys} - \frac{DT}{1 - DT} \times (A_{phys} + A_Q) \tag{4.2}$$

because the deadtime DT is proportional to the rate in a given detector. Deadtime occurs when some events are lost while the electronics is recording a previous event. The probability that an event occurs during the 'dead' period, assuming the rate follows a Poisson distribution, is $f_{dead} = 1 - e^{-R\tau}$ or simply $R\tau$ for $R\tau \ll 1$. The 'deadtime' for a particular electronics element is in general the product of the incident rate R and the characteristic electronic deadtime τ of the element (which needs to be measured). It is an estimate of the amount of time in a given time interval that the element is not taking data, which increases as the incident rate increases.

Some good events with multiple hits in the detectors are thrown out (multihits) because we don't have a tracking algorithm to determine the good track. The effect of multihits and deadtime both cause a decrease in the measured rate. In addition, random coincidences caused by the singles rates, R, in a pair of detectors (a CED and an FPD) or $R_{CED}R_{FPD}\Delta_{trig}$ where Δ_{trig} is the trigger gate width, can tend to increase the rate. The yields that go into the calculation of the asymmetry need to be corrected for the deadtime, randoms and effects from multiple hits in the detectors to reduce the false asymmetries. Special runs are taken in which the charge asymmetry is purposefully made very large (by $\sim$ 3-4 orders of magnitude) in order to make plots of the detector asymmetry vs. the charge asymmetry, called a 'Wells plot'. The effect of the electronics corrections can be determined by looking at a Wells plot that shows the detector asymmetry with and without the electronics corrections applied. Ideally the slope with the corrections applied would be zero. Figure 4.4 shows that the randoms and deadtime corrections have the opposite effect on the slope of the uncorrected Wells plot (red), with the deadtime correction 'overcorrecting' the slope to positive (green).

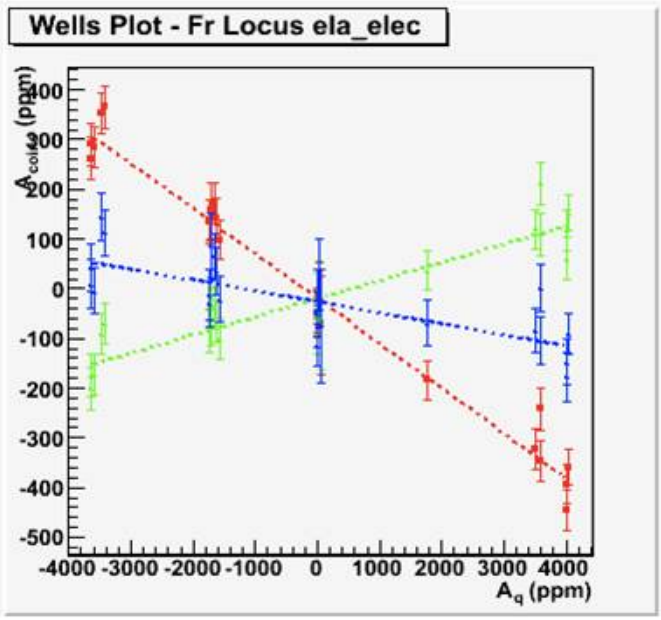

Figure 4.4: Wells plot showing the measured detector asymmetry A_{coinc} for artificially induced large beam charge asymmetries $A_q \sim 4000$ for deuterium with a beam energy of 362 MeV[142]. Typical charge asymmetries during the data taking are <1 ppm. The red line shows the results with no deadtime or randoms correction. The green line shows the results for a deadtime correction only, while the blue line is the result with both the deadtime and randoms corrections.

The addition of the randoms correction then makes the slope more negative (blue). The remaining slope means that there is a residual false asymmetry (in this case about 0.0045 ppm) which must be accounted for in the final estimate of the uncertainty.

The measured yield is given by

$$Y_{meas} = \left[Y_{true}\left(1 - DT_{ced}\right)\left(1 - DT_{fpd}\right) + Y_{rdm}\right]\left(1 - DT_{trig} - MH_{22}\right)\overline{MH_{12}} \tag{4.3}$$

where the true yield is reduced by the deadtime in the CED and FPD electronics and increased by the random rate[58]. The deadtime of the trigger and the effect of the multihits must also be taken into account. The effect of multihits associated with two CEDs and two FPDs hit can be estimated rather simply from the expression $MH_{22} = (R_{trig} - R_{coinc}) \times$

$\Delta_{Trig}/2\times I$, where R_{trig} and R_{coinc} are the trigger and coincidence rates (Hz/μA) respectively, Δ_{Trig} is the trigger gate width (ns) and I is the beam current (μA). The factor $\overline{MH_{12}}$ is more complicated because it includes the effect of either one CED and two FPDs or one FPD and two CEDs being hit[143]. Note that the inversion of these equations in order to calculate the deadtime requires a recursive procedure because, for example, R_{coinc} is Y_{meas}. The deadtime calculations were also verified using a simulation of the entire electronics chain.

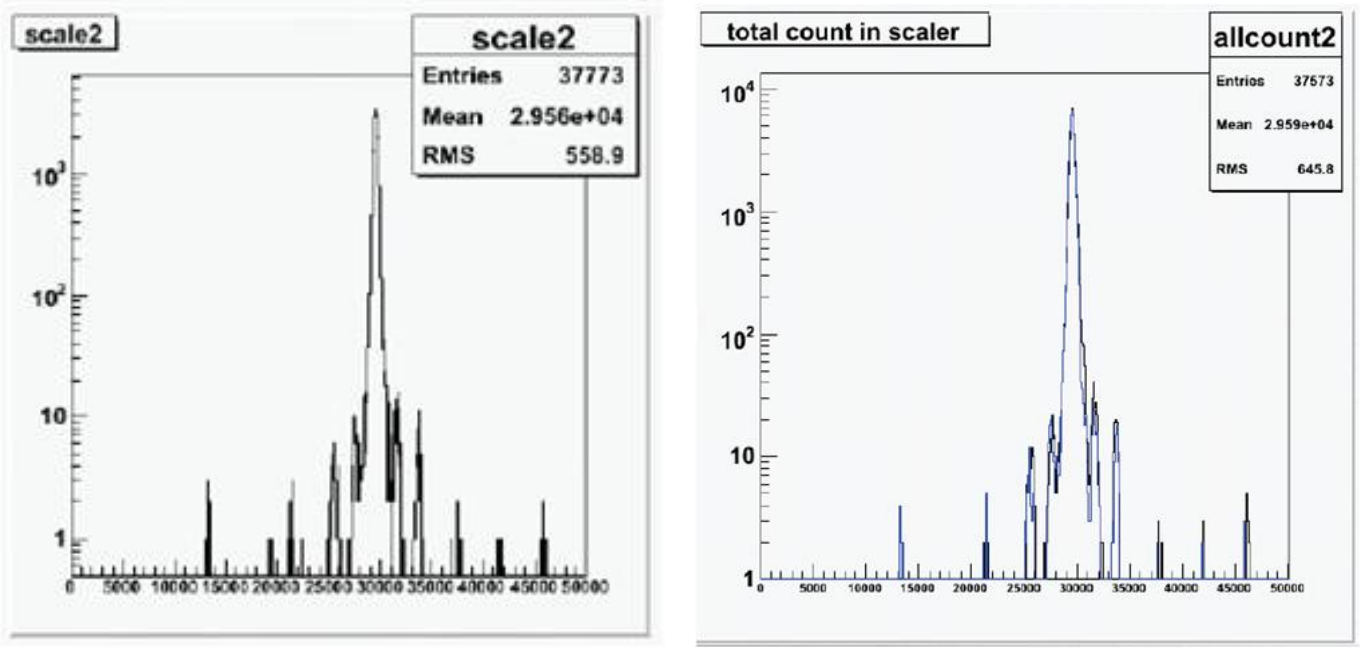

a b

Figure 4.5: The effect of the scaler counting error in scaler channels for one of the NA detectors (a). The simulation can reproduce the effect (b)[17].

In addition to the above electronics corrections, there was an additional correction to the yields due to a scaler counting error (which affected the NA electronics only). An error in a scaler counter in the NA electronics chain occurred when pulses came faster than 1 every 7 ns, causing bits to be dropped. This resulted in extra 'wings' in the yield distribution, because sometimes the dropped bit resulted in a higher than actually yield, and sometimes as a lower yield. The effect can be seen in the scaler channels that are affected (see Figure

4.5, a). It was determined that a 5σ cut on the yields would be used to eliminate these peaks, and a simulation was used to estimate the remaining effect (see Figure 4.5, b). Only a small percentage ($\sim$1%) of the data were affected because it only occured in the NA detectors when the rate was too high. So the effect was corrected for, the remaining false asymmetry was estimated using simulation, only a small fraction of the data were affected and comparison to the detectors in the FR octants (whose electronics do not have the error) shows that the effect is smaller than 5×10^{-4} on the asymmetry[57].

4.1.3 Linear Regression

The measured asymmetry can have a component from false asymmetries due to helicity correlated beam properties

$$A_{meas} = A_{phys} + \sum_{i=1}^{6} \frac{1}{2Y} \frac{\partial Y}{\partial P_i} \Delta P_i \tag{4.4}$$

where P_i is a beam parameter such as charge (intensity), energy, angle (θ_x, θ_y) or position (x, y), in the case of uncorrelated parameters[120], $\Delta P_i = P_{i,+} - P_{i,-}$ and Y is the charge normalized detector yield. The effect of helicity correlated differences in the yield can be mitigated by averaging over a symmetric detector (see Figure 4.6). Even though the slopes are small in the backward running, the correction was performed. In order to correct for residual false asymmetries the measured beam parameters can be used to extract slopes, $(1/Y)(\partial Y/\partial P_i)$, on a run-by-run basis due to the natural beam motion. It is also possible to study the slopes by deliberately causing large position, angle or energy differences in the beam. During every third run, a set of magnetic coils between the entrance to the hall and the target are used to move the beam in x and y in order to measure the sensitivity of the detectors to beam motion. The charge asymmetry and energy differences can also be studied

by deliberately inducing large effects at the source.

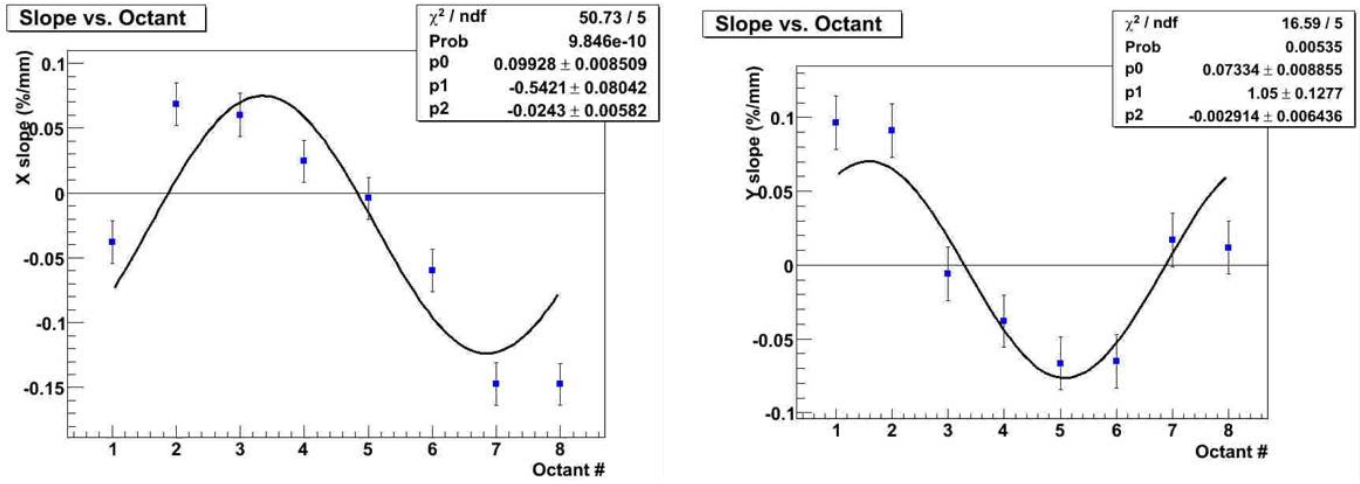

a b

Figure 4.6: Example of a simulation of the octant dependence of the detector sensitivity to position in x (a) and y (b). The slopes are given in %/mm[17].

The beam parameters are correlated so in order to extract the slopes it is necessary to perform linear regression in a method similar to that described for the background asymmetry correction (see Appendix C.1). The change in yield due to the helicity correlations is $\partial Y = \sum_m C_m \partial P_m$ where the coefficients C_m need to be determined[14]. To minimize the χ^2 with respect to the coefficients on each of the 6 beam parameters on a run-by-run basis, it is necessary to satisfy a set of 6 linear equations. Using run averaged values, where

$$\begin{aligned} \partial Y &\equiv Y - < Y > \\ \partial P_m &\equiv P_m - < P_m > \\ < \partial x \partial y > &= < xy > - < x >< y > \end{aligned} \tag{4.5}$$

the set of linear equations is given by

$$< \partial P_n \partial Y >= \sum_m C_m < \partial P_n \partial P_m > \tag{4.6}$$

and the system can be solved by inverting this matrix to obtain the vector of coefficients C_m. The correction is then applied to the yields that go into the asymmetry calculation, and the uncertainty on the correction is accounted for in the final uncertainty on the corrected asymmetries.

4.1.4 Radiative Corrections

There are two types of radiative corrections that need to be applied to the measured asymmetry in order to determine the physics asymmetry of interest. The first is referred to as electromagnetic (EM) radiative corrections, which refer to the radiation of photons before or after the scattering vertex that effectively reduces the energy of the incoming electron. This effect reduces the value of the Q^2 and hence, the asymmetry, so this needs to be accounted for in the determination of the final value of the physics asymmetry. In addition, there can be depolarization of the incident electron due to radiation. The second type of radiative correction is referred to as electroweak radiative corrections, where the effect of various box diagrams are taken into account. These corrections have the effect of increasing the asymmetry for single boson exchange at G^0 backward kinematics. At this point the transverse data have not been corrected for radiative effects, because the radiative corrections are not explicitly calculated for transverse asymmetries.

The EM radiative corrections are taken into account by using the simulation to calculate the asymmetry that corresponds to tree level scattering, and comparing it to the asymmetry that is obtained with the radiative corrections applied[49]. The value of this ratio is the same

as the ratio of the physics asymmetry to that of the measured asymmetry, so the correction is given by

$$A_{phys} = A_{meas} R \tag{4.7}$$

where A_{meas} has been corrected for electronics effects, linear regression and background asymmetries. In the simulation, energy loss before the scattering is taken into account (ionization energy loss and density effect corrections) whether the radiative corrections are being applied or not so that the mean energy before radiation is the same. The unradiated cross section is the same as in Eq. 1.24, except that the beam energy E is replaced by E_s, where E_s takes into account the energy loss in the target. Similarly the unradiated asymmetry is estimated using Eq. 1.40, where estimates of the electroweak form factors are obtained from the 2004 PDG values of the proton and neutron standard model parameters[13].

The radiated cross section and asymmetry are calculated using the prescription provided by Mo and Tsai[104]. The cross section for small and large radiated energies are treated differently, where for small radiated energies, the radiated cross section is proportional to the unradiated cross section, and the asymmetry is calculated using the reduced Q^2. For large radiated energy there are additional effects in the cross section, including taking into account the depolarization of the incident electron. The deuterium radiative corrections are performed in a similar way, except that a model by Rocco Schiavilla, a professor at Old Dominion University, provides estimates of the cross section and asymmetry[126][127], and it is also necessary to take the Fermi motion of the nucleons into account. Because lookup tables were used, sometimes the kinematics were outside those provided by the model, so the static approximation was used (with a y-scaling model), for the calculation of the deuterium asymmetry. The energy of the radiated electron is different than if it were not radiated so the distribution of events at the focal plane is different, which also affects the weighting of the Q^2 and the asymmetry in addition to the modifications of the cross section, though the

effect was small (see Section 4.3).

The EW radiative corrections take into account the interference of two boson exchange (TBE) in the calculation of the physics asymmetry of interest, which is for single boson exchange (SBE). The parity-violating asymmetry for elastic electron scattering from a proton can be written as[13]

$$\begin{aligned} A &= -\frac{G_F Q^2}{4\pi\alpha\sqrt{2}} \times \{\left(1-4sin^2\theta_W\right)\left[(1+R_V^p) - \frac{\epsilon' G_A^{e,p} G_M^{\gamma,p}}{D}\right] \\ &- \frac{1}{D}\left[(1+R_V^n)\left(\epsilon G_E^{\gamma,p} G_E^{\gamma,n} + \tau G_M^{\gamma,p} G_M^{\gamma,n}\right) + \left(1+R_V^{(0)}\right)\epsilon G_E^{\gamma,p}\left(G_E^{\gamma,s} + \eta G_M^{\gamma,s}\right)\right]\} \quad (4.8) \end{aligned}$$

where

$$D = \left[\epsilon\left(G_E^{\gamma,p}\right)^2 + \tau\left(G_M^{\gamma,p}\right)^2\right]$$

and for scattering from the neutron, replace the superscripted p with n (and vice-versa) in the form factors (but not the R values). The effective axial form factor is

$$G_A^e(Q^2) = G_A^{e,T=1} + G_A^{e,T=0} \quad (4.9)$$

with the "effective isovector piece" given by $G_A^{e,T=1} = \mp\left(1+R_A^{T=1}\right)G_A^{T=1}$, where the upper sign is for the proton and the lower sign is for the neutron, has significant radiative corrections including γZ mixing and box diagrams in addition to the anapole corrections (see Section 1.1.3). The isoscalar piece is given by $G_A^{e,T=0} = \sqrt{3}R_A^{T=0}G_A^8 + \left(1+R_A^{(0)}\right)G_A^s$, with $\sqrt{3}R_A^{T=0}G_A^8$ smaller than 10%. The factor $\eta = \tau G_M^{\gamma,p}/\epsilon G_E^{\gamma,p}$ depends on the kinematics of a particular experiment. The EW corrections appear as the standard model parameter R terms[107].

The relationship between the measured asymmetry and the physics asymmetry can be written as[136]

$$A_{meas} = \left(\frac{1+\delta_{Z(\gamma\gamma)}+\delta_{\gamma(Z\gamma)}}{1+\delta_{\gamma(\gamma\gamma)}}\right)A_{phys} \quad (4.10)$$

where the δ terms come from the interference of the subscripted TBE with that of the subscripted SBE. The values of the δ terms vary with Q^2 and angle, so they must be calculated for the particular kinematics of interest. The correction can be approximated as

$$A_{phys} = \frac{A_{meas}}{1+\delta} \tag{4.11}$$

where $\delta = \delta_{Z(\gamma\gamma)} + \delta_{\gamma(Z\gamma)} - \delta_{\gamma(\gamma\gamma)}$ because the electromagnetic two photon exchange correction $\delta_{\gamma(\gamma\gamma)}$ is typically small. For G^0 backward the values of δ for hydrogen are 0.0146 and 0.0120 for the 362 and 687 MeV running, respectively, and for the deuterium they are 0.0041 and 0.0062[102]. The hadronic part of the EM radiative corrections must be removed from the R's before applying the EW correction to avoid double counting[23].

4.1.5 Background Corrections

The asymmetry of interest is that of the elastically scattered electrons

$$\vec{e} + p \rightarrow e + p \tag{4.12}$$

(or quasi-elastic from deuterium). But there are other processes present in the data, including inelastic electron-nucleon scattering (see Appendix A), elastic and inelastic scattering from nucleons in the aluminum cell as well as the helium (and helium cell) in the target and the Dalitz process which provides a source of electrons in the detectors. The Dalitz process (sometimes referred to as the π^0 process in this thesis) is the decay of a neutral pion into an electron-positron pair

$$\pi^0 \rightarrow e^- + e^+ \tag{4.13}$$

where the neutral pion was produced in the liquid hydrogen (or deuterium) in the target. The pions were produced either from electroproduction or from photoproduction by real bremsstrahlung photons (both resonant and non-resonant contributions) where the pion production cross sections were calculated in MAID[101].

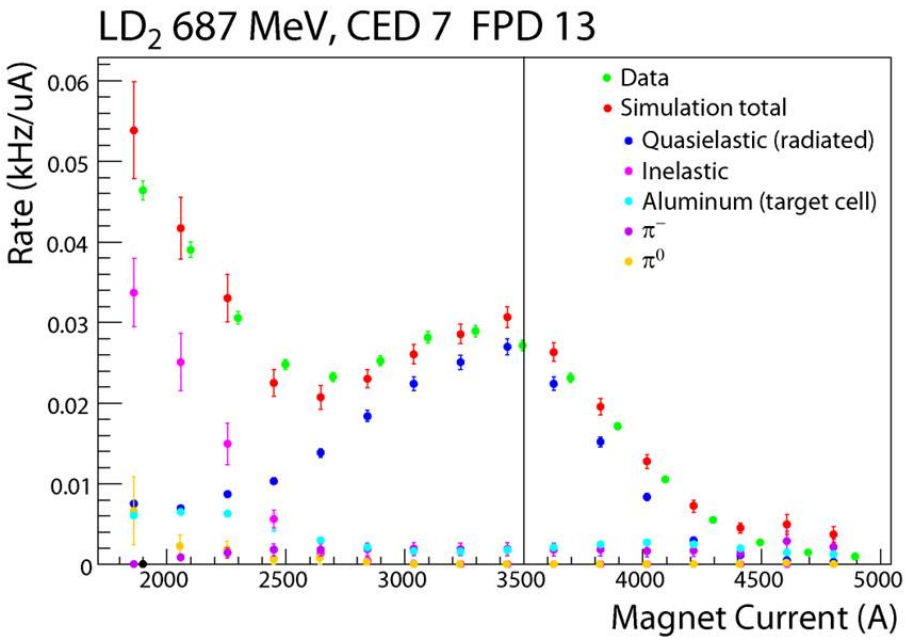

Figure 4.7: Field scan data for CED7/FPD13 coincidence cell in the deuterium electron matrix at 687 MeV[105]. Also shown are the simulation results for each of the processes as well as an estimate of the pion yields.

Not only are the rates of these processes important, but also the size of the asymmetry of each process. The measured asymmetry is a yield averaged asymmetry over all of the processes:

$$A_{meas} = f_{el}A_{el} + \sum_i f_{bi}A_{bi} \tag{4.14}$$

where f_{el} and the f_{bi} are the yield fraction, or dilution, of the elastic and each background process, and A_{el} and A_{bi} are their respective asymmetries. The term dilution refers to the fact that the asymmetries of the other processes 'dilute' the elastic asymmetry. Note

here that if the asymmetries of the other processes were zero (or averaged to zero), then it would still be necessary to know their dilutions; the only case where the asymmetries of the other processes wouldn't matter is if they were the same as the elastic asymmetry. So it is necessary to determine not only the yield fraction of each process, but to have an estimate of the asymmetry for each as well. Both the official method and the alternate 'matrix method' (discussed in Section 4.5) found aluminum from the target windows to be the dominant background ($> 90\%$ of the background in most cells).

The 'official' method of determining the background correction is to take advantage of the information in the field scan data to determine the dilutions[105]. A comparison of the data with the simulation for a field scan in one coincidence cell (CED7, FPD13) is shown in Figure 4.7. This plot is for the high energy deuterium data. The magnetic field was ramped over various currents and yield data were taken at each setting and compared to simulations of the yields for the various settings. The information about the background yields was obtained by fitting the kinematic dependence on the field *in each cell*. There are two scaling factors applied to the simulated yields to fit them to the data yields. One is an 'efficiency' factor, ϵ, applied to each of the simulated yields that is different in each cell (and for each target/energy combination) but is roughly equal in size to the Cerenkov efficiencies (see Section 4.2). Each of the simulated yields for the different processes is scaled by the same factor in a given cell. This factor is determined by minimizing the χ^2 of the difference between the data and the total of the simulated yields (with the scale factor applied) with respect to ϵ.

In order to fit the simulated yields to the data, it was necessary to have a scale factor on the magnetic field current. Note that in the plot the data points (green) do not appear at exactly the same magnet current as the simulation data points (the sum of the simulations is shown as red points) - this is an artifact of the scale factor on the magnet current. This

scale factor varied by octant but for a given octant was consistent in all cells for all four target/energy combinations. It was determined by fitting the (quasi-)elastic peak in data and the (quasi-)elastic simulated yield with gaussians and determining the scale factor which needed to be applied to the magnetic current of the fit to the simulated yield in order to make it match the data. The final values are averages of the results for cells in the elastic locus. It is at least qualitatively consistent with results from the forward angle analysis, and a similar effect is seen in the matrix method discussed in Section 4.5.2. The variation with octant is shown in Figure 4.8; the largest factor (1.05) is in octant 5.

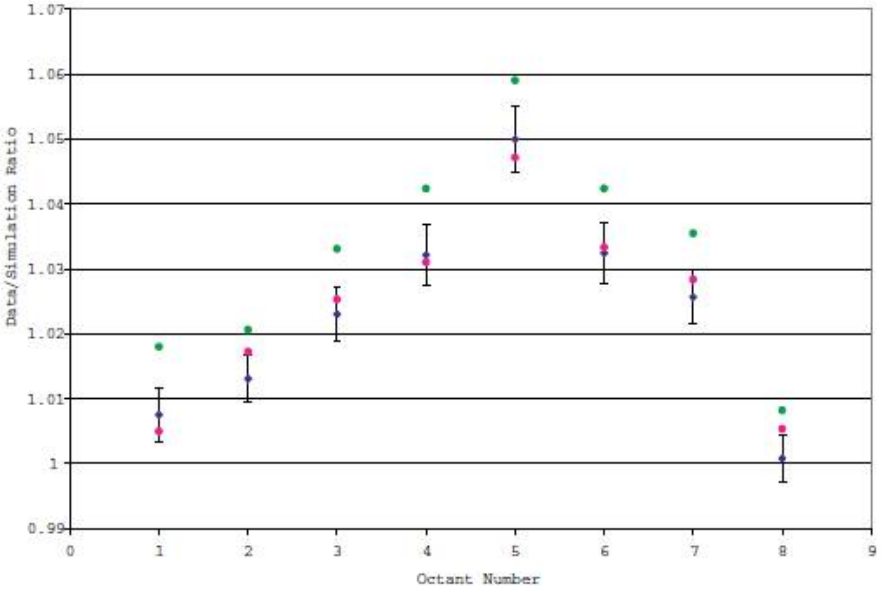

Figure 4.8: The octant-to-octant variation of the scale factor on the magnet current (blue). The same factor is needed in each cell to make the elastic peak in the simulated and data yields match, demonstrated by the values for hydrogen yields in coincidence cell CED7/FPD12 at both high (green) and low (magenta) beam energy[105].

The field scan runs were not long enough to measure asymmetries cell-by-cell, so the deuterium asymmetry was estimated as the aluminum asymmetry (using the quasi-static approximation this is good to $< 2\%$) and an asymmetry of zero was assigned to all other

asymmetries. The 'other' processes are mostly from π^0 and π^- events, the asymmetries of which are zero or close to zero, and a very small inelastic component, the asymmetry of which is not necessarily zero. Large uncertainties (50% and 100%, respectively) were assigned to the aluminum dilutions in the hydrogen data and the 'other' dilutions in all datasets in order to account for this. An alternate method of determining the background asymmetries will be discussed in Section 4.5, in which the asymmetries were determined with the use of simulated asymmetries and yields.

4.1.6 Summary of Corrections

The sizes of the standard corrections which have been discussed in this section are summarized in Table 4.1. The transverse correction is described in more detail in Section 4.4. The radiative corrections are multiplicative; the other corrections are additive. The electronics and linear regression corrections are applied to the yields before the calculation of the asymmetry. The radiative, transverse and background corrections are applied to the asymmetries. In general the corrections are small ($< 15\%$) compared to the size of the physics asymmetries (see Table 5.1). The largest correction is the electronics correction to the high energy deuterium (D 687) data, an effect of the high pion rates in the scintillators creating random coincidences with the cerenkov signals, but even this correction has a small uncertainty. Otherwise the individual corrections are smaller than 5% of the size of the final physics asymmetries.

Table 4.1: Summary of the effect of various corrections to the asymmetries for each dataset. The 687 MeV datasets have periods where the linear regression correction changes sign, but the magnitude in either case is smaller than what is listed. Compare to the sizes of the final backward asymmetries shown in Table 5.1 (lower Q^2 corresponds to lower energy).

Dataset	Electronic Corrections[44] (ppm)	Linear Regression[125] (ppm)	Radiative Corrections[44] (% increase)	Transverse Component (ppm)	Background Correction[44] (ppm)
H 362	-0.31 ± 0.08	-0.075 ± 0.062	3.7 ± 0.2	0.022 ± 0.003	0.5 ± 0.11
D 362	-0.58 ± 0.21	0.010 ± 0.024	3.2 ± 0.4	0.036 ± 0.002	-0.07 ± 0.04
H 687	-1.28 ± 0.18	-0.3 ± 0.036	3.7 ± 0.2	0.008 ± 0.007	-0.13 ± 0.63
D 687	-7.0 ± 1.8	-0.1 ± 0.049	3.4 ± 0.4	0.012 ± 0.013	-2.03 ± 0.38

4.2 Cerenkov Efficiencies

Several methods of determining the Cerenkov efficiencies from data were employed in the backward angle phase of G^0. In addition, a model based on the response of the Cerenkov as a function of distance from the PMTs and angle of incidence was developed. As described in Section 3.5, the Cerenkov counter was used in coincidence mode to identify electrons, because below a momentum of 570 MeV/c, the π^- will not produce Cerenkov light in the aerogel [43]. The efficiency of the Cerenkov is a measure of how often it correctly identifies an electron, $\epsilon = N_{cer}/N_{total}$, where N_{cer} is the number of electrons that trigger the Cerenkov and N_{total} is the total number of incident electrons. Because the data are analyzed on a cell-by-cell basis, it is necessary to know the value of the efficiencies in each cell to compare simulation and data yields in the detector matrix. The default method, referred to as the 31 MHz analysis, used time of flight information to independently distinguish pions and electrons. Due to statistical limitations, these efficiencies were only provided in a narrow band around the elastic electron locus. Certain analyses, including the determination of the background asymmetries using the matrix method (see Section 4.5), need the efficiencies in the whole matrix (or at least some cells outside of this band).

4.2.1 Methods of Determining the Efficiency from Data

The data needed to determine the efficiencies were taken during dedicated runs, either with different trigger schemes (requiring different numbers of PMTs to form a hit in the Cerenkov) or with additional information recorded (FastBus data, see Section 3.6). The M2/M3 efficiencies required taking consecutive runs with a requirement of a minimum of 2 PMTs to form a hit in the Cerenkov (M2) or a minimum of 3 PMTs to trigger a hit in the Cerenkov (M3). The ratio of the rates when comparing these two trigger configurations is used to

determine the efficiency. During a 31 MHz run the beam structure is altered to send the electrons in bunches spaced by about 32 ns. The beam on target (BPO) provides a trigger, and the time of flight (ToF) information is recorded by TDCs. Another method (which is not completely independent of the previous method) uses a software trigger rather than a hardware trigger to determine the ToF. A brief description of the three methods follows, for comparison to the geometric model, which will be discussed in more detail in the following section.

31MHz Analysis

The 31MHz analysis, performed by Maud Versteegen, a student at L'Université Joseph Fourier, was used to obtain Cerenkov efficiencies using time of flight (ToF) information for both 362 MeV[140] and 687 MeV[141]. The electrons and pions have ToF spectra that are approximately gaussian around a central value that is separated because the pions have a longer ToF due to their increased mass. A gaussian was fit to each peak to determine the total number of electrons (see the panel on the left of Figures 4.9 and 4.10). In both panels the total rate in the ToF spectrum for each energy is shown in black. On the right panel in each plot are the events identified as electrons (blue) or pions(red) by the Cerenkov. In the spectrum for 362 MeV it is apparent that there are many electrons not being properly identified as electrons. They appear as electron contamination in the pion matrix, or the red bump at lower ToF under the blue electron peak. The efficiency is the ratio of the number of electrons identified by the Cerenkov over the total number determined by the fit. The efficiency and its error vary depending on the choice of upper and lower ToF cuts used in the fits. The cuts were chosen to minimize the errors on the efficiency and the pion contamination.

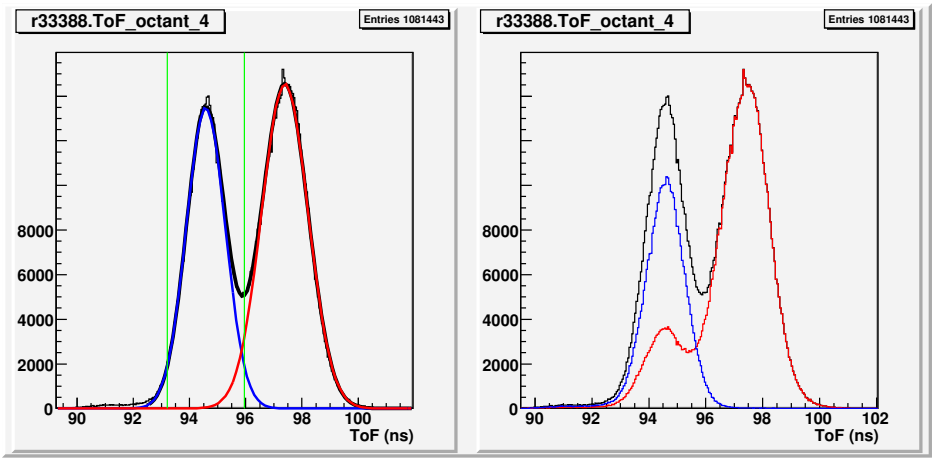

Figure 4.9: 362MeV ToF spectra with the fit results on the left and the Cerenkov pid on the right[140]. The red curves are events identified as pions and the blue are those identified as electrons. Note that the Cerenkov misidentifies some electrons as pions (small red bump in the plot on the right).

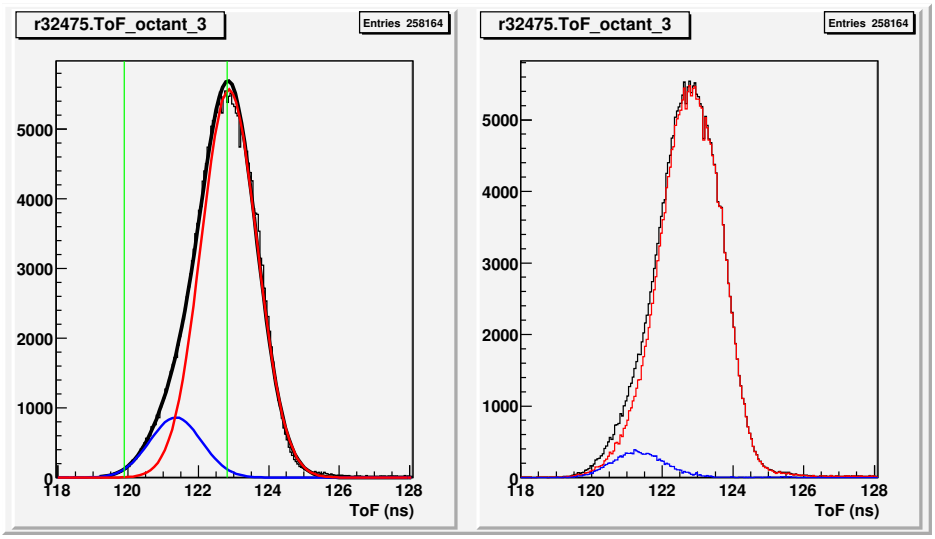

Figure 4.10: 687MeV ToF spectra with the fit results on the left and the Cerenkov pid on the right[141]. Again the red curves are events identified as pions and the blue are those identified as electrons. According to the analysis of the ToF data (left) the cerenkov misidentifies electrons as pions in this energy as well (note the smaller height of the blue peak in the plot on the right).

In the ToF spectra for the 687 MeV data, the pion peak completely overlaps the electron peak (see Figure 4.10). The efficiencies and pion contamination are determined in the same way as the 362 MeV data, except that the 687 MeV efficiencies were with the Cerenkov set to M3 and the 362 MeV efficiencies were for M2. M2 or 3 refers to the minimum number of PMTs in each Cerenkov required to get a coincidence. The M3 efficiencies are smaller due to the increased number of hits required for each event. The analysis was more difficult for this energy due to the large pion rates, but it is still possible to see the effect of the efficiency when comparing the fit result and what the Cerenkov identified as electrons. For this analysis the cuts on the fits were chosen to minimize the error on the efficiency.

ARS Data

The determination of Cerenkov efficiencies from the ARS data, performed by Alexander Coppens, a student at the University of Manitoba, was very similar to that of the 31MHz analysis. The difference is that the Cerenkov trigger was determined in software using the analogue ring sampler (ARS) signals[45]. The ARS consists of a set of 128 capacitors in a ring for each PMT in each Cerenkov, and the signals can be used to determine the number of photoelectrons for each event as well as to form the ToF trigger.

M2/M3 Efficiencies

The so-called M2/M3 efficiencies come from special runs where the data was taken with the Cerenkov set to M2 in one run and M3 in another. The efficiency is determined by comparing the ratio of the probabilities of detecting a photon in two or three PMTs with the ratio of the yields in the M2 and M3 runs. The probability of getting 0 events in a given PMT in a

given time interval is calculated using the Poisson distribution:

$$P_P(x;u) = \frac{u^x e^{-u}}{x!} \tag{4.15}$$

where x = 0. In this formula u is the mean of the distribution of the number of events in a given time interval, or the 'actual' yield, Y_{actual}. From the probability to get 0 photons the probability of getting 1, 2, 3 or 4 PMTs to have at least 1 photon, corresponding to M1, M2, etc. is calculated. The starting value is chosen based on the singles rates in the PMTs and then the value of the mean is increased. When the ratio of the probability of getting at least one photon in each of at least 2 PMTs to that of the probability of getting at least one photon in each of at least 3 PMTs is equal to the ratio of the yields in the M2 and M3 runs, the value of the efficiency is given by $\epsilon_{M2} = Y_{M2}/Y_{actual}$ where

$$\frac{\epsilon_{M2} Y_{actual}}{\epsilon_{M3} Y_{actual}} = \frac{Y_{M2}}{Y_{M3}} = \frac{P(2)}{P(3)} \tag{4.16}$$

Similarly, the efficiency when the Cerenkov was set to M3 can be found from $\epsilon_{M3} = Y_{M3}/Y_{actual}$.

There are a limited number of runs where there was an M2, M3 (and sometimes M4) run taken for the purposes of this analysis. Most of these runs have been analyzed by Herbert Brueur, a professor at the University of Maryland, to get efficiencies in various formats: for the locus in each octant [30], for the whole matrix in each octant, and for each CED/FPD cell in each octant. The full list of runs used in the M2/M3 analysis which have cell-by-cell values are summarized in [99]. Figures 4.11 and 4.12 show all available M2 or M3 efficiencies as a function of FPD for each of the nine CEDs in octant 4, compared to the efficiencies calculated using the default 31 MHz analysis. The same method was used to find the M2 or M3 efficiency, but only one is reported, depending on what the Cerenkov was set to during

normal running at the time. The Cerenkov was set to M3 for a portion of the data in an attempt to reduce the random coincidences caused by neutron capture on the borosilicate phototubes during deuterium running. This was unnecessary during hydrogen running and the Cerenkov was set to M2 after the tubes were replaced with quartz tubes.

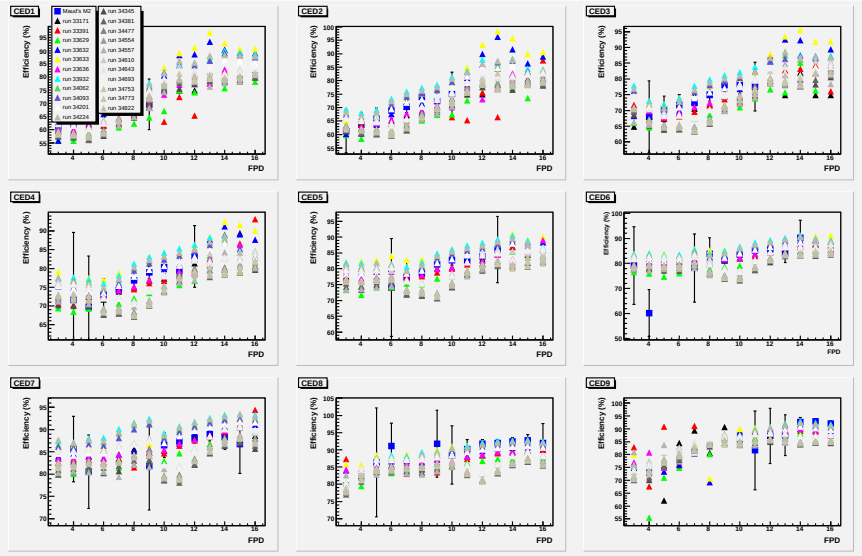

Figure 4.11: Cerenkov efficiencies vs. cell number in octant 4 for all runs where the M2 efficiency was calculated. Both the M2/M3 (Herbert's) and 31 MHz efficiencies (Maud's) are shown. The blue squares are from the 31 MHz analysis, and the data points and errors are hidden by the spread of the data points from the M2/M3 analysis.

4.2.2 Model Based on Geometry

The Cerenkov efficiencies are needed in every cell in the matrix. There is not enough statistics to determine efficiencies using the ToF analysis in cells outside the loci, and the M2/M3 efficiencies varied with time and the shape was expected to be more flat, so the results were not completely understood. An additional method was explored which uses a geometric model of the efficiency, which was fit to the efficiencies in the loci provided by the ToF analysis. The method is described here.

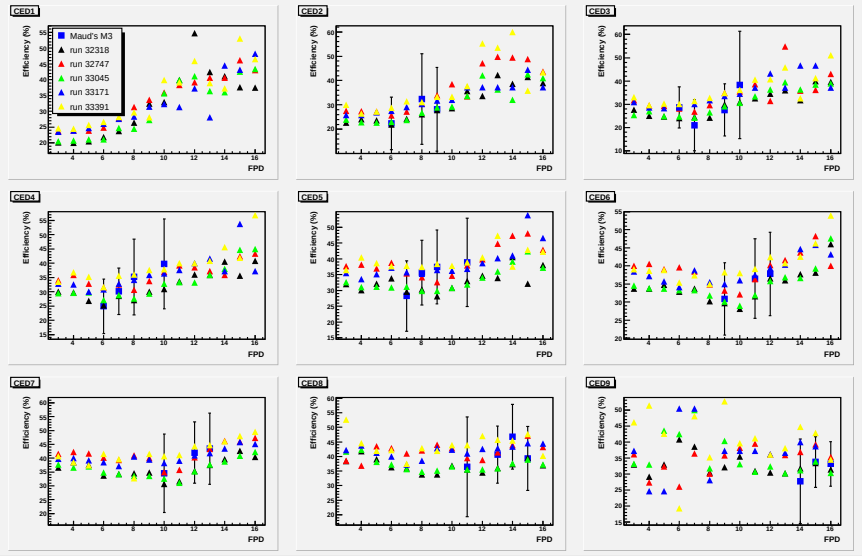

Figure 4.12: Cerenkov efficiencies vs. cell number in octant 4 for all runs where the M3 efficiency was calculated. Both the M2/M3 (Herbert's) and 31 MHz efficiencies (Maud's) are shown. The blue squares are from the 31 MHz analysis, and the data points and errors are hidden by the spread of the data points from the M2/M3 analysis.

The response of the Cerenkov varies as a function of distance from the PMTs and angle of incidence[71]. It is possible to use the simulation to obtain the central angle and distance from the PMT in each CED/FPD cell. In order to obtain an estimate of the efficiencies in each cell, the response of the Cerenkov was parameterized as linear in angle and position, and fit to the efficiencies determined in the 31 MHz analysis (where available) to determine the coefficients. Using the absolute value of the angle provides a better fit, suggesting that the two parameters are actually *distance from the PMT* and *path length* in the aerogel. Whether the track points toward the PMT or not does not seem to matter.

Figure 4.13 shows the M2 efficiencies for each CED as a function of FPD in octant 3, where the blue boxes are from the 31 MHz analysis, the red triangles are from the M2/M3 efficiency analysis, the black circles are from the analysis using the ARS data and the green circles are from the geometrical model in simulation, fit to the 31 MHz efficiencies. Note

that the blue squares do not appear outside of a band around the elastic electron locus, and there are only black circles in a few cells, while both the M2/M3 and model efficiencies have values in every cell. Figure 4.14 shows the M3 efficiencies for each CED as a function of FPD in octant 3 (the model errors are shown as $\frac{1}{10}$ their actual size). A significant amount of production data was taken with the M3 setting for the Cerenkov. There is no ARS data for the M3 efficiencies shown.

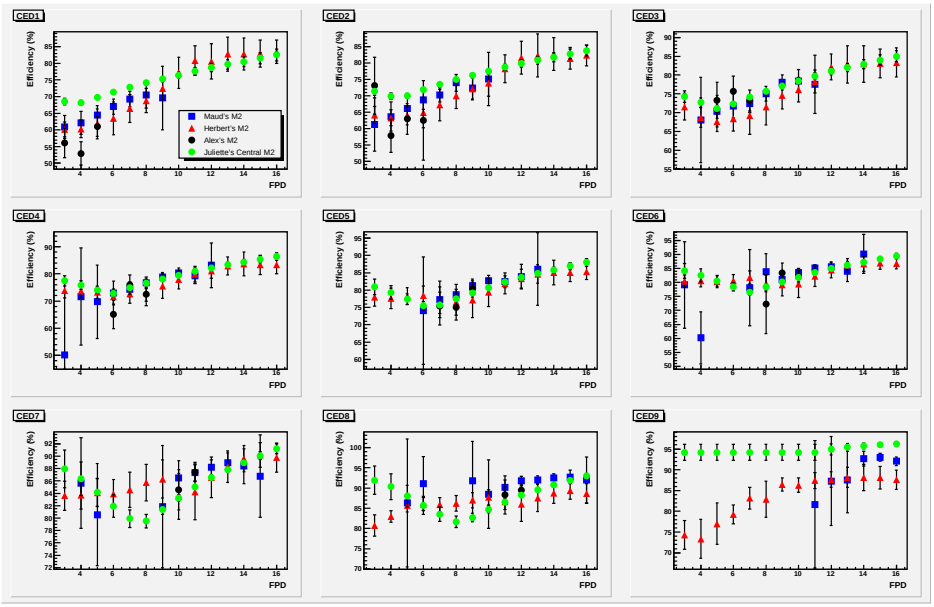

Figure 4.13: Comparing the 4 methods of estimating the Cerenkov efficiency for M2. The green points are the results of fitting the geometric model to the efficiencies determined in the 31 MHz analysis (blue). The resulting shape as a function of FPD explains the behavior of the M2/M3 analysis (red). The black points are from the ARS analysis.

In general all 3 methods of determining the efficiencies from data seem to agree. In addition the model seems to explain some features of the efficiencies in CED/FPD space, such as the deviation of the efficiencies from a constant, or flat, value across the FPDs which was seen in the M2/M3 analysis. It should be noted that in the background asymmetry analysis reported in the final results[105], the Cerenkov efficiencies were not used explicitly in the calculation of the dilutions, but a factor in the fit that comes out is roughly consistent

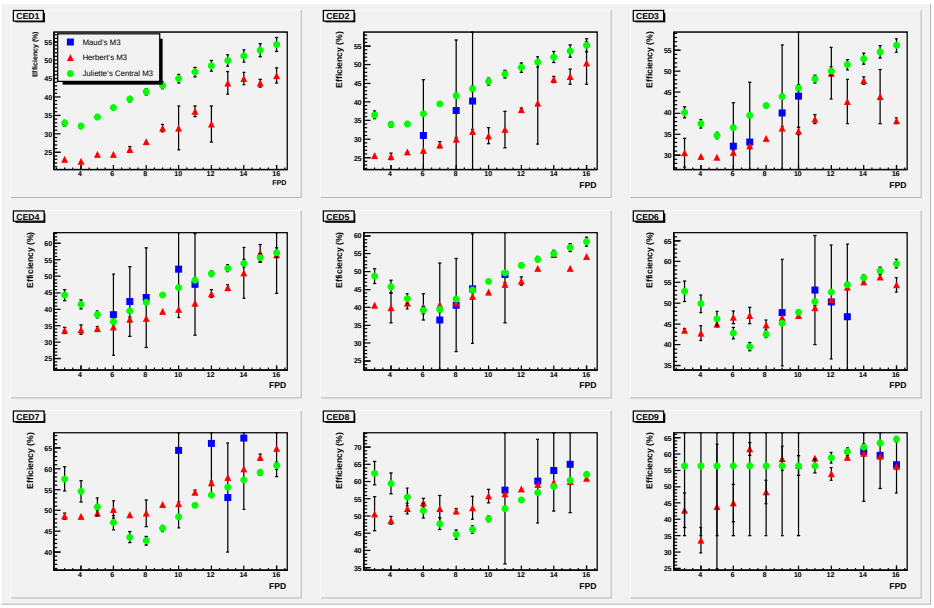

Figure 4.14: Comparing the 4 methods of estimating the Cerenkov efficiency for M3. CED1 does not have any FPDs in the elastic locus. The green points are the results of fitting the geometric model to the efficiencies determined in the 31 MHz analysis (blue). Here the results are not as in good agreement with the M2/M3 analysis (red points) for lower FPDs.

with the efficiencies.

4.3 Q^2 simulations

The quoted precision for the G^0 backward angle Q^2 was 1% (see Table 6.1 in [43]). It is possible to obtain this level of precision by understanding the acceptance of the spectrometer and the detectors. An estimate of the Q^2 and the uncertainties is thus obtained from simulation using the measured energies for the various run periods in the backward angle phase of G^0. The physics asymmetry is proportional to Q^2 (Eq. 1.40) and each of the form factors is a function of Q^2, so it is important to know the value of this quantity and understand the uncertainty in our experiment. In the forward angle it was possible to determine the Q^2 using time-of-flight information[122] but that is not possible in the

backward angle because the ToF resolution is not sufficient, and the 32 ns beam structure was only used for a small subset of the data.

In the backward angle we detect the elastically scattered electrons. Q^2 is a function of the incident energy (see Appendix A), which is measured in the various run periods, and the scattering angle

$$Q^2 = \frac{4E^2 sin^2\frac{\theta}{2}}{1 + \frac{2E}{M_p} sin^2\frac{\theta}{2}} \tag{4.17}$$

which is defined by the acceptance of the collimators, magnetic field and detectors. As stated above, the determination of Q^2 then comes from understanding the acceptances in the experiment. This was done by verifying the positions of the target, collimators and detectors relative to each other in the simulation using hall surveys. In addition, the properly radiated yields from simulation adequately reproduce the measured yields, giving some confidence that the acceptance of the experiment is well understood.

4.3.1 Sensitivity Study

In order to gauge the effects of uncertainties in detector and target position, as well as beam energy and magnetic field, a sensitivity study was performed in simulation. In principle all of the detector positions could have been varied independently (that is each of the 14 FPDs, 9 CEDs and the cerenkov in each octant). In addition there could be effects from having both a misaligned target and a misaligned detector, for example. In the interest of reducing the amount of simulations, five quantities were considered to be the most relevant. Because the three sets of detectors are all mounted on the ferris wheel, the position along the z axis was varied for all of the detectors at once. Similarly the radial position of all of the detectors was shifted together. The target position along the beamline, the incident beam energy and the strength of the magnetic field were also varied, keeping all the other quantities of interest

constant while varying a particular quantity.

For each variable, the locus average Q^2 was calculated for shifts from the nominal value of the quantity, and plots were made of the Q^2 vs. the value of the shift. All of the plots from the study are shown in the Appendix D.4.1. The data were fit with a line and the slope of the line $\partial Q^2/\partial x$ was used to calculate the sensitivity to that quantity assuming that $\Delta Q^2/Q^2 = 1\%$ (see Table 4.2). The units are given by the expected uncertainties, which are shown in the last column. For example, for the H362 MeV case, as shown in figure 4.15, the sensitivity is 5 cm; that is, for this target/energy combination the radial position of the detectors could be misaligned by 5 cm before the mean Q^2 would differ by 1% from the nominal value, while the estimated uncertainty in the radial position of the detectors is only 0.5 cm. The sensitivities to the various quantities are all much smaller than the expected uncertainties in the various quantities, except for the beam energy. The expected uncertainty in the beam energy is close to the sensitivity in Q^2; this number was estimated using the errors on the measured beam energies (see Table 4.3). The spread in the energies from the run starts is smaller, but the central value is different from the measured energies by almost 1 MeV (see Appendix D.4.2).

The effect of a radial shift is perhaps easiest to understand (see Figure 4.15). A negative shift in radius moves the detectors closer to the beamline, thus causing the acceptance to change to higher Q^2, because we are looking at backward angle scattering where the higher angle is at a lower radius. So the slope of the Q^2 with radial shift is negative. A negative shift in the z position of the detectors moves them closer to the target, which is like a shift to higher radius, so the slope of the Q^2 with a shift in z should be positive. A negative shift in target position moves the target upstream. Roughly this should be like moving to a larger radius, or a lower Q^2, so the slope of the Q^2 vs. target shift should be positive. This is not exactly what is happening because the scattered electrons also experience a different

Figure 4.15: Q^2 as a function of a shift in radial position of the detectors for the LH2 362MeV dataset. The slope, $\partial Q^2/\partial R_{det}$,is used to calculate the sensitivity of the Q^2 to the uncertainty in the radial position of the detectors.

field. A shift in magnet current would be proportional to a shift in the field. This would change the radial position of the rays as they exit the collimators. A lower field would be like moving the detectors to a lower radius, or higher Q^2. So the slope of the magnetic field plots should be negative. Shifting the beam energy should result in a positive slope (Eq. A.6). The measured beam energies will be discussed further in Section 4.3.3.

One thing to note is that the nominal Q^2 is about 1% lower in the sensitivity plots than the quoted numbers. This is because the simulations for the study were run with the incorrect eloss. This will be discussed in more detail in Section 4.3.2. It is assumed that the slope of the plots would be unaffected.

Table 4.2: Q^2 sensitivities assuming $\frac{\Delta Q^2}{Q^2} = 1\%$.

x	**362 LH2**	**362 LD2**	**687 LH2**	**687 LD2**	Δx
z_{det}	19	18	23	10	1.0cm
r_{det}	5	3	8	5	0.5cm
z_{tar}	5	4	10	6	0.5cm
E_{beam}	2	2	4	5	1.0MeV
$BFIL$	6	23	7	16	1.3%

4.3.2 Radiative Effects

The radiative correction is applied to the asymmetries and not to the yields. This brings up the question of how to get the "unradiated" Q^2 from the simulation. If one uses a simulation with no radiative effects, then the yield distribution will not be the same as that of the experiment. So one could, in principle, use the "tree level" Q^2 from a fully radiated simulation, where the yield distribution would be more similar to that of the experimental yields, so the averaging over the locus would be more similar. It turns out that the difference between the Q^2 in these two cases is about 0.4% (see Figure 4.16). The proposal is to use the "unradiated" Q^2 with an error bar of 0.4% to make it consistent with the "tree level" Q^2 from a fully radiated simulation. These are the numbers reported in Table 4.3.

The "unradiated" Q^2 was obtained by performing a simulation using eloss_rad with the external, internal and ionization radiation turned off, which has the energy loss before the scattering vertex, but turns off the radiative effects during the scattering. The "tree level" Q^2 was obtained by using the full radiative correction but calculating the Q^2 from the pre-radiated angle and scattered electron energy. The yield distributions in these two cases will be different because when the full radiation is turned on the angle and the energy of

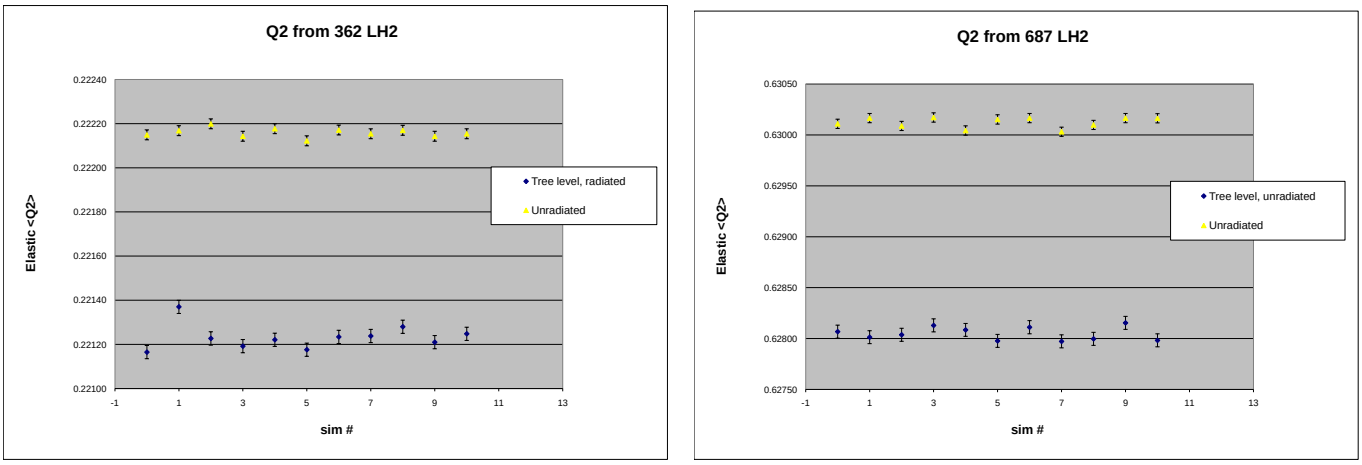

Figure 4.16: Comparing "unradiated" and "tree level, radiated" Q^2 for the 362 (left) and 687 (right) MeV hydrogen simulation. In both cases the 'tree level, unradiated' Q^2 is about 0.4% lower than the Q^2 obtained from the simulation with no radiation. Multiple simulations were performed to check for fluctuations outside of the calculated uncertainties, and to gain higher statistical precision.

the scattered particle are different. This is the case that is more similar to what is really happening in the experiment, but it is the "tree level" Q^2 that is of interest in the calculation of the form factors.

4.3.3 Q^2 for Measured Beam Energies

The final numbers for the mean Q^2, "center of target energies" and uncertainties are presented in Table 4.3. The Q^2 and center of target energy values come from simulations at the measured beam energies for each run period. The additional uncertainty in the center of target energy that comes from the error on the energy loss is negligible. The uncertainty on the Q^2 does not include the systematic uncertainty from an energy variation because that error is included elsewhere in the calculation of the uncertainties on the form factors. It does, however, include a systematic uncertainty that takes into account the other Δx numbers

reported in the last column in Table 4.2. For the high energy running periods the energy was measured by Mark Jones using the Hall C arc method, which measures the dispersion in the arc in the beamline as it bends to enter Hall C. Relative energy measurements are made continuously using the dispersion in a single beam position monitor and automatically stored in an electronic log at the start of each run. For the low energies Hall A provided a measurement for the Summer '06 run period based on measurements using the two Hall A spectrometer arms. They were unable to perform this analysis for the Winter '07 run period, so that energy was obtained by scaling the ratio of the energies from the run starts for the two periods (see Figures D.17 and 4.17). The uncertainty on the Winter '07 energy reflects the error due to this scaling.

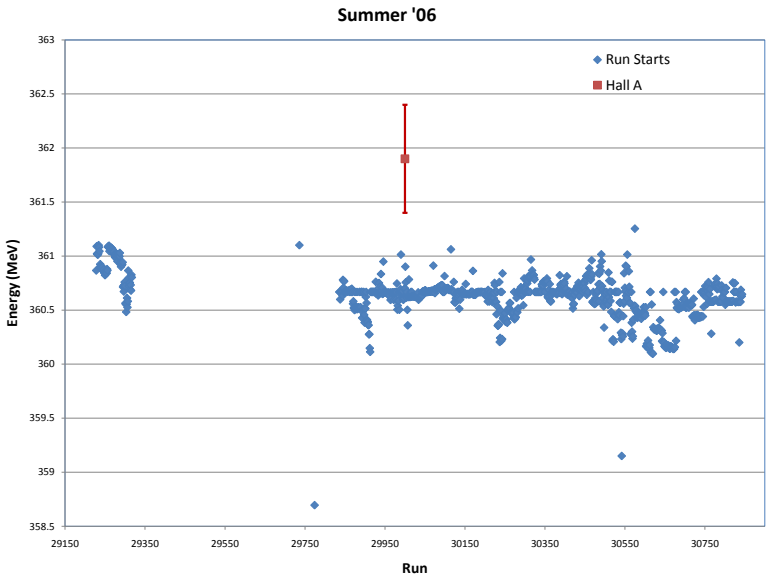

Figure 4.17: Energy from run starts vs. run number with measured energy at approximate time in the Summer '06.

Table 4.3: Q^2 Summary; errors include 0.4% model uncertainty (Section 4.3.2).

Run Period / Date	**Target / Energy**	**Systematic Error (%)**	**Beam Energy (MeV)**	**Energy (MeV)**	**Q^2 ($\frac{GeV^2}{c^2}$)**
April 17, 2006	LH2 / 687	0.21	685.57 ± 0.92	682.45 ± 0.92	0.6275 ± 0.003
Summer 2006	LH2 / 362	0.27	361.90 ± 0.50	358.75 ± 0.50	0.2217 ± 0.001
Sept. 27,2006	LH2 / 687	0.27	684.86 ± 0.92	681.74 ± 0.92	0.6264 ± 0.003
Dec. 19, 2006	LD2 / 687 (M2)	0.19	689.61 ± 0.93	686.07 ± 0.93	0.6300 ± 0.003
Dec. 19, 2006	LD2 / 687 (M3)	0.19	689.61 ± 0.93	686.05 ± 0.93	0.6287 ± 0.003
Winter 2007	LD2 / 362	0.22	363.05 ± 0.66	359.51 ± 0.66	0.2193 ± 0.001
March 14, 2007	LD2 / 687	0.19	689.42 ± 0.93	686.87 ± 0.93	0.6299 ± 0.003

4.4 Transverse Correction

The transverse asymmetries are a parity-*conserving* asymmetry that arises due to the interference of 2γ exchange with that of a single photon[114], and this beam normal single spin asymmetry can be written as in equation 1.45. For an arbitrary polarization, the measured asymmetry has a component from the parity-violating (longitudinal) asymmetry and the parity-conserving (transverse) asymmetry. In order to separate the contributions, it is necessary to measure the asymmetry at the two different polarization directions. In practice the measurement is made when the beam is essentially longitudinal, and then in a mode where it is essentially transverse, and the contributions to the parity-violating and conserving asymmetries (A_{PV} and $\epsilon(\phi)$ respectively) can be written [78]

$$A_{PV} = \frac{cos\beta}{P_{\parallel} cos(\alpha-\beta)} A_m^{\parallel} - \frac{\sin\alpha}{P_{\perp} cos(\alpha-\beta)} A_m^{\perp}(\phi)$$

$$\epsilon(\phi) = \frac{\sin\beta}{P_{\parallel} cos(\alpha-\beta)} A_m^{\parallel} + \frac{cos\alpha}{P_{\perp} cos(\alpha-\beta)} A_m^{\perp}(\phi) \tag{4.18}$$

where $P_{\parallel}$ and $P_{\perp}$ are the values of the polarization and $A_m^{\parallel}$ and $A_m^{\perp}$ are the asymmetries measured during the longitudinal and transverse running modes, respectively.

In the case of the G^0 backward angle running the polarizations in each mode are approximately equal[60] (only the directions are different), so we take $P_{\parallel} \approx P_{\perp}$. $\alpha = \theta_{spin}$ and $\beta = \theta'_{spin} - \frac{\pi}{2}$ are the angles that the spin is different from purely longitudinal or purely transverse during those modes, and $A_m^{\parallel}$ and $A_m^{\perp}$ are the measured longitudinal and transverse asymmetries. Thus we have:

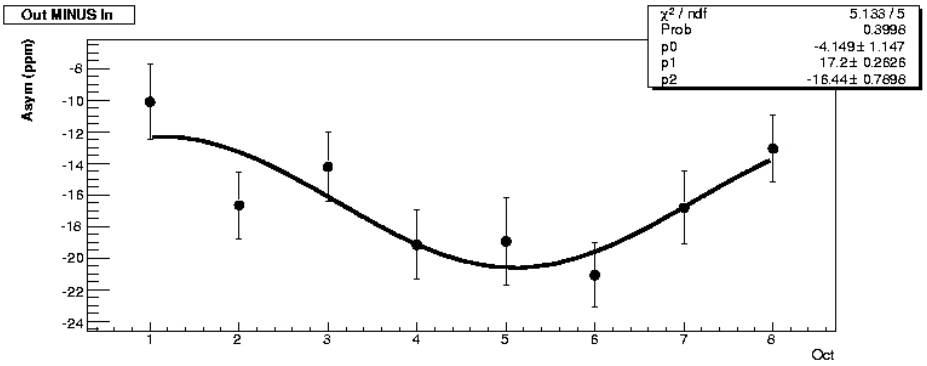

Figure 4.18: The uncorrected D362 longitudinal asymmetry, fit with a sinusoidal fit where the amplitude, offset and the phase free to vary. This dataset had one of the largest transverse components of the polarization during normal running and a large transverse asymmetry, causing a noticeable octant dependence in the longitudinal data.

$$A_{PV} = \frac{1}{Pcos(\alpha-\beta)}(A_m^{\parallel} cos\beta - A_m^{\perp}(\phi)\sin\alpha)$$

$$\epsilon(\phi) = \frac{1}{Pcos(\alpha-\beta)}(A_m^{\parallel}\sin\beta + A_m^{\perp}(\phi)cos\alpha) \tag{4.19}$$

where ideally the parity-violating asymmetry, A_{PV} is not a function of ϕ because the transverse component of the beam during longitudinal running is zero. So, for example, if the spin were perfectly aligned in each mode, then α=β=0, and you would only need to correct the measured longitudinal asymmetry, $A_m^{\parallel}$ for the measured polarization, and similarly for the transverse asymmetry. In practice α and β are small, but not necessarily zero, as shown in Figure 4.18. Based on the size of the transverse component in that dataset and the size of the uncorrected transverse asymmetry for that target/energy combination, the expected value of the amplitude of the sine fit in the longitudinal data is 3.26 ppm, compared to the fit value of 4.15 $\pm$ 1.1 ppm, which is in rough agreement.

The in-plane polarization direction is determined by the Wien angle setting, and the

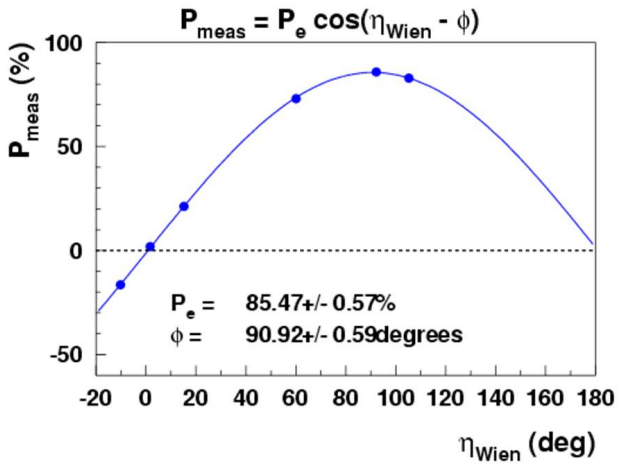

Figure 4.19: Spin dance for 687MeV run period in October 2006[36]. The location of the maximum of the curve indicates the Wien setting for optimum longitudinal polarization, and the zero crossing the optimum setting for the transverse polarization.

out-of-plane component is expected to be small (see Appendix D.7). In order to determine the optimal Wien angle setting, the magnitude of the longitudinal polarization is measured at various Wien angle settings (a *spin dance*). Because the Møller polarimeter only measures longitudinal polarization, the deviation from the maximum polarization ($\sim 85\%$) indicates the size of the transverse component of the beam. Figure 4.19 shows the spin dance for 687 MeV done in October 2006. The maximum polarization is at a Wien angle setting of 90.92°. The polarization crosses zero at about 1.7°, so this would be the ideal setting for the transverse running. A table of the actual Wien angle settings for each run period is given in the Appendix D.6.

In G^0 the transverse asymmetry has a sinusoidal dependence on octant number because of the relationship between the polarization vector and the normal to the scattering plane, as discussed in Section 1.2.4. The measured transverse asymmetry can be written as

$$A_m^{\perp} = \frac{\sigma_{\uparrow} - \sigma_{\downarrow}}{\sigma_{\uparrow} + \sigma_{\downarrow}} = A_n \vec{p}_e \cdot \hat{n} = -A_n \sin(\phi + \phi_o) \tag{4.20}$$

where A_n is the beam normal single spin asymmetry. The angle of the spin out of plane, ϕ, is defined as being zero to beam left when looking downstream, see Figure 4.20b. In the backward angle running, octant 3 is in the beam left position, then clockwise from beam left is 2, 1, 8, 7, 6, 5, and 4 (see Figure 4.20a and b).

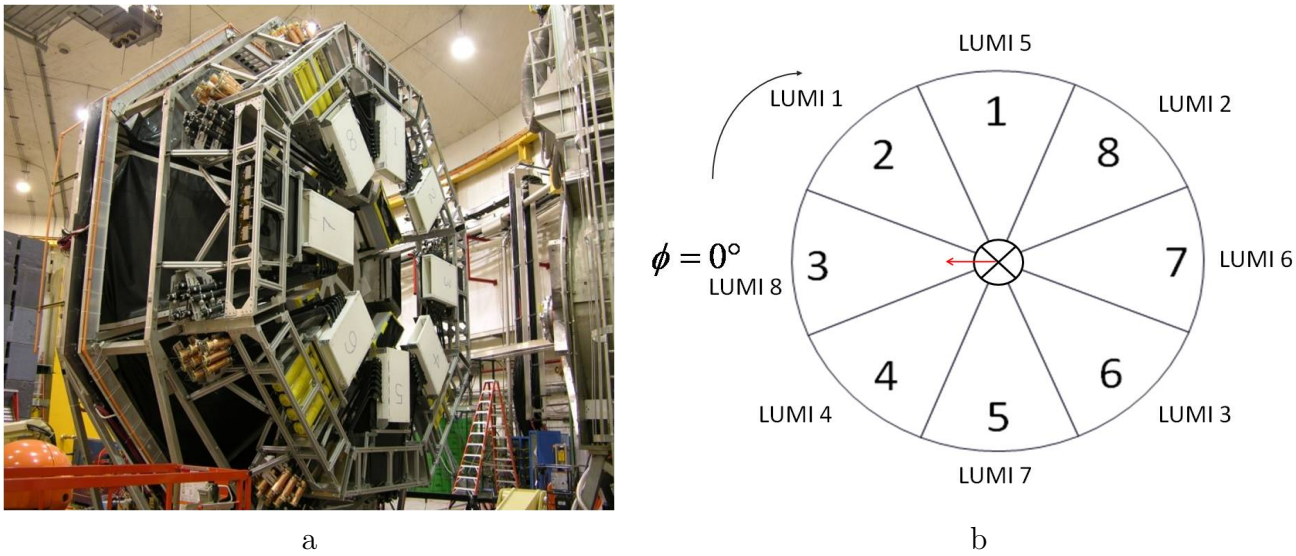

a b

Figure 4.20: View of the ferris wheel looking upstream; the octants are numbered on the cerenkov boxes (a). The octant definition relative to ϕ in the backward angle running, looking downstream (b).

4.4.1 The A_T During Longitudinal Running

In the limit of perfectly symmetric detectors the contribution from any transverse component would disappear when we look at average of the octants, even if it is large. If the detectors are not perfectly symmetric then the transverse component can give an additive correction

to the measured parity-violating asymmetry

$$K_T = A_T \frac{P_T}{P} A_S \tag{4.21}$$

where A_T is the amplitude of the transverse asymmetry $\epsilon(\phi)$ and $\frac{P_T}{P}$ is the relative transverse polarization in the longitudinal running[78]. It is necessary to measure the magnitude of the transverse asymmetries in the detectors in order to estimate the size of the correction. In addition, an estimate must be made of the size of the detector asymmetry, A_S (see Section 4.4.2).

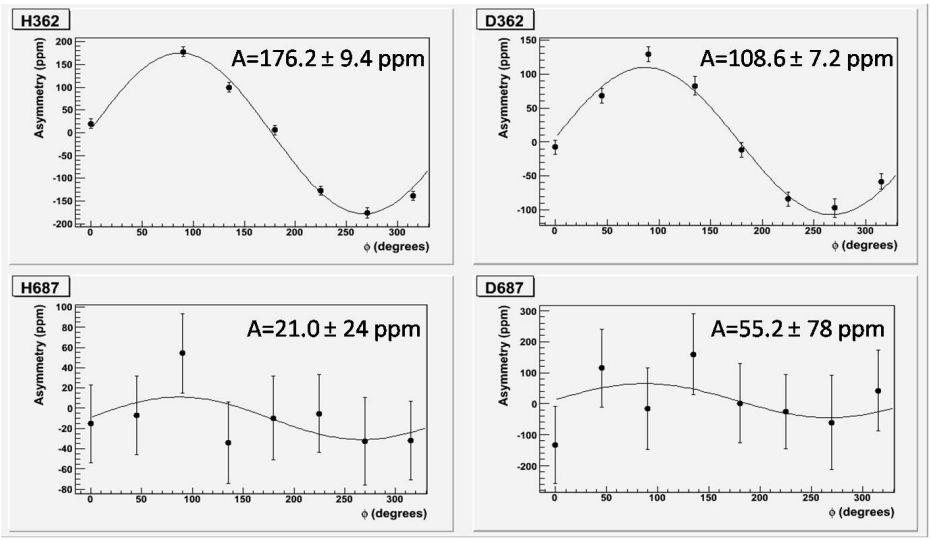

Figure 4.21: The background asymmetry corrected electron transverse asymmetries, vs. ϕ. The corrections to the transverse asymmetries are discussed in Section 4.6.

In order to measure the size of the transverse asymmetries dedicated transverse runs were taken for each target energy combination for a total of about 50 hours of beam. The fully corrected transverse asymmetries for each dataset are shown as a function of ϕ in Figure 4.21. The magnitude of the transverse asymmetry is the beam normal single spin asymmetry. In order to determine the size of the transverse asymmetries in the luminosity

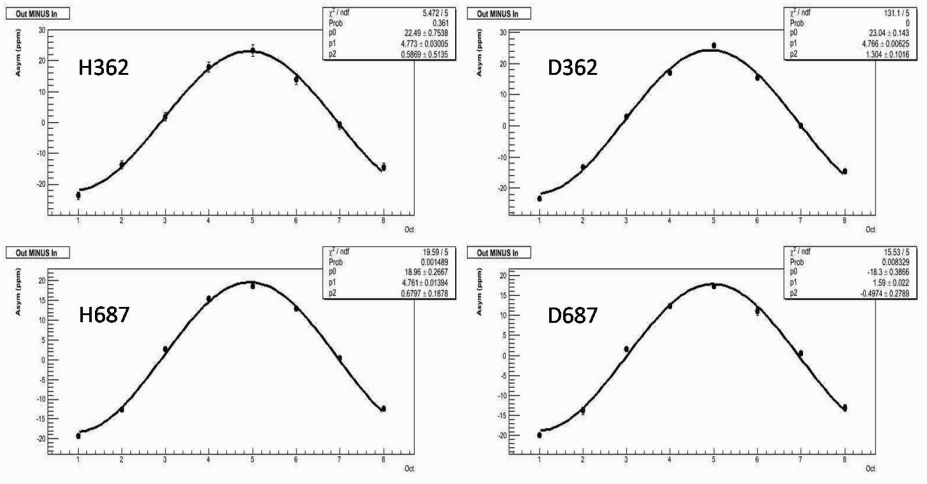

Figure 4.22: The raw luminosity monitor asymmetries during transverse runs, vs. octant. This amplitude is needed in order to estimate the component of transverse polarization in the longitudinal running, from P_T/P=$A_{L,lumi}/A_{T,lumi}$.

monitors (see Figure 4.22) the asymmetries as a function of octant number are fit with a sinusoidal function which allows the amplitude, phase and offset to vary. The amplitude of the fit is the value of the transverse asymmetry $A_{T,lumi}$ in the luminosity monitors. The analysis of the detector asymmetries is discussed in more detail in Section 4.6.

It is possible to see the sinusoidal variation caused by a large enough transverse component of the beam in the data (see Figure 4.18), and in the luminosity monitors (see Figure 4.23) (even when it is not visible in the main detector data) because they have such high rates. The amplitude of the transverse asymmetry in the luminosity monitors during longitudinal running $A_{L,lumi}$ is determined from the amplitude of a sinusoidal fit as in the transverse data. See Figure 3.7 for a description of the LUMI layout relative to the main detectors (note that the LUMI monitors need to be properly ordered in order to match the octants). The ratio $\frac{P_T}{P}$, the relative transverse polarization in the longitudinal running, can be found by comparing the amplitudes of sine fits for the LUMIs in longitudinal and transverse running $A_{L,lumi}/A_{T,lumi}$. The sign of the asymmetry depends on whether the transverse component

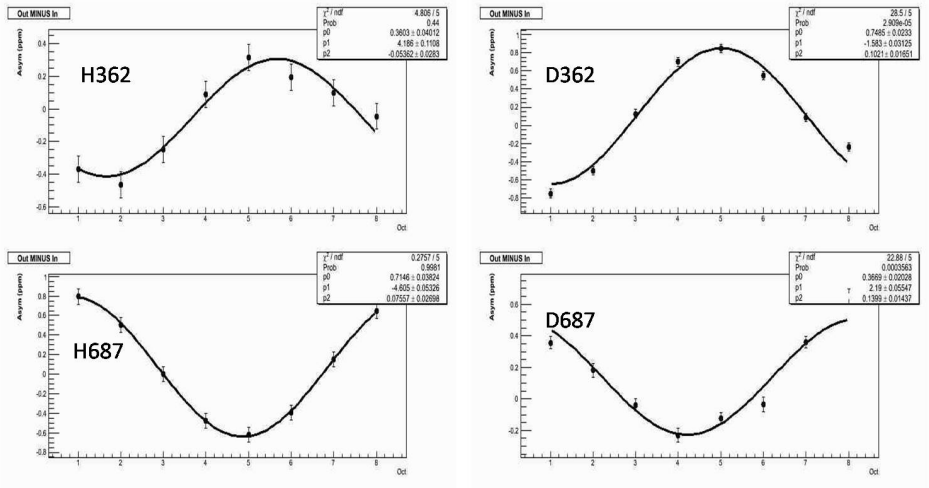

Figure 4.23: The raw luminosity monitor asymmetries during longitudinal runs, vs. octant. The statistical uncertainty is small because the luminosity monitors experience such high incident rates.

is to beam right or beam left. The phase in the low energy hydrogen longitudinal data indicates an out-of-plane component to the transverse polarization, which is not an issue for the longitudinal data (assuming the detector asymmetry is small, see Section 4.4.2). The LUMI transverse and longitudinal amplitudes are summarized in Table 4.4, along with the main detector transverse asymmetries and the size of the transverse correction for each dataset.

4.4.2 Correction or Uncertainty?

In order to estimate the size of the additive correction, K_T, to the measured longitudinal asymmetries due to a transverse component in the beam polarization, it is necessary to know the size of the detector asymmetry, A_S. An estimate can be made using the variation in the yields from octant to octant [117], for example, as shown in Figure 4.24. The variation is about $\pm 6\%$ around the mean yield. If you assume that all of the variation comes from a difference in the scattered electron angle (surely an overestimate) then you can make

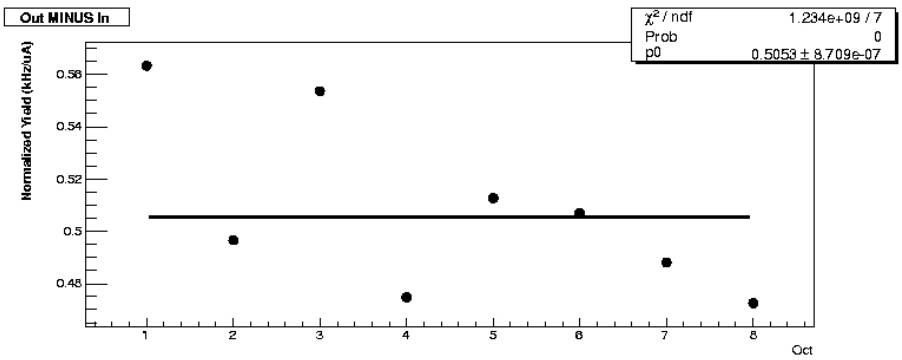

Figure 4.24: An example of the octant to octant yield variation in the D687 dataset.

an estimate about how much the transverse asymmetry would vary from octant to octant. Figure 4.25 shows a prediction for the magnitude of the transverse asymmetry for various energies as a function of lab scattering angle by Pasquini and Vanderhaeghen[114]. This theory closely matches the available data for backward angles [98]. The estimate of the variation of the cross section with angle is $\frac{1}{\sigma}\frac{d\sigma}{d\theta} \sim 4\%/degree$. From the theory plot it can be estimated that the variation of the asymmetry with scattering angle $\frac{1}{A}\frac{dA}{d\theta} \sim -0.76\%/degree$ for 300 MeV and $\sim +0.16\%/degree$ at 570 MeV. The estimate of the detector asymmetry was made assuming a 6% variation in the yields around the mean, or $\frac{1}{4}\times 6\% \sim 2\%$ (taking the variation of the asymmetry with angle as the larger of the two target energies ($\sim 1\%/degree$).

4.4.3 Summary

For the purposes of the transverse asymmetry correction, what really matters is an asymmetry between opposite octants. In order to actually apply a correction, it would be necessary to know the nature of the detector asymmetry, and there is no reliable way to determine this from the data. Differences in yields from octant to octant could be for any number of reasons, some of which would be relevant to this detector asymmetry, such as a misplacement

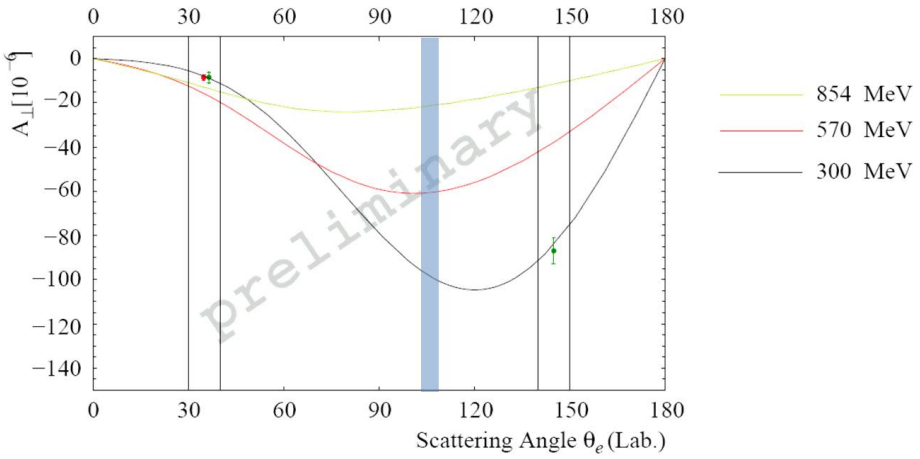

Figure 4.25: Theory calculation at different energies vs. lab scattering angle used to estimate the dependence of the asymmetry on the lab scattering angle[114]. The datapoints are from preliminary PVA4 measurements (two at forward angles, one at a backward angle). The colors on both the datapoints and curves correspond to the incident beam energy. The blue band shows the approximate scattering angle of the G^0 backward angle measurements.

in radius or an actual variation in the magnetic field. Or the thresholds for the detectors could be different in that octant which would not be a detector asymmetry. Conversely there are effects that would impact the detector asymmetry but would not be reflected in the yields, such as a misplacement of the detectors in phi. More subtle would be a difference in the statistical contribution from octant to octant, which would affect the weighting of the asymmetries in an octant dependent manner. The use of the estimate of the detector asymmetry, A_S, using the variation in the yields from octant to octant is meant to provide an upper limit on how big the transverse correction could be (see Table 4.4). The transverse component of the longitudinal polarization is small ($< 4\%$), and because the detector asymmetry is also small ($< 2\%$), the transverse correction is very small. Because the nature of the detector asymmetry is not understood, the 'transverse corrections' are not actually used as corrections, but are included as an additional systematic uncertainty.

Table 4.4: Summary of the magnitude of the transverse correction in each dataset, assuming a detector asymmetry of 2%.

Dataset	A_L^{lumi} (ppm)	A_T^{lumi} (ppm)	P_T/P	A_T (ppm)	K_S (ppm)
H362	0.36 ± 0.04	22.5 ± 0.8	0.016	-176.2 ± 9.4	0.056 ± 0.007
D362	0.75 ± 0.02	23.0 ± 0.1	0.033	-108.6 ± 7.2	0.071 ± 0.005
H687	0.71 ± 0.04	19.0 ± 0.3	0.037	-21 ± 24	0.016 ± 0.018
D687	0.37 ± 0.02	18.3 ± 0.4	0.020	-55.2 ± 78	0.022 ± 0.032

4.5 Background Asymmetry Correction

In the field scan method of determining the background asymmetries (see Section 4.1.5), there is much more information about the yields in each cell because as the field changes the focus of the various processes changes and the peaks are 'swept' across the matrix. There are not enough data to fit the asymmetries in the field scan method, so the alternate method described here, called the 'matrix method' is used as a cross-check on the high energy hydrogen data. It is a two step process - a fit to the yields to determine the dilutions and then those dilutions are used in a fit to the asymmetries to determine the background asymmetry correction. The simulated processes in both methods include (quasi-)elastic scattering from hydrogen (or deuterium), inelastic scattering from hydrogen (or deuterium), and quasi-elastic scattering from the aluminum endwindows (included in this is quasi-elastic scattering from the helium in the helium cell as well). The negative pions (which are only relevant at this energy in deuterium) are estimated from the measured pion contamination, which is about 5%[45]. At this energy there is a non-trivial negative pion rate which generates delta rays or 'knock-on' electrons with significant enough momentum to cause the Cerenkov to fire. The neutral pions refer to charged particles detected in a simulation of the decay of neutral pions in the simulation, referred to as dalitz scattering. In the matrix method, there is only one yield (or asymmetry) in each cell, but the simulation provides estimates of the various asymmetries which are then fit to the measured asymmetry.

4.5.1 The Matrix Method

The term 'matrix' used previously in this thesis refers to the compact way the data are represented as a color-coded plot over CED/FPD space, where the color represents the yield, the asymmetry or some other quantity of interest (see Figure 3.8, b). Here it refers

to the fact that a matrix solution to a least squares fit is used to estimate the dilutions and background asymmetries. Early attempts to fit the yield data in each CED as a function of FPD proved difficult because while the kinematic dependence of the yields is apparent, it doesn't necessarily have an easily definable shape (see Figure 4.26). A suggestion was made to attempt to fit the simulation yields to the data yields in each cell in the coincidence matrix directly without resorting to functional forms, that is, scale the simulation yields directly instead of fitting them first. This is accomplished by treating the problem as a matrix equation and finding the matrix solution to a least squares fit, where the scale factor on each process is assumed to be the same in each cell.

This method is described by Bevington as "the more elegant and general matrix method for solving the multiple regression problem"[25]. The term 'matrix' now refers to an $N \times n$ matrix where n is the number of data points, and N is the number of parameters used in the fit. This method is useful when the fit function(s) can be linearized. If the function cannot be linearized (if a parameter appears in an exponent, for example) then other methods, such as the gradient search method, may be required. If all of the parameters of the fit are simple coefficients of functions of the independent variable, x, then this method provides the exact solution to the least χ^2. A benefit of this method is that in the process of solving the matrix equation the error matrix naturally falls out, which provides not only the variances on each of the coefficients, but also the covariances. It involves the calculation of the pseudo-inverse, because in general the resulting system of linear equations is over-determined, that is, results in a non-square matrix. The method is described in more detail in Appendix C.

4.5.2 Dilutions

The background corrections will be performed on a cell by cell basis in each octant, then averaged over the locus, then the octant-by-octant locus averages will be further averaged to form the final correction[1]. The cell-by-cell dilutions are calculated as the difference in the total scaled yield minus the scaled elastic yield over the total yield:

$$f_{bkgd_i} = \frac{Y_{scaledsim,total_i} - Y_{scaledsim,ela_i}}{Y_{scaledsim,total_i}} = 1 - f_{ela_i} \tag{4.22}$$

where f_{bkgd_i} is the fraction of the total yield in cell i that comes from background processes. The "inelastic dilutions" are calculated in a similar way, where the elastic yield is now part of the background and the inelastic rate is subtracted from the total (see Figure 4.27). In this method it is necessary to fit each individual simulated process, so in the end there is a yield fraction for each. The term dilution refers to the fraction of the total yield that comes from backgrounds, and the algebra of the yield fractions, which are sometimes called dilutions, has some interesting properties, for example:

$$f_{bkgd} = f_{ine} + f_{Al+He} + f_{pi0} \tag{4.23}$$

where $f_{process} = Y_{scaledsim,process}/Y_{scaledsim,total}$ and the fraction of the background yield of each process is

$$f'_{process} = f_{process}/f_{bkgd} \tag{4.24}$$

where the i subcripts have been dropped. It should be noted that the field scan method does not work well in the inelastic region, and although the matrix method provides estimates of the dilutions in that region, a more careful analysis is being pursued to determine the

[1]All of the plots and tables shown here are for fits on the octant average yields and asymmetries unless otherwise stated.

'inelastic dilutions'.

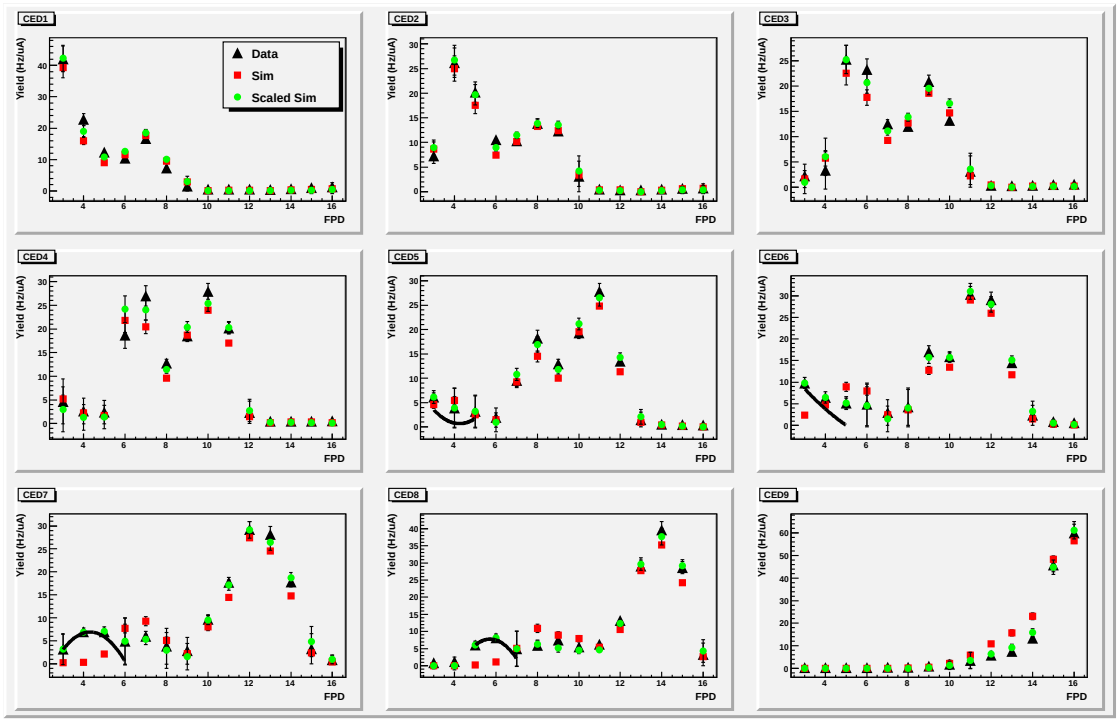

Figure 4.26: Comparison of the data yields (black) with the unscaled simulation (red) and the simulation from the fit (green). There is an elastic and inelastic peak in each CED except for CEDs 1 and 9, where the inelastic and elastic peaks are at the edges of the acceptance. The black curves in CEDs 5-8 are artificial rates put in to provide a simulated rate in certain low FPDs where none of the simulated processes have any rate. The elastic cells are in general far from the bumps, the origin of which is not understood.

In order to calculate the background asymmetry we need to know the yield fraction of each of the individual processes that contributes to the total asymmetry. The yields for each of the individual processes from the simulation are shown in various plots in Appendix D.5.1. Figure 4.26 shows the result of the fit (green) compared to the data (black), in addition to the unscaled sum of the simulations (red). The total data yields here are with corrections

for deadtime/randoms, the scalar counting error and linear regression. It is interesting to note that the unscaled sum of the simulations (red) does a fairly good job of reproducing the total yield (with the exception of several low FPDs in each of CEDs 5-8). So we expect the scale factors on each simulation process to come out close to 1. In several of the CEDs there is a yield in low FPDs such that there is no simulation yield that could possibly reproduce those rates. In order to perform the fits a completely artificial quadratic fit to the yields was added in those cells, and the results are shown as black lines. They do not extend under the elastic peak, and those cells do not appear in either the elastic or inelastic loci (see Appendix D.5.1 for more detail).

There were several variations that were studied including varying the number of parameters in the fits, using the empty target data instead of the simulation for the aluminum yields (or allowing the simulated aluminum and helium yield to vary independently), comparing various error "schemes", and varying the magnetic field of the simulation. The results of these studies are summarized in Appendix C (see Table C.2). The default is to use a 16 parameter fit with a "flat error" (determined by optimizing the χ^2/ndf) with the simulation error used to inflate this error going into the fit. The parameters are the scale factors on the elastic, inelastic, combined simulated aluminum and helium, and pi^0 yields, plus 12 parameters necessary for the quadrature fits in the 4 CEDs (3 parameters each) with the yields in low FPDs. The value of the error of $1.0Hz/\mu A$ per cell yields is estimated by finding the error that gives a reduced $\chi^2 \approx 1$ (this is equivalent to a 1.6% error on the highest yield cell) and the coefficient on the elastic asymmetry is essentially 1 in this case. Note that the number of degrees of freedom is the number of cells minus the number of parameters in the fit (126-16) so the χ^2 in each cell should be close to 1 (see Figure C.1).

In order to study the effect of varying the magnetic field, the default fit is used for various field settings, and the error is kept the same in order to compare the quality of the

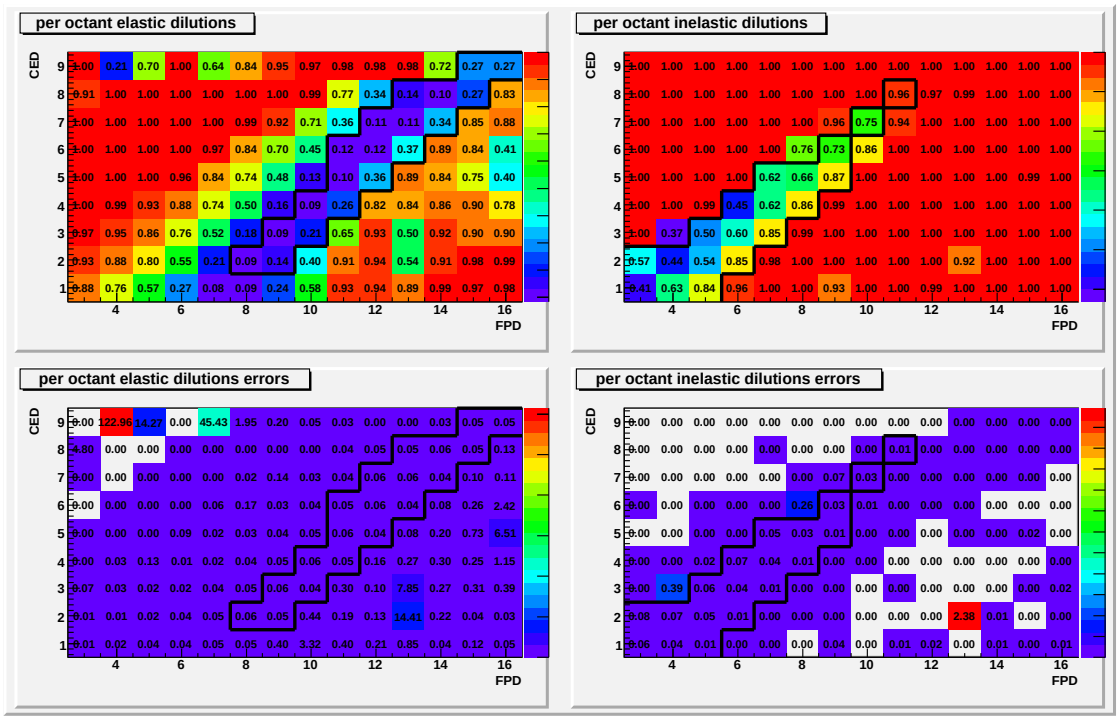

Figure 4.27: The elastic (left) and inelastic (right) dilutions (top) and errors (bottom) in the matrix. The electron locus is outlined in each case.

fits. When the fit was performed on each octant individually it became apparent that there was a variation in not only the fit coefficients octant to octant but on the calculated value of the background dilution as well (see Figure 4.28). The variation in the f_{bkgd} values vs. octant when the nominal field setting is used in all octants is well outside the error bars. This seems to be a similar effect to that seen in the field scan method, in that it seems to be at least partially explained by differences in the fit as a function of simulated magnetic field. The yield fit was performed with 3 different magnetic field settings in each octant, and the one with the best reduced χ^2 in that octant is the one that is used. The nominal field

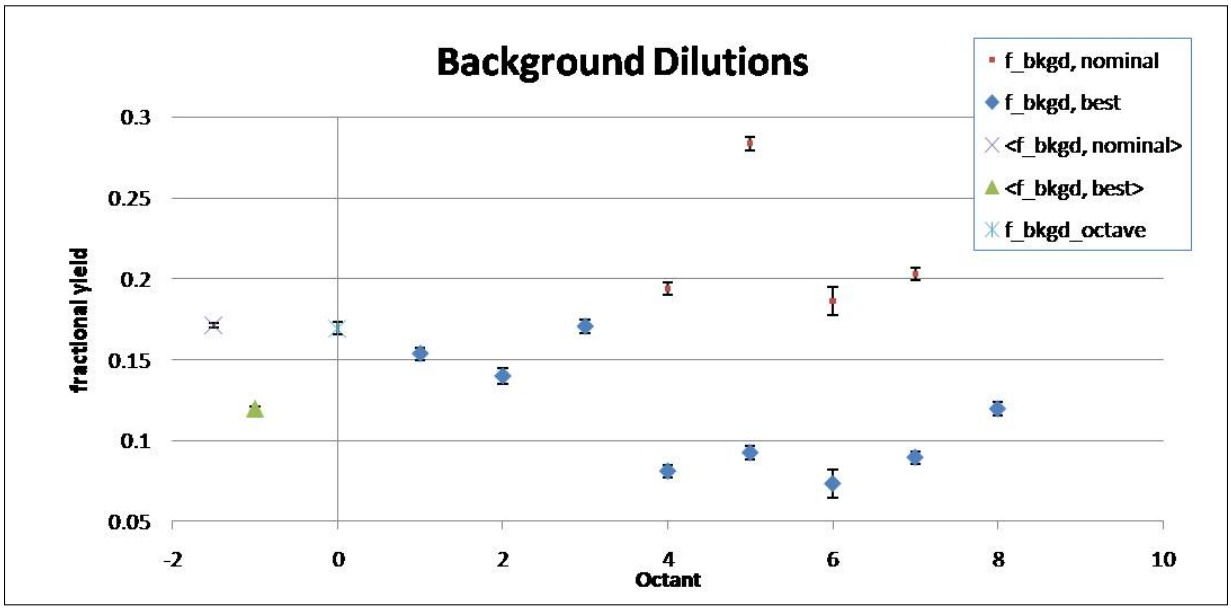

Figure 4.28: The background dilutions vs. octant for the case where all octants are with the nominal field, and the case where the fit with the best χ^2 in each octant is used (best), and the averages.

as well as 2.5% and 5% lower fields were used. Also taken into consideration was a reduced χ^2 in each of the elastic and inelastic loci (each containing 19 cells) where the number of parameters used in the calculation is 4 instead of 16 (none of the cells with quad fits appears in either loci). The settings with the best reduced χ^2 over the whole matrix are also the best compromise of elastic and inelastic loci values as well.

When the 'best fit' values of the magnetic field are used in each octant, the variation in the magnetic field setting is comparable to what is seen in the 'official method'. The largest variation is in octant 5, where a 5% lower field is needed (the scale factor from the field scan method is 5%). In addition, the largest source of background is the aluminum yield, and it is the scale factor on this simulated yield that seems to influence the χ^2 the most in the fits. 'Empty target' yield data were taken in which the target was filled with cold hydrogen gas instead of liquid hydrogen in order to measure the rate from the aluminum in the target

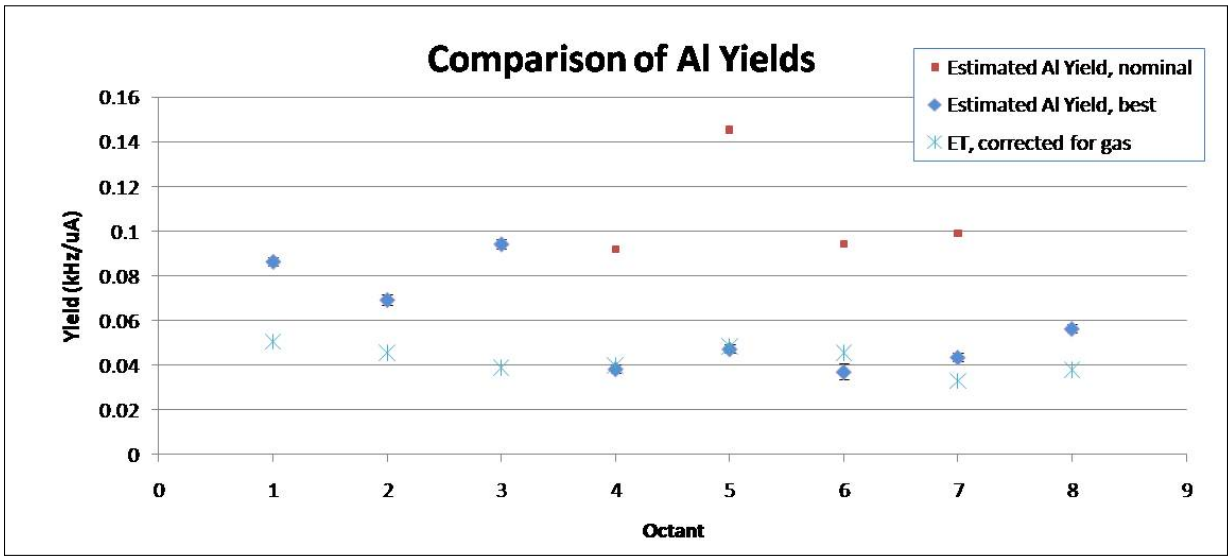

Figure 4.29: The calculated aluminum yields using the coefficients from the dilution fits with the magnetic field setting that gives the best χ^2, and that for the nominal field setting. The empty target yields (corrected for the hydrogen gas) are also shown. The calculated aluminums yields for the 'best' dilutions seem to agree with the empty target yields reasonably well.

cells. The yield data need to be corrected for the contribution from the hydrogen gas

$$Y_{et,corr} = (Y_{et} - \alpha Y_{meas})/(1 - \alpha) \tag{4.25}$$

where $\alpha \sim 0.025$ is the relative density of the cold hydrogen gas to that of the liquid hydrogen. The corrected empty target rates are then essentially the aluminum rates that would be seen in the normal running. Figure 4.29 shows a comparison of the estimates of the aluminum yields using the scale factors determined with the nominal and best field settings with that of the 'empty target' yields in which it is clear that the 'best' field settings also yield a better estimate of the empty target yield.

The largest contribution to the background in the elastic locus is the aluminum. The other processes contribute nearly negligibly, except in CED 9 where there is a significant

pi0 yield in the background. This qualitative statement is true in all of the various fits and error schemes, even though the values of the coefficients may vary, and also agrees with the field scan method (see Figure 4.30). The dilutions calculated with the matrix method tend to be higher, though with the BFIL adjustment in each octant the average is actually equal to or slightly lower than that obtained in the field scan method (0.116 ± 0.001 vs. 0.133) depending on whether the nominal field is used in octant 7 or not. In the field scan method, all processes except for aluminum are lumped into an "f_{other}" and assigned an asymmetry of $A_{other} = 0$. In this method there is a yield fraction for each process, and it is possible to fit the asymmetries individually as well. The asymmetry fits will be discussed in the following section.

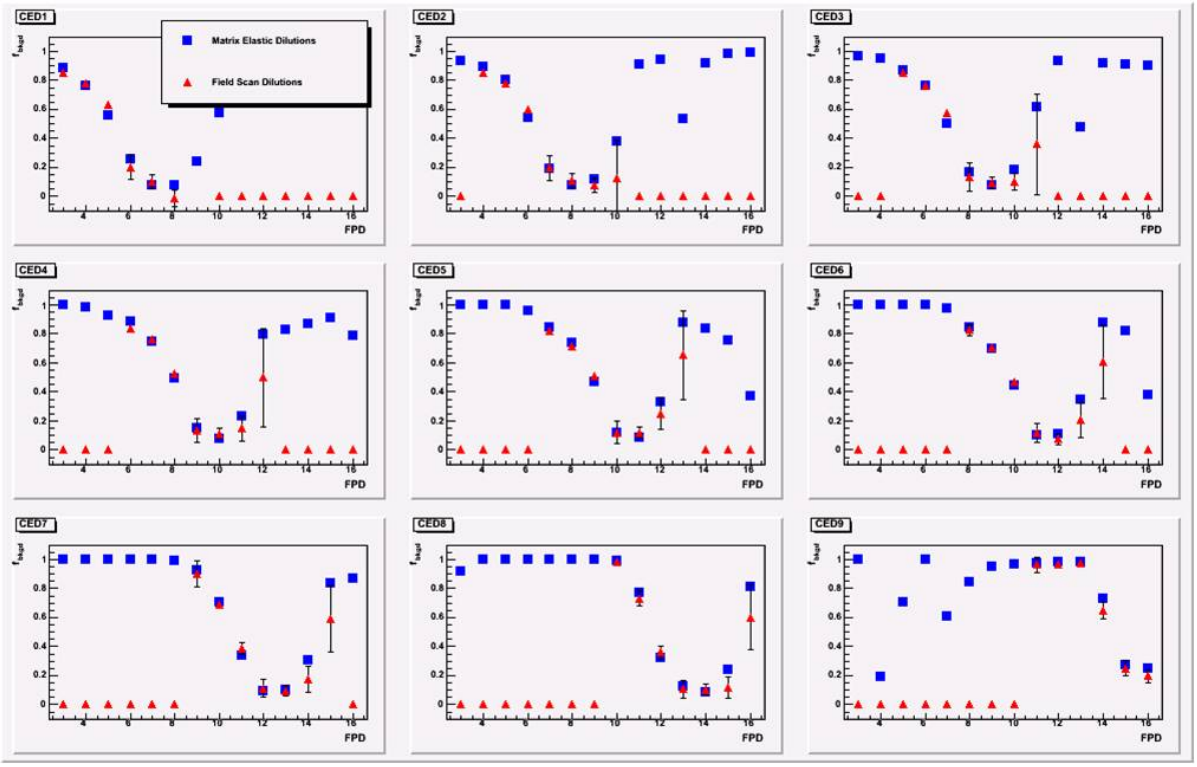

Figure 4.30: A cell-by-cell comparison of the dilutions as determined from a matrix fit of the octant averaged yields (blue) compared to those of the field scan method in octant 1 (red). An f_{bkgd} of 1 means there is no elastic rate in that cell; the cells with 0 for the red points simply mean there was no field scan dilution calculated for that cell.

4.5.3 Asymmetries

The measured asymmetry is commonly written in this way:

$$A_{meas} = (1 - f)A_{ela} + fA_{bkgd} \tag{4.26}$$

where A_{meas} is the measured asymmetry (as in the yield fit, the data are after corrections for deadtime/randoms, the scalar counting error and linear regression). Here the background dilution is given as f, so the elastic fraction is $1 - f$. The measured asymmetry is the yield average of the elastic asymmetry, A_{ela} and the yield averaged background asymmetry, A_{bkgd}. In order to do the asymmetry fit it is necessary to allow the contribution from each of the background processes to scale separately. A_{meas} is the yield averaged asymmetry over all processes, and in the fit of the simulated asymmetries to the data asymmetries it is necessary to scale the product of the dilution and the asymmetry for each process.

The yield average total simulation asymmetry (red) as well as the scaled result (green) are compared to the data (black) in Figure 4.31. The scaled simulated total asymmetry in a particular cell is given by

$$A_{scaledsim,total_i} = a_{elai}A'_{elai} + a_{inei}A'_{inei} + a_{Al+Hei}A'_{Al+Hei} + a_{pi0_i}A'_{pi0_i} + a_{quad_i}A'_{quad_i} \tag{4.27}$$

where $f_{process_i}$ is the yield fraction and $A_{process_i}$ is the asymmetry for an individual process in a given cell. The fit must be performed on the combined quantities $A'_{process_i} = f_{process_i}A_{process_i}$, but it is assumed that the scaling in the asymmetry fit is on the asymmetry and not the yield fraction. The fit is performed in a similar way to that of the yields, except that it is a 4 parameter fit, because $A_{pi0} \approx 0$ and the "quad" value is constrained to have the same coefficient in each cell where it appears (limited to the same cells as the yield fit).

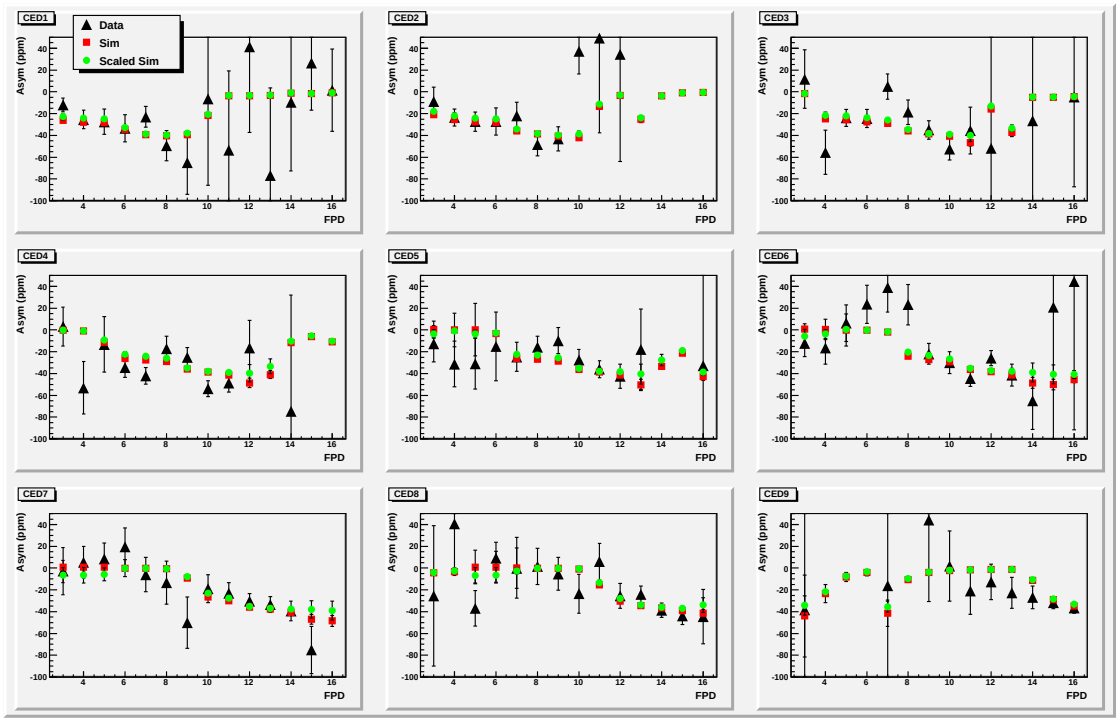

Figure 4.31: Comparison of the simulated (scaled - green, raw - red) and data (black) asymmetries.

The matrix that goes into the fit (before the errors are applied) is shown in the appendix, Equation C.10, where $A'_{process}$ is defined as it is here. The error used to weight the fit and calculate the reduced χ^2 is the error on A_{meas} added in quadrature with the simulated asymmetry error (properly combined with the error on the dilution) in each cell. The error on A_{pi0} is taken into account here as well. The fit is performed separately on each octant. As in the case of the yield fit, the χ^2 in each cell should be approximately 1. The asymmetry of the background using the scaled simulation asymmetries and dilutions (black) is compared to the background asymmetry for this target energy combination which is approximated as

the deuterium asymmetry for this energy, using the dilutions from the field scan method (red) in Figure 4.32.

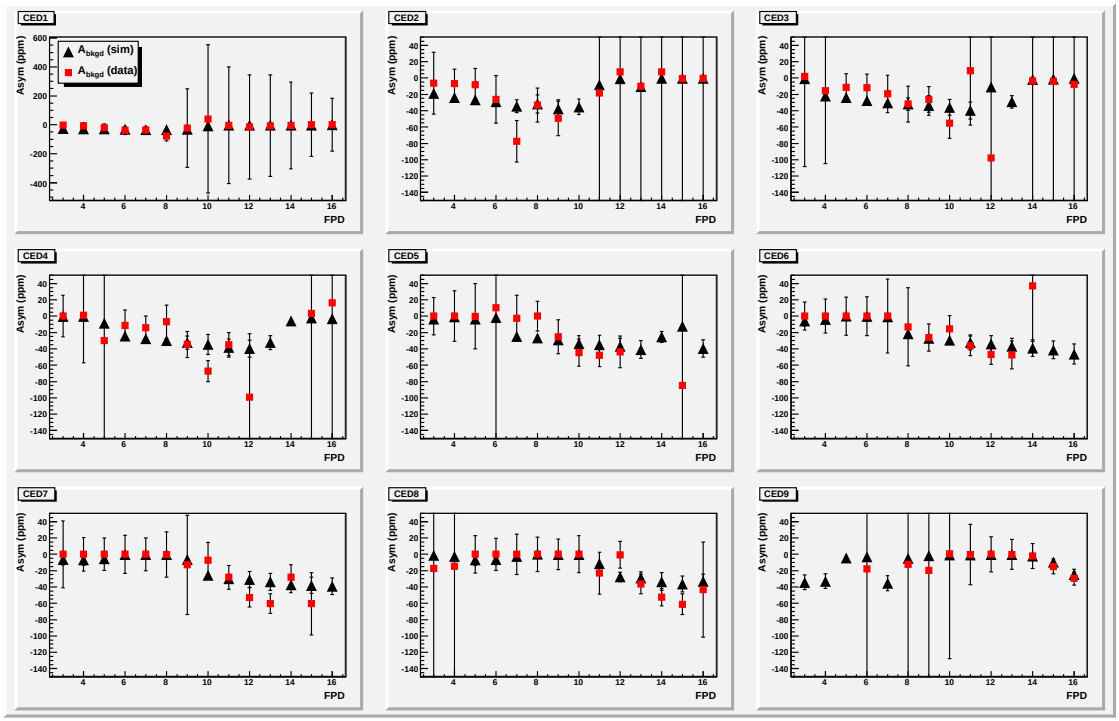

Figure 4.32: Comparison of the background asymmetries estimated with the matrix method in the simulation (black) with the background asymmetries estimated from field scan dilutions and the deuterium data asymmetries (red).

4.5.4 The Background Correction

Once the fit has been performed, the correction to the measured asymmetry can be applied. The corrected elastic asymmetries are calculated using

$$A_{ela} = \frac{A_{meas} - f A_{bkgd}}{1 - f} = A_{meas} \frac{1 - R}{1 - f} \tag{4.28}$$

where the ratio R is used to try to account for possible scaling of the dilution that may be occurring in the fit

$$R = \frac{f_{sim} A_{bkgd_{sim}}}{A_{meas_{sim}}} \tag{4.29}$$

This effect cannot fully be removed because the dilution still appears in the numerator. The resulting background corrected elastic asymmetry is $A_{ela} = -39.910 \pm 2.273$, compared to the 'official method' value of -38.198 ± 2.391 (this number is the raw asymmetry corrected for the background asymmetry, in both cases). In order to calculate the correction on the locus it is necessary to perform the correction on a cell-by-cell basis in each octant. One reason for this is the acceptance dependence which manifests itself as a variation of the optimum magnetic field in the fits for each octant. The corrected asymmetry is then averaged over the locus in each octant, and then over the octants, using only the pt-pt[2] errors to weight the average in each case (see Figure 4.33). In order to calculate the uncertainties, the various quantities that go into the calculation are averaged with the same weight as used in the average of the corrected asymmetry, and the error analysis is applied using these weighted average quantities. This is in order to apply the global errors only after all the averaging has been done. For the purposes of the averaging, the only pt-pt error comes from the error on the data asymmetry, A_{meas}. The coefficients for both the yield fit and the asymmetry fit are the same in every cell, so the uncertainties are considered global and are not used in

[2]Point to point errors are errors which are different from data point to data point (in this case, cell by cell and then octant to octant) as opposed to global errors which are the same for each data point.

the weighting of the averages. Note that the corrected asymmetries using the 'best' vs. the 'nominal' field in each case agree within errors.

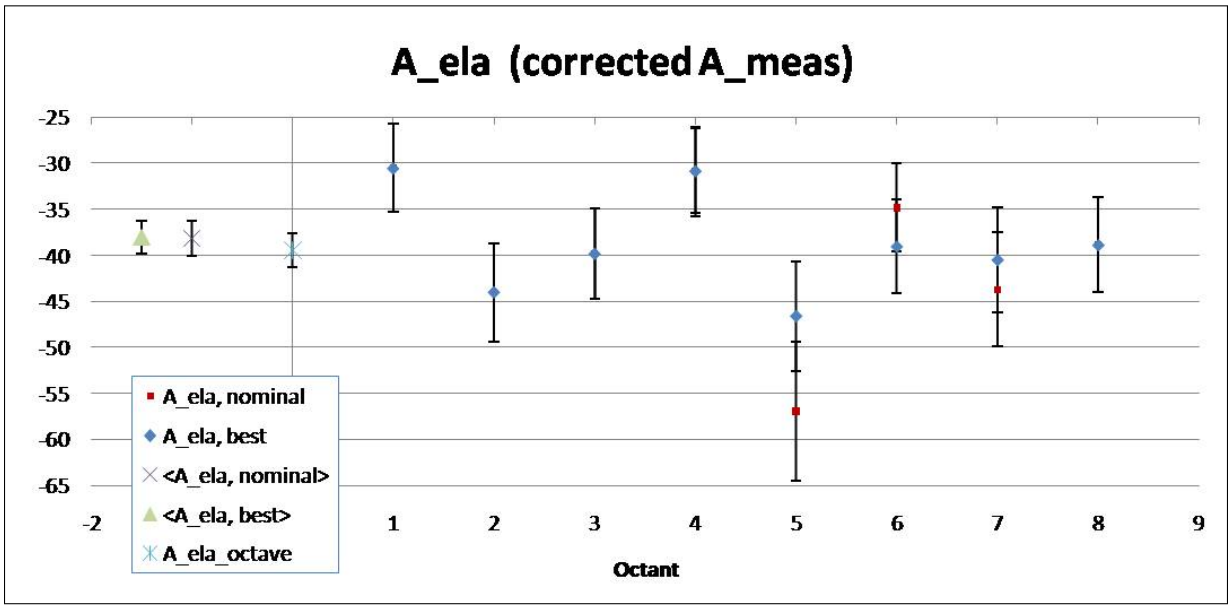

Figure 4.33: The background asymmetries vs. octant for the case where the dilution fits in all octants are with the nominal field, and the case where the dilutions fits with the best χ^2 in each octant is used (best), and the averages.

4.5.5 Summary

The matrix method and the field scan methods of determining the background asymmetries for the hydrogen at 687 MeV seem to yield consistent results for the dilutions and the background asymmetry correction. The sizes of the background asymmetries in both methods are consistent (Figure 4.32). The effect that manifests itself as having a different simulated magnetic field to optimize the fits is evident in both methods (Figures 4.8 and 4.28) and doesn't seem to overly influence the determination of the elastic asymmetry in the matrix method (Figure 4.33). The matrix method is limited in the finite number of simulations with different magnetic field settings, but presumably more simulations could be performed

with smaller step sizes over a larger range of magnetic fields in order to try to optimize the fits. The matrix method seems to yield a larger correction, although it agrees within errors with the size of the correction in the field scan method and is smaller than the uncertainty on the measured asymmetry. This correction is larger than that obtained in the field scan method mostly because the background dilutions are coming out slightly higher, as well as the estimated size of the asymmetry being slightly smaller. The results of this analysis, in which each of the simulated processes was allowed to have a different scale factor, seem to justify the approximations that were made for the asymmetries in the field scan method, as well as the determination of the dilutions.

4.6 Transverse Asymmetries

The beam normal single spin asymmetries are extracted from the data that are taken during dedicated runs when the electron beam is polarized transverse to the direction of its momentum. The helicity is flipped in the same way as during the longitudinal running, and the result is an asymmetry that varies sinusoidally with octant. In order to extract the value of the beam normal single spin asymmetry, it is necessary to fit the data as a sinusoidal function of angle around the beam axis to obtain the amplitude (see Figure 4.35). The fit was performed on the transverse data from each target/energy combination, hydrogen and deuterium at 362 MeV and 687 MeV. The phase was fixed to the average phase obtained in preliminary fits to the low energy data where the phase was allowed to vary. In the final fits only the amplitude and vertical offset were allowed to vary; the results are summarized in Table 4.6.

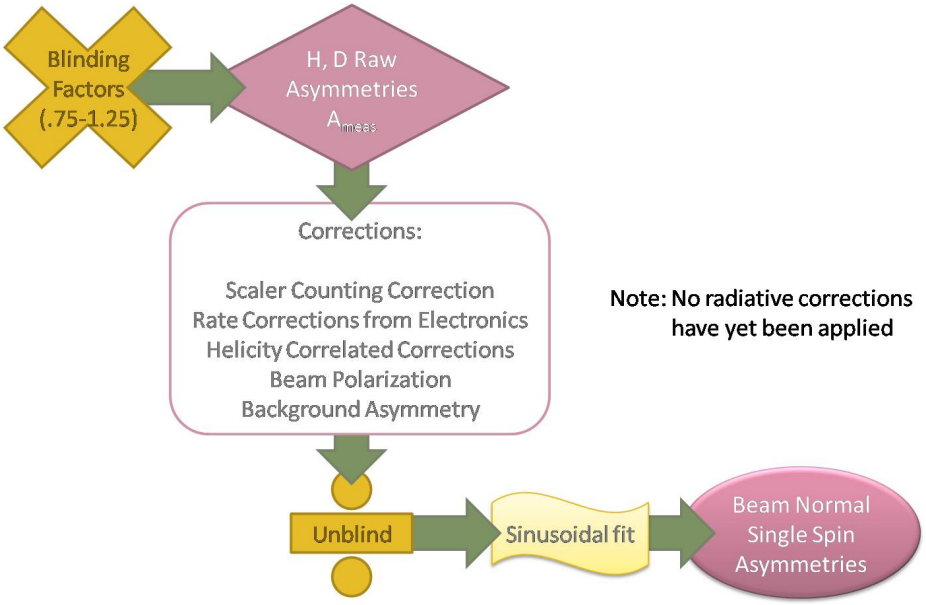

Figure 4.34: Overview of the analysis process from raw asymmetries to beam normal single spin asymmetries. The data are looped through at the yield level for each of four passes (standard cuts and blinding factors are applied, then the scalar counting correction, rate corrections from electronics and helicity correlated corrections). The run averaged cell-by-cell yields and asymmetries are then used to correct for background asymmetries. Finally the asymmetries are corrected for beam polarization and unblinded. The asymmetries in each octant are fit as a function of ϕ and the amplitude of the fit is the magnitude of the beam normal single spin asymmetry.

4.6.1 Corrections to the Transverse Data

The transverse data have been fully corrected for the electronics effects and linear regression, but have not been corrected for radiative effects because no prescription yet exists to calculate the radiative effects for the beam normal single spin asymmetry. They have also been unblinded and corrected for the beam polarization. The background correction was applied using the "official method", where the asymmetry of the aluminum was estimated as the asymmetry of the deuterium. The sizes of the corrections and the final asymmetries are summarized in Table 4.5. The data after each correction were fit with sinusoidal fits and the difference in the amplitude of the fits is the change in the asymmetry. The errors

Table 4.5: Changes to the asymmetries due to each of the corrections.

Correction	Change Due to Correction (ppm)			
	D687	H687	D362	H362
Electronics	14	-1.5	2.3	6.4
Linear Regression	0.01	0.2	0.5	-2.2
Background Asymmetry	6	2.0	0.4	6.9
Final Asymmetries	-55.2 ± 78	-21.0 ± 24	-108.6 ± 7.2	-176.2 ± 9.4

associated with each correction are calculated as the quadrature difference in the errors on the amplitudes of the fits before and after a given correction (see Table 4.7). The exception is the error for the linear regression in the high energy data, where the error on the amplitude decreases or stays the same after the correction. In this case the error is approximated by scaling the linear regression errors for the lower energy by the square root of the ratios of the number of quartets in each dataset. The statistical error is estimated as the error on the amplitude of the fit to the raw asymmetries.

The expected value of the beam normal single spin asymmetry at the low energy is quite large, and can clearly be seen in the data for both hydrogen and deuterium. At the higher energy the magnitude of the asymmetry is expected to be smaller, and in addition there was very little data taken on deuterium. The result is that the octant dependence of the asymmetries is not as apparent as in the data taken at the lower energy, even for the hydrogen. The hydrogen data at the lower energy were missing a scalar channel in octant two that made it impossible to perform the electronics corrections, so that octant has been omitted from the final results, though there didn't seem to be any problems with the raw asymmetry. The data quality for the higher energy for both targets and the deuterium at the lower energy revealed no major issues.

Table 4.6: Summary of the magnitude of the transverse asymmetries in each dataset.

Dataset	Phases from 'Free' Fits		Fits with Fixed Phase (2.3°)		
	LUMI (degrees)	Detector (degrees)	Amplitude (ppm)	Offset (ppm)	$\frac{\chi^2}{ndf}$
H362	-86.5 ± 1.7	-92.6 ± 1.9	176.2 ± 9.4	-1.7 ± 4	1.9
D362	-86.9 ± 0.4	-91.6 ± 3.4	108.6 ± 7.2	1.4 ± 4	1.6
H687	-87.2 ± 0.8	-79.1 ± 68	21.0 ± 24	-9.9 ± 14	0.4
D687	-88.9 ± 1.3	-66.2 ± 63	55.2 ± 78	10 ± 46	0.5

4.6.2 Fitting the Octant Dependence

As discussed in Appendix D.6, the out of plane component should be very small, so the phase due to this component is expected to be small. In plots versus octant the form of the fit is

$$A_m^{\perp} = A \sin\left(\frac{360}{8}(x-1) + \phi_o\right) + \Delta \tag{4.30}$$

where A is the amplitude of the fit, x is the octant number and Δ is the offset The phase ϕ_o is $90^\circ \pm \delta$ where δ could be from an actual out of plane phase of the electron's spin, or it could be a geometrical phase of the detector. The phases from sinusoidal fits of the LUMI and main detector data, where the phases were allowed to be vary in addition to the amplitude and offset, are shown in Table 4.6 ('Free' fit phases). The LUMI data are essentially consistent with each other, and likewise the detector data are consistent, though the higher energy phases have large errors. But the LUMI phase is not consistent with the main detector phase. This is most likely because of an actual geometrical offset between the main detectors and the LUMIs. Both are close to 90°, as expected. There is no physics that would explain a difference in phase between the two sets of detectors.

The consistency of the LUMI phases in the transverse data from dataset to dataset gives some confidence that whatever out of plane phase of the electron's spin existed was the same in each dataset. Because there may be a geometrical offset between the LUMIs and the main detectors, however, the weighted average of the detector phases at the lower energy is used in order to fix the phases of the sinusoidal fits to the main detector data versus ϕ

$$A_m^{\perp} = A \sin(\phi + 2.3^{\circ}) + \Delta \tag{4.31}$$

in each data set (fixed phase fits, Table 4.6). The value of δ, the difference from 90° of the weighted average of the phases of the main detectors at the lower energy setting is $-2.3^{\circ} \pm 1.6^{\circ}$. The main detector plots in 4.21 reflect this choice of phase. The difference in phase in a plot vs. octant and a plot vs. phi involves a 90° rotation as well as a reversal of order, so the $-\delta$ becomes the value of the phase, or 2.3°. The choice to fix the phase to this value does not change the amplitude of the sine fits to the low energy data significantly.

4.6.3 Summary

The results of the analysis of the transverse data are summarized in Figure 4.35 and the uncertainties are broken down in Table 4.7. There is an explicit minus sign in equation 1.46 which means that the values of the beam normal single spin asymmetries have the opposite sign as the amplitudes of the fits and are all negative. The uncertainties in the low energy data are small compared to the size of the asymmetries, and the quality of the data is apparent in the plots. The high energy data have much larger errors relative to the size of the asymmetries; indeed there were only 2 good runs for the deuterium data at this energy. Even with more data the hydrogen result is consistent with zero. However, when compared with the theory (see Figure 5.4), the results are more encouraging.

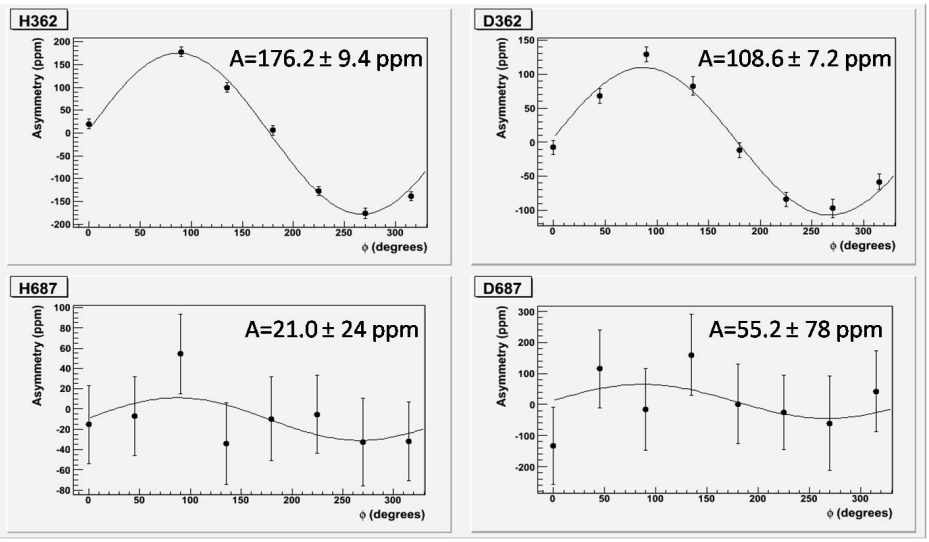

Figure 4.35: The background asymmetry corrected electron transverse asymmetries vs. ϕ. The amplitude of the fit is the value of the beam normal single spin asymmetry, shown on the plot for each target/energy combination. The upper plots are for the 362 MeV, and the lower plots are for the 687 MeV data, with hydrogen data on the left and deuterium data on the right.

Table 4.7: Estimates of the various contributions to the uncertainties in each dataset. If a source of systematic error has a contribution that is global, it is listed in parentheses.

Correction	Uncertainty (ppm)			
	D687	H687	D362	H362
Statistics	57.8	17.0	5.6	5.17
Electronics	42.0	4.6	3.5	1.2
Linear Regression	6.0	2.4	1.6	2.0
Background Asymmetry	30.6	15.2 (2.5)	0.7	3.7 (5.1)
Polarization	0.6 (0.6)	0.2 (0.2)	2.1 (1.3)	3.4 (2.0)

Chapter 5

Results and Conclusions

The G^0 experimental program is a rich program that has several auxiliary physics measurements in addition to the main measurement to determine the strange quark contribution to the charge and magnetization distributions of the nucleon. Measurements of the pion asymmetries and inelastic asymmetries will be presented in other theses. The primary physics focus of this thesis is the measurement of the beam normal single spin asymmetries, obtained during the transverse polarization runs during the backward angle phase of the G^0 experiment. For completeness, the results of the main G^0 measurement will be presented here, as well as its impact on Q_{weak}. The transverse results are then presented.

5.1 Strange Electric and Magnetic Form Factors

5.1.1 From Asymmetries to Form Factors

Several steps are required in order to extract the strange form factors G_E^s and G_M^s, as well as the isovector piece of the effective axial form factor, G_A^e from the measured asymmetries

at each Q^2. The mean Q^2 must be determined, and then it is necessary to parameterize the proton and neutron electromagnetic form factors as a function of Q^2. It is then possible to extract the linear combination of the strange form factors

$$G_E^s + \eta G_M^s = \frac{4\pi\alpha\sqrt{2}\left(\epsilon\left(G_E^{\gamma,p}\right)^2 + \tau\left(G_M^{\gamma,p}\right)^2\right)}{G_F Q^2 \epsilon G_E^{\gamma,p}\left(1 + R_V^{(0)}\right)} \times (A_{phys} - A_{NVS}) \tag{5.1}$$

where A_{NVS} is the theoretical "no vector strange" asymmetry given in equation 4.8 and A_{phys} is the measured physics asymmetry. The linear combination coefficient, η is given by

$$\eta = \frac{\tau G_M^{\gamma,p}}{\epsilon G_E^{\gamma,p}} \tag{5.2}$$

and is different for different kinematics. The G^0 forward angle results for a range of Q^2 are shown with the world data in Figure 5.1. Until the G^0 backward angle data were taken, no single experiment was able to fully extract the three form factors at multiple Q^2, although enough data were taken by different experiments at $Q^2 = 0.1 GeV^2/c^2$ to make an estimate of the strange electric and magnetic form factors (limited by knowledge of G_A^e) (see Figure 1.18).

As discussed in Section 1.2.2, the proton electric and magnetic and the neutron magnetic form factor all approximately follow an approximate dipole form as in Eq. 1.25. The neutron electric form factor, however, does not follow the same form, and a modified dipole form, suggested by S. Galster, is used[59]

$$G_E^n(Q^2) = \frac{A_\tau}{1 + B_\tau} G_D(Q^2) \tag{5.3}$$

where A_τ and B_τ are varied to fit the data. In the original analysis of the forward angle data, the Kelly parameterization[77] for the form factors was used, including the Galster

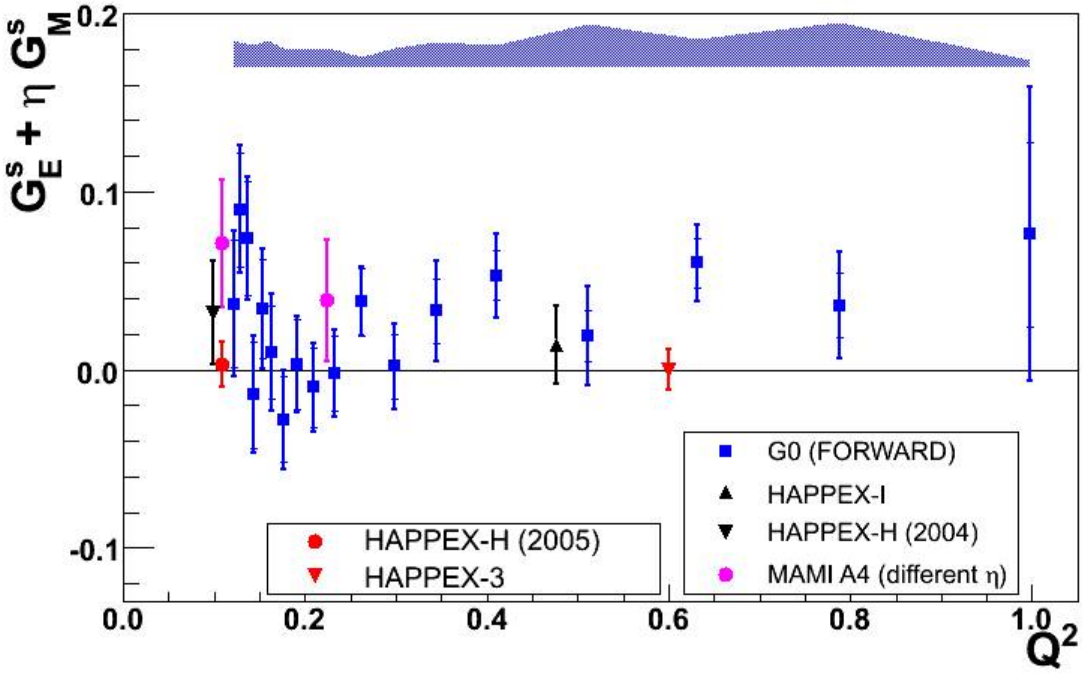

Figure 5.1: World data on $G_E^s + \eta G_M^s$ as a function of Q^2 as of the release of the G^0 forward angle data in 2005 [10].

parameterization of the neutron electric form factor. The fits require only 4 parameters (except for the neutron electric form factor, which requires only the 2 parameters A_τ and B_τ). Various additional parameterizations of the form factors have been made, including several that include two boson exchange (TBE) corrections that have been published since the release of the forward angle data[23]. It was decided to use the Kelly parameterization to be consistent with the deuterium model, however, as discussed in Section 4.1.4, the electroweak radiative corrections include the TBE effects from Melnitchouk, Blunden and Tjon[136].

The deuterium asymmetry of interest for G^0 is that of the quasi-elastic scattering (QE), or scattering from the nucleons in the deuterium. The measured asymmetry

$$A_D = \frac{\sigma_{QE} A_{QE} + \sigma_{el} A_{el} + \sigma_{ted} A_{ted} + \sigma_\Delta A_\Delta}{\sigma_{QE} + \sigma_{el} + \sigma_{ted} + \sigma_\Delta} \tag{5.4}$$

where A is asymmetry and σ is the cross section for the various contributions, would also have effects from elastic electron deuterium scattering (el), threshold breakup (ted) and delta production (Δ), but these effects are estimated to be small because the cross sections are small (<3%) and/or the asymmetries are approximately equal to the quasi-elastic asymmetry[43]. The simplest model for the asymmetry from deuterium quasi-elastic scattering is the quasistatic model

$$A_{QE} = \frac{\sigma_p A_p + \sigma_n A_n}{\sigma_p + \sigma_n} \tag{5.5}$$

in which the protons (p) and neutrons (n) are treated as non-interacting, stationary particles. This model can be improved by including the Fermi motion of the nucleons. The interactions between the nucleons can be calculated using a parameterization of the nucleon form factors to calculate the nuclear response functions. The deuterium model provided by Rocco Schiavilla, a professor at Old Dominion University, included effects of nucleon-nucleon interactions as well as Fermi motion[19]. The Kelly parameterization is used for the proton form factors in this model.

By measuring the asymmetry at backward angles on the proton and on the deuteron, linear combinations of the strange form factors with different sensitivities to the strange electric, magnetic and axial form factors can be determined. In order to combine the forward and backward angle data, it is necessary to interpolate the forward angle data to the Q^2 values measured at backward angles. The forward angle data on $A_{phys} - A_{NVS}$ was fit using a linear function, and the error on the interpolated values was taken as 70% of the nearest measured value[44]. For a given Q^2 the system of three equations, formed from equation 1.40, for forward and backward measurements of the asymmetry on the proton and a backward angle measurement on the deuteron, can be solved to determine $G_{E,M}^{Z,p}$ as well as G_A^e. The values of $G_{E,M}^{Z,p}$ can then be used to extract G_E^s and G_M^s, using equation 1.32. The G^0 backward and the interpolated forward angle physics asymmetries and uncertainties at $Q^2 =$

Table 5.1: Table summarizing the physics asymmetries (after all corrections) for each of the datasets, including the interpolated forward angle results[55]. The errors shown are statistical and systematic (point-to-point and global).

Q^2 GeV^2/c^2	Dataset	Corrected Asymmetry (ppm)
0.22	H, backward	-11.25 ± 0.86 ± 0.27 ± 0.43
	D, backward	-16.93 ± 0.81 ± 0.41 ± 0.21
	H, forward	-4.74 ± 0.36 ± 0.21 ± 0.23
0.63	H, backward	-45.9 ± 2.4 ± 0.8 ± 1.0
	D, backward	-55.5 ± 3.3 ± 2.0 ± 0.7
	H, forward	-20.68 ± 0.78 ± 0.90 ± 1.31

Table 5.2: Table summarizing the extracted form factors at the two Q^2 values for G^0 backward angle[55]. The errors shown are statistical and systematic (point-to-point and global).

Q^2	0.22 GeV^2/c^2	0.63 GeV^2/c^2
G_E^s	-0.014 ± 0.036 ± 0.018 ± 0.018	0.110 ± 0.049 ± 0.030 ± 0.024
G_M^s	0.083 ± 0.183 ± 0.086 ± 0.078	-0.124 ± 0.110 ± 0.061 ± 0.032
G_A^e	-0.501 ± 0.317 ± 0.193 ± 0.088	-0.197 ± 0.425 ± 0.257 ± 0.095

0.22 and 0.63 GeV^2/c^2 are shown in Table 5.1.

5.1.2 The Strange and Axial Form Factors

Figure 5.2 shows the results of the G^0 experimental program to measure the strange form factors and the effective axial form factor. The strange quark contribution to the ground state

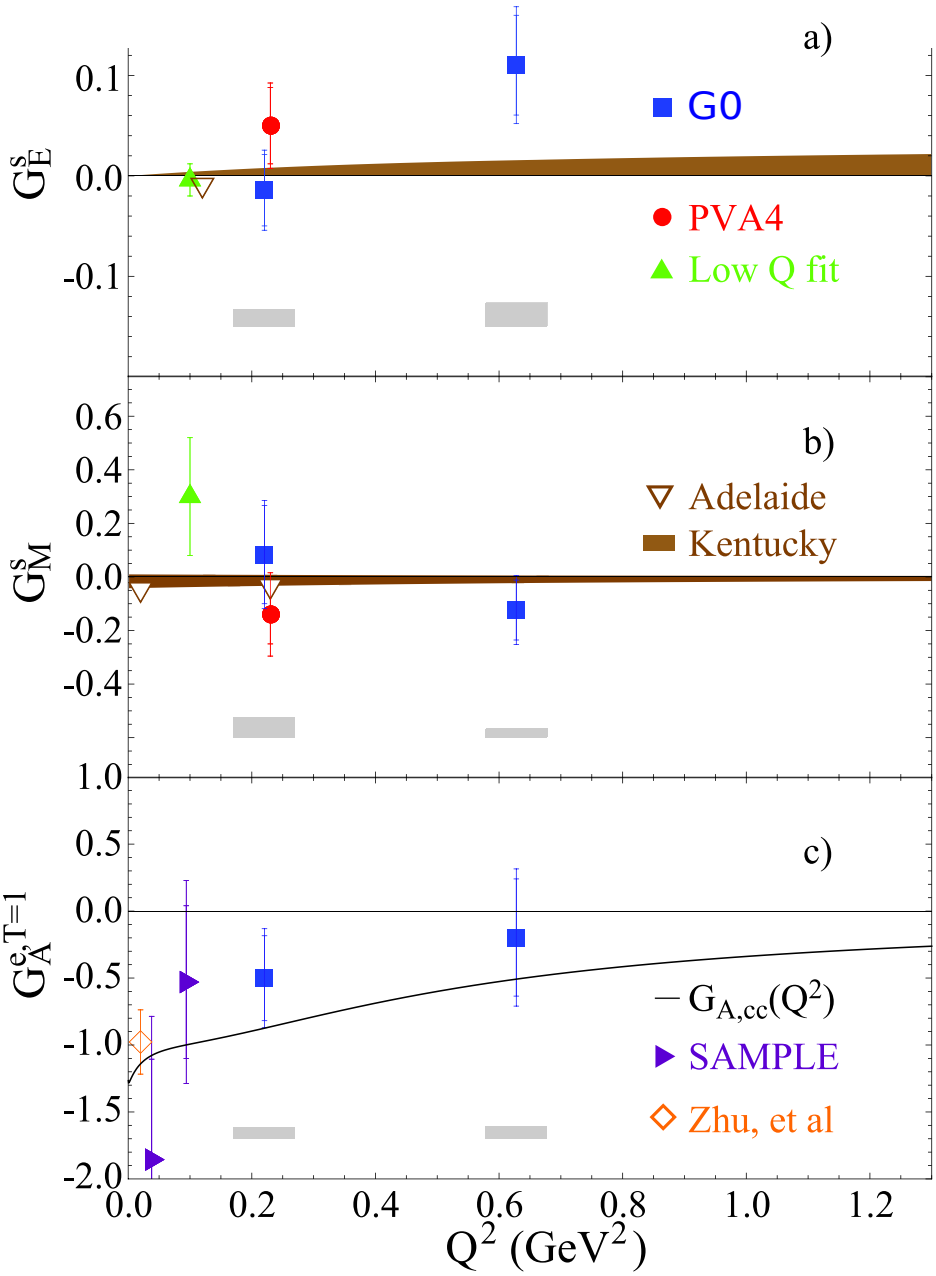

Figure 5.2: Final G^0 results for the strange electric (a) and magnetic (b) form factors as well as the effective axial form factor (c)[44][106]. The error bars are statistical and statistical+point-point (added in quadrature). The global errors are indicated by the grey regions under each G^0 measured value.

proton electric and magnetic form factors is small (<10%). The PVA4 values[16] assume a value for G_A^e using a dipole form that is normalized to the Zhu, et. al.[152] point shown in (c). The low Q^2 fit was performed with a global analysis of the nucleon strange form factors including the SAMPLE, HAPPEx and PVA4 measurements summarized in Table 1.4 prior to 2007 as well as the lowest 14 G^0 Q^2 values[88]. Various models make predictions of the form factors as functions of Q^2. Some models that are consistent with small values of G_E^s and G_M^s include those by the Adelaide and Kentucky groups. The Adelaide group uses heavy baryon chiral perturbation and low-mass quenched lattice QCD calculations, assuming charge symmetry, to estimate the strange form factors[86][87][144]. The Kentucky group uses a full lattice QCD calculation to calculate the strange form factors [48].

The effective axial form factor measurements at the two values of Q^2 measured in G^0 are shown in Figure 5.2c. The SAMPLE values assume a value for $G_M^s = 0.23 \pm 0.36 \pm 0.40$ where the contributions from G_M^s and G_E^s are small compared to the uncertainties[21]. The Zhu et. al. point calculates the anapole moment contribution to the axial form factor in chiral perturbation theory[152]. The black line labeled $G_{A,cc}(Q^2)$ is a parameterization of the vector and axial form factors of the nucleon that uses quark-hadron duality constraints at high momentum transfers (where quark structure dominates) and simultaneously satisfies the constraints at low momentum transfers (where nucleon structure is important)[28]. This parameterization does not include effects from anapole moment contributions. The G^0 measurements of the effective axial form factor puts an upper limit on the contributions of the anapole moment and its dependence on Q^2.

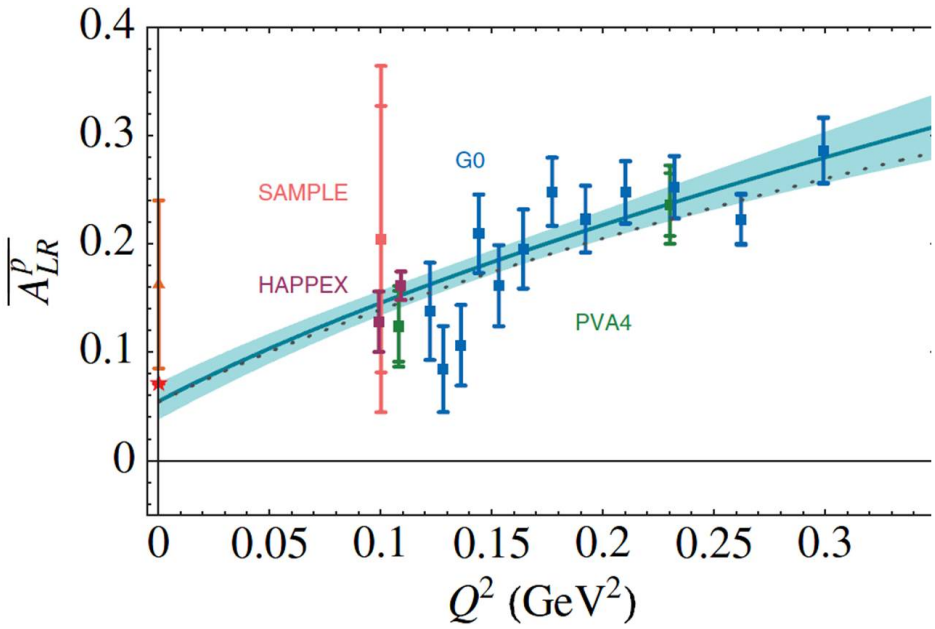

Figure 5.3: Extrapolation of the world data on the longitudinal asymmetries in elastic electron-proton scattering, normalized to $A_0 = G_F Q^2/(4\pi\alpha\sqrt{2})$[149]. At $Q^2 = 0$ this is a measure of the weak charge of the proton. The solid curve is the best fit, and the shaded region is the 1σ bound. The dotted line incorporates theoretical estimates of the anapole form factors of the nucleon (see section 1.1.3).

5.1.3 The Impact of G^0 on Q_{weak}

The measurement of the weak charge of the proton in Q_{weak} will be made at $Q^2 \sim 0.026 GeV^2/c^2$ with a scattered electron angle $\theta \sim 8°$, and it is necessary to extrapolate to $Q^2 \to 0$ and far forward scattering angles, $\theta \to 0$. This extrapolation is sensitive to hadronic structure, and though the nucleon electric and magnetic form factors are well known, there is still uncertainty due to the unknown contribution from strange quarks and the axial form factor. To first order the normalized asymmetry is Q_W^p, the weak charge of the proton

$$\overline{A_{LR}} = \frac{A_{LR}^p}{A_0 Q^2} = Q_W^p + B(Q^2)Q^2 \tag{5.6}$$

where $A_0 = -G_\mu Q^2/(4\pi\alpha\sqrt{2})$ and $B(Q^2)$ is the first term where hadronic structure enters. The fit to the world data on $\overline{A_{LR}}$ is shown in Figure 5.3 where the G^0 measurements included in the fit span a range of Q^2 from 0.12 to 0.41 GeV^2. In the plot the dotted line shows that including theoretical constraints on the axial form factor does not affect the value of the asymmetry at low Q^2, and in fact the difference is never larger than 1σ, so experimental values should be sufficient to constrain the hadronic term for Q_{weak}[149].

5.2 The Beam Normal Single Spin Asymmetries

During the G^0 backward angle running, transverse data were taken for hydrogen and deuterium at beam energies of 362 MeV and 687 MeV, corresponding to four momentum transfers of $Q^2 \sim 0.21\ GeV^2/c^2$ and $0.63\ GeV^2/c^2$, respectively. From this data it was possible to extract the beam normal single spin asymmetries for elastic scattering from the proton and quasi-elastic scattering from deuterium. The analysis of the data is described in Section 4.6. These asymmetries are parity-conserving asymmetries that arise due to the interference of the imaginary part of two photon exchange with single photon exchange. One theory that is relevant for these kinematics is a resonance region calculation that treats the two photon exchange as doubly virtual Compton scattering (see Section 1.2.4). In this section the results for the hydrogen beam normal single spin asymmetries are compared to this theory, and a summary of the world data is presented. In addition, the first results from deuterium and estimates for scattering from the neutron are presented.

5.2.1 Results for Hydrogen

Most of the experiments described in Section 1.3 took transverse asymmetry data not only as a measurement of the systematic uncertainty in the longitudinal asymmetry measurement, but also as a measurement of the beam normal single spin asymmetries (BNSSA) (see Table 5.3). Most of the measurements are from elastic electron proton scattering, although HAPPEx has a measurement on ^{4}He, and PVA4 has taken deuterium data which is still being analyzed. G^0 measured the BNSSA at two values of Q^2 in the forward angle. At backward angles G^0 more than doubled the amount of world data, including the first measurement of scattering from deuterium. Together these measurements help to benchmark the theories that calculate the electroweak radiative corrections including two boson exchange effects.

The two G^0 backward angle measurements of the beam normal single spin asymmetries are shown on a plot with the PVA4 and SAMPLE backward angle measurements (see Figure 5.4). The data are shown in comparison to the inelastic contribution to the asymmetry as calculated by Pasquini and Vanderhaeghen[114]. The solid curve shows the full inelastic calculation, while the other three are estimates of the different intermediate states of the nucleon (π^0p, π^+n) and the sum. The estimates were made by evaluating the hadronic tensor at the endpoint of W_{max} so that it could be taken out of the W integration, corresponding to the quasireal Compton scattering contributions. The full calculation was performed by integrating the full curve over W, using MAID for the calculation of the invariant amplitudes $\tilde{F}_i(\nu, Q^2)$ introduced in section 1.2.4.

The theory calculations are for a center of mass (COM) scattered electron angle of 120°, while the data have different COM angles. However, as shown in Figure 1.14, the magnitude of the beam normal single spin asymmetries as a function of COM angle seems to peak near 125° for the energies where data have been taken at backward angles. The angle at which

Table 5.3: Beam normal single spin asymmetry summary. Adapted from [138].

Experiment	Energy (GeV)	Q^2 (GeV^2/c^2)	B_n (ppm)
Forward Angles			
PVA4[91]	0.570	0.11	-8.59 ± 0.89
PVA4[91]	0.855	0.23	-8.52 ± 2.31
HAPPEx (H) [76]	3.0	0.11	-6.7 ± 1.5
HAPPEx (^{4}He) [76]	2.75	0.08	-13.51 ± 1.4
G^0[11]	3.0	0.15	-4.06 ± 1.17
G^0[11]	3.0	0.25	-4.82 ± 2.11
E-158[138]	46	0.06	3.5→2.5
Backward Angles			
SAMPLE[21]	0.192	0.10	-16.4 ± 5.9
PVA4[31]	0.315	0.23	-87 ± 6
G^0 (H)	0.362	0.21	-176.2 ± 9.4
G^0 (H)	0.687	0.63	-21 ± 23.6
G^0 (D)	0.362	0.21	-108.6 ± 7.2
G^0 (D)	0.687	0.63	-55.2 ± 77.9

the peak occurs seems to increase with energy, but is still $\sim 120^\circ$ at 570 MeV, though at 855 MeV it is as low as 100°. Because the COM angles at which the data were taken are all relatively close to the angle at which the peak occurs (within 20°) for the energy at which the data were taken, this plot is a useful comparison of the existing world data for the beam normal single spin asymmetries at backward angles and the theory presented by Pasquini and Vanderhaeghen.

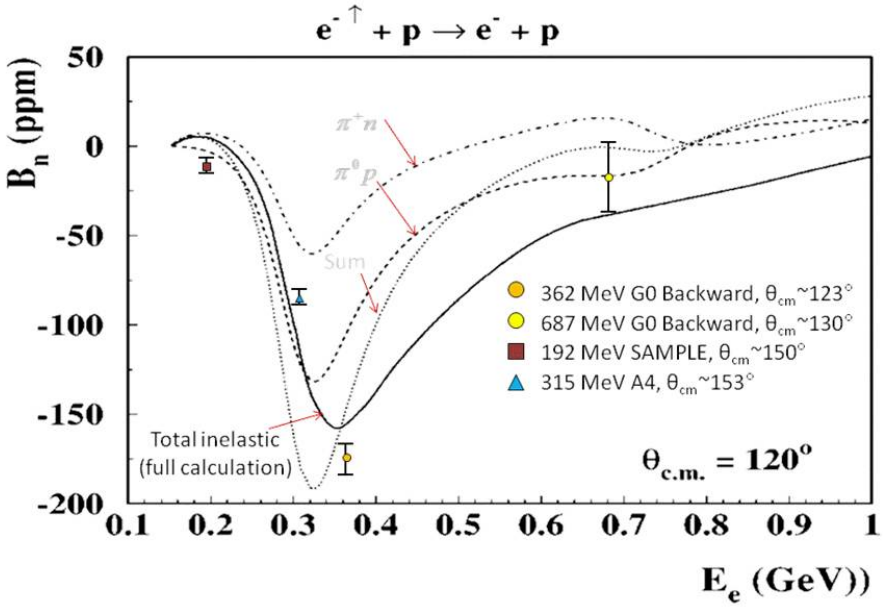

Figure 5.4: Summary of the world data for beam normal single spin asymmetries in elastic electron-proton scattering at backward angles. Curves are for the calculation of the inelastic contribution to the beam normal single spin asymmetries at a center of mass scattered electron angle of 120°, vs. incident beam energy[114]. The solid curve was generated using the full calculation (see text) and the other three curves are estimates of the contributions from different intermediate hadronic states and the sum as labeled in the figure.

5.2.2 Results for Deuterium

In addition to the asymmetries for hydrogen, summarized in Figure 5.4, the first measurement of the beam normal single spin asymmetry for the neutron has been made. The asymmetries were measured with a deuterium target as well as with a hydrogen target at both energies. In order to estimate the neutron asymmetry, it is necessary to make an assumption about the relative size of the proton and neutron asymmetries. Figure 1.16 shows the prediction of the asymmetries vs. COM angle for the proton and the neutron at a beam energy of 570 MeV. Again, the peaks occur at angles within ∼20° of each other. Barring this and other subtleties of the shape, the predicted asymmetries for the proton and neutron are approximately equal

Table 5.4: Estimate of the proton and neutron cross sections for each G^0 backward energy.

Energy/ Target	Cross Section (μb/sr)
362, proton	23
362, neutron	8
687, proton	2.6
687, neutron	1.1

and opposite.

Using the static approximation, the asymmetry for deuterium can be estimated as the cross section weighted asymmetry for the proton and the neutron, as is the case for the longitudinal asymmetry[21]

$$A_d = \frac{\sigma_p A_p + \sigma_n A_n}{\sigma_p + \sigma_n} \tag{5.7}$$

where σ is the proton (p) or neutron (n) cross section, and $A_{p,d}$ is the beam normal single spin asymmetry determined from a fit to the data vs. the angle around the beam axis as described in Section 4.6. Estimates of the proton and neutron cross sections are given in Table 5.4. The estimate for the neutron asymmetry for each energy is made by using the static approximation and solving for A_n. The resulting neutron asymmetry is in fact, smaller than the proton asymmetry, though it is positive (see Table 5.5). The measurement at the higher energy has very large uncertainties, mostly because of the limited amount of data taken on deuterium, but the resulting neutron asymmetry there is larger in magnitude than the proton asymmetry and negative rather than positive. In order to make a better estimate of the neutron asymmetry it will be necessary to use a more sophisticated deuterium model, similar to the calculation of Rocco Schiavilla[126][127] for the estimate of the longitudinal

Table 5.5: Estimates of the neutron asymmetries from the G^0 data. The proton asymmetries are shown here again for comparison.

Energy	Estimated Asymmetry (ppm)	
	Neutron	Proton
G^0 362	86.7 ± 41	-176.2 ± 9.4
G^0 687	-136 ± 267	-21 ± 24

asymmetries (see Section 4.1.4).

As discussed in section 1.2.4 there are many models for the beam normal single spin asymmetries, though they are usually relevant only at specific kinematics. The recent surge in interest in calculating two boson exchange corrections is responsible for the attempts to predict the beam normal single spin asymmetries. Unfortunately there is no prediction for the neutron asymmetry presented in any model other than that provided by Pasquini and Vanderhaeghen, which happens to be the relevant model for the G^0 backward angle kinematics. A measurement of the target normal spin asymmetries on the neutron (polarized ^{3}He) at Q^2 values of 1.0 and 2.3 GeV^2 at 3.3 and 5.5 GeV respectively, was completed in early 2009[138][81]. It will be interesting to compare the results for the neutron target normal single spin asymmetry measured in that experiment to the results for the neutron beam normal single spin asymmetries presented here.

5.3 Conclusions

The primary goal of the G^0 experimental program was to gauge the strange quark contribution to the charge and magnetization distributions of the nucleon. In addition it was able to make the first determination of the Q^2 dependence of the effective axial form factor, in-

cluding the anapole moment. The strange quark makes a small ($\leq 10\%$) contribution to the electromagnetic form factors of the nucleon, indicating that the charge and magnetization distributions of the s and $\bar{s}$ do not differ significantly. The first measurement of the Q^2 dependence of the effective axial form factor places an upper limit on anapole moment effects. These measurements, combined with the world data, will also provide the measurement of the hadronic contribution to the asymmetry measured in Q_{weak}.

The measurement of the imaginary part of the two photon exchange contribution to elastic electron nucleon scattering via the measurement of parity-conserving beam normal single spin asymmetries was one of the auxiliary measurements that make the G^0 experiment such a rich program. Together with the data from the PVA4 and SAMPLE measurements, they agree in a general sense with the prediction that includes the πN intermediate states. In addition, the first measurement of beam normal single spin asymmetries for the neutron at Q^2=0.21 GeV^2 was presented. These measurements will serve as valuable benchmarks for the theoretical framework that calculates the γZ and W^+W^- box diagrams that are important corrections to precision electroweak measurements.

Bibliography

[1] A. Acha et al. Precision measurements of the nucleon strange form factors at $Q^2 \sim 0.1$ GeV^2. *Physical Review Letters*, **98**:032301, (2007).

[2] T. Adams et al. Strange content of the nucleon (NuTeV), (1999).

[3] A. V. Afanasev and N. P. Merenkov. Collinear photon exchange in the beam normal polarization asymmetry of elastic electron-proton scattering. *Physics Letters B*, **599**:48–54, (2004).

[4] C. Amsler et al. Review of particle physics. *Physics Letters B*, **667**:1, (2008).

[5] K. A. Aniol et al. Parity-violating electroweak asymmetry in e→p scattering. *Physical Review C*, **69**:065501, (2004).

[6] K. A. Aniol et al. Parity-violating electron scattering from ^{4}he and the strange electric form factor of the nucleon. *Physical Review Letters*, **96**:022003, (2006).

[7] P. L. Anthony et al. Precision measurement of the weak mixing angle in møller scattering. *Physical Review Letters*, **95**:081601, (2005).

[8] J. Apostolakis. GEANT - detector description and simulation tool, (2003).

[9] D. Armstrong. Qweak tracking system. Qweak Document 952-v1, Jefferson Laboratory, May (2009).

[10] D. S. Armstrong et al. Strange-quark contributions to parity-violating asymmetries in the forward G0 electron-proton scattering experiment. *Physical Review Letters*, **95**:092001, (2005).

[11] D. S. Armstrong et al. Transverse beam spin asymmetries in forward-angle elastic electron-proton scattering. *Physical Review Letters*, **99**:092301, (2007).

[12] J. Arrington, W. Melnitchouk, and J. A. Tjon. Global analysis of proton elastic form factor data with two-photon exchange corrections. *Physical Review C (Nuclear Physics)*, **76**:035205–11, (2007).

[13] J. Arvieux et al. Towards a common PVA4-SAMPLE analysis: a first step. G0 Document 609-v1, Jefferson Laboratory, July (2005).

[14] S. L. Bailey. Parity violation in elastic electron scattering - a first measurement of the parity-violating asymmetry at Q^2=0.631 (GeV/c)^2 at backward angle. Thesis, The College of William and Mary, (2007).

[15] S. Baunack. Single spin asymmetries from the mainz A4 experiment. *Nuclear Physics A*, **755**:249–252, (2005).

[16] S. Baunack et al. Measurement of strange quark contributions to the vector form factors of the proton at $Q^2 = 0.22$ (GeV/c)^2. *Physical Review Letters*, **102**:151803, (2009).

[17] D. Beck. The G0 backward angle experiment. G0 Document 833-v1, Jefferson Laboratory, May (2009).

[18] D. H. Beck and B. R. Holstein. Nucleon structure and parity-violating electron scattering. *International Journal of Modern Physics E: Nuclear Physics*, **10**:1, (2001).

[19] E. Beise. Summary of the deuterium asymmetry model for G0. G0 elog, Simulation 92, (2009).

[20] E. Beise and F. Benmohktar. G0 backward analysis summary. G0 Document 718-v1, Jefferson Laboratory, October (2007).

[21] E. J. Beise, M. L. Pitt, and D. T. Spayde. The SAMPLE experiment and weak nucleon structure. *Progress in Particle and Nuclear Physics*, **54**:289–350, (2005).

[22] F. Benmohktar. G0 results. G0 Document 834-v1, Jefferson Laboratory, June (2009).

[23] F. Benmohktar. Nucleon form factors and electroweak radiative corrections (two boson exchange). G0 Document 825-v1, Jefferson Laboratory, April (2009).

[24] S. C. Bennett and C. E. Wieman. Measurement of the 6s→ 7s transition polarizability in atomic cesium and an improved test of the standard model. *Physical Review Letters*, **82**:2484, (1999).

[25] P. R. Bevington and D. K. Robinson. *Data Reduction and Error Analysis for the Physical Sciences*. McGraw-Hill Higher Education, (1992).

[26] J. Birchall. Effect on Q^2 of mis-aligned beam and collimators. Qweak Document 656-v1, Jefferson Laboratory, May (2007).

[27] J. Birchall. Updated requirements on beam properties for Qweak. Qweak Document 818-v1, Jefferson Laboratory, August (2008).

[28] A. Bodek, S. Avvakumov, R. Bradford, and H. Budd. Vector and axial nucleon form factors: A duality constrained parameterization. *The European Physical Journal C - Particles and Fields*, **53**:349–354, (2008).

[29] E. Bonnell. Wire plane summary document. VT Qweak elog (Drift Chamber) 65, Virgnia Tech, April (2009).

[30] H. Breuer. Cerenkov efficiency report. G0 Document 699-v1, Jefferson Laboratory, May (2007).

[31] L. Capozza. Transverse single spin asymmetry at the A4 experiment. *The European Physical Journal A - Hadrons and Nuclei*, **32**:497–499, (2007).

[32] R. Carlini. Q^2 defining collimation system, infrastructure and some misc. parts. Qweak Document 1033-v1, Jefferson Laboratory, July (2009).

[33] R. Carlini, S. Page, and M. Pitt. Beam parameter specifications for the G0 experiment (back angle running). *G0 Document*, 640-v1, (2006).

[34] T. P. Cheng. Chiral symmetry and the higgs-boson nucleon coupling. *Physical Review D*, **38**:2869, (1988).

[35] CDF Collaboration. Measurement of the forward-backward charge asymmetry of electron-positron pairs in p-$\bar{p}$ collisions at s=1.96 TeV. *Physical Review D*, **71**:052002, (2005).

[36] G0 Collaboration. Spin dance results. http://g0web.jlab.org/g0log/0610_archive/061009120421.html 123900, Jefferson Laboratory, (2007).

[37] G^0 Collaboration. Apparatus for the g0 experiment. *Jefferson Lab*, *to be published.

[38] Qweak Collaboration. The Qweak Experiment: "A Search for New Physics at the TeV Scale via a Measurement of the Proton's Weak Charge". Qweak Document 1-v1, Jefferson Laboratory, (2001).

[39] Qweak Collaboration. The Qweak Experiment: "A Search for New Physics at the TeV Scale via a Measurement of the Proton's Weak Charge". Qweak Document 190-v1, Jefferson Laboratory, (2004).

[40] Qweak Collaboration. Qweak beam and target boiling tests. http://g0web.jlab.org/g0log/0703_archive/logdir.html 136184 (136150-136431), Jefferson Laboratory, (2007).

[41] Qweak Collaboration. The Qweak Experiment: "A Search for New Physics at the TeV Scale via a Measurement of the Proton's Weak Charge". Qweak Document 703-v5, Jefferson Laboratory, (2007).

[42] Qweak Collaboration. The Qweak Experiment: "A Search for New Physics at the TeV Scale via a Measurement of the Proton's Weak Charge". http://www.jlab.org/qweak/, Jefferson Laboratory, (2008).

[43] The G^0 Collaboration. The G^0 experiment backward angle measurements update. G0 Document 642-v2, Jefferson Laboratory, June (2005).

[44] The G0 Collaboration. Strange quark contributions to parity-violating asymmetries in the backward angle G0 electron scattering experiment, (2009).

[45] A. Coppens. Pion contamination for LD2 687 MeV ARS study. G0 Document 797-v1, Jefferson Laboratory, (2008).

[46] S.D. Covrig et al. The cryogenic target for the G0 experiment at jefferson lab. *Nuc. Ins. and Meth. in Phys. Res. A*, **551**:218–235, (2005).

[47] L. Diaconescu and M. J. Ramsey-Musolf. Vector analyzing power in elastic electron-proton scattering. *Physical Review C*, **70**:054003, (2004).

[48] T. Doi et al. Nucleon strangeness form factors from $N_f = 2 + 1$ clover fermion lattice QCD, (2009).

[49] C. Ellis. Electromagnetic radiative corrections for the G0 experiment at backward angles. G0 Document 840-v1, Jefferson Laboratory, September (2009).

[50] C. Ellis. Luminosity monitors for the Gzero backward angle measurement. G0 Document 845-v1, Jefferson Laboratory, September (2009).

[51] F. Englart and R. Brout. Broken symmetry and the mass of the gauge vector bosons. *Physical Review Letters*, **13**:321, (1964).

[52] Jens Erler, Andriy Kurylov, and Michael J. Ramsey-Musolf. Weak charge of the proton and new physics. *Physical Review D*, **68**:016006, (2003).

[53] B. W. Filippone and Xiangdong Ji. The spin structure of the nucleon. *ADV.NUCL.PHYS.*, **26**:1, (2001).

[54] K. Finelli. Calibration and performance characterization of Q^p_{weak} Region II drift chambers. VT Qweak elog (Drift Chamber) 79, Virgnia Tech, May (2009).

[55] M. Muether for the G^0 Collaboration. g^0 backward angle results, (2009).

[56] T. Forest. Region I tracker. Qweak Document 1118-v1, Jefferson Laboratory, (2009).

[57] C. Furget. RCS residual false asymmetry. G0 Document 821-v1, Jefferson Laboratory, (2009).

[58] C. Furget and P. Pillot. Deadtime correction addendum. G0 Document 697-v1, Jefferson Laboratory, (2007).

[59] S. Galster, H. Klein, J. Moritz, K. H. Schmidt, D. Wegener, and J. Bleckwenn. Elastic electron-deuteron scattering and the electric neutron form factor at four-momentum transfers 5 fm^{-2} ¡ q^2 ¡ 14 fm^{-2}. *Nuclear Physics B*, **32**:221–237, (1971).

[60] D. Gaskell. Private communation. Email regarding beam polarization.

[61] D. Gaskell. Beam polarization for G0 backward angle. Technical report, Jefferson Lab, 2008.

[62] J. Gasser, H. Leutwyler, and M. E. Sainio. Form factor of the sigma-term. *Physics Letters B*, **253**:260–264, (1991).

[63] J. Gasser, H. Leutwyler, and M. E. Sainio. Sigma-term update. *Physics Letters B*, **253**:252–259, (1991).

[64] M. Gorchtein. Dispersive contributions to e^+p/e^-p cross section ratio in forward regime. *Physics Letters B*, **644**:322–330, (2007).

[65] M. Gorchtein, P. A. M. Guichon, and M. Vanderhaeghen. Normal spin asymmetries in elastic electron-proton scattering. *Nuclear Physics A*, **755**:273–276, (2005).

[66] M. Gorchtein and C. J. Horowitz. Dispersion γZ box correction to the weak charge of the proton. *Physical Review Letters*, **102**:091806, (2009).

[67] J. M. Grames et al. Unique electron polarimeter analyzing power comparison and precision spin-based energy measurement. *Physical Review Special Topics - Accelerators and Beams*, **7**:042802, (2004).

[68] K. Grimm. Presentation at the PAVI04 conference. June (2004).

[69] Data Acquisition Group. CEBAF Online Data Aquisition, ongoing.

[70] F. Halzen and A. Martin. *Quarks and Leptons: An Introductory Course in Modern Particle Physics*. John Wiley & Sons, (1984).

[71] L. Hannelius et al. Beam tests of the Caltech prototype cerenkov counter. G0 Document 268-v1, Jefferson Laboratory, (2002).

[72] P.W. Higgs. Broken symmetries and the masses of the gauge bosons. *Physical Review Letters*, **13**:508, (1964).

[73] Universitt Mainz Institut fr Kernphysik. Photo- and electroproduction of pions, etas and kaons on the nucleon, (2007).

[74] G. M. Jones. A precision measurement of the weak mixing angle in møller scattering at low Q^2, (2004).

[75] D. B. Kaplan and A. Manohar. Strange matrix elements in the proton from neutral-current experiments. *Nuclear Physics B*, **310**:527–547, (1988).

[76] L. Kaufman. Transverse beam asymmetries measured from 4He and hydrogen targets. *The European Physical Journal A - Hadrons and Nuclei*, **32**:501–503, (2007).

[77] J. J. Kelly. Simple parametrization of nucleon form factors. *Physical Review C*, **70**:068202, (2004).

[78] P. King, S.P. Wells, and the G0 Collaboration. Measurement of the vector analyzing power in e-p scattering using the G0 forward angle apparatus. G0 Document 437-v1, Jefferson Laboratory, (2003).

[79] M. Kohl. Elastic form factors of the proton, neutron and deuteron. *Nuclear Physics A*, **805**:361c–368c, (2008).

[80] G. Krafft and A. Hofler. How the linac beam position monitors "work". *Jefferson Lab Technote*, 93-004, (1993).

[81] Jefferson Lab. completed exp. http://www.jlab.org/exp_prog/generated/6GeV/completed.html, (2009).

[82] J. Leacock. Luminosity monitor update. Qweak Document 1121-v1, Jefferson Laboratory, November (2009).

[83] J. Leacock. Presentation at the DNP09 conference. (2009).

[84] J. Leckey. Region 3 VDCs. Qweak Document 1112-v1, Jefferson Laboratory, (2009).

[85] L. Lee. G0 north american cryostat-exit detector manual. G0 Document 633-v1, Jefferson Laboratory, March (2006).

[86] D. B. Leinweber et al. Precise determination of the strangeness magnetic moment of the nucleon. *Physical Review Letters*, **94**:212001, (2005).

[87] D. B. Leinweber et al. Strange electric form factor of the proton. *Physical Review Letters*, **97**:022001–4, (2006).

[88] J. Liu, R. D. McKeown, and M. J. Ramsey-Musolf. Global analysis of nucleon strange form factors at low Q^2. *Physical Review C*, **76**:025202, (2007).

[89] F. E. Maas et al. Measurement of strange-quark contributions to the nucleon's form factors at Q^2=0.230 (GeV/c)^2. *Physical Review Letters*, **93**:022002, (2004).

[90] F. E. Maas et al. Evidence for strange-quark contributions to the nucleon's form factors at Q^2=0.108 (GeV/c)^2. *Physical Review Letters*, **94**:152001, (2005).

[91] F. E. Maas et al. Measurement of the transverse beam spin asymmetry in elastic electron-proton scattering and the inelastic contribution to the imaginary part of the two-photon exchange amplitude. *Physical Review Letters*, **94**:082001, (2005).

[92] D. Mack. low current monitoring with hall C BCM cavities. http://g0web.jlab.org/g0log/0703_archive/070328041403.html 136405, Jefferson Laboratory, (2007).

[93] D. Mack. Presentation at the DNP09 conference. (2009).

[94] J. Mammei. Luminosity monitor. http://www.phys.vt.edu/ jmammei/lumi_monitor.html, (2004).

[95] J. Mammei. Minitorus update. Qweak Document 218-v1, Jefferson Laboratory, November (2005).

[96] J. Mammei. Qweak: beam motion estimates. http://g0web.jlab.org/g0log/0703_archive/070328074812.html 136422, Jefferson Laboratory, (2007).

[97] J. Mammei. Target studies, (http://www.phys.vt.edu/ jmammei/for_greg.html), (2007).

[98] J. Mammei. Presentation at the PAVI09 conference. (2009).

[99] J. Mammei. Summary of cerenkov efficiencies for the backward running phase of the G^0 experiment. G0 Document 839-v1, Jefferson Laboratory, (2009).

[100] D. Marchand et al. G0 electronics and data acquisition (forward-angle measurements). *Nuc. Ins. and Meth. in Phys. Res. A*, **586**:251–269, (2008).

[101] J. Martin. Possibility to measure parity violation in DELTA photoproduction. G0 Document 226-v1, Jefferson Laboratory, November (2001).

[102] W. Melnitchouk. private communication with Fatiha Benmohktar. G0 elog, Analysis 325, (2009).

[103] G. A. Miller. Nucleon charge symmetry breaking and parity violating electron-proton scattering. *Phys. Rev. C*, **57**:1492–1505, (1998).

[104] L. W. Mo and Y. S. Tsai. Radiative corrections to elastic and inelastic ep and μp scattering. *Rev. Mod. Phys.*, **41**:205–235, (1969).

[105] M. Muether. Background asymmetry analysis for G0 backward angle elastic electron measurement. G0 Document 850-v1, Jefferson Laboratory, (2009).

[106] M. Muether. private communication, (2009).

[107] M. J. Musolf, T. W. Donnelly, J. Dubach, S. J. Pollock, S. Kowalski, and E. J. Beise. Intermediate-energy semileptonic probes of the hadronic neutral current. *Physics Reports*, **239**:1–178, (1994).

[108] J. Musson and M. Pitt. Beam diagnostics for qweak. Qweak Document 917-v1, Jefferson Laboratory, March (2009).

[109] K. Myers. Reducing backgrounds generated by the primary collimator. Qweak Document 851-v1, Jefferson Laboratory, November (2008).

[110] K. Myers. The beryllium target window background in GEANT3 and a comparison to aluminum. Qweak Document 950-v2, Jefferson Laboratory, May (2009).

[111] K. Myers. Private communication. final collimator email, (2009).

[112] K. Myers. Target window backgrounds: Detector radial location. Qweak Document 1096-v1, Jefferson Laboratory, November (2009).

[113] ALEPH DELPHI L3 OPAL and SLD Collaborations. Precision electroweak measurements on the Z resonance. *Physics Reports*, **427**:257–454, (2006).

[114] B. Pasquini and M. Vanderhaeghen. Resonance estimates for single spin asymmetries in elastic electron-nucleon scattering. *Physical Review C*, **70**:045206, (2004).

[115] M. M. Pavan, I. I. Strakovsky, R. L. Workman, and R. A. Arndt. The pion-nucleon sigma term is definitely large: results from a G.W.U. analysis of pion nucleon scattering data. *PIN NEWSLETT.*, **16**:110, (2002).

[116] S. Phillips. Møller polarimetry in the G0 experiment. Technical report, Jefferson Lab, 2006.

[117] M. Pitt. Private communation. Email regarding estimate of detector asymmetry.

[118] M. Pitt. Minitorus update. Qweak Document 508-v1, Jefferson Laboratory, October (2005).

[119] M. Pitt. Primary collimator working group report. Qweak Document 217-v5, Jefferson Laboratory, (2005).

[120] M. Pitt. Electroweak physics. (2006).

[121] M. Pitt. Results from low current beam test, March 2007. Qweak Document 1138-v1, Jefferson Laboratory, July (2007).

[122] G. Que'me'ner. Q^2 determination in the G^0 experiment. G0 Document 548-v1, G^0 France, (2005).

[123] M. J. Ramsey-Musolf and S. Su. Low-energy precision tests of supersymmetry. *Physics Reports*, **456**:1–88, (2008).

[124] D. Rios. Presentation at the PAVI09 conference. (2009).

[125] J. Schaub. Summary of pass 3, 4 linear regression problem, (2009).

[126] R. Schiavilla. private communication with E. J. Beise. email, (2006).

[127] R. Schiavilla, J. Carlson, and M. Paris. Parity-violating interaction effects in the np system. *Phys. Rev. C*, **70**, (2004).

[128] N. Simicevic. Design of the scintillators and light guides for the cryostat exit detector system. G0 Document 70-v1, Jefferson Laboratory, February (1999).

[129] C. K. Sinclair et al. Development of a high average current polarized electron source with long cathode operational lifetime. *Physical Review Special Topics - Accelerators and Beams*, **10**:023501, 2007.

[130] G. Smith. Quarterly report for FY07 quarter 4. Qweak Document 698-v1, Jefferson Laboratory, October (2007).

[131] G. Smith. Presentation at the PAVI09 conference. (2009).

[132] G. Smith. Quarterly report for FY09 quarter 3. Qweak Document 989-v2, Jefferson Laboratory, July (2009).

[133] G. Smith. Qweak liquid hydrogen target: Preliminary design and safety document. Qweak Document 1041-v2, Jefferson Laboratory, August (2009).

[134] D. T. Spayde et al. Parity violation in elastic electron-proton scattering and the proton's strange magnetic form factor. *Physical Review Letters*, **84**:1106, (2000).

[135] D. T. Spayde et al. The strange quark contribution to the proton's magnetic moment. *Physics Letters B*, **583**:79–86, (2004).

[136] J. A. Tjon, P. G. Blunden, and W. Melnitchouk. Detailed analysis of two-boson exchange in parity-violating e-p scattering. *Physical Review C*, **79**:055201–12, (2009).

[137] R. Tribble et al. The frontiers of nuclear science a long range plan, (2007).

[138] M. Vanderhaeghen. Two-photon physics. *Few-Body Systems*, **41**:103–115, (2007).

[139] R. Veenhof. Garfield - simulation of gaseous detectors, (2008).

[140] M. Versteegen. Cerenkov efficiency estimation; beam energy 362 MeV on LD2 target. G0 Document 764-v1, Jefferson Laboratory, (2008).

[141] M. Versteegen. Cerenkov efficiency estimation; beam energy 687 MeV on LD2 target. G0 Document 765-v1, Jefferson Laboratory, (2008).

[142] M. Versteegen. Status on global dead time correction. *G0 Document*, 736-v1, (2008).

[143] M. Versteegen. Mesure de la contribution trange aux proprits lectromagntiques des nuclons -Exprience G0-. G0 Document 849-v1, Jefferson Laboratory, October (2009).

[144] P. Wang, D. B. Leinweber, A. W. Thomas, and R. D. Young. Strange magnetic form factor of the proton at $Q^2 = 0.23 GeV^2$. *Physical Review C*, **79**:065202–7, (2009).

[145] S. P. Wells et al. Measurement of the vector analyzing power in elastic electron-proton scattering as a probe of the double virtual compton amplitude. *Physical Review C*, **63**:064001, (2001).

[146] S. Williamson, A. Kenyon, K. Nakahara, and D. Spayde. G0 superconducting magnet system operational safety procedure (update). G0 Document 289-v3, Jefferson Laboratory, December (2005).

[147] C. S. Wood, S. C. Bennett, D. Cho, B. P. Masterson, J. L. Roberts, C. E. Tanner, and C. E. Wieman. Measurement of parity nonconservation and an anapole moment in cesium. *Science*, **275**:1759–1763, (1997).

[148] C. Yan et al. Superharp – a wire scanner with absolute position readout for beam energy measurement at CEBAF. *Nuclear Instruments and Methods in Physics Research Section A: Accelerators, Spectrometers, Detectors and Associated Equipment*, **365**:261–267, (1995).

[149] R. D. Young, R. D. Carlini, A. W. Thomas, and J. Roche. Testing the standard model by precision measurement of the weak charges of quarks. *Physical Review Letters*, **99**:122003, (2007).

[150] R. D. Young and A. W. Thomas. Recent results on nucleon sigma terms in lattice QCD, (2009).

[151] G. P. Zeller et al. Precise determination of electroweak parameters in neutrino-nucleon scattering. *Physical Review Letters*, **88**:091802, (2002).

[152] Shi-Lin Zhu, S. J. Puglia, B. R. Holstein, and M. J. Ramsey-Musolf. Nucleon anapole moment and parity-violating ep scattering. *Physical Review D*, **62**:033008, (2000).

Appendix A

Kinematic Calculations

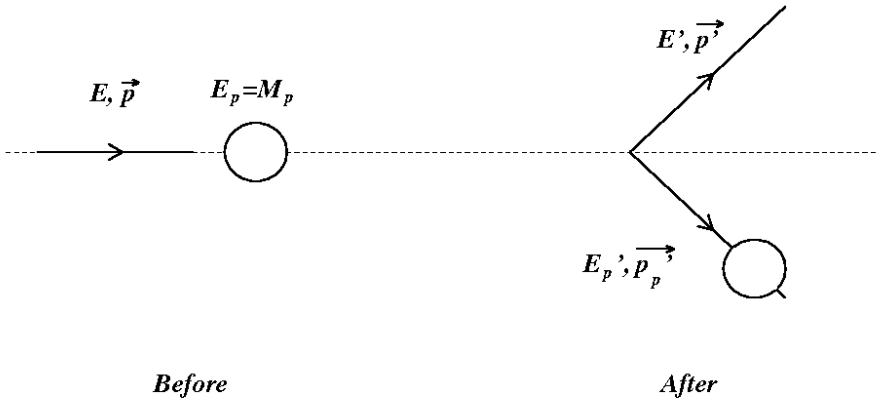

Figure A.1: Scattering diagram depicting electron-proton scattering with the kinematic quantities before and after the scattering labeled.

Scattering processes are described in terms of the Lorentz invariant quantity q^2, which is the square of the four momentum transferred by the exchange boson. Cross sections, form factors and asymmetries are in general all functions of Q^2. In this thesis the reaction of interest is elastic electron-proton (or quasi-elastic electron-deuteron) scattering (see Figure A.1). The incoming electron has energy E and momentum $\vec{p}$, while the proton is considered

to be at rest. In scattering from deuterium it is necessary to take into account the Fermi motion of the nucleons (see below). The electron scattered energy and momentum are given by E' and $\vec{p}'$ while the proton scattered energy and momentum are given by E'_P and $\vec{P}'$ The energy of the exchange boson is given by

$$\nu = E' - E \tag{A.1}$$

and the three momentum transfer is given by

$$\vec{q} = \vec{p} - \vec{p}' \tag{A.2}$$

The square of the four momentum transfer $q = (\nu, \vec{q})$ is then given by

$$q^2 = \nu^2 - \vec{q}^2 = -Q^2 \tag{A.3}$$

where the positive value $Q^2 = -q^2$ is used.

The square of the four momentum transfer, Q^2, is a function of the incident electron energy E, the scattered electron energy E' and the scattering angle θ

$$Q^2 = 4EE' sin^2 \frac{\theta}{2} \tag{A.4}$$

Because we are primarily interested in elastic scattering, the scattered energy and angle are related by

$$E' = \frac{E}{1 + \frac{2E}{M_p} sin^2 \frac{\theta}{2}} \tag{A.5}$$

where M_p is the mass of the proton. So the Q^2 can be written as a function of incident

energy and scattering angle

$$Q^2 = \frac{4E^2 sin^2\frac{\theta}{2}}{1 + \frac{2E}{M_p} sin^2\frac{\theta}{2}} \tag{A.6}$$

where the incident energy is the beam energy. So the Q^2 is determined by the scattered electron angle.

In quasi-elastic scattering the Fermi motion of the struck nucleon within the nucleus must be taken into account. In elastic scattering the energy transfer can be related to the $Q^2 = 2M_p\nu$. In the scattering from deuterium, the neutron or proton can have an initial momentum, rather than assuming the momentum is zero. The prescription for accounting for the Fermi motion is to treat the energy transfer, ν, as having a symmetric distribution around an average value

$$\nu_0 = \frac{\vec{q}^2}{2M_p} + S \tag{A.7}$$

with a width given by

$$\sigma_\nu = \frac{|\vec{q}|}{M_p}\sqrt{\frac{1}{3}\left\langle \vec{P}^2 \right\rangle} \tag{A.8}$$

where S is the effective average nuclear potential. The Fermi momentum is related to the mean square momentum by $P_F = 5/3\left\langle \vec{P}^2 \right\rangle$. The maximum Fermi momentum used in the deuterium simulations is $\sim 120 MeV/c$.

Inelastic scattering involves exciting the struck nucleon, with the lowest energy resonance being Δ, with a mass of 1232 MeV/c^2. In a neutral current interaction, charge is not exchanged so the Δ^+ charge state is the one that is observed in the case of scattering from the proton, and the Δ^0 is observed in the scattering from the neutron. The excited nucleon

decays primarily via the following reactions:

$$\begin{aligned} \Delta^+ &\rightarrow p + \pi^0 \\ \Delta^0 &\rightarrow n + \pi^0 \\ or\ \Delta^0 &\rightarrow p + \pi^- \end{aligned} \tag{A.9}$$

though non-resonant inelastic scattering also occurs, for example, the following reactions

$$\vec{e} + p \rightarrow e + p + \pi^0 \tag{A.10}$$

$$\vec{e} + n \rightarrow e + n + \pi^0 \tag{A.11}$$

in which a neutral pion may be produced without the production of a Δ. In any case, the scattered electron has less energy from inelastic scattering than for elastic scattering, resulting in the kinematic separation of the elastic and inelastic electrons in the electron matrix.

Appendix B

Statistical Uncertainties

It is common to see the fractional statistical uncertainty in a counting experiment as $\partial N/N = 1/\sqrt{N}$. The statistical uncertainty in an asymmetry measurement, however, is $1/\sqrt{N_{tot}}$ where N_{tot} is the number of counts in a given asymmetry measurement. The G^0 helicity structure is a quartet, which means that the asymmetry is formed from the difference of two states of one helicity and two states of opposite helicity, or for example

$$A = \frac{N_1 - N_2 - N_3 + N_4}{N_1 + N_2 + N_3 + N_4} \tag{B.1}$$

where N_i is the number of counts in a given helicity state. The statistical error on the asymmetry is given by

$$\sigma_A^2 = \sum_i \sigma_{N_i}^2 \left(\frac{\partial A}{\partial N_i}\right)^2 \tag{B.2}$$

where the statistical error on the number of counts in a given helicity state is $\sigma_{N_i} = \sqrt{N_i}$. The partial derivatives of the asymmetry with respect to the number of counts in a given helicity state is

$$\frac{\partial A}{\partial N_i} = \frac{\pm 4N}{N_{tot}^2} \tag{B.3}$$

where each of the $N_i \approx N$ and the total number of counts in a given quartet is $N_{tot} = \sum_i N_i = 4N$. The statistical error on the uncertainty is then given by

$$\sigma_A^2 = \sum_i \sigma_{N_i}^2 \left(\frac{\partial A}{\partial N_i}\right)^2 = \sum_i N_i \left(\frac{4N_i}{N_{tot}^2}\right)^2 = 4N\frac{16N^2}{N_{tot}^4} = N_{tot}\frac{N_{tot}^2}{N_{tot}^4} = \frac{1}{N_{tot}} \tag{B.4}$$

making the statistical uncertainty on a given asymmetry measurement equal to

$$\sigma_{A_{stat}} \approx \frac{1}{\sqrt{N_{tot}}} \tag{B.5}$$

making it relatively easy to estimate the ratio to counting statistics (RCS) by comparing the measured asymmetry width to the expected statistical width.

Appendix C

Matrix Solution to a Least Squares Fit

C.1 The Method

The general form of the problem is to fit a set of data with an equation:

$$y(x_i) = \sum_k a_k f_k(x_i) \tag{C.1}$$

where the data value y_i is approximated by the function $y(x_i)$ which is a sum of functions of the independent variable x_i, multiplied by coefficients a_k. The coefficients are determined by minimizing the square of the difference between the error weighted value of the data and the function, that is, χ^2 minimization. The χ^2 is defined as

$$\chi^2 = \sum_i \frac{1}{{\sigma_i}^2}(y_i - y(x_i))^2 \tag{C.2}$$

and the minimum can be found by differentiating this expression with respect to the coefficients a_k and setting the result equal to zero. This results in a set of system of N coupled linear equations,

$$\frac{\partial \chi^2}{\partial a_k} = -2\sum_i \frac{1}{{\sigma_i}^2}\frac{\partial y(x_i)}{\partial a_k}(y_i - y(x_i)) = -2\sum_i \frac{f_k(x_i)}{{\sigma_i}^2}(y_i - y(x_i)) = 0 \tag{C.3}$$

for determining the minimum χ^2, which can be expressed in matrix form.

As a simple example, consider a fit to data using a 2^{nd} order polynomial. We would like to represent the system of linear equations obtained for the χ^2 minimization in equation(s) C.3 in matrix form. The equation of the polynomial can be represented as a matrix equation:

$$y(x) = a_0 + a_1 x + a_2 x^2 \Rightarrow \vec{y} = \vec{\mathbf{A}}\vec{x} \tag{C.4}$$

where, naturally, the coefficients are the same for each data point. The vectors $\vec{y}$ and $\vec{x}$ and the matrix are defined as follows[1]:

$$\vec{y} = \begin{pmatrix} y(x_1) \\ y(x_2) \\ \vdots \\ y(x_n) \end{pmatrix}, \quad \vec{\mathbf{A}} = \begin{pmatrix} 1 & x_1 & {x_1}^2 \\ 1 & x_2 & {x_2}^2 \\ \vdots & \vdots & \vdots \\ 1 & x_n & {x_n}^2 \end{pmatrix} \quad and \quad \vec{x} = \begin{pmatrix} a_0 \\ a_1 \\ a_2 \end{pmatrix} \tag{C.5}$$

Normally the solution to such an equation would be to multiply by the inverse of $\vec{\mathbf{A}}$ on both sides of the equation to solve for $\vec{x}$. In general, however, there is no reason to expect the matrices of linear systems to be square (in which case the number of data points is equal to the number of parameters in the fit). The solution is to multiply both sides of the equation

[1]Note here that the matrix $\vec{\mathbf{A}}$ contains the functions of the x_i's, and the vector $\vec{x}$ is a vector of the coefficients, despite the unfortunate notation.

by the 'pseudo-inverse' of the matrix $\vec{\mathbf{A}}$. The pseudo-inverse is obtained by multiplying a matrix by its transpose, which results in a square matrix, $\vec{\alpha} = \vec{\mathbf{A}}^T \vec{\mathbf{A}}$. Then the pseudo-inverse of $\vec{\mathbf{A}}$ is the inverse of $\vec{\alpha}$.

If the errors on all the data points were the same, the equation

$$\vec{x} = \vec{\alpha}^{-1}\vec{y} \tag{C.6}$$

(with data values y_i in the place of the $y(x_i)$) would provide the solution to equation C.3 for a fit with three parameters, though the resulting error matrix would not properly take into account the errors. The errors can be taken into account in practice by dividing each data value by the error on each data point, as well as dividing each element in a given row in the matrix $\vec{\mathbf{A}}$ by the error on the corresponding data point. In this simple example, I can write the equation out:

$$\begin{pmatrix} \frac{f_1(x_1)}{\sigma_1} & \frac{f_1(x_2)}{\sigma_2} & . & \frac{f_1(x_N)}{\sigma_N} \\ \frac{f_2(x_1)}{\sigma_1} & \frac{f_2(x_2)}{\sigma_2} & . & \frac{f_2(x_N)}{\sigma_N} \\ \frac{f_3(x_1)}{\sigma_1} & \frac{f_3(x_2)}{\sigma_2} & . & \frac{f_3(x_N)}{\sigma_N} \end{pmatrix} \begin{pmatrix} \frac{y_1}{\sigma_1} \\ \frac{y_2}{\sigma_2} \\ \vdots \\ \frac{y_N}{\sigma_N} \end{pmatrix} = \begin{pmatrix} \frac{f_1(x_1)}{\sigma_1} & \frac{f_1(x_2)}{\sigma_2} & . & \frac{f_1(x_N)}{\sigma_N} \\ \frac{f_2(x_1)}{\sigma_1} & \frac{f_2(x_2)}{\sigma_2} & . & \frac{f_2(x_N)}{\sigma_N} \\ \frac{f_3(x_1)}{\sigma_1} & \frac{f_3(x_2)}{\sigma_2} & . & \frac{f_3(x_N)}{\sigma_N} \end{pmatrix} \begin{pmatrix} \frac{f_1(x_1)}{\sigma_1} & \frac{f_2(x_1)}{\sigma_1} & \frac{f_3(x_1)}{\sigma_1} \\ \frac{f_1(x_2)}{\sigma_2} & \frac{f_2(x_2)}{\sigma_2} & \frac{f_3(x_2)}{\sigma_@} \\ \vdots & \vdots & \vdots \\ \frac{f_1(x_N)}{\sigma_N} & \frac{f_2(x_N)}{\sigma_N} & \frac{f_3(x_N)}{\sigma_N} \end{pmatrix} \begin{pmatrix} a_1 \\ a_2 \\ a_3 \end{pmatrix} \tag{C.7}$$

where $f_1(x_i) = 1$, $f_2(x_i) = x_i$ and $f_3(x_i) = x_i^2$. This is consistent with the definition of the problem given in Bevington[25], where he begins with the equivalent of $\vec{\mathbf{A}}^T\vec{y} = \vec{\mathbf{A}}^T\vec{\mathbf{A}}\vec{x}$, with the errors applied in this way. More generally, for a given row, l, the equation can be written as

$$\sum_i \frac{1}{{\sigma_i}^2} y_i f_l(x_i) = \sum_{k,i} \frac{a_k}{{\sigma_i}^2} f_k(x_i) f_l(x_i) \tag{C.8}$$

where l is used to indicate the index in the sum over functions in the transpose of $\vec{\mathbf{A}}$. The solution to this set of linear equations is the same as that in C.3, substituting the right hand

side of equation C.1 for $y(x_i)$ (and accounting for the indices properly).

For the purposes of the fits described here, the number of data points is equal to the number of cells in CED/FPD space - 126. Instead of fitting with a polynomial, the yields (or asymmetries) from the various simulation processes are scaled. The solution is exactly the same as described above, where the $f_k(x_i)$ are the values of the simulated quantity for each process, k, in each cell, i, although they are much more complex functions of cell number. The dependence originates because of the rough kinematic separation, rather like a crude drift chamber, provided by a CED/FPD coincidence. These functions are then integrated, via simulation, over the finite acceptance of each CED/FPD pair, resulting in discrete function values in each cell.

C.2 The Matrices

The matrix shown in Equation C.9 is the matrix of the cell-by-cell yields for each process that goes into the 16 parameter fits listed in Table C.1. For a weighted fit each row (corresponding to individual cells) would be divided by the error, σ_i (Eq. C.12), for that cell. The matrix for the asymmetry fit is shown in Equation C.10.

$$\vec{\mathbf{A}} = \begin{pmatrix}
Y_{ela1} & Y_{ine1} & Y_{Al+He1} & Y_{pi0_1} & 0 & 0 & 0 & 0 & 0 & 0 & 0 & 0 & 0 & 0 & 0 & 0 \\
Y_{ela2} & Y_{ine2} & Y_{Al+He2} & Y_{pi0_2} & 0 & 0 & 0 & 0 & 0 & 0 & 0 & 0 & 0 & 0 & 0 & 0 \\
\vdots & & & & & & & \vdots & & & & & & & & \vdots \\
Y_{ela56} & Y_{ine56} & Y_{Al+He56} & Y_{pi0_{56}} & 1 & fpd & fpd^2 & 0 & 0 & 0 & 0 & 0 & 0 & 0 & 0 & 0 \\
Y_{ela57} & Y_{ine57} & Y_{Al+He57} & Y_{pi0_{57}} & 1 & fpd & fpd^2 & 0 & 0 & 0 & 0 & 0 & 0 & 0 & 0 & 0 \\
Y_{ela58} & Y_{ine58} & Y_{Al+He58} & Y_{pi0_{58}} & 1 & fpd & fpd^2 & 0 & 0 & 0 & 0 & 0 & 0 & 0 & 0 & 0 \\
\vdots & & & & & & & \vdots & & & & & & & & \vdots \\
Y_{ela70} & Y_{ine70} & Y_{Al+He70} & Y_{pi0_{70}} & 0 & 0 & 0 & 1 & fpd & fpd^2 & 0 & 0 & 0 & 0 & 0 & 0 \\
Y_{ela71} & Y_{ine71} & Y_{Al+He71} & Y_{pi0_{71}} & 0 & 0 & 0 & 1 & fpd & fpd^2 & 0 & 0 & 0 & 0 & 0 & 0 \\
Y_{ela72} & Y_{ine72} & Y_{Al+He72} & Y_{pi0_{72}} & 0 & 0 & 0 & 1 & fpd & fpd^2 & 0 & 0 & 0 & 0 & 0 & 0 \\
\vdots & & & & & & & \vdots & & & & & & & & \vdots \\
Y_{ela84} & Y_{ine84} & Y_{Al+He84} & Y_{pi0_{84}} & 0 & 0 & 0 & 0 & 0 & 0 & 1 & fpd & fpd^2 & 0 & 0 & 0 \\
Y_{ela85} & Y_{ine85} & Y_{Al+He85} & Y_{pi0_{85}} & 0 & 0 & 0 & 0 & 0 & 0 & 1 & fpd & fpd^2 & 0 & 0 & 0 \\
Y_{ela86} & Y_{ine86} & Y_{Al+He86} & Y_{pi0_{86}} & 0 & 0 & 0 & 0 & 0 & 0 & 1 & fpd & fpd^2 & 0 & 0 & 0 \\
Y_{ela87} & Y_{ine87} & Y_{Al+He87} & Y_{pi0_{87}} & 0 & 0 & 0 & 0 & 0 & 0 & 1 & fpd & fpd^2 & 0 & 0 & 0 \\
\vdots & & & & & & & \vdots & & & & & & & & \vdots \\
Y_{ela100} & Y_{ine100} & Y_{Al+He100} & Y_{pi0_{100}} & 0 & 0 & 0 & 0 & 0 & 0 & 0 & 0 & 0 & 1 & fpd & fpd^2 \\
Y_{ela101} & Y_{ine101} & Y_{Al+He101} & Y_{pi0_{101}} & 0 & 0 & 0 & 0 & 0 & 0 & 0 & 0 & 0 & 1 & fpd & fpd^2 \\
Y_{ela102} & Y_{ine102} & Y_{Al+He102} & Y_{pi0_{102}} & 0 & 0 & 0 & 0 & 0 & 0 & 0 & 0 & 0 & 1 & fpd & fpd^2 \\
\vdots & & & & & & & \vdots & & & & & & & & \vdots \\
Y_{ela126} & Y_{ine126} & Y_{Al+He126} & Y_{pi0_{126}} & 0 & 0 & 0 & 0 & 0 & 0 & 0 & 0 & 0 & 0 & 0 & 0
\end{pmatrix} \tag{C.9}$$

$$\vec{\mathbf{A}} = \begin{pmatrix} A'_{ela1} & A'_{ine1} & A'_{Al+He1} & 0 \\ A'_{ela2} & A'_{ine2} & A'_{Al+He2} & 0 \\ \vdots & & & \vdots \\ A'_{ela56} & A'_{ine56} & A'_{Al+He56} & 1 \\ A'_{ela57} & A'_{ine57} & A'_{Al+He57} & 1 \\ A'_{ela58} & A'_{ine58} & A'_{Al+He58} & 1 \\ \vdots & & & \vdots \\ A'_{ela70} & A'_{ine70} & A'_{Al+He70} & 1 \\ A'_{ela71} & A'_{ine71} & A'_{Al+He71} & 1 \\ A'_{ela72} & A'_{ine72} & A'_{Al+He72} & 1 \\ \vdots & & & \vdots \\ A'_{ela84} & A'_{ine84} & A'_{Al+He84} & 1 \\ A'_{ela85} & A'_{ine85} & A'_{Al+He85} & 1 \\ A'_{ela86} & A'_{ine86} & A'_{Al+He86} & 1 \\ A'_{ela87} & A'_{ine87} & A'_{Al+He87} & 1 \\ \vdots & & & \vdots \\ A'_{ela100} & A'_{ine100} & A'_{Al+He100} & 1 \\ A'_{ela101} & A'_{ine101} & A'_{Al+He101} & 1 \\ A'_{ela102} & A'_{ine102} & A'_{Al+He102} & 1 \\ \vdots & & & \vdots \\ A'_{ela126} & A'_{ine126} & A'_{Al+He126} & 0 \end{pmatrix} \tag{C.10}$$

C.3 Uncertainties

In order to get a good χ^2 it is necessary to provide an artificial yield to fit the low FPDs in each of the CEDs where there is no simulation yield that could possibly reproduce those rates. I chose to fit those FPDs with a different quadratic in each CED. Figure 4.26 shows the results of the quadratic fits in the particular cells where they are used. There is no physics in these fits; they are used solely to provide rate where there is none in the simulation, and there is no tail that extends beyond the actual cells. The default fit has 16 parameters because it has the 4 simulation processes, where the aluminum and helium rates have been combined, as well as quadratic fits in CEDs 5-8. An additional 13 parameter fit was performed with no quadratic fit in CED 5. The coefficients on the simulation processes are fairly stable whether I use the quadratic fits or not, but the χ^2/ndf is close to 1 when the quadratic fits are there, and range up to 8 if they are not (see Table C.1).

Description	a_{ela}	a_{ine}	a_{alu}	a_{pi0}	χ^2/ndf
4, flat	1.00 +/- 0.02	0.95 +/- 0.04	2.65 +/- 0.17	0.63 +/- 0.02	1.75
13, flat	1.00 +/- 0.02	0.95 +/- 0.04	2.66 +/- 0.17	0.59 +/- 0.03	0.84
16, flat	1.01 +/- 0.02	0.96 +/- 0.04	2.66 +/- 0.17	0.57 +/- 0.03	0.80
4, %	0.91 +/- 0.02	0.93 +/- 0.09	3.07 +/- 0.24	0.79 +/- 0.04	7.85
13, %	0.92 +/- 0.02	0.96 +/- 0.09	3.13 +/- 0.24	0.64 +/- 0.04	1.33
16, %	0.92 +/- 0.02	0.96 +/- 0.09	3.14 +/- 0.24	0.61 +/- 0.04	1.23

Table C.1: Dilution fit coefficients for various fit scenarios. In the description the number refers to the number of parameters in the fit.

For the purposes of the fits shown in Table C.1, the aluminum and helium (elastic and inelastic) yields were all combined into one total yield. The other contributions are the elastic, the inelastic, the pi0 and quadratic fits to particular low fpds in CEDs 5-8 (see the matrix in Equation C.9 for the details). The total scaled simulation yield in each cell i is the sum of the simulated yield for each process multiplied by the cerenkov efficiency [99] in

that cell and the coefficient determined by the fit for that process,

$$Y_{scaledsim,total_i} = a_{elai}Y_{elai} + a_{inei}Y_{inei} + a_{Al+Hei}Y_{Al+Hei} + a_{pi0_i}Y_{pi0_i} + a_{quad_i}Y_{quad_i} \quad \text{(C.11)}$$

where $Y_{process_i}=\epsilon_i Y'_{process_i}$ and $Y'_{process_i}$ is the raw simulation yield and ϵ_i is the cerenkov efficiency in the cell. The "quad yields" are just quadratic functions of fpd in the specific cells. The quad yields do not extend beyond the particular cells in which they are used to allow the fit to better match the yields in those cells; without them the reduced χ^2 is very large even though the coefficients on the simulation processes are consistent.

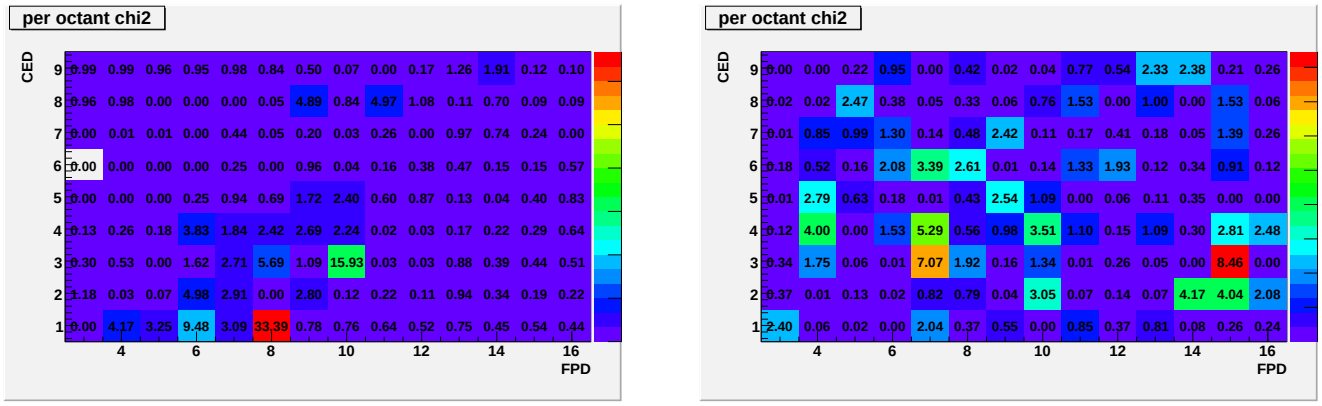

a b

Figure C.1: The cell-by-cell χ^2 values from the yield (a) and asymmetry (b) fit.

The error on the dilutions includes uncertainties in the cerenkov efficiencies, the simulated yields and the data yields. Four "schemes" were considered for the calculation of the errors. As in most of the plots and tables in this document, the results discussed below are for fits to the octant average yields or asymmetries unless otherwise stated.

1. The error that is assumed for the data yield is a 6% error on the yield except in cells with $\leq 5Hz/\mu A$ where 100% error on the yield in that cell is assumed. The simulation error is added in quadrature with this error and then used to weight the fit:

$$\sigma_i^2 = {\sigma_{data}}_i^2 + {\sigma_{sim}}_i^2 \tag{C.12}$$

2. Same as above, except the simulation error is is not added before the fit, but is added in quadrature with the fit errors later.

3. The error is determined from the fit, assuming it is the same in every cell, and is obtained by setting $\chi^2/ndf \approx 1$. An error of $1.5Hz/\mu A$ per cell is obtained. The simulation error is added in quadrature with the fit errors after the fit.

4. Same as above, except the simulation errors are used to inflate the flat data error going into the fit; a data error of $1.0Hz/\mu A$ per cell is obtained.

In all cases the error on the simulated yield includes the error on the cerenkov efficiency and the statistical error on the yield from the simulation. If the simulation error is not added to the data error before the fit, an error analysis on equation C.11 reveals that the uncertainties from the simulation yields need to be added with the uncertainties on the coefficients if they are to be taken into account. The more traditional thing to do is to include the simulation errors in the weighting of the fit (as in schemes 1 and 4), similar to what would be done in practice if there were a finite bin size in the independent variable. In this case it is mostly the statistical error on the simulation. The same error that is used to weight the cells is used in the calculation of the χ^2.

An error of $1.5Hz/\mu A$ in each cell is assumed for the calculation of the reduced χ^2 for each of the fits shown in Tables C.1 and C.2 for comparison purposes. This corresponds to a

# par	Error	Al	a_{ela}	a_{ine}	a_{alu}	a_{hel}	a_{pi0}	χ^2/ *ndf*
4	flat	sim	1.00 +/- 0.02	0.95 +/- 0.04	2.65 +/- 0.17		0.63 +/- 0.02	1.75
4	flat	et	0.88 +/- 0.02	0.87 +/- 0.04	3.27 +/- 0.17		0.51 +/- 0.03	1.31
5	flat	sim	1.01 +/- 0.02	0.95 +/- 0.04	2.07 +/- 0.93	3.5 +/- 1.4	0.63 +/- 0.02	1.76
13	flat	sim	1.00 +/- 0.02	0.95 +/- 0.04	2.66 +/- 0.17		0.59 +/- 0.03	0.84
13	flat	et	0.93 +/- 0.02	0.96 +/- 0.04	2.77 +/- 0.18		0.50 +/- 0.03	0.82
14	flat	sim	1.01 +/- 0.02	0.96 +/- 0.04	2.03 +/- 0.93	3.6 +/- 1.4	0.59 +/- 0.03	0.85
16	flat	sim	1.01 +/- 0.02	0.96 +/- 0.04	2.66 +/- 0.17		0.57 +/- 0.03	0.80
16	flat	et	0.93 +/- 0.02	0.97 +/- 0.04	2.75 +/- 0.18		0.48 +/- 0.03	0.80
17	flat	sim	1.01 +/- 0.02	0.96 +/- 0.04	2.01 +/- 0.93	3.7 +/- 1.4	0.57 +/- 0.03	0.81
4	%	sim	0.91 +/- 0.02	0.93 +/- 0.09	3.07 +/- 0.24		0.79 +/- 0.04	7.85
4	%	et	0.71 +/- 0.02	0.48 +/- 0.08	4.48 +/- 0.19		0.56 +/- 0.04	4.37
5	%	sim	0.93 +/- 0.03	0.91 +/- 0.09	1.69 +/- 1.30	5.5 +/- 2.3	0.79 +/- 0.04	7.90
13	%	sim	0.92 +/- 0.02	0.96 +/- 0.09	3.13 +/- 0.24		0.64 +/- 0.04	1.33
13	%	et	0.89 +/- 0.02	0.99 +/- 0.08	2.72 +/- 0.21		0.54 +/- 0.04	1.28
14	%	sim	0.93 +/- 0.03	0.94 +/- 0.09	1.73 +/- 1.30	5.6 +/- 2.3	0.64 +/- 0.04	1.33
16	%	sim	0.92 +/- 0.02	0.96 +/- 0.09	3.14 +/- 0.24		0.61 +/- 0.04	1.23
16	%	et	0.89 +/- 0.02	1.00 +/- 0.08	2.68 +/- 0.21		0.52 +/- 0.04	1.22
17	%	sim	0.93 +/- 0.03	0.94 +/- 0.09	1.74 +/- 1.30	5.6 +/- 2.3	0.60 +/- 0.04	1.23
4	flat	no ine	1.07 +/- 0.02	1.41 +/- 0.02	1.94 +/- 0.20		0.64 +/- 0.02	2.26
5	flat	no ine	1.08 +/- 0.02	1.41 +/- 0.02	1.24 +/- 1.03	3.0 +/- 1.6	0.64 +/- 0.02	2.28
13	flat	no ine	1.07 +/- 0.02	1.42 +/- 0.02	1.95 +/- 0.20		0.60 +/- 0.03	1.41
14	flat	no ine	1.08 +/- 0.02	1.42 +/- 0.02	1.19 +/- 1.03	3.1 +/- 1.6	0.60 +/- 0.03	1.42
16	flat	no ine	1.07 +/- 0.02	1.42 +/- 0.02	1.96 +/- 0.20		0.58 +/- 0.03	1.38
17	flat	no ine	1.08 +/- 0.02	1.42 +/- 0.02	1.17 +/- 1.03	3.2 +/- 1.6	0.58 +/- 0.03	1.39
4	%	no ine	0.99 +/- 0.02	1.69 +/- 0.06	2.46 +/- 0.28		0.81 +/- 0.04	8.56
5	%	no ine	0.99 +/- 0.03	1.69 +/- 0.06	2.69 +/- 1.47	2.1 +/- 2.5	0.81 +/- 0.04	8.63
13	%	no ine	1.00 +/- 0.02	1.73 +/- 0.06	2.48 +/- 0.28		0.66 +/- 0.04	2.14
14	%	no ine	0.99 +/- 0.03	1.73 +/- 0.06	2.70 +/- 1.47	2.1 +/- 2.5	0.66 +/- 0.04	2.16
16	%	no ine	1.00 +/- 0.02	1.74 +/- 0.06	2.49 +/- 0.28		0.63 +/- 0.04	2.07
17	%	no ine	1.00 +/- 0.03	1.74 +/- 0.06	2.70 +/- 1.47	2.1 +/- 2.5	0.63 +/- 0.04	2.09

Table C.2: Dilution fit coefficients for various fit scenarios.

2.5% error in the highest rate cells, and naturally provides a higher percentage error in the lower rate cells. In these tables only error schemes 1 and 3 are considered. The flat error consistently gives a better reduced χ^2, and the fits that include the aluminum and helium inelastic simulated yields work best.

The chosen default is a 16 parameter fit, using the simulated aluminum yields, with error scheme 4. Somewhat by design the 16 parameter fit yields the best reduced χ^2, and in most cases if this is the only consideration then the empty target data yields a better fit. However, the simulated aluminum yields are used in the final fit simply because it is assumed that the elastic yield coefficient should be 1, and in all cases where the empty target data were used, it seems to reduce the elastic coefficient significantly. The simulated aluminum yields do not fit the empty target data very well, but because the flyswatter yields are reproducible, it is currently assumed that it is the empty target data that are flawed, rather than the simulated yields. Error scheme 4 will yield smaller reduced χ^2 values, mostly because the errors are bigger than in scheme 3, and since this is what is more traditionally done scheme 4 is what was chosen.

The error on the asymmetries includes uncertainties in the dilutions in addition to the simulated and data asymmetries. The additional issue here is the problem of what error to assign the pi0 asymmetry (which doesn't actually go into the fit because there would be a zero in every cell for it's value), but an error as large as 10 ppm doesn't have much effect on the final asymmetry fit. The effect of varying the number of fit parameters as in the dilution fits is also negligible because the dominant contribution to the uncertainty is the error on the measured asymmetry.

Appendix D

Additional Plots and Tables

Contained in this appendix are additional plots or tables for the various analyses that did not fit in the text. Some plots that appear in the main text will be repeated here for ready comparison. Plots related to the Q_{weak} target boiling tests and the acceptance optimization are shown. In addition there are plots from the G^0 Q^2 sensitivity studies, including the energy measurements during the four major run periods.

D.1 Q_{weak} Target Boiling Tests

The Q_{weak} target boiling tests performed in March 2007, at the end of the G^0 backward running, involved running the target with various raster sizes, fan speeds and helicity reversal rates. There were two helicity reversal rates, the nominal G^0 30 Hz and 250 Hz. In addition, square raster sizes of 1.2x1.2 mm^2 and 1.8x1.8 mm^2 were compared. The circulating fan speed was also increased by 5x from 8 Hz to 40 Hz in order to gauge the effects. Figure D.1 shows examples of LUMI widths for a current of $\sim 25 \mu A$, and Figure D.2 shows plots of LUMI widths vs. current for various conditions for the different luminosity monitors.

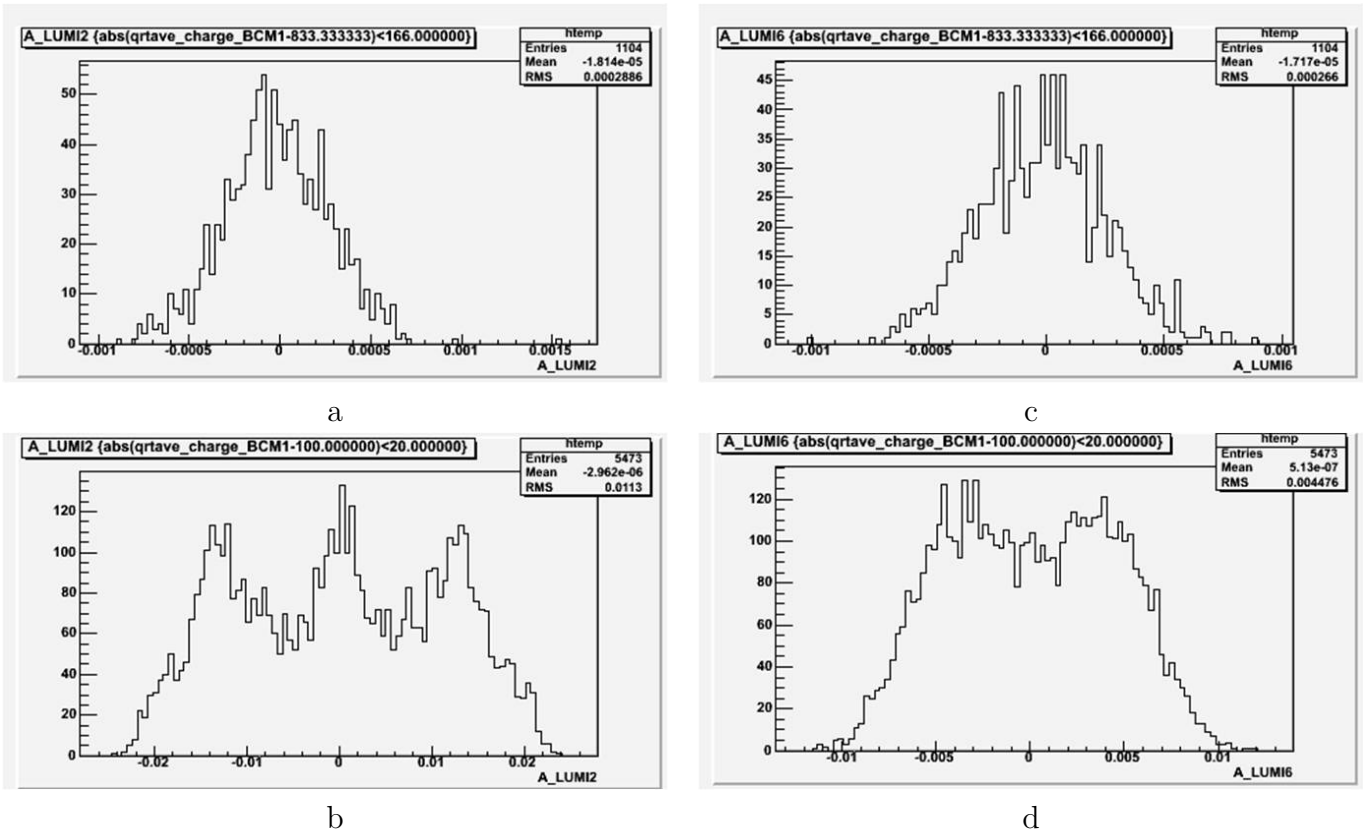

Figure D.1: Examples of LUMI widths for a fan speed of 8 Hz and a 1.2x1.2 mm^2 fast raster for helicity reversal rates of 30 Hz (LUMI2, a and LUMI6 b) and 250 Hz (LUMI2, c and LUMI6 d) for an approximate beam current of 25 μA.

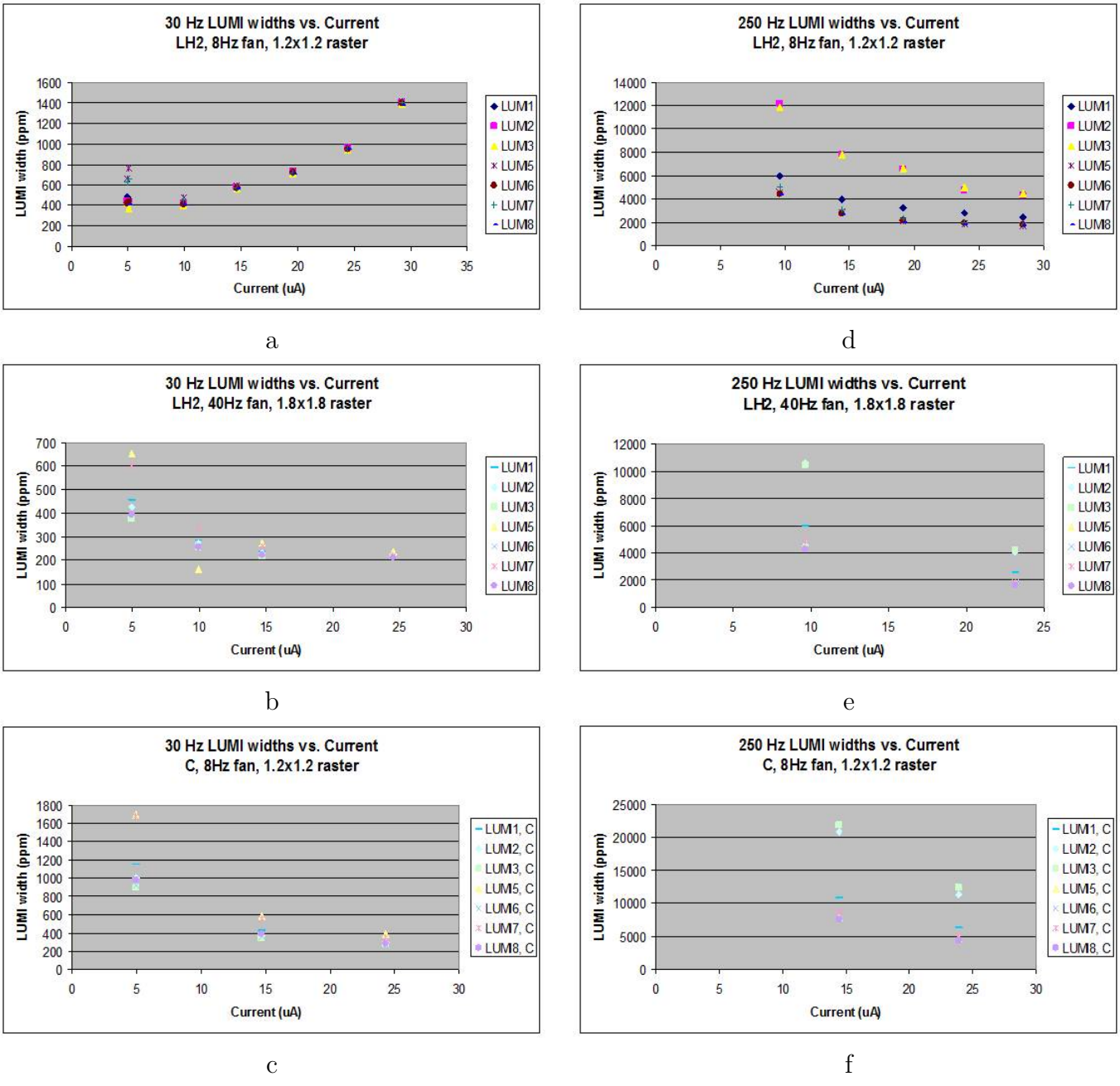

Figure D.2: Lumi widths vs. beam current for various combinations of fan speed, fast raster size and helicity reversal rate, described in the titles for each plot.

D.2 Q_{weak} Acceptance Study

As part of the Q_{weak} collimator optimization the position of the main detector quartz bars was also studied (see Figure D.3). For a given collimator design, the rate, mean Q^2, error on Q_W^p and the inelastic percentage were calculated as a function of the lower edge of the bar in the upper octant, or "lower x" in order to find the optimum position of the bars for each iteration of the collimator design. The figure of merit was originally estimated as the rate$\times < Q^2 >^2$ (because the asymmetry is proportional to the Q^2), but the true figure of merit is the error on Q_W^p. Unfortunately, even though the error on Q_W^p has a minimum, the inelastic percentage increases as the lower x of the bar is increased, so the optimum position is one that keeps the inelastic percentage low while giving as small an error as possible, though not necessarily the minimum. In addition to the position and size of the collimator openings and the position of the quartz bars, the field of the QTOR could be varied from its nominal setting (BFIL=1), and the results of two higher field settings (increased by 2% and 4%) are shown in the plots as well.

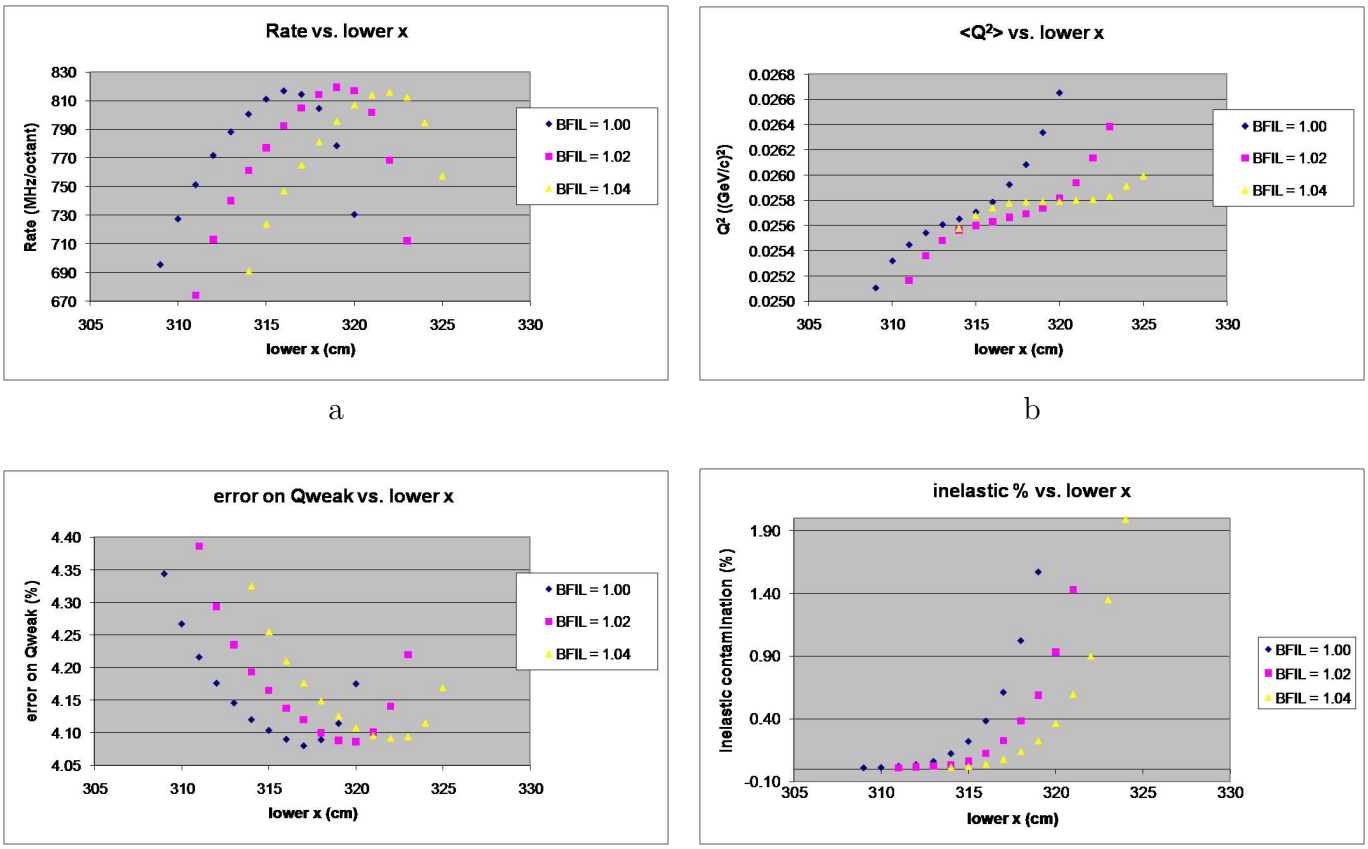

Figure D.3: The rate as a function of the x position of the lower edge of the main detector quartz bar (a). The $< Q^2 >$ as a function of the x position of the lower edge of the main detector quartz bar (b). The error on Q_W^p as a function of the x position of the lower edge of the main detector quartz bar (c). The inelastic percentage as a function of the x position of the lower edge of the main detector quartz bar (d).

D.3 Locus Definitions in CED/FPD Space

The data are conveniently represented in "matrix plots" which show the average values of a particular quantity for each CED/FPD coincidence with a color-coded plot. The CED number is on the y-axis, while the FPD number is on the x-axis. A CED/FPD coincidence is related to the angle and position that the particle enters the magnetic field, as well as the particle momentum, giving a crude but sufficient kinematic separation. Elastic events lie in particular cells, called a locus. There is also a locus for inelastic events, as well as a pion locus in the pion matrix. The locus definitions are chosen using the simulation, and depend only on beam energy. The yield distribution is slightly different for the hydrogen vs. deuterium, so the yield matrix for both targets at each energy is shown. The elastic electron locus in each case is outlined in black. The loci have the same definitions in the transverse analysis.

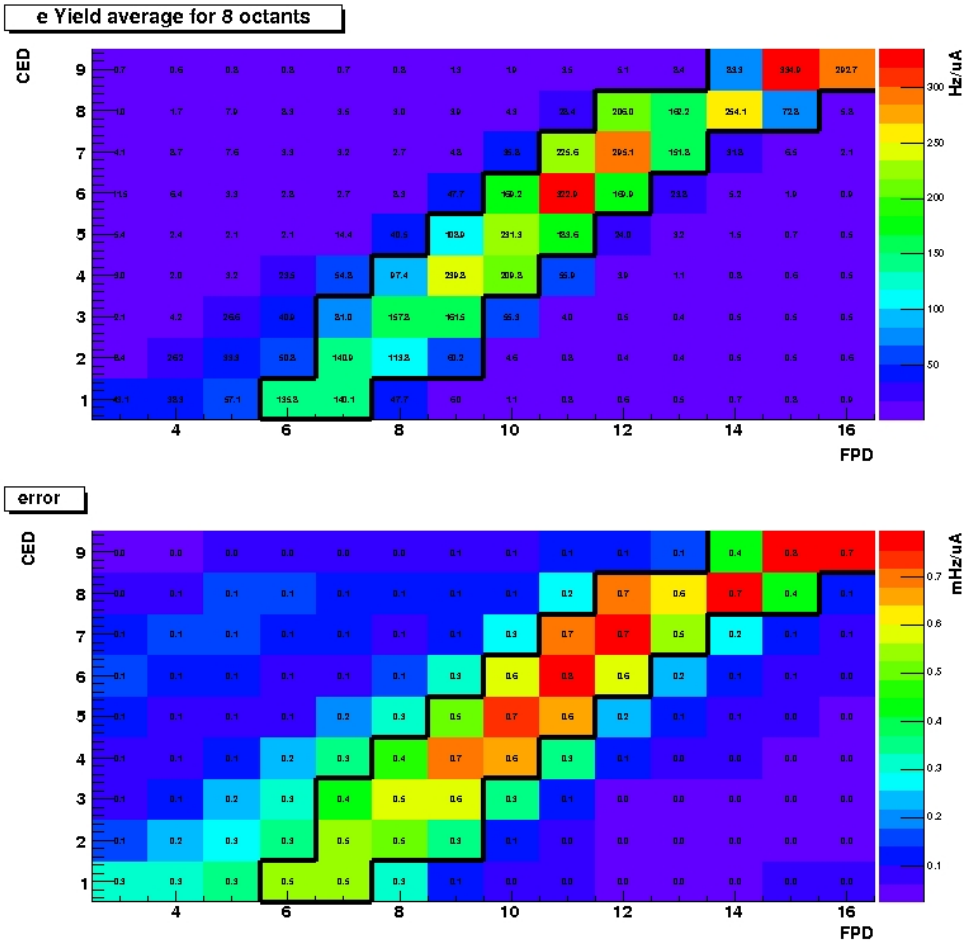

Figure D.4: Locus definition and yield matrix for the H362 dataset.

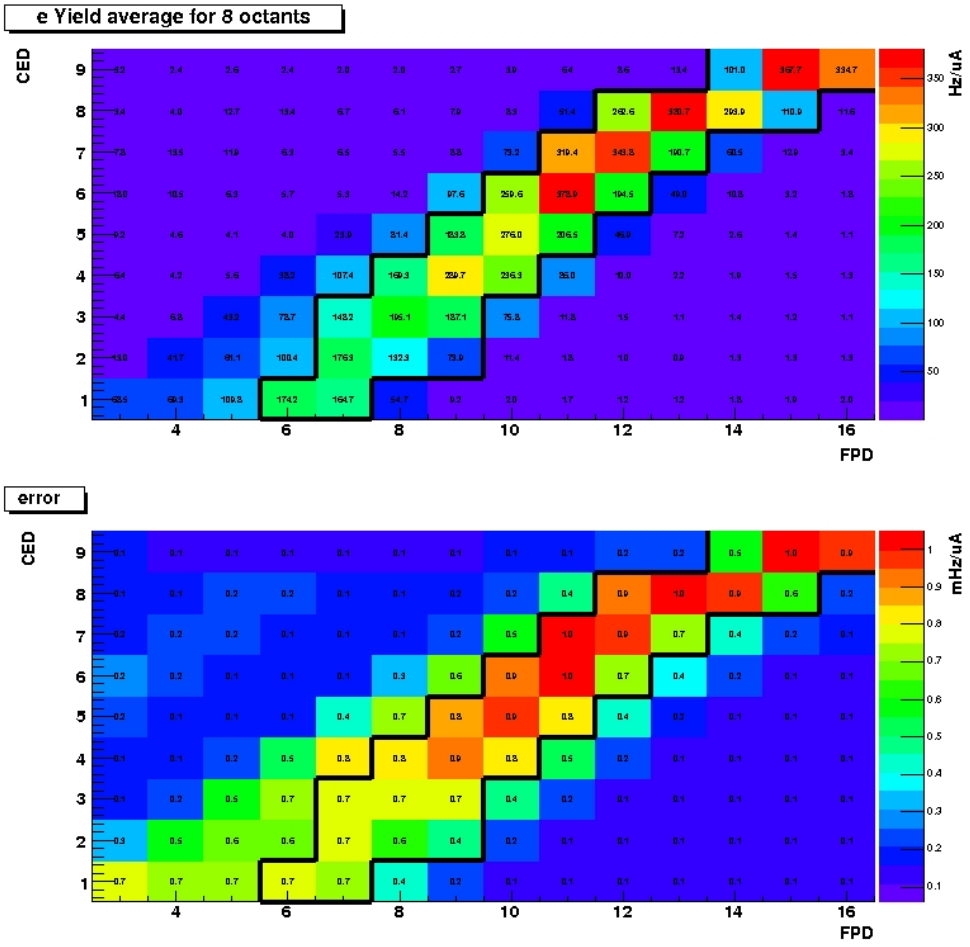

Figure D.5: Locus definition and yield matrix for the D362 dataset.

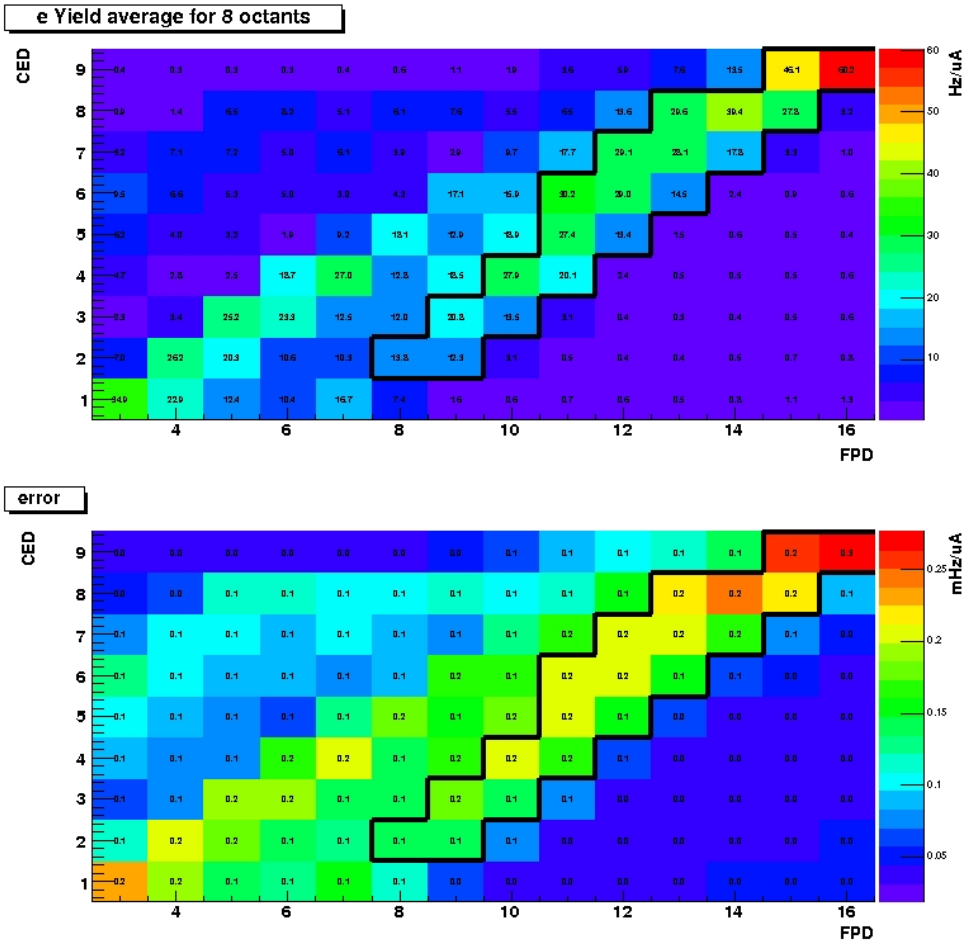

Figure D.6: Locus definition and yield matrix for the H687 dataset.

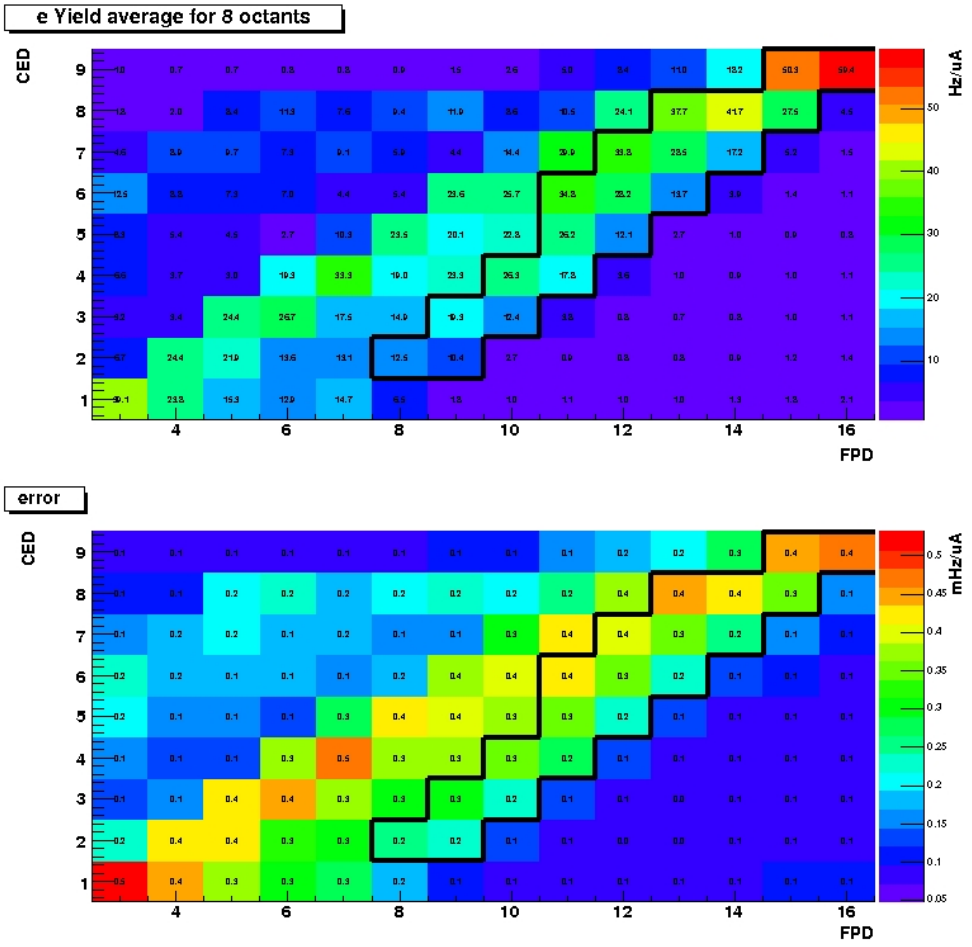

Figure D.7: Locus definition and yield matrix for the D687 dataset.

D.4 Q^2 Determination Plots

D.4.1 Sensitivity Study

These plots are from the sensitivity study described in section 4.3.1. For each variable the results of the study for each target/energy combination are shown, with the label underneath. The 362 MeV results are on the top, the 687 MeV results are on the bottom, and the deuterium results are on the left and the hydrogen results are on the right. The result of the fit is also plotted.

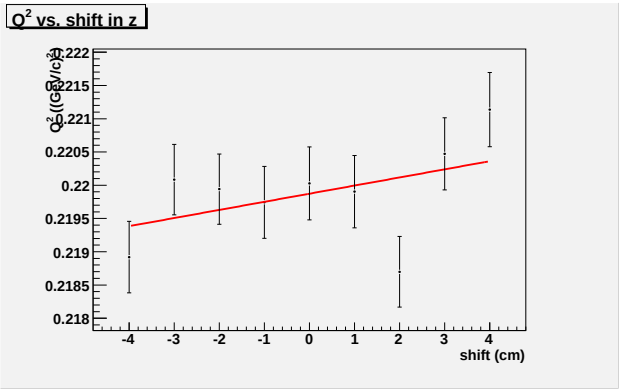

LD2 362

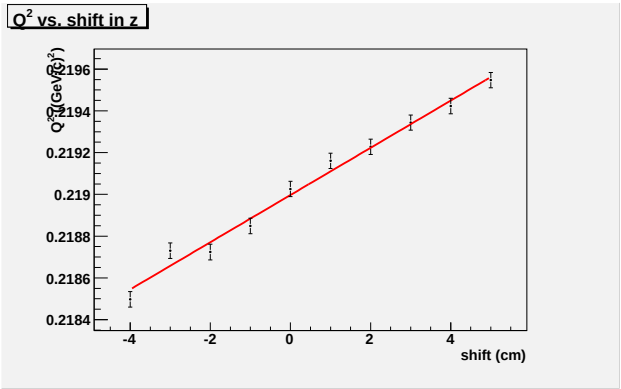

LH2 362

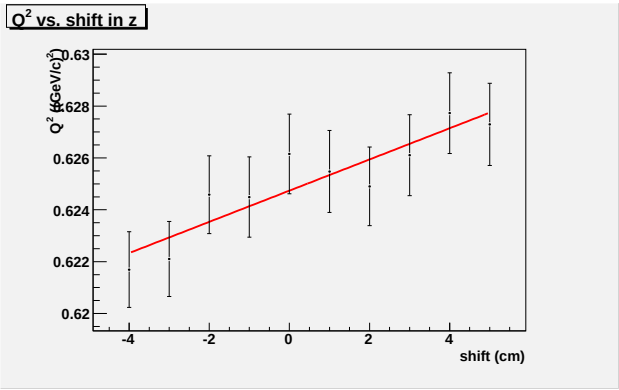

LD2 687

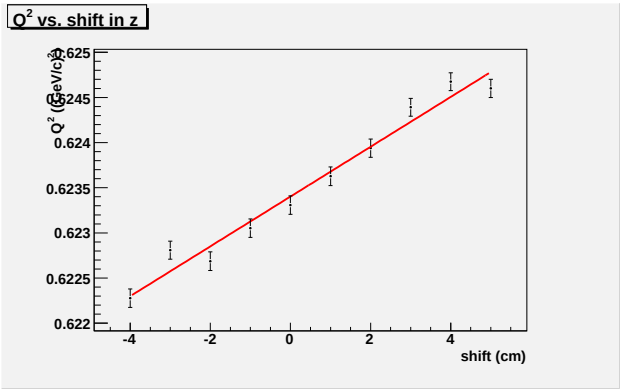

LH2 687

Figure D.8: Q^2 as a function of a shift in z of the detectors for all target/energy combinations.

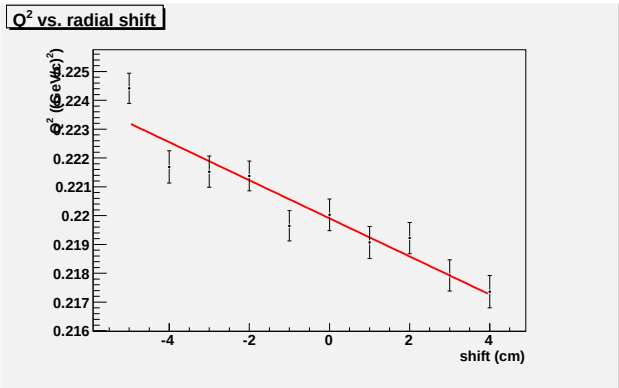

LD2 362

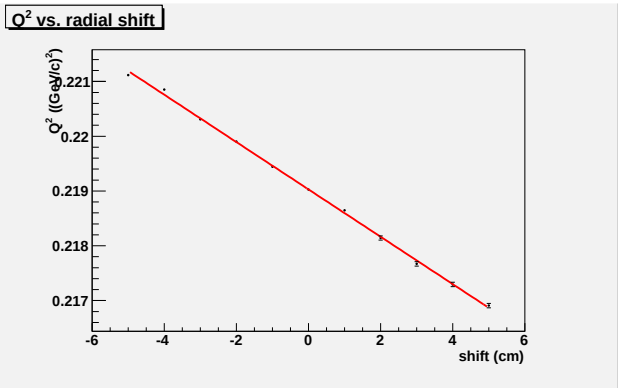

LH2 362

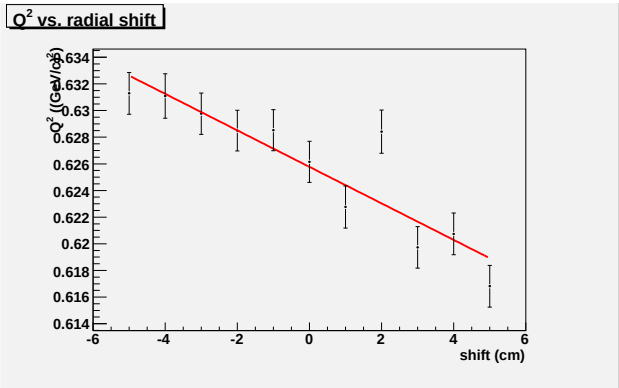

LD2 687

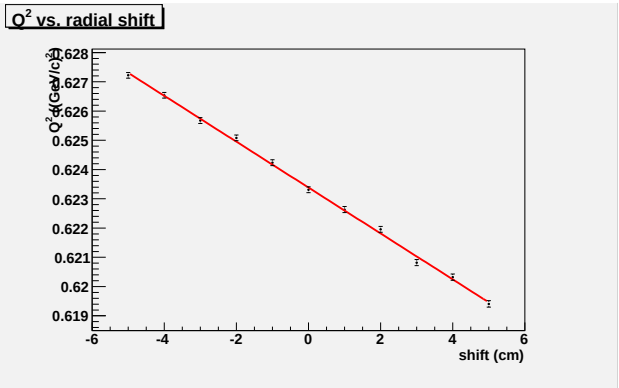

LH2 687

Figure D.9: Q^2 as a function of a shift in radial position of the detectors for all target/energy combinations.

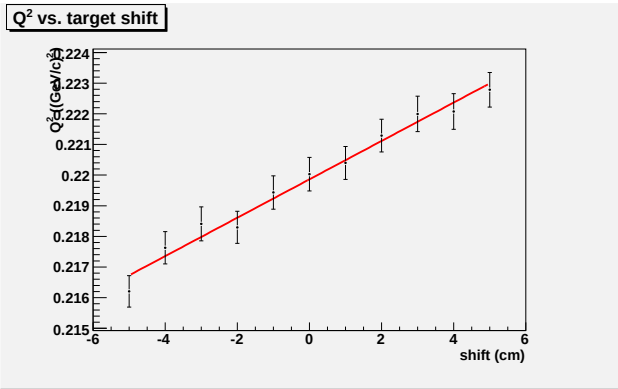

LD2 362

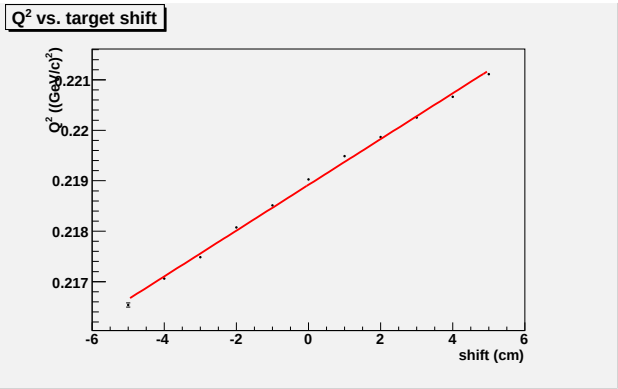

LH2 362

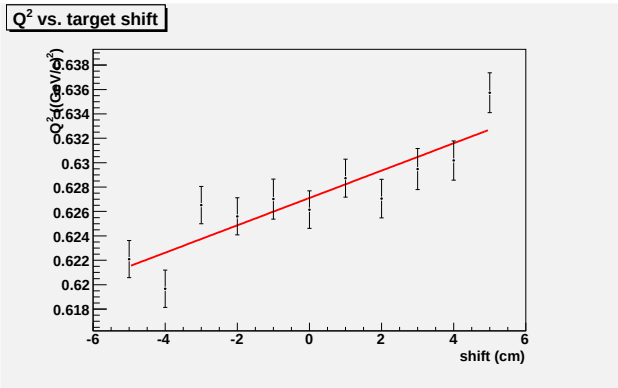

LD2 687

LH2 687

Figure D.10: Q^2 as a function of a shift in energy for all target/energy combinations.

LD2 362

LH2 362

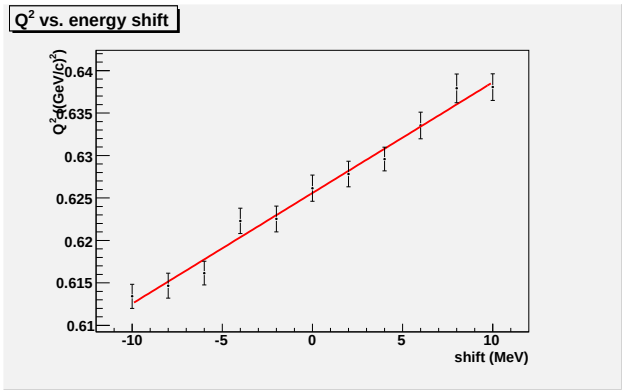

LD2 687

LH2 687

Figure D.11: Q^2 as a function of a shift in energy for all target/energy combinations.

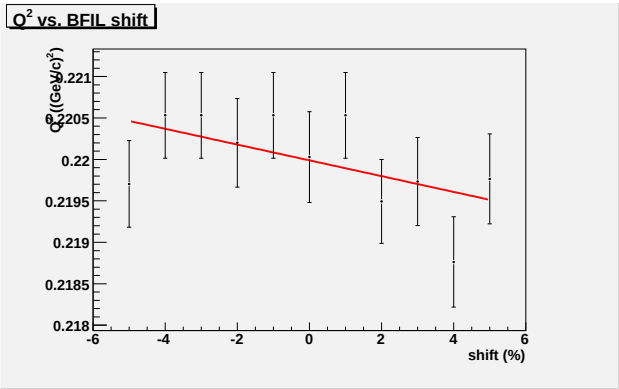

LD2 362

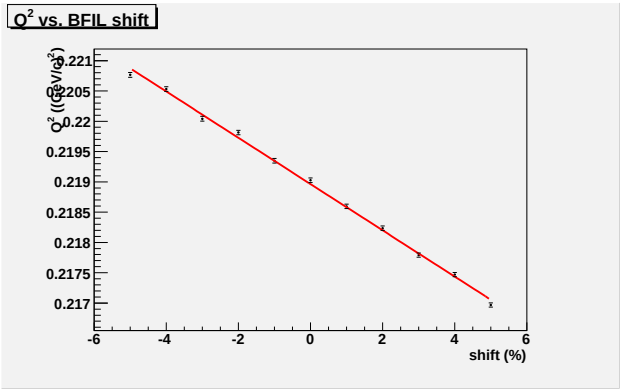

LH2 362

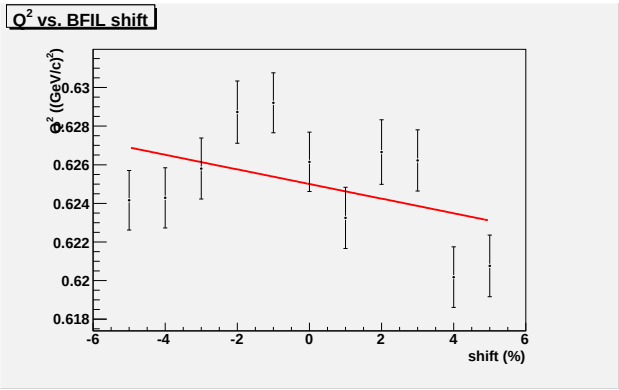

LD2 687

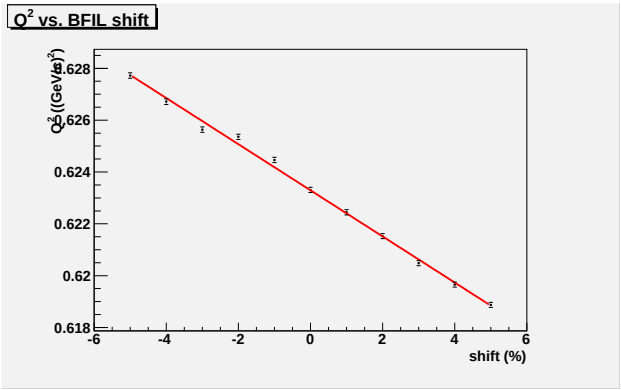

LH2 687

Figure D.12: Q^2 as a function of a shift in magnetic field for all target/energy combinations.

D.4.2 Energy Measurements

These plots are of the energy recorded in the run starts (blue points) in each run period, as well as the measured energy in each period, either using the Hall C arc method or the measurement from Hall A. The only exception is the Winter 2007 "'measurement"' which is actually scaled from the Summer 2006 measurement using the run starts. See section 4.3.3 for more details.

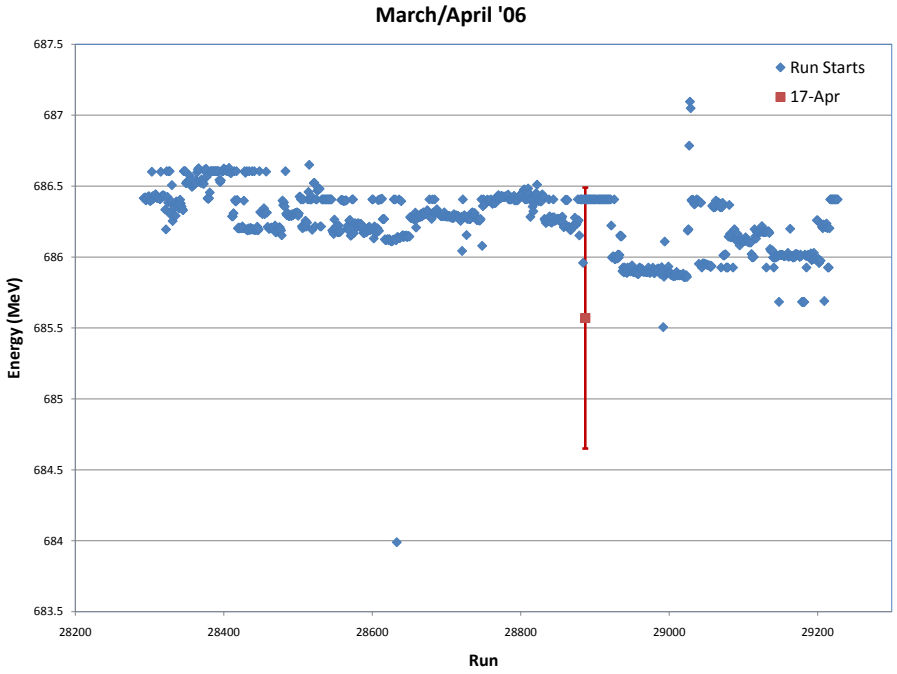

Figure D.13: Energy from run starts vs. run number with measured energy at approximate time in March 2006.

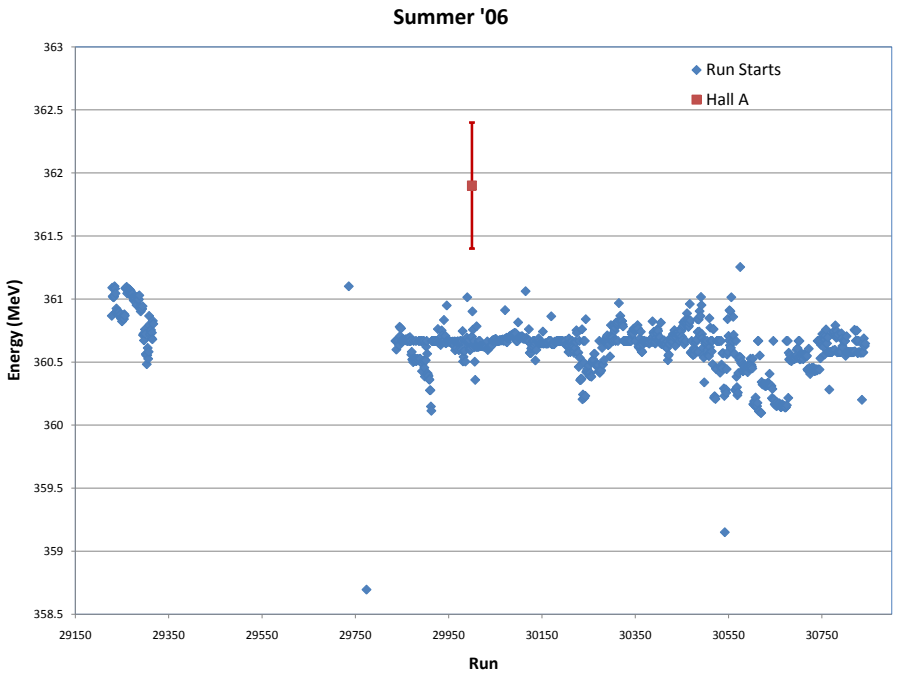

Figure D.14: Energy from run starts vs. run number with measured energy at approximate time in the summer '06.

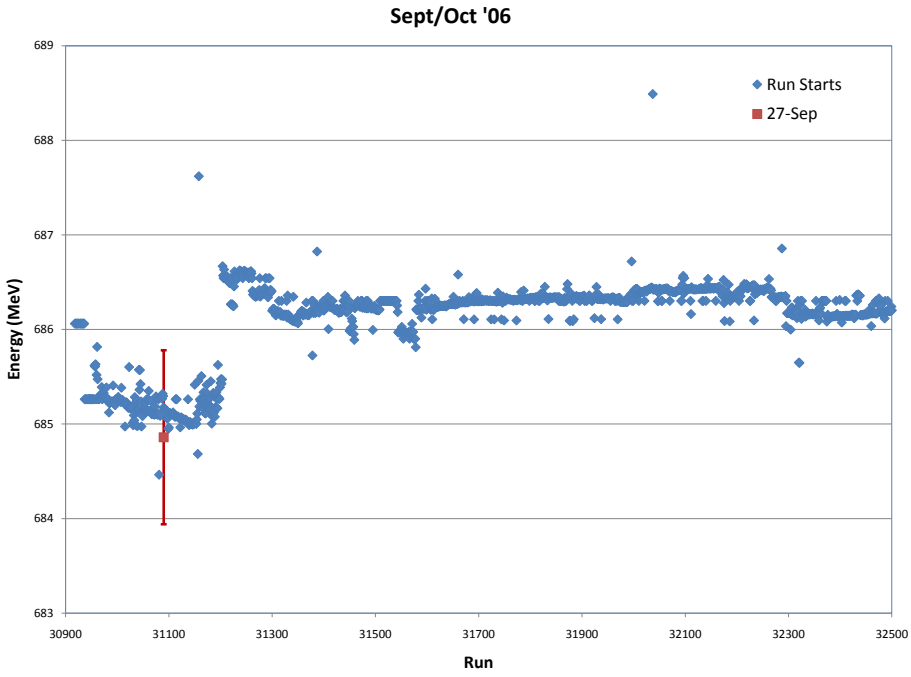

Figure D.15: Energy from run starts vs. run number with measured energy at approximate time in September 2006.

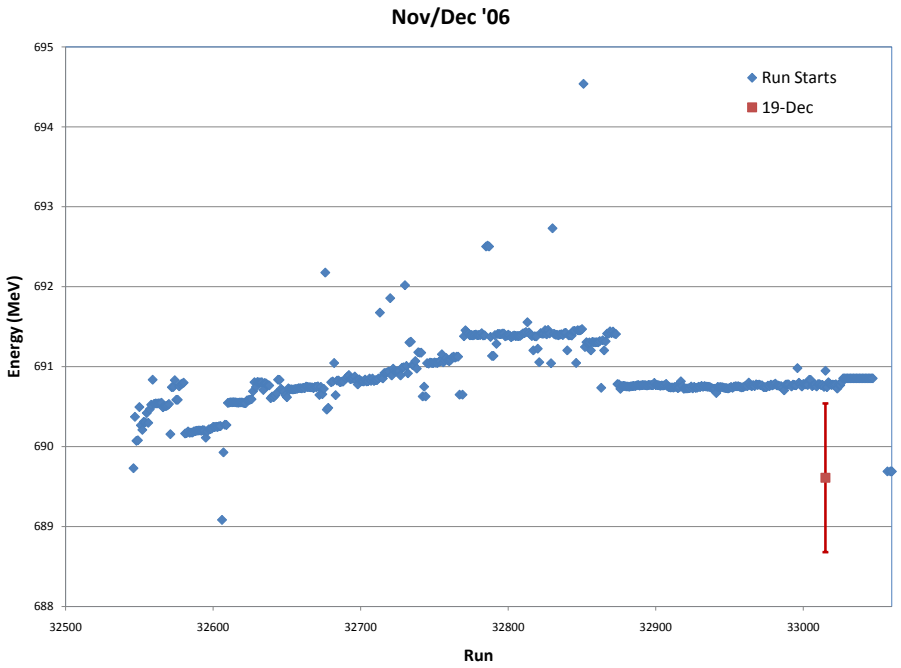

Figure D.16: Energy from run starts vs. run number with measured energy at approximate time in December 2006.

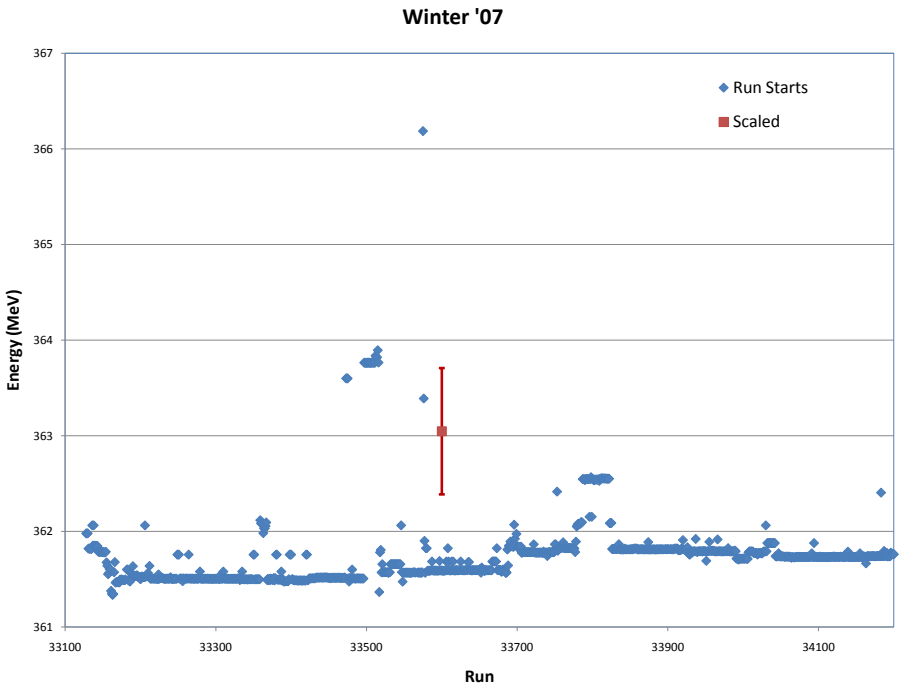

Figure D.17: Energy from run starts vs. run number with measured energy at approximate time in winter '07.

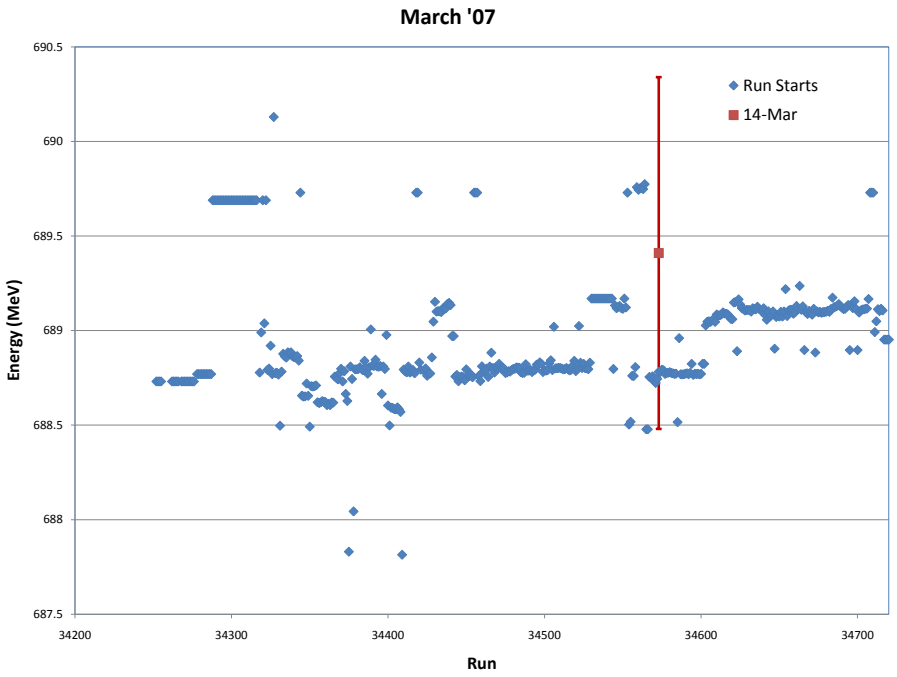

Figure D.18: Energy from run starts vs. run number with measured energy at approximate time in March 2007.

D.5 The Background Asymmetry Correction

D.5.1 Dilutions Plots

Because there are 7 individual processes - elastic, inelastic, pi0, aluminum entrance window, aluminum exit window and helium and helium window (and the inelastic counterparts of the aluminum and helium) it is difficult to represent them all on one plot. So they have been combined here in several plots in a way that hopefully makes some useful comparisons.

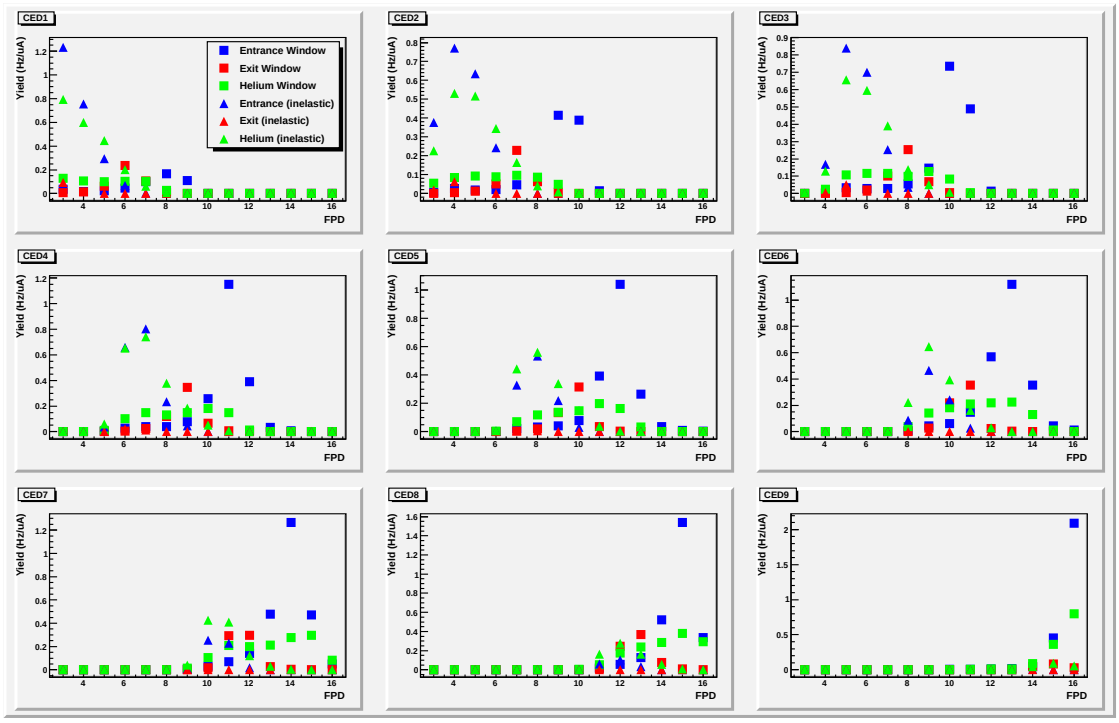

Figure D.19: The 'elastic' and 'inelastic' yield contributions from the aluminum windows.

The largest contribution to the aluminum yield is from the entrance window, but there

is also a significant contribution from the helium window (see Figure D.19) and also from the helium. The largest contribution to the total background yield in the matrix overall is the pi0 (Dalitz) yield. Luckily, however, the contribution from the pi0 reaction is small in most cells in the elastic locus, except for CED 9, FPDs 15 and 16 (see Figure D.20).

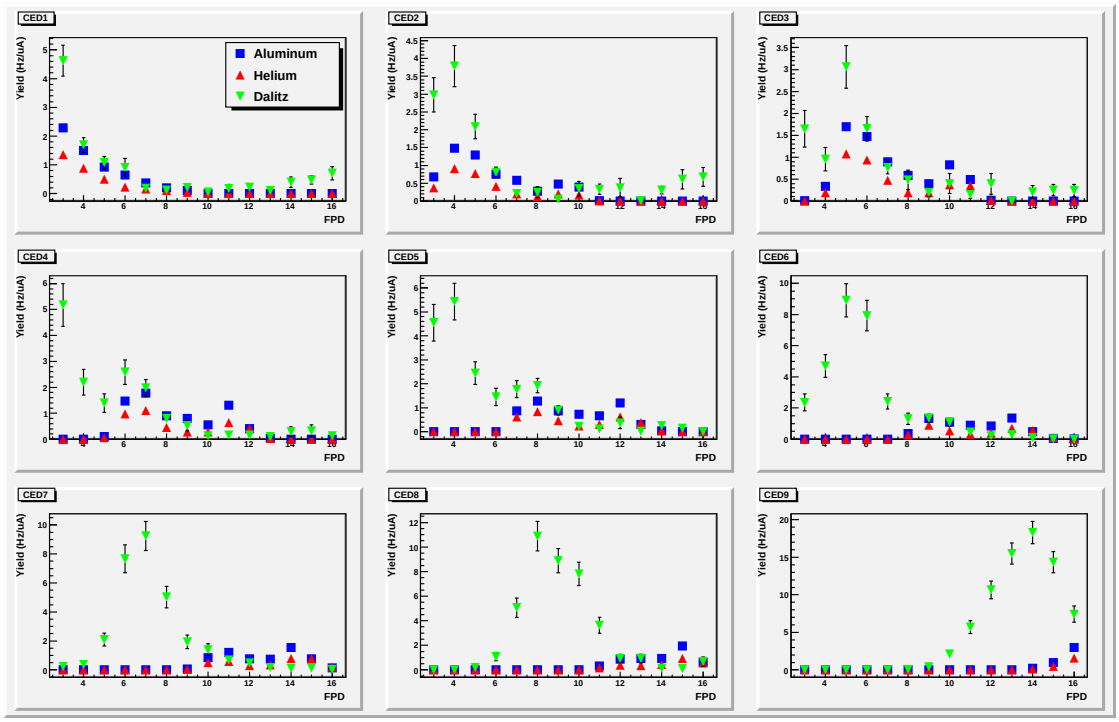

Figure D.20: The total aluminum and helium rates compared to the pi0 yields.

The total background yields are also compared to the inelastic and elastic yields (see Figure D.21). Another goal of this analysis was to provide inelastic dilutions (see Figure 4.27). While the inelastic yield is a relatively small contribution to the elastic dilution, the elastic yields are a significant fraction of the yield in the inelastic locus.

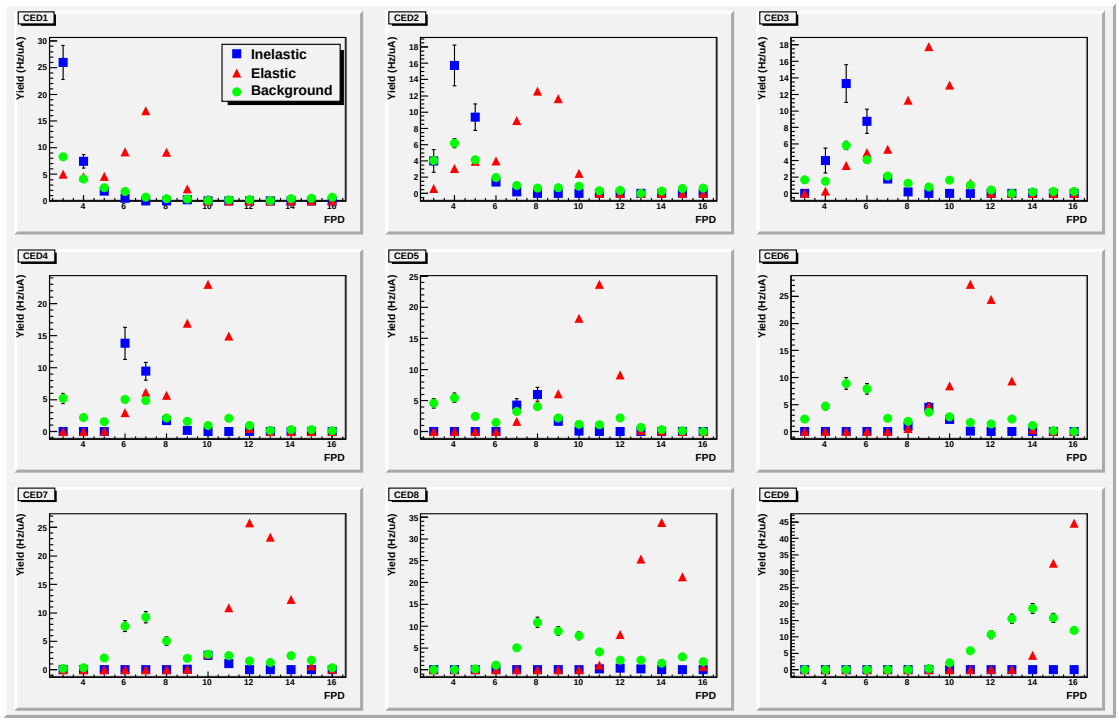

Figure D.21: The total background, inelastic and elastic yields.

D.5.2 Asymmetry Plots

The asymmetries are functions of Q^2 so they do have a bit of a variation across the matrix due to the kinematic dependence even for a given simulated process. Just as the yields vary from cell to cell because of the z location of the various 'targets', so do the asymmetries. The contributions from the elastic and inelastic scattering from each of the aluminum and helium windows and the helium itself is shown in Figure D.22. The asymmetry was calculated from the asymmetries for the proton and neutron using the quasi-static approximation.

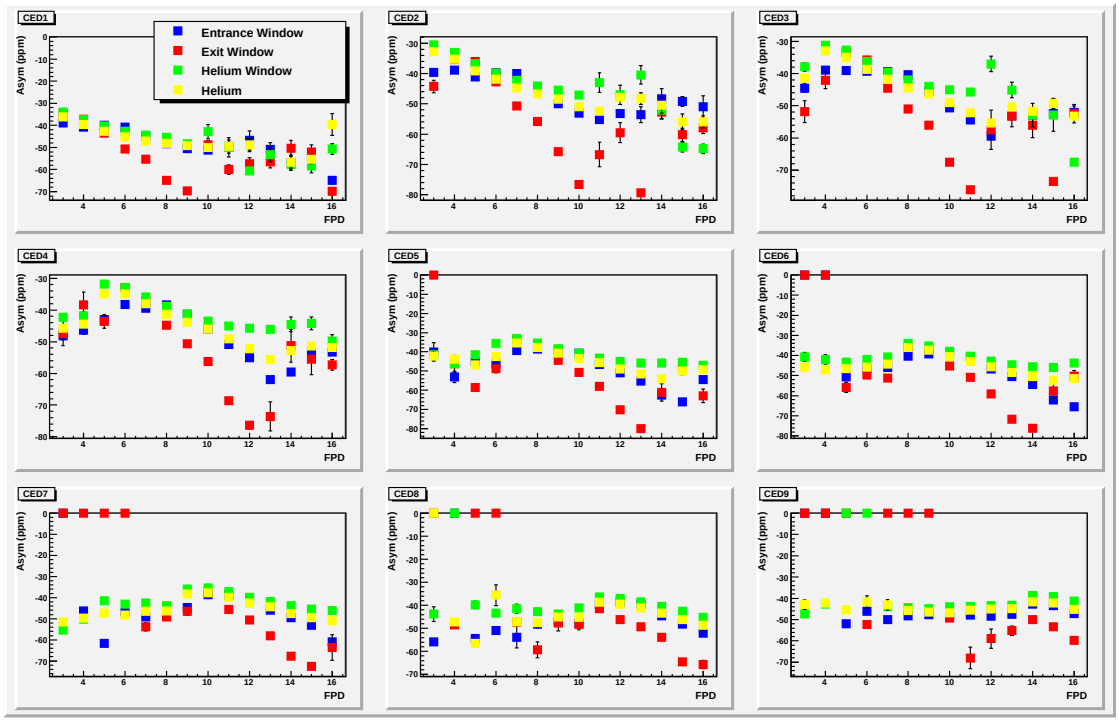

Figure D.22: The 'elastic' and 'inelastic' asymmetries from the aluminum windows.

The asymmetries from various simulation processes are combined using the yield fractions

calculated from the dilution analysis. The pi0 and quad asymmetries are set to zero, and the aluminum and helium are combined (see Figure D.23). The background asymmetries are then calculated from the yield average of the aluminum+helium asymmetry and the pi0 and quad asymmetries. The background asymmetry is compared to the simulated elastic and inelastic asymmetries in Figure D.24 (the inelastic asymmetries are set to zero if the yield in the cell was zero).

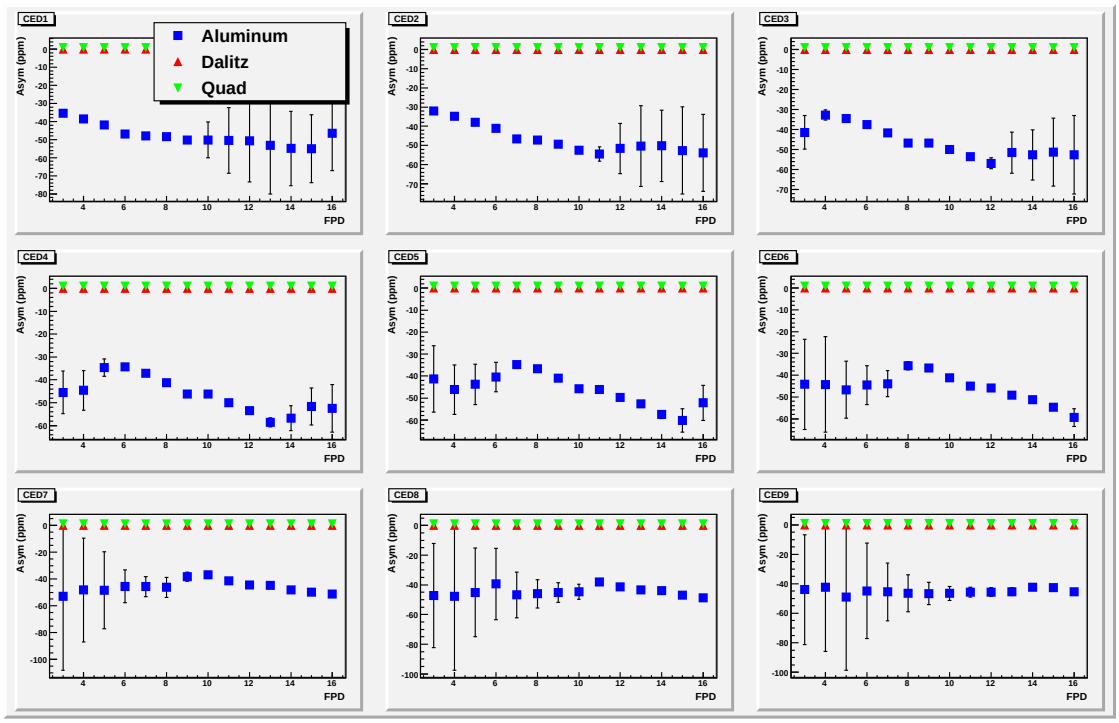

Figure D.23: The combined, yield averaged aluminum and helium asymmetries (the pi0 and quad asymmetries are set to zero).

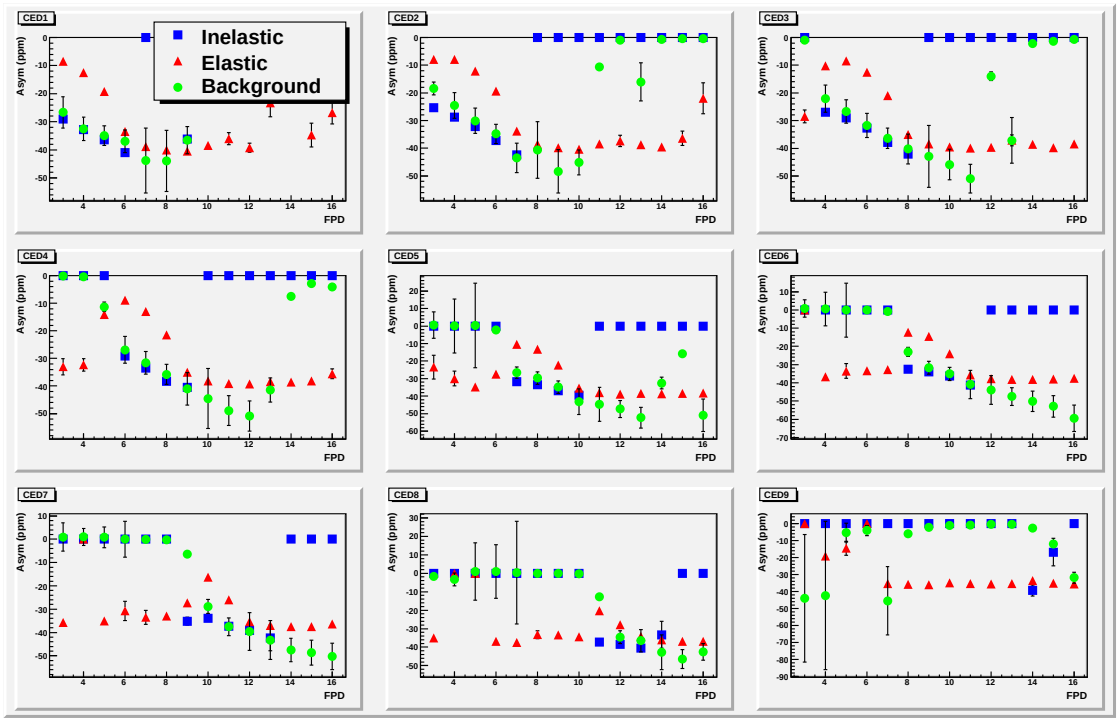

Figure D.24: The yield averaged background, inelastic and elastic asymmetries.

D.6 Wien Angle Settings

The wien angle settings were stored in epics data and written out in the logfiles. I wrote a routine to grep the settings from the log files and have summarized them here in Table D.1. The wien filter is used to account for the precession of the electron's spin as it goes through the bending magnets in the accelerator. There are no elements that would cause the spin to precess out of plane, although there may be some very small residual fields. So the precession occurs mostly in plane (see Figure D.25). In this example, the spin and velocity start out in the same direction, and the spin has precessed by an amount

$$\Delta\phi = \frac{g-2}{2}\frac{E}{m_e}\Delta\theta \tag{D.1}$$

where θ is the bend angle. There are two linacs and also a bend angle of $\sim -37^\circ$ going into the hall, so it is necessary to split the calculation into parts with a constant energy. In the case of the higher energy, both linacs were used, and they were set to about 325.2 MeV (and an injector energy of 36.6MeV [60]). So in the first arc the precession was about 148°, but then the electrons were further accelerated in the south linac, so it is necessary to take that into account when calculating the precession into the hall, which is about 57°, for a total precession of 91°. In the case of the lower energy, only the north linac was used. So the precession of the electrons spin is $\sim 148^\circ$ through the first arc and $\sim 30^\circ$ in the hallc arc, for a total precession of about 118°. In both the high and low energy the initial polarization was actually opposite the electron's momentum, so without the wien filter the polarizations would be roughly beam left, so in the higher energy the wien angle is set to $\sim 90^\circ$, and in the lower energy it is set to $\sim 70^\circ$ to get positive helicity in the hall with the polarization in the same direction as the electron's momentum. For the transverse polarization, the wien filter is set 90° lower so that the polarization is positive to beam left.

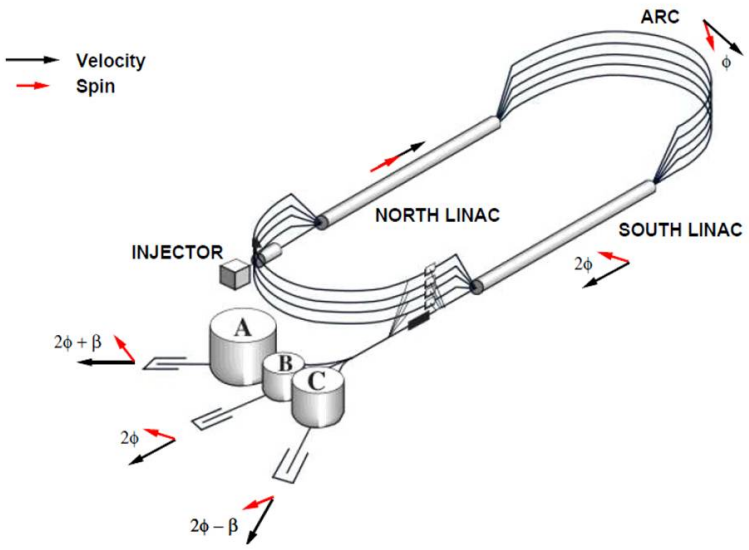

Figure D.25: An example of how the spin precesses through the accelerator.

Table D.1: Summary of the Wien angle settings for each dataset.

Dates	Dataset	Polarization	Run Range	Wien Angle Setting
March '06 - April '06	H687a	Longitudinal	28330 - 29072	92.492
July '06 - August '06	H362	Longitudinal	29973 - 30795	71.224
July '06 - August '06	H362	Transverse	30803 - 30838	-18.97
July '06 - August '06	H362	Transverse	30839	-16.26
Sept. '06 - Oct. '06	H687b	Longitudinal	30992 - 31820	92.246
Sept. '06 - Oct. '06	H687b	Transverse	31350 - 31370	1.6959
Oct. '06 - Dec. '06	D362	Longitudinal	31938 - 32551	92.246
Oct. '06 - Dec. '06	D362	Longitudinal	32552 - 32565	90.844
Oct. '06 - Dec. '06	D362	Longitudinal	32566 - 33040	90.043
Jan. '07 - Feb. '07	D687a	Longitudinal	33143 - 33999	69.223
Jan. '07 - Feb. '07	D687b	Longitudinal	34000 - 34251	69.223
Jan. '07 - Feb. '07	D362	Transverse	33992 - 34018	-20.99
March '07	D687b	Longitudinal	34319 - 34454	90.549
March '07	D687b	Longitudinal	34459 - 34851	93.247
March '07	D687b	Transverse	34762 - 32765	1.1959

D.7 Transverse Asymmetries

The octant to octant asymmetries and uncertainties for insertable half wave plate (IHWP) state IN and OUT for each transverse dataset are presented, along with the differences (middle, In PLUS OUT) and averages (bottom, Out MINUS In) of the two states. The data are after the electronics and linear regression corrections and has also been unblinded and beam polarization corrected, but do not have the background asymmetry correction. Each is fit with a sinusoidal fit of the form $y = Asin(x + \phi) + \Delta$ where the amplitude, A, the phase, ϕ and the offset, Δ are allowed to vary freely. The fit parameters p0, 1, and 2 correspond to the amplitude phase and offset, respectively.

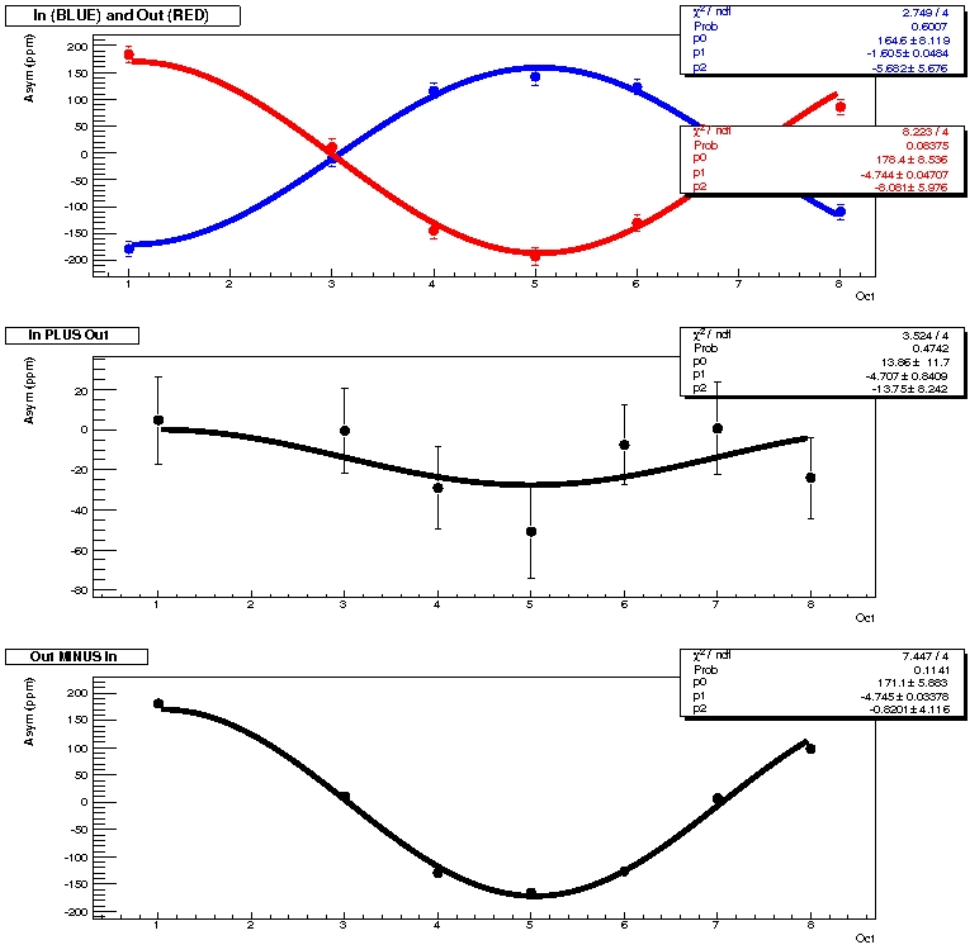

Figure D.26: H362 transverse asymmetries, pass 4, sinusoidal fit with free phase, amplitude and offset, unblinded and beam polarization corrected.

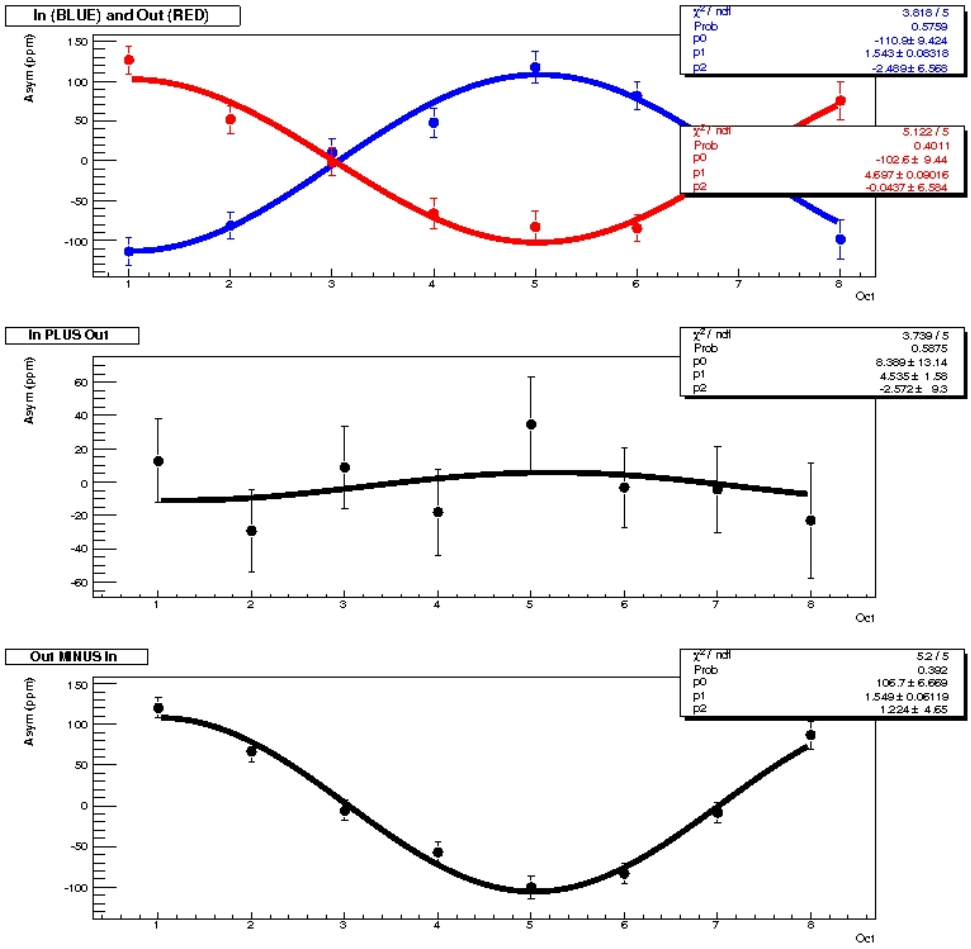

Figure D.27: D362 transverse asymmetries, pass 4, sinusoidal fit with free phase, amplitude and offset, unblinded and beam polarization corrected.

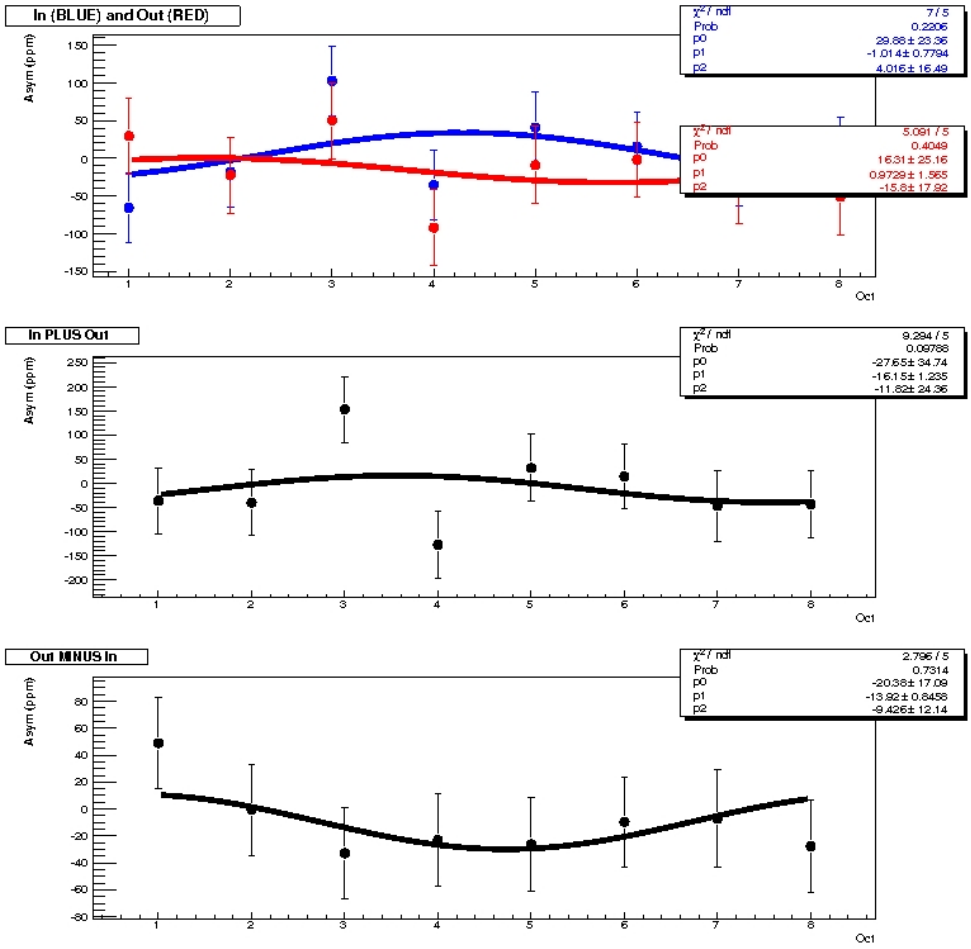

Figure D.28: H687 transverse asymmetries, pass 4, sinusoidal fit with free phase, amplitude and offset, unblinded and beam polarization corrected.

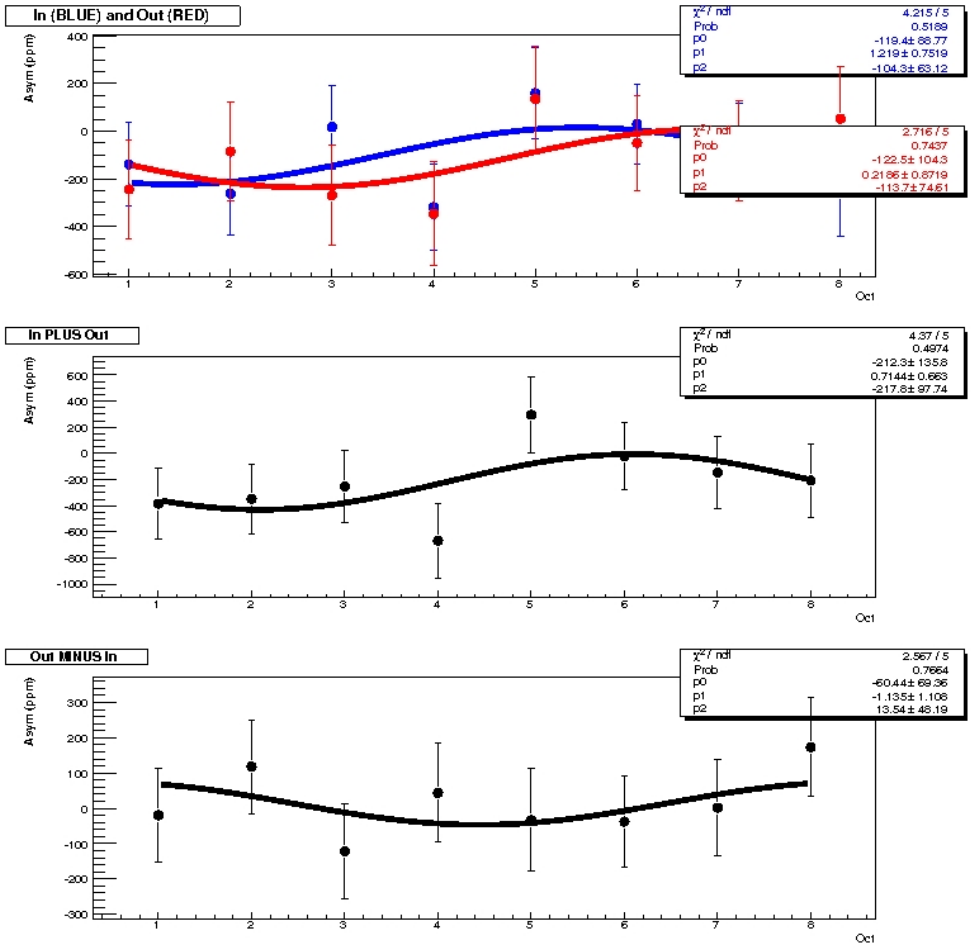

Figure D.29: D687 transverse asymmetries, pass 4, sinusoidal fit with free phase, amplitude and offset, unblinded and beam polarization corrected.